UNIVERSITY OF SOUTHAMPTON

FACULTY OF NATURAL & ENVIRONMENTAL SCIENCES

Chemistry

Electrochemical Studies of Diffusion in Supercritical Fluids

by

Jack Anthony Branch

Thesis for the degree of Doctor of Philosophy

January 2015

UNIVERSITY OF SOUTHAMPTON

ABSTRACT

FACULTY OF NATURAL & ENVIRONMENTAL SCIENCES

Chemistry

Thesis for the degree of Doctor of Philosophy

ELECTROCHEMICAL STUDIES OF DIFFUSION IN SUPERCRITICAL FLUIDS

Jack Anthony Branch

The challenges and specialised equipment associated with supercritical electrochemistry means standard reference electrodes (such as the saturated calomel electrode) cannot be used. The aim of the thesis is the investigation of a range of metallocenes as model redox systems against a Pt pseudo reference electrode in supercritical fluids. This work was then extended to the development of a new high pressure reactor. Initially, a range of metallocenes were investigated in liquid analogues of the supercritical fluids (acetonitrile and dichloromethane) to investigate their suitability. Cyclic voltammetry performed at both micro and macro electrodes were used to examine the behaviour of each individual redox couple. Electrochemistry of the metallocenes were then evaluated in supercritical fluids (supercritical carbon dioxide with acetonitrile and supercritical difluoromethane) for investigation as model redox systems. The diffusion coefficients have been determined at both micro and macro electrodes for both supercritical fluids. The implementation of baffled micro and macro electrodes has shown that the intrinsic convection (at the electrode surface) within supercritical fluids can be dampened. The diffusion of metallocenes in nanoporous aluminium oxide membranes (13 – 55 nm diameter cylindrical pores), in both supercritical fluids has also been investigated. This work was then extended to the development of a new high pressure plastic reactor leading to the first, successful, supercritical fluid electrodeposition of bismuth in the plastic reactor.

Table of Contents

DECLARATION OF AUTHORSHIP

I, Jack Anthony Branch declare that this thesis and the work presented in it are my own and has been generated by me as the result of my own original research.

Electrochemical Studies of Diffusion in Supercritical Fluids

I confirm that:

1. This work was done wholly or mainly while in candidature for a research degree at this University;
2. Where any part of this thesis has previously been submitted for a degree or any other qualification at this University or any other institution, this has been clearly stated;
3. Where I have consulted the published work of others, this is always clearly attributed;
4. Where I have quoted from the work of others, the source is always given. With the exception of such quotations, this thesis is entirely my own work;
5. I have acknowledged all main sources of help;
6. Where the thesis is based on work done by myself jointly with others, I have made clear exactly what was done by others and what I have contributed myself;
7. Parts of this work have been published as:

J. A. Branch, D. A. Cook, P. N. Bartlett; Electrochemical studies of decamethylferrocene in supercritical carbon dioxide mixtures; *Phys. Chem. Chem. Phys.* **2015**, 17 (1), 261-267

Signed: .....

Date:.....

Acknowledgements

First and foremost I would like to thank my supervisor Prof. Phil Bartlett for his extensive support and knowledge, along with his unrelenting patience. I would also like to thank my advisor Prof. John Owen for his help and support and not deterring me from a PhD in my transfer viva. I would also like to give a special thanks to Prof. George Attard and Prof Andrea Russell, both of whom encouraged me to pursue a PhD.

I would like to especially thank Dr. David Cook for all of his help and support throughout my PhD, thanks for answering all my stupid questions! I would also like to acknowledge past and present members of the Bartlett group. Dr. Gabriela Kissling for teaching me everything I was doing was wrong. Dr. Charlie Cummings for always showing an interest in my work and helping me wherever possible. Dr. Pete Richardson for showing me how easy supercritical electrochemistry should be. I would also like to thank the Friday night stags crew, Dr. Andy Naylor, Dr. Thomas Foley, Jacob Locke, Jimmy Frith, Dr. Douglas Offin, Dr. Maciek Sosna, and Michael Palmer, I still maintain most of my PhD ideas came from conversations with you guys in the pub. I would also like to thank George Sanderson, Pierre de Jager and Rick Foti for keeping me sane over the last three years. I would also like to acknowledge and thank Prof. David Smith and Dr. Mehrdad Alibouri for their help with the plastic reactor. I would also like to acknowledge anyone in the SCFED group who has helped me throughout the last three years.

I would like to send a huge thanks to my family, Mum, Dad, Oliver, Harry, Rebecca & Ed, your love and support has been pivotal to me making this far. Last of all I would like to dedicate this Thesis to my Grandparents, Reginald and Joyce Coppen, who sadly passed away during the course of my PhD. Sorry you could not be here to see this, I miss you, and I probably should have finished it sooner.

Chapter 1: Introduction

1.1 Supercritical Fluids

The supercritical phase was first discovered by Baron Charles Cagniard de la Tour in 1822. Cagniard de la Tour's first experiment in which he observed the supercritical phase involved rolling a flint ball in a sealed Papin digester (predecessor to the steam engine) filled with liquid (water, alcohol, ether and carbon disulphide)[1-3]. Rolling the device resulted in a splashing noise as the flint penetrated the liquid-vapour interface[3]. Cagniard de la Tour noticed by heating the device to far beyond the point of the liquid, the splashing sound stopped[3]. At this point the boundary between the liquid and gaseous phase was gone, and marked the discovery of the supercritical phase[3]. Cagniard de la Tour also described how he heated a sealed glass tube of alcohol under pressure[1,3]. He observed that the liquid expanded to twice its original volume until it vanished altogether making the tube appear completely clear[3]. When the system was re-cooled, a thick cloud appeared[3]. Cagniard de la Tour named his discovery "*état particulier*"[1-3]. He also measured the critical temperature at which the interface tension vanished and discovered that at certain temperatures beyond which total vaporisation of the liquid occurs no increase in pressure would liquefy the gas[2,3].

In 1845, Michael Faraday[4] wrote and commented on the critical point, he referred to this as "*Cagniard de la Tour's state"* and "*the Cagniard de la Tour point"*. Later in 1861, Dmitri Mendeleev also commented on the phenomenon and referred to it as the "*absolute Siedetemperatur"* or absolute boiling point[3,5]. Eventually, Thomas Andrews coined the term *critical point*, which is still used today[3,6].

In 1869, Andrews[6] described his experiments on the effects of temperature and pressure on sealed glass tubes of partially liquefied carbonic acid. In his paper, he describes the critical point as the temperature is raised to 88º Fahr. (304 K) "the surface of demarcation between the liquid and gas became fainter, lost its curvature, and at last disappeared"[6]. Andrews further noted that the space was occupied by a "homogenous fluid, which exhibited, when the pressure was suddenly diminished or the temperature slightly lowered, a peculiar appearance of moving or flickering striae throughout its entire mass"[6]. Andrews noted that the "great changes of density which occur about this point (critical point) produce the flickering movements"[6]. Andrews also commented on attempting to take the substance above its critical temperature and pressure. Andrews noted, "at temperatures above 88º Fahr. No apparent liquefaction of carbonic acid, or separation into two distinct forms of matter, could be effected, even when a pressure of 300 or 400 atmospheres was applied"[6].

A substance that has been taken above its critical temperature (T_C) and pressure (p_C) is called a supercritical fluid, Figure 1.1. Romang and Watkins[7] took selected properties to illustrate the different properties of gases, liquids and supercritical fluids, this information makes up Table 1.1.

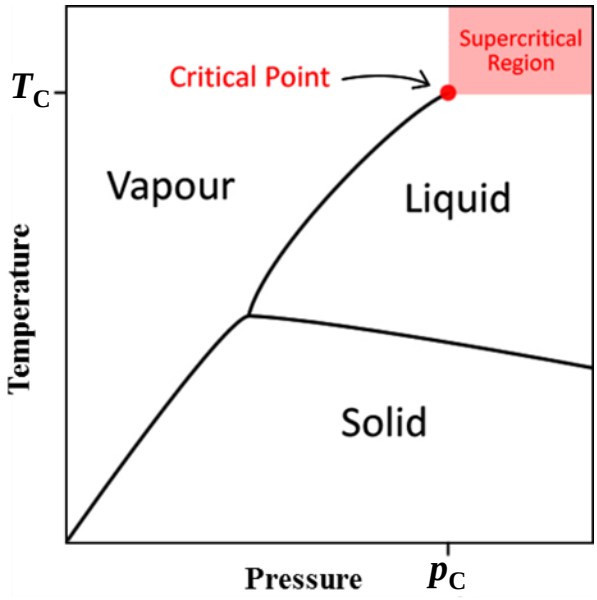

Figure 1.1. Generic phase diagram of a substance above its critical pressure and temperature.

Table 1.1. Comparison of selected properties of supercritical fluids to liquids and gases[7].

	Liquid	**SCF**	**Gas**
Density (g cm^{-3})	1	0.1 – 1	10^{-3}
Viscosity (Pa s)	10^{-3}	10^{-4} – 10^{-5}	10^{-5}
Diffusivity (cm^2 s^{-1})	10^{-5}	10^{-3}	10^{-1}
Surface Tension (dyn cm^{-1})	20-50	0	0

Supercritical fluids (hereby referred to as SCFs) have increased transport properties which are a result of the low viscosity of these media[8]. The low viscosity of SCFs leads to enhanced mass transport to and from the electrode surface[9]. SCFs solvent properties can be dramatically altered with only modest changes to temperature or pressure, making them attractive as solvation media[9]. SCFs gas-like properties include low viscosities and the absence of surface tension, while their liquid-like properties allow for the dissolution and transport of materials, making them well suited for processing nanostructures[7]. SCFs allow for a wide range of techniques to be employed for making nanowires[10], nanostructures[11], nanocrystalline materials[12], thin film

deposition[13], and deposition into mesoporous silica templates[14]. SCFs have additionally been applied to fine and speciality chemistry, polymer and material modification, biotechnology and pharmaceuticals, dry cleaning[14], extraction and chromatography[15]. A range of different substances have been used as a SCF for electrochemistry including ammonia (NH_3), sulphur dioxide (SO_2), acetonitrile (CH_3CN) and water (H_2O)[16]. More recently hydrofluorocarbons have been employed as a SCF for electrochemistry. Hydrofluorocarbons are useful SCFs due to their easily accessible critical temperatures and pressures, high polarity[17], and very high densities in the supercritical state[18].

1.2 Supercritical Fluids as a Solvent for Electrochemistry

1.2.1 Supercritical Fluids Studied for Electrochemistry

Although SCFs have unique properties and have received increasing attention, there is very little literature on the use of SCFs as a solvent for electrochemistry. The earliest publication of SCFs being used for electrochemical processes was in 1981 and was performed by Silvestri *et al*[19]. The SCFs they investigated involved carbon dioxide (CO_2), bromotrifluoromethane ($CBrF_3$), hydrogen chloride (HCl) and NH_3[19]. Their research showed that CO_2 was a poor conductor in both the liquid and supercritical state[19]. They also noted that $CBrF_3$ was also a very poor conductor and that electrolytes were practically insoluble, they concluded that both CO_2 and $CBrF_3$ were unsuitable as solvents[19]. Work with scHCl, although having a higher dielectric constant and appreciable solvent properties in the supercritical state, was unsuitable due to its high corrosivity[19]. Even though it was unsuitable for further experiments, elemental iodine was produced at the anode in a scHCl/KI system[19]. Ammonia was also noted to have a higher dielectric and appreciable solvent properties in sc conditions, these investigations accomplished the anodic dissolution of silver and iron[19,20].

Bard and co-workers provided the most extensive work on the use of SCFs as a solvent for electrochemistry by performing voltammetric studies at near-critical and supercritical conditions. Bard *et al.* studied a range of inorganic compounds in a range of sc solvents; these solvents included NH_3, H_2O, CO_2/H_2O, CH_3CN and SO_2[15,21-27]. The aim of their work was to understand the thermodynamics and kinetics of chemical reactions in SCFs, then use SCF solutions for electrosynthetic purposes[20]. Initial work with NH_3 showed through chronocoulometric techniques that the diffusivity and thus mass transport of *m*-chloronitrobenzene was enhanced in supercritical conditions[27]. Crooks and Bard[23,24] also reported on the first electrochemistry of organic compounds in $scNH_3$, they noted that reactions in liquid NH_3 could be accomplished in $scNH_3$. Their work also demonstrated that the dielectric

constant and density could be manipulated in $scNH_3$ by changing the pressure or temperature[23]. Bard and co-workers[25,26,28] studied the use of H_2O as a SCF for electrochemistry. The unique properties of water near its critical point render it a good solvent for both organics and salts[20]. The experimental difficulties associated with scH_2O, including high critical temperatures, pressures (T_C = 647 K, p_C = 22.1 MPa) and corrosion make it a difficult SCF to employ[20,25]. McDonald *et al.*[25] described additional difficulties associated with working with scH_2O which included long equilibration times and electrodes could not be removed and replaced for cleaning or inspection, this is a problem when working with any SCF.

1.2.2 Supercritical Carbon Dioxide as a Solvent for Electrochemistry

Although being dismissed as a SCF for preparative electrolyses by Silvestri *et al.*[19] carbon dioxide has been used as a SCF[7,8,11-14,29-56] for electrochemistry due to it being non-toxic, inexpensive and non-flammable. Supercritical CO_2 although having a low dielectric constant ($\varepsilon < 2$)[30], is of interest as a sc solvent for electrochemistry due to its inert nature. The easily accessible critical temperature and pressure (T_C = 304 K, p_C = 7.3 MPa) also made it an attractive solvent for electrochemical investigations[30]. The most extensive fundamental electrochemical studies of CO_2 as a SCF have been performed by Abbott and co-workers. Abbott and Harper[30] carried out electrochemical investigations in $scCO_2$ by dissolving hydrophobic electrolytes (tetrakis(decyl)ammonium tetraphenylborate) to give a conducting media. They found some conductivity (~ 10^{-6} S cm^{-1}) and obtained some, poorly resolved, voltammetry[30]. Abbott and Harper[8] then used tetraalkylammonium tetraarylborates to make the first measurements of double layer capacitance and conductivity in $scCO_2$. In their work they showed that tetraalkylammonium tetraarylborates in $scCO_2$ led to an increased conductivity of the system[8]. They also noted that high concentrations of the supporting electrolyte led to an increase in the viscosity of the sc media, thus small concentrations were used ranging from 0 to 0.03 mol dm^{-3} [8].

The use of tetraalkylammonium tetraphenylborates can therefore increase the conductivity of $scCO_2$ for use as a SCF. Additionally the use of polar co-solvents has been investigated with the aim of raising the dielectric constant of $scCO_2$. Goldfarb and Corti[31] used varying amounts of methanol with $scCO_2$ and studied the dielectric and voltammetric properties. Increasing the mole fraction of methanol resulted in a rise of the dielectric constant for the mixture[31]. The most extensive study of the use of co-solvents on the phase behaviour and conductivity of $scCO_2$ has been studied by Bartlett *et al*[46]. The investigation used both acetonitrile (CH_3CN, ε = 37) and methanol as potential co-solvents for $scCO_2$. The high dielectric constant and complete miscibility with CO_2 under easily accessible experimental conditions made both viable candidates[46]. Using a fixed molar ratio of co-solvent to CO_2 (0.14), tetrabutylammonium

tetrafluoroborate ([NBu_4^n][BF_4]) was found to be five times more soluble (for similar pressures and temperatures) when acetonitrile was used as a co-solvent compared to methanol in $scCO_2$ mixtures[46]. The high solubility of supporting electrolyte meant acetonitrile was chosen as a co-solvent over methanol. Although increasing the concentration of [NBu_4^n][BF_4] in $scCO_2$/MeCN raises the pressure required to form a homogenous solution[46]. Figure 1.2 demonstrates the phase behaviour of $scCO_2$/MeCN (13 wt%) with 20 mM [NBu_4^n][BF_4] as supporting electrolyte.

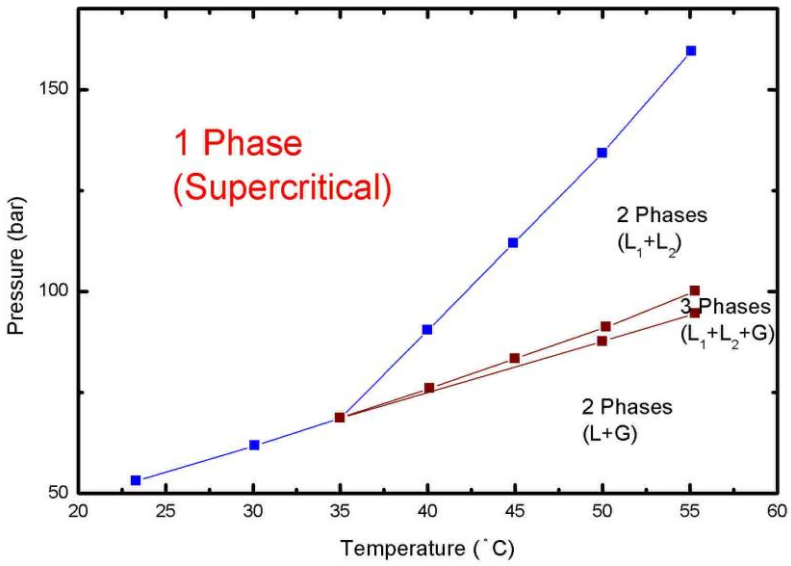

Figure 1.2. Phase diagram demonstrating the different phases exhibited by $scCO_2$/MeCN (13 wt%) with 20 mM [NBu_4^n][BF_4] at varying temperature and pressures[46].

The use of a view cell revealed four distinct phase regions at varying temperatures and pressures[46]. The temperature of the system was held at 319 K (46 °C) and the pressure of the system was varied from ≈ 13 MPa (130 Bar) to ≈ 6 MPa (60 Bar)[46]. When the highest pressure was employed (13 MPa), a single phase was observed showing the mixture in the supercritical phase[46]. When the pressure was lowered to 10 MPa (100 Bar), two distinct liquid phases were observed, which was attributed to liquid MeCN containing electrolyte and was surrounded by liquid CO_2[46]. A triple phase was observed at pressures of ≈ 8 MPa (80 Bar) which comprised of two liquid phases with a gaseous phase observed at the top[46]. This was considered a combination of liquid MeCN with dissolved electrolyte, along with a liquid CO_2 layer and a gaseous CO_2 layer above[46]. When the pressure was lowered to its lowest point of ≈ 6 MPa another distinct two phase system was observed[46]. This was attributed to a liquid and gas phase, where the bottom layer was liquid MeCN with dissolved electrolyte (possibly with some dissolved gaseous CO_2) with a gaseous layer of CO_2 on top[46]. This experiment highlights the need to fully characterise the phase behaviour of a supercritical system as only modest changes in pressures can take the system away from the supercritical region.

To enhance the conductivity of $scCO_2$/MeCN mixtures, a range of electrolyte salts were synthesised. The salts replaced the tetrabutylammonium cation or the tetrafluoroborate anion with varying derivatives. It was found that changing the anion from tetrafluoroborate to BARF (fluorinated derivatives of $[BPh_4]^-$) had the largest effect on the conductivity[46]. A tetrabutylammonium cation with a BARF anion ($[NBu_4^n][B(3,5\text{-}C_6H_3(CF_3)_2)_4]^-$) was the most suitable supporting electrolyte. The electrolyte was found to have an order of magnitude higher molar conductivity compared to $[NBu_4^n][BF_4]$[46].

1.2.3 Supercritical Hydrofluorocarbons as a Solvent for Electrochemistry

Another approach is to use hydrofluorocarbons (HFCs) as supercritical solvents as these are polar and give higher dielectric fluids whilst retaining reasonable critical temperatures and pressures. Fundamental studies of the conductivity of scHFCs with $[NBu_4^n][BF_4]$ have also been reported in literature by Abbott[57,58] and Olsen and Tallman[59]. Abbott and co-workers also performed additional fundamental studies in scHFCs, which included double layer structure[60], solubility of aromatic hydrocarbons[61], hydrogen bond interactions[17], electrochemical reduction of CO_2 (performed in $scCO_2$ with 1, 1, 1, 2-tetrafluoroethane as a polar modifier)[32] and effects of electrolyte concentration on viscosity and voltammetry[62].

Bartlett *et al.*[63] reported the phase behaviour and conductivity of electrolytes in scHFCs in a study analogous to their work in $scCO_2$. HFCs have a higher dielectric constant compared to $scCO_2$ and thus avoid needing a polar co-solvent. The phase behaviour of trifluoromethane (CHF_3), difluoromethane (CH_2F_2) and 1, 1, 1, 2-tetrafluoroethane (CH_2FCF_3) containing $[NBu_4^n][BF_4]$, $[NBu_4^n][B(3,5\text{-}C_6H_3(CF_3)_2)_4]$ and $Na[B(3,5\text{-}C_6H_3(CF_3)_2)_4]$ was studied and the conditions for forming a single supercritical phase was established[63]. All three HFCs were found to be good solvents for $[NBu_4^n][BF_4]$, but the results showed that CH_2F_2 system had the lowest p_C for dissolving a given amount of $[NBu_4^n][BF_4]$[63], Table 1.2 gives the physical properties of the HFCs. Additionally the solubility of $Na[B(3,5\text{-}C_6H_3(CF_3)_2)_4]$ in CH_2F_2 was found to be unexpectedly high[63]. The conductivity of $[NBu_4^n][B(C_6F_5)_4]$, $[NBu_4^n][B(3,5\text{-}C_6H_3(CF_3)_2)_4]$, $[NR_fBu_3^n][B(3,5\text{-}C_6H_3(CF_3)_2)_4]$ ($R_f = (CH_2)_3C_7F_{15}$) and $Na[B(3,5\text{-}C_6H_3(CF_3)_2)_4]$ were studied in $scCH_2F_2$[63]. The results showed that these salts were more conducting than $[NBu_4^n][BF_4]$ under the same conditions but the increase was much less significant than that reported for $scCO_2$/MeCN[63]. It was concluded, however, that both the $[NBu_4^n][BF_4]$ or BARF salts would be suitable background electrolytes for electrodeposition from $scCH_2F_2$[63].

Table 1.2. Physical properties of some hydrofluorocarbons[64].

Physical Property	CHF_3	CH_2F_2	CH_2FCF_3
T_C / K	299.29	351.26	374.21
p_C / MPa	4.832	5.782	4.049
ρ_C / kg m^{-3}	526.5	424.00	511.90
μ / D	1.65	1.98 ± 0.02	1.80 ± 0.22

1.2.4 Electrodeposition, Electroplating and Synthesis from Supercritical Fluids

Electrodeposition from supercritical fluids is also sparse in literature. The earliest work is that of Williams and Naiditch[65] in 1976 with Silvestri *et al*[19]. five years later. Williams and Naiditch[65] presented the deposition of silver from near- and supercritical NH_3. In the report, Williams and Naiditch used silver nitrate ($AgNO_3$) to electrodeposit silver in the form of needles and dendrites on a Pt cathode[65]. $AgNO_3$ was chosen due to its solubility in liquid NH_3, additionally electrodeposited Ag metal is insoluble in NH_3[65]. Although depositing Ag from the mixture, there is no identification as to the phase behaviour of the system. The temperature of the system is quoted by the authors but there is no identification as to the pressure of the system. Having the system above a critical pressure and temperature is fundamental to being in the supercritical phase. Williams and Naiditch[65] concluded that electrodeposition had been performed in the supercritical phase. However with no indication as to the pressure of the system, it is not clear that the system was indeed supercritical. Finally, McDonald *et al*.[25] in 1986 reported on the deposition of Cu from copper (I) chloride ($CuCl_2$) under supercritical, or close to supercritical, H_2O containing KCl at 573 K and 8.2 MPa.

Sone and co-workers recently reported the electroplating of nickel from emulsions of $scCO_2$[34,38,47,55]. To achieve a CO_2 in water emulsion, a non-ionic block co-polymer, poly(ethylene oxide)-b-poly(propylene oxide) was added[34]. The electroplating bath used was a mixture of nickel sulphate, nickel chloride and boric acid[34]. The electroplated films were found to be smoother than films plated by conventional aqueous electroplating[34]. Electroplating in aqueous electrolytes leads to cathode reactions, including H^+ reduction, the hydrogen gas formed leads to voids and defects in the plated films[34]. This is overcome in supercritical conditions as the hydrogen gas evolved is completely miscible with $scCO_2$[55]. The dissolved hydrogen gas therefore diffuses away from the electrode surface leading to smoother films. This is not suitable for electrodeposition within micro- and meso-porous templates; also the presence

of water negates the advantages of the electrochemical potential window gained by using $scCO_2$[14].

Electrochemical syntheses of polymers from $scCO_2$ and $scCHF_3$ have also been reported in the literature[36,40,66]. Anderson *et al.*[36] first reported the electrochemical synthesis and characterisation of polypyrrole and polyaniline from $scCO_2$ in 2002[36]. The group used CO_2 containing 13.1 vol % MeCN, 0.16 M pyrrole and 0.16 M $[NBu_4^n][PF_6]$ at 323 K and 9.65 MPa[36]. The results of the study were put into question by Yan *et al*[40]. Yan *et al.*[40] using a view cell, showed that for the same concentration of materials, at the same temperature and pressure, that a biphasic mixture (2 separate phases) was observed and not a supercritical phase. Their work showed, that to gain a single phase for the mixture at the same temperature and pressure, the concentration of the supporting electrolyte needed to be lowered from 0.16 to 0.04 M[40]. This illustrates the problems associated with work in supercritical fluids. It is not sufficient to rely on the critical temperature and pressure of the pure fluid, but it is essential to fully characterise the phase behaviour of the whole system. Yan *et al.*[40] successfully electrochemically synthesised polypyrrole onto an ITO electrode from a single phase $scCO_2$/MeCN mixture. The polypyrrole was found to have a smoother film than those deposited from acetonitrile[40]. It was found that additional CO_2 decreased the polymerisation rate of the film in $scCO_2$/MeCN, suggesting that the low viscosity of the sc system was not important in the growth rate of the smooth polypyrrole film[40]. Atobe *et al.*[66] reported the first successful electrochemical synthesis of polypyrrole and polythiophene from $scCHF_3$ containing 10 mM pyrrole or thiophene with 40 mM $[NBu_4^n][PF_6]$ at 323 K and 15 MPa in 2004. Cyclic voltammetry performed in the system indicated that polymerisation rates were increased in $scCHF_3$ compared to MeCN[66]. It was reported that the films polymerised from $scCHF_3$, although being thinner than those produced in acetonitrile, exhibited a higher electrochemical capacity (~ 6x bigger for polypyrrole and ~ 10x higher for polythiophene). It was also observed that adjusting the pressure of $scCHF_3$ resulted in switching the polymerisation on or off[66]. This was attributed to the precipitation of $[NBu_4^n][PF_6]$ at lower pressures[66].

Watkins and co-workers have reported the deposition of metal and metal oxide films from SCFs onto etched silicon substrates[11,13,33,37,41,49]. To deposit gold films onto the substrates, a technique called chemical fluid deposition (CFD) was used[11]. CFD involves the chemical reduction of organometallic compounds (in this case dimethyl(acetylacetonate)gold (III)) in SCFs; the reducing agent used was H_2[11]. It was shown that void-free trench filling had occurred in features less than 100 nm wide by 1 µm deep. CFD was also used to deposit Co and Ni films from their metallocenes, using H_2 reduction, onto various substrates, including Si, TaN/Si and TiN/Si[37]. To restrict the deposition to the heated substrates only, the reactor walls were maintained between

90 and 120 ºC[37]. A review by Romang and Watkins[7] highlighted the advantages of supercritical fluids for the fabrication of semi-conductor devices.

The most conventional way of making semiconductor materials is through chemical vapour deposition (CVD). CVD is not a suitable method for deposition into high aspect ratio nanopores (small diameter pores with long pore lengths), this is due to blocking of pores due to non-conformal filling. As SCFs have the best properties of liquid and gas, the lack of surface tension allows full penetration of high aspect ratio nanopores[14]. Supercritical fluid chemical vapour deposition (SCFCVD) and supercritical fluid electrodeposition (SCFED) could be used in conjunction to deposit conducting and semiconducting materials into high aspect ratio nanopores, Figure 1.3.

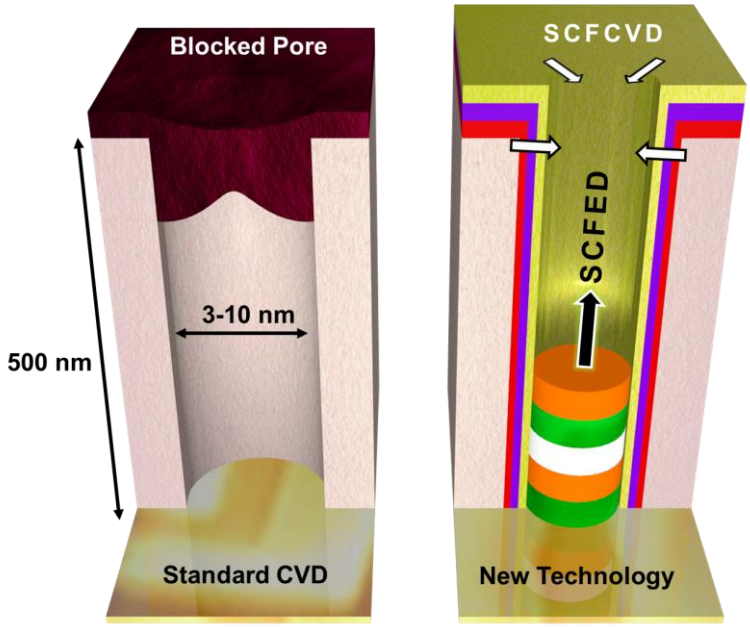

Figure 1.3. Schematic highlighting the advantages of sc systems for pore filling and the complimentary properties of SCFED and SCFCVD.

The first demonstration of electrodeposition into nanoporous templates was performed by Ke *et al.*[14] in 2009. Their work reported the deposition of 3 nm diameter copper nanowires in mesoporous silica templates. Indium tin oxide (ITO) slides were dip coated in a solution of Brij56:TMOS:0.5 M HCl:MeOH (1:1.8:1:3.8 by weight) to produce mesoporous silica templates[14]. The templates were roughly 200 nm thick with a hexagonal array of approximately 3 nm diameter cylindrical pores approximately 6 nm apart[14]. Depositions were carried by specially selected metal precursors, $[Cu(MeCN)_4][B(3,5\text{-}C_6H_3(CF_3)_2)_4]$, and supporting electrolyte, $[NBu_4^n][B(3,5\text{-}C_6H_3(CF_3)_2)_4]$, all in $scCO_2$/MeCN (12.1 wt%) at 311 K and 17.2 MPa[14]. Ke *et al.*[14] also demonstrated the deposition of copper (from $[Cu(MeCN)_4][BF_4]$,

silver ($[Ag(MeCN)_4][BF_4]$) and cobalt ($[Co(Me(CN)_6][BF_4]_2$) in $scCO_2$/MeCN (13 wt%) using $[NBu_4^n][BF_4]$ as a supporting electrolyte onto both micro and macro electrodes[14]. This was extended to bulk deposition by plating Cu onto macroscopic (0.4 to 1 cm^2) evaporated gold on glass electrodes[14]. Four-point probe measurements gave film resistivities for the best films of 4 x 10^{-6} Ω cm, which are comparable to deposition from aqueous solutions[64] (1.75 to 2 x 10^{-6} Ω cm) or by chemical deposition in $scCO_2$ reported by Watkins *et al*[67]. (2 x 10^{-6} Ω cm). It was concluded that due to the lack of evidence of impurities (incorporated from the plating bath) that the quality was high and close to that required for device applications.

In 2010, Cook *et al.*[43] reported the deposition of copper from two precursors, $[Cu(hfac)_2]$ (where hfac is hexafluoroacetylacetonate) and $[Cu(MeCN)_4][BF_4]$ in $scCO_2$/MeCN and supercritical trifluoromethane (CHF_3) at 310 – 311 K and 17 – 20 MPa using either $[NBu_4^n][BF_4]$ or $[NBu_4^n][B(3,5\text{-}C_6H_3(CF_3)_2)_4]$ as the supporting electrolyte. Investigations with $[Cu(hfac)_2]$ in $scCO_2$/MeCN showed no single, distinct plating wave in the voltammetry and more problems were met when trying to deposit[43]. The long time needed to vent and disassemble the cell after deposition meant the electrodeposited copper was often stripped from the working electrodes before they could be removed from solution[43]. This was overcome by venting the cell quickly or venting slowly and holding the electrode at the plating potential, although only a few copper films could be deposited, these were dark grey in colour and rough[43]. Through EDX analysis, it was shown that these films were contaminated with fluorine and carbon and it was concluded to not perform further detailed studies of $[Cu(hfac)_2]$ in $scCO_2$/MeCN[43]. Investigations with $[Cu(MeCN)_4][BF_4]$ in $scCO_2$/MeCN showed copper reduction with a single wave which reached a plateau along with a clear stripping peak on the reverse anodic scan, indicating it was a more suitable complex for electrodeposition[43]. To determine the solubility of $[Cu(MeCN)_4][BF_4]$ in $scCO_2$/MeCN a series of microelectrode experiments were carried out with varying concentrations of the copper (I) complex. It was observed that the limiting current increased linearly at low concentrations and then reached a plateau at higher concentrations leading to a solubility of 0.49 mM[43]. The diffusion coefficient for $[Cu(MeCN)_4][BF_4]$ in $scCO_2$/MeCN containing 20 mM $[NBu^n_4][BF_4]$ at 310 K was calculated to be 2.30 x 10^{-5} cm^2 s^{-1} which was only a small increase from the corresponding value for the complex in liquid MeCN at 296 K[43]. The deposits gave a smooth, reflective film with only trace impurities and a resistivity of 7.0 x 10^{-6} Ω cm. This was repeated by changing the counter anion of the copper complex from $[BF_4]$ to $[B(3,5\text{-}C_6H_3(CF_3)_2)_4]$, this allows for a higher concentration to be used due to its greater solubility[43]. The supporting electrolyte was also changed to $[NBu^n_4][B(3,5\text{-}C_6H_3(CF_3)_2)_4]$, the conductivity is an order of magnitude larger than that of $[NBu^n_4][BF_4]$ in $scCO_2$/MeCN[43]. Voltammetry performed showed identical features to that obtained with $[NBu_4^n][BF_4]$, with an increased solubility up to at least 16 mM[43]. The diffusion

coefficient for $[Cu(MeCN)_4]^+$ in $scCO_2$ with 12.1 wt% MeCN and 20 mM $[NBu_4^n][B(3,5\text{-}C_6H_3(CF_3)_2)_4]$ at 310-311 K was calculated to be 3.30 x 10^{-5} cm^2 s^{-1}, which is approximately 1.5 times larger than the corresponding value in $scCO_2$/MeCN with 20 mM $[NBu_4^n][BF_4]$[43]. It was again shown that smooth, reflective films could be plated onto gold evaporated glass slides with a resistivity of 4.0 x 10^{-6} Ω cm.

Cook *et al*[43]. also studied the voltammetry and electrodeposition of copper complexes from $scCHF_3$. As mentioned above $[Cu(hfac)_2]$ showed poor voltammetry and there were difficulties associated with deposition in $scCO_2$/MeCN, so a more polar SCF was chosen in the form of CHF_3. The easily accessible critical temperature and pressure (T_C = 299.3 K, p_C = 4.83 MPa) of the SCF would allow deposition to be carried out at relatively low temperautres[43]. The electrolyte consisted of $[Cu(hfac)_2]$ in $scCHF_3$ with 20 mM $[NBu_4^n][BF_4]$ as the supporting electrolyte with hexafluoroacetylacetone (hfacH) added to the solution and voltammetry was recorded at 311 K and 17 MPa[43]. The voltammetry recorded was analogous to that recorded in $scCO_2$/MeCN with the copper complex being reduced to metallic copper in one step with a poorly defined plateau and broad stripping peak[43]. Depositions performed at different potentials all gave copper films but those held as more cathodic potentials appeared to give more homogenous films[43]. Although deposited films gave good resistivities, when hfacH was removed from the system the resistivity increased ~ 5 times[43]. It was concluded that the presence of hfacH appeared to result in higher purity films[43].

In 2012, Ke *et al*[68]. reported the electrodeposition of germanium from both $scCO_2$/MeCN and supercritical difluoromethane ($scCH_2F_2$). Germanium is an extremely important material in a wide range of technologies from fibre optics to photovoltaics[68]. The most common form of deposition of germanium is CVD from $GeCl_4$; electrodeposition of germanium would offer lower temperature growth and open up the possibility of electrodeposition of silicon-germanium layers[68]. The electrodeposition of germanium is challenging due to its reduction occurring at high cathodic potentials in aqueous solutions and proton reduction quickly becomes the dominant cathodic process[68]. Supercritical fluids overcome this problem by having a larger potential window and any protons produced are completely miscible (at least in the case of CO_2) with solution[55,68]. The electrochemistry and electrodeposition of $[NBu_4^n][GeCl_3]$ was studied in both liquid MeCN and in $scCO_2$/MeCN[68]. Although deposition of germanium from liquid MeCN was possible, the deposited material was heavily contaminated by other species (carbon, fluorine and chlorine) from the solution[68]. The contamination most likely came from the electrochemical breakdown of the solvent and background electrolyte[68]. Nevertheless the results were encouraging enough to attempt electrodeposition from the supercritical phase. In $scCO_2$/MeCN, amorphous deposits were produced on platinum and silicon working electrodes at low over potentials (-1.4 V and 0.9 V *vs.* Pt) with long plating times which produced only

thin films[68]. The films deposited in the supercritical phase contained very high levels of impurities of oxygen and carbon compared to liquid MeCN along with additional contamination from chlorine, fluorine and iron (which was attributed to chemical attack of the steel vessel of the reactor)[68].

Ke *et al*[68]. further investigated Ge (IV) reagents in both $scCO_2$/MeCN and $scCH_2F_2$. Investigations using $[GeF_4(MeCN)_2]$ were unsuccessful as a fine white precipitate fouled the electrodes and gave a pale brown oil at the counter electrode in both $scCO_2$ and $scCH_2F_2$, it was also noted that the complex was simply not soluble in $scCH_2F_2$[68]. Due to these problems, $GeCl_4$ was investigated as a Ge (IV) reagent. Phase boundary measurements in $scCH_2F_2$ confirmed a binary mixture; it was also found that $GeCl_4$ was more stable at higher temperatures providing a wider operating temperature range for electrodeposition[68]. Voltammetry of $GeCl_4$ in liquid CH_2F_2 showed two peaks for a 2 and 4 e^- reduction process. Although no Ge oxidation peak was observed suggesting an irreversible process[68]. In $scCH_2F_2$, an initial reduction peak was observed at -0.7 V *vs.* Pt followed by a less resolved increase in cathodic current at -1.5 V *vs.* Pt, which was presumed to be the two step reduction of $GeCl_4$ observed in liquid CH_2F_2[68]. Depositions were carried out on Au-coated glass slides, in both liquid and $scCH_2F_2$ a brown deposit was observed[68]. SEM images showed cracks on the surface of the Ge sample obtained from liquid CH_2F_2 but not from $scCH_2F_2$, it was also noted that both samples appeared amorphous[68]. EDX confirmed the presence of Ge, other elements detected (Au, Si, O and Cl) were attributed to either the Au-coated glass substrate or from the Ge precursor[68]. Raman spectroscopy was performed and the data confirmed that elementary Ge was electrodeposited from $scCH_2F_2$, the as-deposited film is amorphous, but can be converted to the crystalline Ge by applying laser annealing when carried out *in situ*[68]. The lowest diameter Ge nanowires that have been produced in the literature are > 7 nm in diameter[68,69]. It was concluded from the study that the electrodeposition of Ge could be extended to high aspect ratio nanopores (< 3 nm diameter), leading to the lowest diameter Ge nanowires reported in literature[68].

Bartlett *et al.*[45] reported on the electrodeposition of silver from $scCO_2$/MeCN in 2014. Silver is also of interest as an electrodeposited material in ultra-large-scale integration/interconnect due to its lower resistivity and higher electro-migration resistance compared to copper[45]. In the study, five silver precursors were investigated, these included (1,5-cyclooctadiene)(hexafluoroacetylacetonato) silver(I) [Ag(hfac)(COD)], (hexafluoroacetylacetonato)(triphenylphosphine) silver(I) $[Ag(hfac)(PPh_3)]$, (perfluorooctanoato)-bis(triphenylphosphine) silver(I) $[Ag(CF_3(CF_2)_6CO_2)(PPh_3)_2]$, tetrakis(triphenylphosphine) silver(I) tetrafluoroborate $[Ag(PPh_3)_4][BF_4]$ and tetrakis(acetonitrile) silver(I) tetrafluoroborate $[Ag(CH_3CN)_4][BF_4]$[45]. All five silver precursors were investigated in liquid acetonitrile and four were investigated in $scCO_2$/MeCN[45]. In

acetonitrile, two precursors ($[Ag(CH_3CN)_4][BF_4]$ and [Ag(hfac)(COD)]) gave typical features for Ag deposition with a clearly defined nucleation loop on the cathodic scan and an anodic stripping peak on the return scan[45]. The other three precursors investigated in liquid MeCN gave problematic CVs. [Ag(hfac)(PPh_3)] and $[Ag(CF_3(CF_2)_6CO_2)(PPh_3)_2]$ never reached an expected steady state plateau, the current rose slowly in both cases at higher cathodic potentials[45]. This was attributed to an additional reduction process involving the triphenylphosphine ligand in both cases[45]. In the case of $[Ag(PPh_3)_4][BF_4]$ in MeCN, the voltammetry recorded would change upon repeated cycling, suggesting the surface of the electrode is altered[45]. On the first scan, no nucleation loop was observed. However, the second scan showed a narrow nucleation loop. On the third scan, the difference in current values for the forward and reverse scans in the loop were larger and the nucleation overpotential increased[45].

The four silver precursors investigated in $scCO_2$/MeCN were $[Ag(CH_3CN)_4][BF_4]$, [Ag(hfac)(COD)], [Ag(hfac)(PPh_3)] and $[Ag(CF_3(CF_2)_6CO_2)(PPh_3)_2]$[45]. For the precursor, $[Ag(CH_3CN)_4][BF_4]$, typical cathodic metal deposition and anodic stripping were observed, fluctuations were seen on the steady state current and these were attributed to the convection in the cell caused by temperature gradients and are exacerbated by the low viscosity of the media[45]. The [Ag(hfac)(COD)] precursor shows evidence of Ohmic loss (*iR* drop) due to solution resistance in its cyclic voltammetry[45]. However a nucleation loop and stripping peak are observed, along with a convective steady state at cathodic potentials[45]. It was found that when the cell was disassembled, excessive fouling of the counter electrode (by a dark brown viscous oil) had occurred[45]. This was attributed to an electrochemically induced polymerisation reaction of the COD ligand with either the acetonitrile or itself[45]. Cyclic voltammetry for the [Ag(hfac)(PPh_3)] precursor showed electrodeposition of silver with a further reduction wave starting beyond -0.4 V *vs* Ag[45]. This second wave is attributed to the reduction of triphenylphosphine coupled with a bulk catalytic reaction involving the tetrabutylammonium cation[45]. $[Ag(CF_3(CF_2)_6CO_2)(PPh_3)_2]$ showed similar results in its voltammetry to [Ag(hfac)(PPh_3)]. $[Ag(CF_3(CF_2)_6CO_2)(PPh_3)_2]$ showed a nucleation loop and stripping peak along with an additional reduction process at high cathodic potentials, again it was concluded this was reduction of the triphenylphosphine ligand[45]. Although all four silver complexes could successfully electrodeposit silver in $scCO_2$/MeCN, the complicated electrochemical reduction of the triphenylphosphine ligand, [Ag(hfac)(PPh_3)] and $[Ag(CF_3(CF_2)_6CO_2)(PPh_3)_2]$ were not chosen as candidates for electrodeposition[45]. [Ag(hfac)(COD)] was also not chosen for electrodeposition due to the excessive fouling caused at the counter electrode[45]. It was decided that $[Ag(CH_3CN)_4][BF_4]$ was the best and most suitable precursor for electrodeposition from the SCF due to its high diffusion coefficient (6 to 36 x 10^{-5} cm^2 s^{-1} in the range 9 to 19.8 MPa and 305 to 314 K), no unwanted by products and good resolved voltammetry in both MeCN and

$scCO_2$/MeCN[45]. Electrodeposited films shown were 10 μm thick, had a silver-metallic appearance and showed low impurity content with energy-dispersive X-ray (EDX) analysis[45]. Further deposition was carried out into anodic alumina membranes (AAO) which provide a convenient hard template for the electrodeposition of nanowires[45]. Silver nanowires were successfully deposited into 200 nm and 13-nm diameter AAO membranes[45]. EDX analysis of the wires confirmed they were made of silver[45].

Bartlett *et al*[64]. also released a perspective article in 2014. In their perspective they discuss the physical chemistry and cover both the practical and scientific challenges and aspects of electrodeposition from supercritical fluids[64]. The review also discusses the possible applications for supercritical fluid electrodeposition and suggests some key developments that are required to take the field to the next stage[64].

1.3 Metallocenes as an Internal Reference Standard for Supercritical Fluids

1.3.1 Metallocenes as Redox Probes in Non-Aqueous Solutions

Supercritical fluids require specialist equipment for safety reasons, thus conventional reference electrodes constructed in glass (such as the saturated calomel electrode, SCE) are unsuitable and cannot be used. For this reason, a suitable internal reference standard (such as metallocenes) that can be used in combination with a Pt *pseudo* (also known as Quasi) reference electrode is required. Internal standards are used to overcome the problem of potential variations due to changes in liquid junction potentials between the solution and reference electrode[70]. In the case of non-aqueous solutions, the International Union of Pure and Applied Chemistry (IUPAC) recommends the use of the ferrocene/ferrocenium (Fc/Fc^+) redox couple[71-73]. In 1999, Noviandri *et al*[70]. questioned the use of the ferrocene/ferrocenium redox couple as an internal standard as some studies had shown that the chemical reversibility of the Fc/Fc^+ couple in some media was incomplete because of the tendency of the Fc^+ ion to react with nucleophiles. As the solvent might interact with the Fc/Fc^+ couple in several ways, this would lead to significant solvent dependence of the redox potential of the Fc/Fc^+ couple[70]. The decamethylferrocene/decamethylferrocenium ($DMFc/DMFc^+$) had been proposed as an internal reference standard on the basis of its stability to molecular oxygen and other factors by Bashkin and Kinlen[73]. The bulky methyl groups of $DMFc/DMFc^+$ are expected to give a greater steric interference to specific and nonspecific interactions between solute and solvent molecules[70]. The electrochemistry of the $DMFc/DMFc^+$ couple has been studied by a number of groups under a variety of conditions and the couple exhibits a reversible one electron redox process at

the electrode with facile electron transfer kinetics[15,70,73-78]. Noviandri *et al.*[70] extensively studied the solvent dependences of the formal redox potential of the Fc/Fc^+, $DMFc/DMFc^+$ and 1,2,3,4,5-pentamethyl-ferrocene (Me_5Fc) couples in 29 solvents including water. It was concluded from the study that the little scope for specific interactions of the $DMFc/DMFc^+$ satisfied the criteria required for it to be a more suitable redox standard compared to Fc/Fc^+[70]. It was also concluded that the $DMFc/DMFc^+$ couple complied with all of the IUPAC requirements for a reference redox standard and was superior to the Fc/Fc^+ redox system for studying solvent effects on the thermodynamics of electron transfer of other couples[70]. As the $DMFc/DMFc^+$ couple had been shown to be a superior redox couple compared to the Fc/Fc^+ couple and it had been studied previously under sc conditions, it was chosen as one of the redox couples to be studied, Figure 1.4.

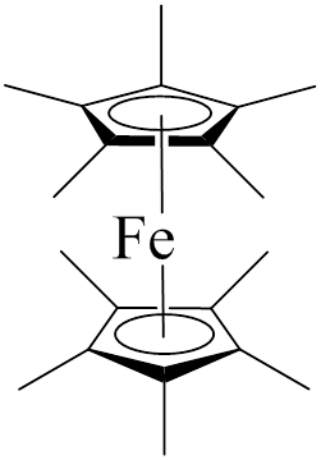

Figure 1.4. Structure of decamethylferrocene

Cobaltocenium hexafluorophosphate was chosen as an additional internal reference standard due to its ideal reversibility and one-electron electrochemistry[72]. The cobaltocenium ($CoCp^+/CoCp_2$) redox couple should give a formal redox potential that is sufficiently separated to the $DMFc/DMFc^+$ to give a half-wave potential separation which is constant and solvent independent. Stojanovic and Bond[79] examined the $CoCp_2^+/CoCp_2$ couple with respect to the Fc/Fc^+ couple and found that the half-wave potential separation calculated was essentially independent of electrode material, electrolyte and solvent used[79]. In contrast, the half-wave potential for the $CoCp_2^+/CoCp_2$ couple when used in isolation was found to be considerably more solvent dependent and could not always be accurately measured at 25 ºC because of overlap interaction with the "solvent" response and for "a range of other reasons"[79]. To overcome this problem, the decamethyl- version of the metallocene can be used, in this case decamethylcobaltocene. Aranzaes *et al*[80]. made measurements of the redox potential ($E_{1/2}$) of a variety of metallocenes (including decamethylferrocene and decamethylcobaltocene) in a range of solvents (including acetonitrile and dichloromethane). It was found that the difference in $E_{1/2}$

values for decamethylferrocene and decamethylcobaltocene was solvent independent[80]. Both cobaltocenium hexafluorophosphate and decamethylcobaltocene were chosen as redox probes for the study detailed within, Figure 1.5. These metallocenes have also been studied as internal reference standards in room temperature ionic liquids (RTILs), where conventional reference electrodes also cannot be used[72,81-83].

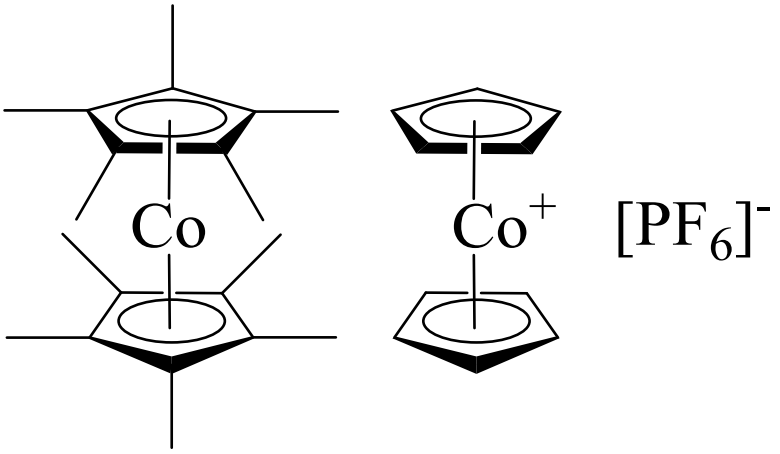

Figure 1.5. Structures of decamethylcobaltocene (left) and cobaltocenium hexafluorophosphate (right)

1.3.2 Metallocenes as Redox Probes in Supercritical Fluids

In 1988, Crooks and Bard[22] studied the electrochemistry of ferrocene and phenazine in near-critical and supercritical acetonitrile between 298 and 573 K. It was found that the one-electron oxidation wave of ferrocene at low scan rates was reversible or nearly reversible throughout the entire temperature range studied[22]. The diffusion coefficient and heterogeneous electron transfer rate for ferrocene was also estimated in supercritical acetonitrile[22]. The Fc/Fc^+ couple was chosen for its use as an internal standard in non-aqueous solutions and because the oxidation of Fc is relatively insensitive to small amounts of water and other impurities[22]. Due to the high temperatures employed, tetraalkylammonium salts could not be used as they are not thermally stable; therefore, CF_3SO_3Na was used as the supporting electrolyte[22]. When CF_3SO_3Na was used as a supporting electrolyte in $scNH_3$ the resistance of the solution increased with increasing temperature, however in acetonitrile the conductivity of the system approximately doubled as the temperature was increased from 298 to 373 K and continued to rise up to 573 K[22]. At subcritical temperatures an uncomplicated one electron oxidation of Fc to Fc^+ was observed[22]. Near theoretical peak to peak potential separation was seen at low scan rates, also the peak potential was found to be independent of scan rate over four decades with the ratio of peak anodic and peak cathodic current being unity over 523 K[22]. The diffusion coefficient of ferrocene was also measured at both 298 and 548 K. It was found the diffusion coefficient

increased from 2.6 x 10^{-5} cm^2 s^{-1} at 298 K to 2.4 x 10^{-4} cm^2 s^{-1} at 548 K (12.5 MPa)[22]. This order of magnitude increase in the diffusion coefficient was comparable to that measured for phenazine[22]. It was also noted that "mild filming" of the electrode occasionally occurred above T_C, but when the solution was cooled no evidence for the filming was observed[22]. Despite this, it was still concluded that ferrocene could serve as an internal reference standard as the results were constant for several hours *vs.* Ag-QRE[22].

In 1989, Cabrera and Bard[15] studied the electrochemistry of various organometallic complexes, including decamethylferrocene, in near and supercritical acetonitrile. Decamethylferrocene exhibited reversible or quasi-reversible behaviour from 298 to 555 K (supercritical region)[15]. As the temperature was increased the peak to peak potential separation increased, this was attributed to an increase in uncompensated resistance[15]. To calculate the diffusion coefficient of decamethylferrocene in the system, Cabrera and Bard used the peak anodic current and assumed a reversible wave at the given temperature[15]. It was found the diffusion coefficient increased from 1.8 x 10^{-5} cm^2 s^{-1} at 298 K (0.1 MPa) to 9.3 x 10^{-5} cm^2 s^{-1} at 521 K (11.6 MPa)[15]. This large increase in D parallels Fc in MeCN (as described above) and reflects the strong decrease in viscosity of the solution at higher temperatures[15]. It was concluded that both Fc and DMFc should be a convenient redox couple for measuring potentials of other supercritical systems[15].

In 1994, Olsen and Tallman[84] studied the voltammetry of ferrocene in sub- and supercritical chlorodifluoromethane (scCHClF$_2$). Chlorodifluoromethane has a critical temperature and pressure of T_C = 369.15 K and p_C = 4.97 MPa, along with a higher dielectric constant (ε = 2.31 at the critical point) compared to carbon dioxide (ε = 1.18 at the critical point)[84]. Furthermore, the more polar solvent permits the dissolution of a small quantity of electrolyte, making voltammetric measurements at microelectrodes possible with minimal Ohmic distortion[84]. Electrochemistry of ferrocene was obtained at three conditions, normal liquid conditions (299 K, 5.2 MPa), near critical and supercritical (378 K, 15 MPa) conditions[84]. Although it was possible to obtain voltammetry near the critical point, it was not possible to obtain reproducible electrochemistry[84]. This is attributed to the changes in fluid composition with respect to the amount of electrolyte added, making the precise control of the density and dielectric constant extremely difficult[84]. Olsen and Tallman[84] confirmed electrochemistry performed in the supercritical phase by visual inspection with an optical cell. Cyclic voltammetry of ferrocene performed in the supercritical phase showed a typical microelectrode response and was analogous to that performed at 299 K[84]. Although, the similar limiting current recorded for both conditions was ascribed to some passivation of the electrode surface[84]. The diffusion coefficient of ferrocene was determined for both liquid and supercritical conditions and showed an increase from 2.36 x 10^{-5} cm^2 s^{-1} (298 K, 5.20 MPa) to 1.30 x 10^{-4} cm^2 s^{-1} (388 K, 9.00 MPa), this order of magnitude increase is consistent with that performed by Crooks and Bard[22,84].

Olsen and Tallman[84] also demonstrated the reduction of cobaltocenium hexafluorophosphate to cobaltocene. The steady state voltammogram displayed nearly reversible behaviour from Nernstian analysis[84]. Voltammetry was also performed in liquid $CHClF_2$ containing both ferrocene and cobaltocenium, the half wave potential separation of 1.33 V was in good agreement with literature value and further tests were to be performed in supercritical conditions[84].

In 1996, Olsen and Tallman reported further on the conductivity and voltammetry of ferrocene and cobaltocenium in liquid and $scCHClF_2$[59]. Voltammetry of both ferrocene and cobaltocenium at equal concentration in liquid conditions (298 K, 5.20 MPa) show Nernstian behaviour[59]. At 298 K, the half wave potential difference was found to be 1.32 V and is again in good agreement with literature[59]. The hydrodynamic radii of both ferrocene and cobaltocenium in both acetonitrile and dichloromethane were estimated from the Stokes-Einstein equation. Ferrocene has an estimated hydrodynamic radius of 2.8 Å in acetonitrile and 4.0 Å in dichloromethane, cobaltocenium has an estimated hydrodynamic radius of 3.5 Å in acetonitrile and 5.5 Å in dichloromethane[59]. Voltammetry of the metallocenes performed in $scCHClF_2$ at varying pressures (12, 20 and 30 MPa) showed two interesting changes in the responses for ferrocene oxidation and cobaltocenium reduction; one is that both waves were shifted to more negative potentials but not to the same magnitude, the second is that the limiting current for ferrocene decreased with pressure but those for cobaltocenium remained constant[59]. The potential of the quasi-reference is likely a function of pressure but should shift each potential wave by identical amounts and not have an effect on $\Delta E_{1/2}$, although the shift is small (~ 40 mV) the behaviour was noted as reproducible[59]. The variation in $\Delta E_{1/2}$ with pressure was attributed to the variation in fluid resistance with pressure and the variation in ohmic distortion of the voltammograms[59]. Analysis of the limiting current for ferrocene at increasing pressure showed a decrease whereas cobaltocenium remained constant. The diffusion coefficient was measured from multiple concentrations of ferrocene at the same pressure; the diffusion coefficient was shown to decrease rapidly with pressure which is the result of a rapid increase in density and viscosity with pressure[59]. Voltammetry of ferrocene was also performed in supercritical trifluoromethane (CHF_3) where reversible Nernstian behaviour was observed[59].

In 2000, Goldfarb and Corti[85] studied the electrochemistry of decamethylferrocene and decamethylferrocenium hexafluorophosphate ($DMFc^+$) in supercritical trifluoromethane. In the study, linear sweep voltammetry was performed at a platinum microelectrode (25 μm Ø) on both DMFc and $DMFc^+$ at 323.15 K at several densities with and without supporting electrolyte (tetrabutylammonium hexafluorophosphate)[85]. It was found that even in the complete absence of supporting electrolyte that the shape of the voltammogram (for DMFc) was still preserved, and despite the large Ohmic drop seen the analysis of the limiting current obtained from the

curve did not lose accuracy[85]. A plot of *E vs.* $\log[(I_L - I)/I]$ was performed for DMFc and gave a value of 64.1 mV for the exchange of a single e^- under reversible conditions at 323.15 K, in excess of supporting electrolyte the value was as high 192 mV[85]. This is attributed to the lower dielectric constant of the solvent at lower densities, leading to a higher degree of association and consequently less free ions from the supporting electrolyte[85]. In the absence of supporting electrolyte, impurities from the solvent contribute (to some extent) to the conductivity of the medium[85]. In contrast, it was found that $DMFc^+$ is strongly influenced by the concentration of supporting electrolyte[85]. The decrease in concentration of supporting electrolyte increases the limiting current of $DMFc^+$; this is due to the increases of the migrational current[85].

In 2004, Goldfarb and Corti[86] further studied the diffusion of decamethylferrocene and decamethylferrocenium hexafluorophosphate in supercritical trifluoromethane. The diffusion coefficients of DMFc and $DMFc^+$ in $scCHF_3$ were measured at a temperature of 323.15 K as a function of density with $TBAPF_6$ as the supporting electrolyte on a platinum microelectrode. For $DMFc^+$, the temperature of the system and concentration of $DMFc^+$ and $TBAPF_6$ were kept constant and the pressure of the system was altered to give a different density and thus a varying viscosity[86]. At 323.15 K and a concentration of $c_{DMFc+} = 1 \times 10^{-6}$ mol dm^{-3} the pressure was varied from 7.67 to 15.73 MPa to give a density range from 0.4971 to 0.9058 g cm^{-3} and a viscosity of 3.23 to 6.88 x 10^{-5} Pa s[86]. This increase in density decreases the diffusion coefficient from 12.3 x 10^{-5} to 7.1 x 10^{-5} cm^2 s^{-1} as indicated by the decrease in the limiting current from 60 to 35 pA, and the trend is repeated for lower and higher concentrations of $DMFc^+$ used and when the temperature of the system is lowered[86]. The same study was performed on DMFc, at 323.15 K and $c_{DMFc} = 4.83 \times 10^{-6}$ mol dm^{-3} the pressure was varied from 8.45 to 15.66 MPa to give a density range from 0.6011 to 0.9045 g cm^{-3} and a viscosity of 3.90 to 6.86 x 10^{-5} Pa s[86]. The increase in density again decreases the diffusion coefficient from 13.0 to 7.3 x 10^{-5} cm^2 s^{-1} and the limiting current decreases from 292 to 171 pA and again this trend continues for varying temperatures and concentrations[86].

In 2013, Toghill *et al*[44]. studied the steady-state macroscale voltammetry of decamethylferrocene in a supercritical carbon dioxide medium (containing acetonitrile). In their experiments they used DMFc as the redox probe in $scCO_2$ with up to 0.41 mole fraction MeCN and tetradecylammounium tetrakis(pentafluorophenyl)borate (TDATFPB, a room temperature ionic liquid) as the supporting electrolyte[44]. Cyclic voltammetry performed with 0.5 mM DMFc and 10 mM TDATFPB in $scCO_2$/MeCN (0.41 mole fraction) at 100 Bar and 313 K showed a redox process occurring with typical peak shape (above 25 mV s^{-1}) attributed to semi-infinite linear diffusion[44]. Performing Randles-Sevcik (R-S) analysis (I_{PA} *vs.* $\sqrt{v}$) yielded a straight line but which does not extrapolate to the origin as dictated by theory[44]. Despite this an estimation of the diffusion coefficient was made and found to be $D = 1.86 \times 10^{-5}$ cm^2 s^{-1} [44]. The same analysis

performed with DMFc in liquid MeCN yields a Randles-Sevcik plot that does extrapolate to the origin and the diffusion coefficient was found to be $D = 1.85 \times 10^{-5}$ cm^2 s^{-1} [44]. It should be noted that the voltammetry performed under supercritical conditions at 25 mV s^{-1} appears to be slanted and is not addressed by the author; this is most likely due to a fault in the electrode construction. This slant is apparent for all cyclic voltammetry presented in the paper, which may give an inaccurate estimation of the peak current required for R-S analysis. From the diffusion coefficients calculated it was suggested that a liquid-like acetonitrile phase was formed at the electrode surface[44]. The thickness of this layer was estimated to be 60 µm which was determined from the limiting current in the near steady state voltammetry obtained at 25 mV s^{-1} [44]. To confirm the presence of a liquid like film, Toghill *et al.* performed computational studies of the system[44]. Two simulation conditions were performed, the first kept the scan rate constant and varied the thin layer thickness, and the second kept the thin layer thickness constant and varied the scan rate[44]. The simulations conducted both agree with the experimental data (without the slant) and suggest an approximately 60 µm thick acetonitrile film on the electrode surface[44]. This hypothesis and evidence against a film in a similar system will be discussed further in Chapter 4. Toghill *et al*[87]. also released a mini review on supercritical fluids in 2014, which gives a brief overview of the literature relating to the electrochemistry in supercritical fluids.

1.4 Diffusion into nanopores

1.4.1 Templates for Studying Diffusion and Electrodeposition

Electrodeposition into small and high aspect ratio nanopores is a specific advantage of SCFED. This provides opportunities to grow high aspect ratio nanowires or to construct multi-component devices in electrically directed locations from a bottom up approach[64]. In order to design nanostructures in nanopores, the pores will need to be aligned in the structure[64]. A porous membrane with cylindrical pore geometry can be used as a template for the synthesis of quasi-1D nanostructures[88]. Two types of porous membranes are commonly used: anodic aluminium oxide (AAO) and track-etched polymers[88]. However, the random nature of the pore production process for polymer membranes can lead to irregular structures with intersecting pores within the membrane[88]. AAO membranes are commercially produced and can be described as a close-packed hexagonal array of parallel cylindrical nanopores which are perpendicular to the aluminium substrate[89]. Fabrication of AAO templates is facile and the pore diameter, inter pore distance, wall thickness, pore length and barrier layer thickness can all be controlled and varied based on the anodizing conditions[89]. The pore sizes can range from 5 to 500 nm and the resulting templates are electrically and thermally insulating, optically

transparent and robust[64]. Many of the commercially produced porous films are cleaved from the aluminium surface to produce self-supporting membranes[64], which can then have chromium and gold evaporated onto to form an electrode. These AAO templates were used to study the diffusion of decamethylferrocene under supercritical conditions and can be found in Chapter 5.

1.4.2 Diffusion at Microdisc and Nanoelectrode Array Electrodes in Literature

Davies and Compton[90] discussed the theory of cyclic and linear sweep voltammetry of regular and random arrays of microdisc electrodes. In their paper they discussed the theory of diffusion at microelectrode arrays. They noted that the shape and magnitude of the voltammetric response are highly dependent on two factors: the size of the individual microelectrodes *vs*. the size of the diffusion zones; and the size of the diffusion zone *vs.* the size of the insulating material which separates neighbouring microdiscs (the centre to centre separation, *d*, of the microdiscs)[90]. The voltammetry of a microelectrode can be assigned to one (or a combination) of four categories depending on the two factors[90]. The first category, the diffusion layer thickness, δ, is small compared to the size of the microelectrodes resulting in linear diffusion dominating mass transport, thus giving a macroelectrode response; this corresponds to very fast scan rates and widely separated electrodes[90]. The second category, δ is larger than the microelectrodes but not so large as to cause adjacent diffusion layers to overlap, this is the most common fabrication of microelectrode arrays[90]. Arrays in this category produce scan rate independent voltammograms with steady-state characteristics[90]. The third category, δ is greater than the size of the insulating material resulting in the overlap of adjacent diffusion layers, which gives scan rate dependence and peak currents in microelectrode array voltammetry[90]. As diffusion zones overlap, the adjacent microelectrodes effectively deplete the same region of solution leading to a decrease in current compared to the second category[90]. The fourth category, δ far exceeds the size of the insulating layer, resulting in complete overlap and a linear concentration profile[90]. The paper then discusses and simulates different types of arrays including regular and random arrays of microdiscs[90]. Cyclic voltammetry and simulation of recessed microdisc arrays have also been studied by various groups[91-93].

Arrigan[94] provided a review of nanoelectrodes, nanoelectrode arrays and their applications, including the benefits and fabrication of nanoscale electrodes. Due to the small size of nanoelectrodes, they exhibit fast (three-dimensional) diffusion field and produce steady state voltammograms (sigmoidal shape) analogous to those at microelectrodes[94]. This voltammogram shape is independent of the nanoelectrode geometry including hemispherical, inlaid disc and recessed disc electrodes. Arrigan[94] also summarised some of the steady state voltammetric characterisation of nanoelectrodes and the parameters of the electrode obtained from analysis, (*i.e.* model assumption, effective radius and redox probe species employed). The review also

discusses the diffusion regimes for nanoelectrode ensembles and nanoelectrode arrays[94]. Arrigan[94] notes the issue of diffusion regimes and whether they are independent for each electrode element of the array or whether they interact (overlap), Figure 1.6.

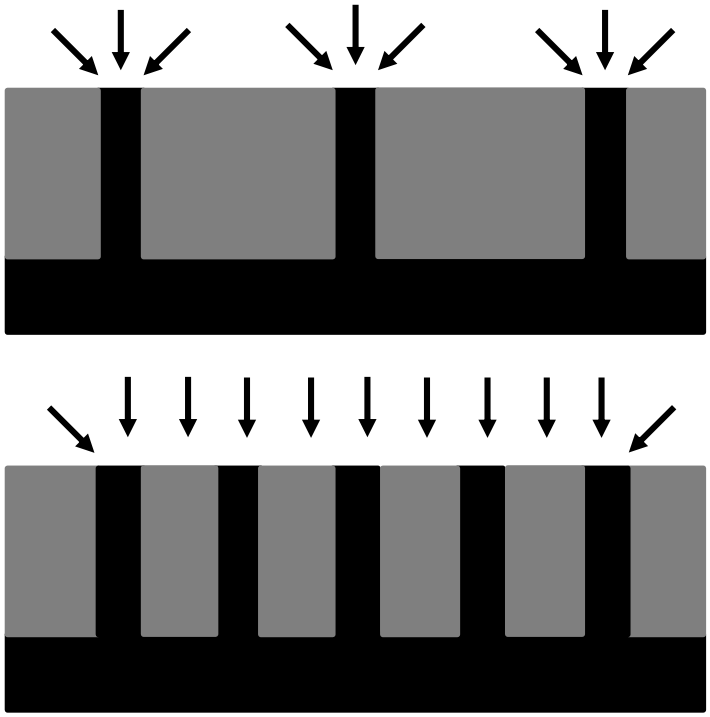

Figure 1.6. Diffusion regimes of nanoelectrode arrays at varying separation distance[94].

The shape of the diffusion regimes will depend on the electrode dimensions, geometry, whether inlaid, recessed or protruding, and the separation between the adjacent electrodes of the array[94]. When the electrodes are sufficiently separated, each electrode experiences its own diffusion regime, however when the separation is not sufficient (nanoelectrode ensemble), they experience overlapping diffusion regimes such that one-dimensional diffusion dominates[94]. At nanoelectrode arrays the spacing of the array is controlled and only steady state voltammetry will be obtained except at the fastest scan rates[94].

Neluni *et al*[95]. studied the cyclic voltammetry on recessed nanodisk-array electrodes (RNE) prepared from track-etched polycarbonate membranes with 10-nm diameter pores. The paper describes cyclic voltammetry performed at nanodisk-array of track-etched polycarbonate membranes (TEPCM) which have been prepared *via* sputtering of a gold thin film onto the TEPCM whose pores were coated with polyvinylpyrrolidone[95]. The redox couple studied was 1,1'-ferrocenedimethanol in a buffer solution, it was observed that the CVs transitioned from sigmoidal to peak-shaped with increasing scan rate[95]. The sigmoidal CVs were attributed to the radial diffusion of redox molecules from outside of the pores (< 50 mV s^{-1}), where-as the peak-shaped CV (> 50 mV s^{-1}) originated from their linear diffusion within the nanopore[95]. The

observation of sigmoidal CVs at slower scan rates suggested that the spacing between the pores was so large that the diffusion layers from individual pores did not overlap[95]. Neluni *et al*[95]. reported that the currents observed on the RNEs were larger than those calculated using the theoretical equations. The author attributed these large currents to the enhanced electron/mass transport (*i.e.* larger apparent D_p) within the nanopores such as electron hopping through a nanopore surface that contains the redox species at higher concentrations[95]. The author comments that these results may reflect the presence of a distinct surface layer on the 10-nm diameter nanopores to which the redox species partition preferentially[95]. Additional CVs performed using 1,1'-ferrocenedimethanol at varying pH showed that the limiting current was not affected[95].

1.5 Research Objectives and Thesis Overview

This Chapter has provided an introduction to supercritical fluids from initial observations to a functioning electrochemical solvent for the study and electrodeposition of metals. A brief overview of metallocenes as internal reference standards has also been provided for both non-aqueous and supercritical solvents. The overall research objective is to study the use of metallocenes as internal reference standards for supercritical fluids. This standard can then be applied to diffusion into nanopores and in the development of a new supercritical reactor.

In Chapter two, the equipment, chemicals and methods used throughout this thesis are described. A detailed description of the construction of electrodes, loading of materials and supercritical experimental setup (including cell designs) are described.

In Chapter three, the study of metallocenes in non-aqueous solvents at macro and micro electrodes is described. The study of various metallocenes in acetonitrile and dichloromethane has laid the foundation for the study of the metallocenes in supercritical solvents.

In Chapter four, the study of metallocenes as internal reference standards at macro and micro electrodes in supercritical fluids is described. The study of these metallocenes has led to the most accurate determination of the diffusion coefficient for the supercritical system used in this project.

In Chapter five, the study of the diffusion of decamethylferrocene in nanoporous templated electrodes in both acetonitrile and supercritical fluids is described. This study has given the first measurements of the diffusion of decamethylferrocene in nanoporous electrodes under supercritical conditions.

In Chapter six, the development of a new high speed plastic reactor for supercritical electrochemistry is described. The study of decamethylferrocene and the electrodeposition of bismuth have shown that the new reactor is faster and leads to uncontaminated electrodeposited films.

In Chapter seven, conclusions of the work have been described along with recommendations for future work. The results of the previous Chapters are described and the insight gained into the study of metallocenes as internal reference standards at micro, macro and templated electrodes under supercritical conditions along with how this helped to develop a new supercritical reactor. Finally, further experiments are recommended that could give further insight into these systems.

Chapter 2: Experimental

2.1 Reagents

2.1.1 Solvents and Supporting Electrolyte

The solvents used were acetonitrile (CH_3CN, Rathburn Chemicals Ltd.) purified by reflux over anhydrous calcium hydride, dichloromethane (CH_2Cl_2, Fisher Scientific, 99%) purified by reflux over anhydrous calcium hydride, supercritical grade carbon dioxide (CO_2, BOC gases, 99.999%) and difluoromethane (CH_2F_2, Apollo Scientific Ltd., 99.9%). The supporting electrolytes were tetrabutylammonium tetrafluoroborate ($[NBu_4^n][BF_4]$, Aldrich, 99%), tetrabutylammonium chloride ($[NBu_4^n][Cl]$, Aldrich, ≥97.0%) and sodium tetrakis[3,5-bis(trifluoromethyl)phenyl]borate ([Na][BARF]). [Na][BARF] was prepared by the Inorganic group at University of Southampton by a method described in literature[46].

2.1.2 Metallocenes and other Compounds for Internal Reference

The metallocene compounds investigated were decamethylferrocene ($C_{20}H_{30}Fe$, Aldrich, 97%), cobaltocenium hexafluorophosphate ($[C_{10}H_{10}Co]^+[PF_6]^-$, Aldrich, 98%), decamethylcobaltocene ($C_{20}H_{30}Co$, Aldrich), decamethylcobaltocenium hexafluorophosphate ($[C_{20}H_{30}Co]^+[PF_6]^-$, Aldrich, 98%) and tetrabutylammonium niobium chloride ($[NBu_4^n][NbCl_6]$). Sodium cobalticarborane ($C_4H_{22}B_{18}CoNa$, Strem Chemicals inc., 100%) was also investigated. The decamethylferrocene and decamethylcobaltocene were sublimed prior to use, the other cobaltocene complexes were used as received. The niobium complex was prepared by the Inorganic group at University of Southampton.

2.1.3 Complex for Electrodeposition in Plastic Reactor

The metal complex used for electrodeposition was tetrabutylammonium bismuth(III)trichloride ($[NBu_4^n][BiCl_4]$) and was prepared by the Inorganic group at University of Southampton.

2.2 Electrodes

The working electrodes were platinum microdiscs sealed in glass, platinum and gold macrodiscs were either sealed in glass or in polyether-ether ketone (PEEK, Supelco, Thames Restek, Upchurch Scientific, Vici) 1/16” tubing. All electrodes were polished prior to each experiment on a polishing cloth (12” microcloth, Buehler) with alumina paste (1 μm followed by 0.3 μm

average particle diameter, Buehler). Electrodes for the plastic reactor were washed with 2-Propanol (isopropyl alcohol, HPLC grade, Rathburn) prior to each experiment.

2.2.1 Electrodes for Non-Aqueous Solvents

Platinum wires of varying size (10 – 500 µm diameter, Goodfellow, Advent Research Materials Ltd.) sealed in glass were used as working electrodes. The fabricated microelectrodes (≤ 50 µm diameter) were characterised by means of cyclic voltammetry in 1 M sulphuric acid (H_2SO_4, trace metal analysis grade, Fisher Scientific) and additionally the diameters were estimated by scanning electron microscopy (SEM, Philips XL30SEM).

A platinum (0.5 mm diameter) disc was used as a *pseudo* reference electrode. This electrode was rough polished prior to experiment on 5 µm lapping film (Norton abrasive films). A Ag/AgCl reference electrode was also used for some experiments in DCM. A platinum gauze was used as a counter electrode and was cleaned in flame prior to experiment. Argon (pureshield argon, BOC) was bubbled through the solution for 20 minutes prior to experiment to remove O_2; this was then repeated every 15 minutes. After purging, electrodes were inserted into the cell under Ar and the cell then sealed. Additional experiments (those in DCM and MeCN) were carried out in a N_2 purged glove box.

A 5-neck glass cell was used. Experiments were carried out using an Autolab101 and a micro Autolab type III potentiostat/galvanostat was used in some cases along with GPES and NOVA software.

Characterisation of Platinum Microwires:

The fabricated microelectrodes were characterised by cyclic voltammetry in 1 M H_2SO_4. Performing cyclic voltammetry in H_2SO_4 provides information about the real surface area of the electrode[96,97]. This can also be used to clean the surface of the electrode. To gain a reproducible result, multiple scans were run. Figure 2.1 shows a representative cyclic voltammetry response at a fabricated 50 µm Ø electrode.

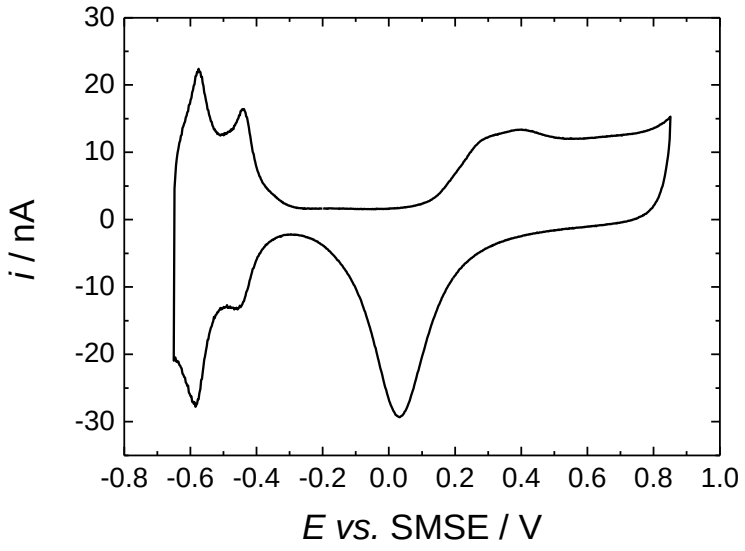

Figure 2.1. Cyclic voltammetry in 1M H_2SO_4 aqueous solution for a fabricated 50 µm diameter Pt electrode, recorded at 0.2 V s^{-1}, at 297 K.

The scan was started at -0.2 V and swept anodically; the first feature seen (0.1 to 0.85 V) corresponds to the formation of oxide on electrode surface. Reactions 2.1, 2.2 and 2.3 outline this process.

$$Pt + H_2O \rightarrow PtOH^{\bullet}_{ads} + H^+ + e^- \quad (2.1)$$

$$PtOH \rightarrow OHPt \quad (2.2)$$

$$OHPt \rightarrow OPt + H^+ + e^- \quad (2.3)$$

Reaction 1.1 represents the formation of an adsorbed hydroxyl group on the surface from the oxidation of a water molecule[98]. Reaction 1.2 represents the interfacial place exchange between OH_{ads} and surface Pt atoms that leads to the formation of a quasi-3D lattice[98]. Reaction 1.3 shows the subsequent oxidation of OH within the lattice resulting in the departure of an H^+ [98]. When sweeping from positive to negative potentials, this interchange has to be reversed before the oxygen can be reduced and desorbed (0.3 to -0.3 V) from the Pt electrode surface; hence a higher overpotential is required.

Two waves (-0.4 to -0.65 V) are observed upon cathodic scanning; this is due to hydrogen adsorption onto the surface of the Pt, reaction 2.4.

$$Pt + H^+ + e^- \leftrightarrow PtH^{\bullet}_{ads} \quad (2.4)$$

The polycrystalline Pt surface consists of different crystal faces at which the hydrogen can adsorb (Pt(100), Pt(110), Pt(111)) and the hydrogen adsorption and desorption waves are a combined result of electron transfer reactions at these faces.

A gap between oxidation and reduction current is observed (-0.35 to -0.2 V) where no electron transfer occurs, it corresponds to double layer charging current, which forms between bulk solution and electrode surface. When cycled above +0.85 V *vs.* SMSE, oxygen evolution occurred, similarly when cycled below -0.65 V *vs*. SMSE hydrogen evolution occurred.

The surface area of the characterised electrode was calculated from Equation 2.5.

$$A = \frac{Q}{f} \tag{2.5}$$

where Q corresponds to the charge of the hydrogen absorption or desorption (-0.65 to -0.35 V *vs.* SMSE) and is defined by Equation 2.6

$$Q = \int I\, dt = \int I \left(\frac{dt}{dE}\right) dE = \frac{1}{\nu} \int I\, dE \tag{2.6}$$

and f is a coefficient, which corresponds to the adsorption of a monolayer of hydrogen at a polycrystalline Pt surface, and equals 210 μC cm^{-2} in sulphuric acid under ambient conditions and corrected for double layer charging over potential range of -0.65 to -0.35 V[96,97]. It is assumed that at the potential of hydrogen evolution, the coverage of the Pt electrode with H_{ads} equals unity (= 1).

Microelectrode diameters were also confirmed by SEM. Each electrode was measured several times and measured from many different positions. These measurements were then compared to the size quoted by the supplier. A representation of a fabricated 25 and 50 um diameter Pt electrode is shown in Figure 2.2.

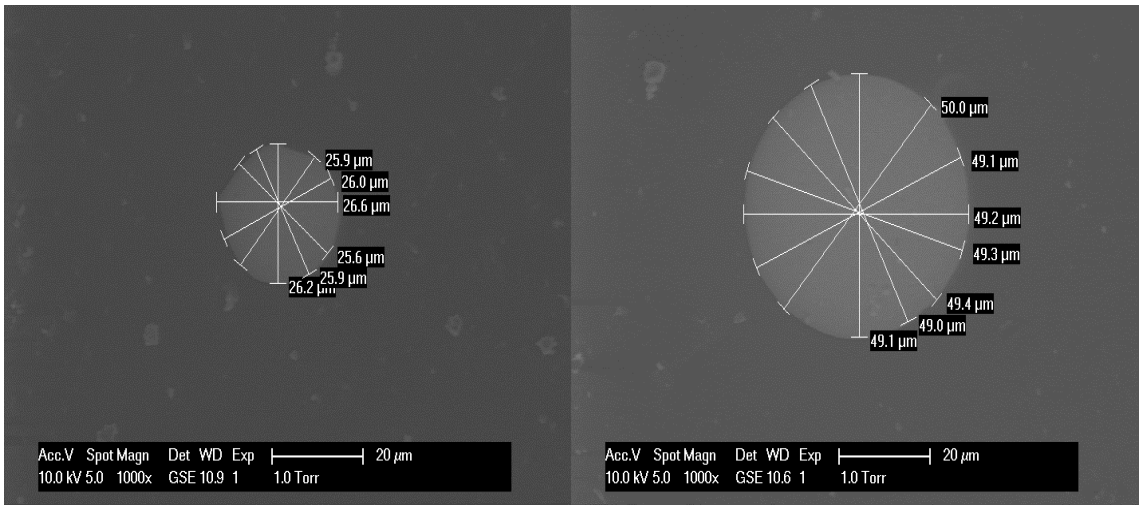

Figure 2.2. Examples of microelectrodes sealed in glass and PEEK tubing (not visible) for cyclic voltammetry experiments in supercritical fluids.

2.2.2 Electrodes for Supercritical Electrochemistry

All electrodes for supercritical conditions were sealed in PEEK (1.6 mm diameter OD, 0.5 – 1 mm ID, Supelco.) tubing with bisphenol A epoxy resin (EpoFix kit, Struers). Platinum and gold (0.5 mm Ø, Goodfellow, Advent Research Materials Ltd.) macrodiscs along with platinum (10-50 µm Ø) microdiscs were used as working electrodes. For supercritical carbon dioxide-acetonitrile mixtures ($scCO_2$/MeCN), microwires were sealed in a soda-glass capillary and then contacted to a 0.5 mm diameter stainless steel wire *via* Ag loaded epoxy (2 x 7 g conductive epoxy, Chemtronics), then further sealed in PEEK. For supercritical difluoromethane (scR32), microwires were directly contacted to a 250 µm diameter NiCr wire in a soda glass capillary, the whole section is then sealed. This section is then further sealed in PEEK. Representations for $scCO_2$/MeCN and scR32 electrodes (and a schematic for the baffle electrode) are shown in Figures 2.3 and 2.4 respectively. The baffle electrode simply consists of an extended piece of PEEK tubing which extends approximately 5 mm beyond the face of the electrode and surrounding insulation.

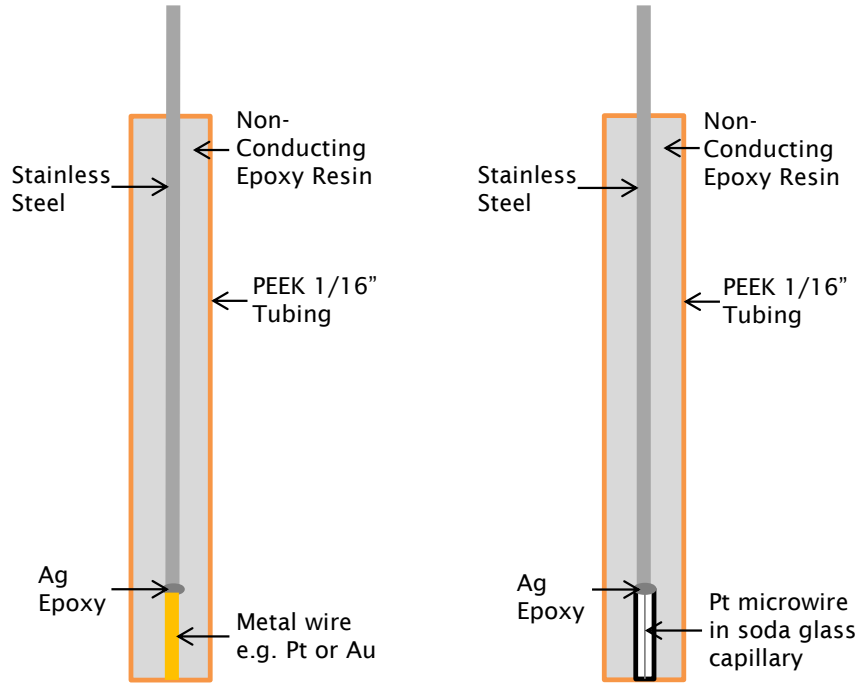

Figure 2.3. Schematic drawing for the electrodes used in scCO$_2$/MeCN.

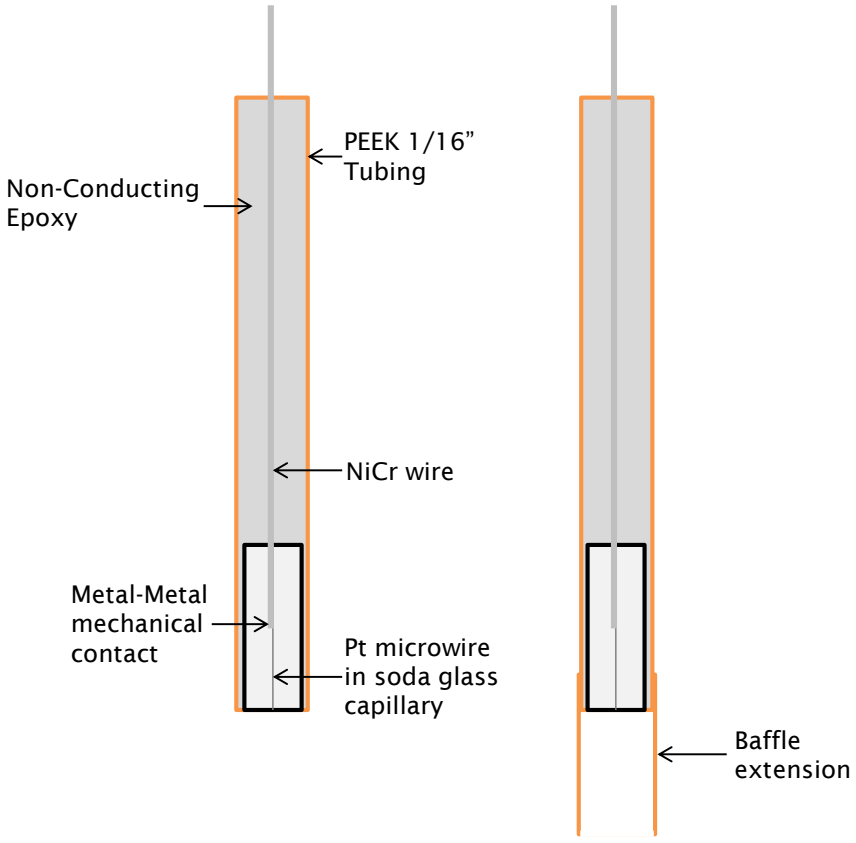

Figure 2.4. Schematic drawing for the electrodes used in scR32 (left), schematic for a baffle extended electrode (right).

Platinum wires (0.5 mm Ø) were used for both counter and *pseudo* reference electrodes. These were sealed in PEEK as presented in Figure 2.3. An Autolab 101 was used to perform voltammetry and chronoamperometry. The experiments were carried out at elevated pressures (≥ 18 MPa). $scCO_2$/MeCN experiments were carried out at 309 K. scR32 experiments were carried out at 360 K. Temperatures and pressures were adjusted accordingly to obtain a single phase in the reactor.

2.2.3 Templated Electrodes for Ambient and Supercritical Electrochemistry

Anodised aluminium oxide (AAO) templates were purchased from Synkera Technologies Inc., with an average pore diameter of 13 nm (± 2 nm) and 55 nm (± 6 nm) with an average thickness of 50 µm (± 1 µm). The back side of the membrane was evaporated with a 5 nm Cr adhesion layer and then further evaporated with 100 nm Au layer for contacting. These membranes are then split into quarters to give approximately the same area for each electrode. The Au layer was then further contacted to a stainless steel wire (sealed in 1/16" PEEK) *via* a quick set Ag epoxy (as described in Section 2.2.2). The back contact of the membrane and the stainless steel contact were then sealed in a non-conducting epoxy resin (EpoFix kit, Struers) to avoid any exposed Au to the solution. A schematic for the electrode can be seen in Figure 2.5. As depressurisation can be strenuous on the membrane leading to cracking, these electrodes were only used once.

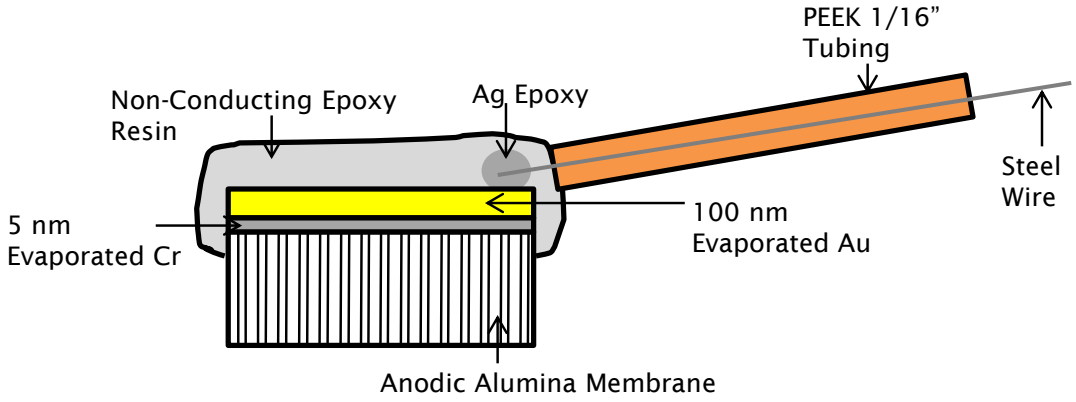

Figure 2.5. Schematic drawing for the templated electrodes used in supercritical fluids.

2.2.4 Electrodes for Supercritical Experiments in the Plastic Reactor

2.2.4.1 Gold Coated Substrates

The electrodes were a Si wafer (10 mm x 50 mm x 381 µm) which was then further coated with TiN (300 nm) and SiO_2 (200 nm). The surface of the electrode is then masked leaving two strips

on the surface. The surface is then evaporated with a chromium (5 nm) adhesion layer followed by a further evaporation of Au (250 nm), Figure 2.7. The electrodes were evaporated and constructed by members of the Department of Physics at the University of Southampton. The Au strips are then contacted to Cu wires *via* Ag epoxy. To avoid softening of the Ag epoxy the connections are then further coated with a non-conductive epoxy resin (EpoFix kit, Struers). Single strip gold electrodes were constructed in a similar fashion.

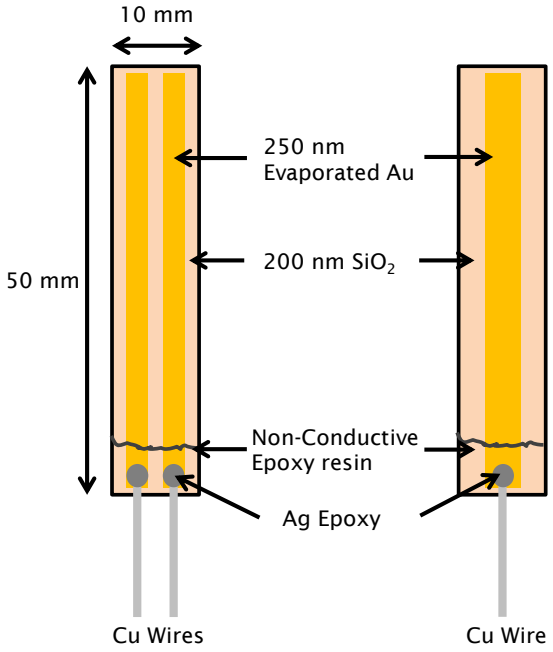

Figure 2.7. Schematic drawing for the double (left) and single (right) gold strip electrodes used in plastic reactor.

2.3 Experimental Setup

2.3.1 Ambient Pressure and Temperature

A 5-neck electrochemical cell, a PGSTAT101 with NOVA software or a µ-Autolab type III with GPES software were used. Experiments performed in Faraday cage were purged with argon for ~ 20 mins prior to experiment. Electrodes were inserted under an argon blanket and the cell sealed. Experiments performed in a Faraday cage used a PGSTAT101 potentiostat. Experiments performed in a N_2 purged glove box required the use of a µ-Autolab type III potentiostat. The cables were fed into the N_2 glove box through a specially made port. All experiments were performed at room temperature, 297±1 K.

2.3.2 Cell Design – Steel and Plastic Reactor

2.3.2.1 Steel Reactor

A review by Giovanelli *et al.*[99] describes the equipment and setups used by various research groups for electrochemical investigations at high pressures. The cell used in these experiments is unique to this project and has been described in the literature[14]. All the high pressure electrochemical experiments were carried out with the use of the 316L stainless steel or plastic reactor. The working volume was 8.65 mL for the steel cell. The steel cell consists of two parts, the top part contains 7 1/16" female SSI type fittings through which a thermocouple (XF-341-FAR sensor type K, Farnell), a CO_2/R32 feeding line and the 5 electrodes could be fed and sealed. The last port is where the safety key is screwed in to perform the final seal. The bottom part contained an 8.65 mL volume where the solution was confined after pressurisation, along with an area for the O-ring (EPDM 42 mm ID x 2 mm, Engineering Services Fasteners Ltd.) to be placed. The two parts of the cell were held together with a belt clamp and safety seal, Figures 2.8 and 2.9.

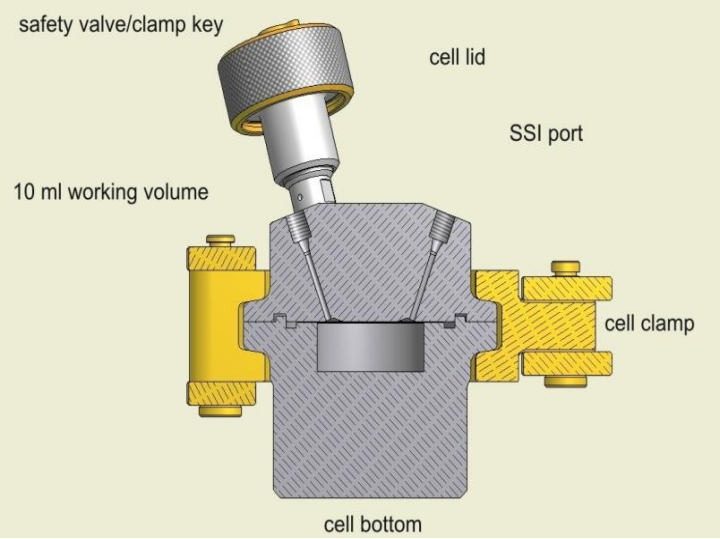

Figure 2.8. Schematic drawing of the high pressure reactor. Courtesy of the Engineering Workshop of the Department of Physics, University of Southampton, UK.

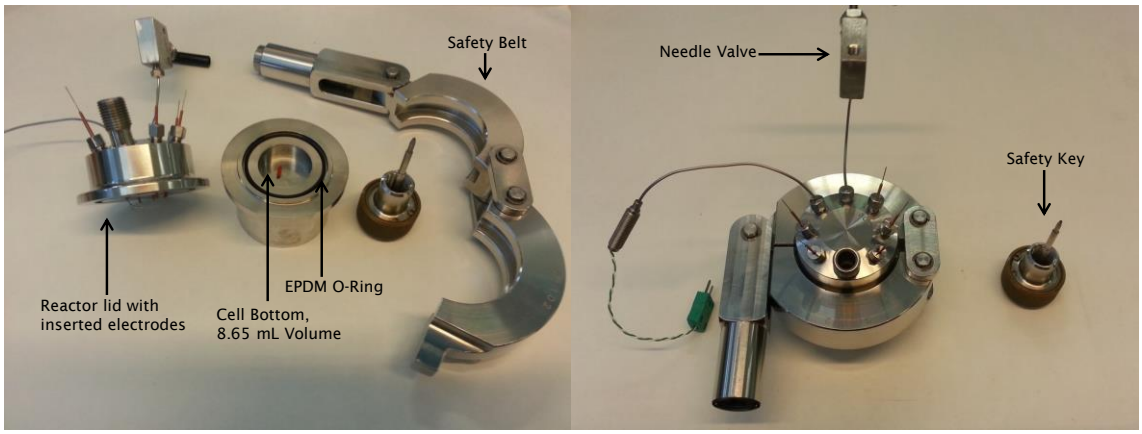

Figure 2.9. Picture of the dismantled (left) and sealed steel cell (right), the reactor (not including needle valve) is approximately 10 cm high and 12 cm wide when fully assembled.

2.3.2.2 Plastic Reactor

The plastic reactor was designed and produced in the University of Southampton and was specially made for this project. The working volume was 1.1 mL for the plastic reactor. The body of the reactor is constructed from PEEK and has 3 inlets where a thermocouple (XF-341-FAR sensor type K, Farnell), inlet and outlet tubing can be fed and sealed. The top and bottom of the PEEK reactor have areas where an O-ring (top O-ring 5 mm ID x 0.99 mm Kalrez custom O-ring compound 4079, bottom O-ring EPDM 70 13 mm ID x 1.5 mm Blue Diamond Technologies) can be placed. The reactor is then placed into a housing which is made of copper. The copper housing consists of two parts, the bottom has an area where a gold coated sapphire slide (UQG Optic Ltd., 1 mm thickness) is placed and the bottom O-ring seals to this electrode. The bottom also contains two screws (left and right) to hold the PEEK reactor in place. The top consisted of a track where a BVT electrode (AC13 sensor, BVT technologies) could be placed and held by a PEEK strip. This was later modified, the track was polished flat and a series of PEEK stubs are used to house a TiN substrate which was held in place by two plastic screws. The two copper housings are held together by two spring screws. The whole construction is then placed into a heating box. The heating box also contains an additional copper safety clamp, which is screwed down until hand tight to ensure a good O-ring seal in the reactor, Figure 2.10.

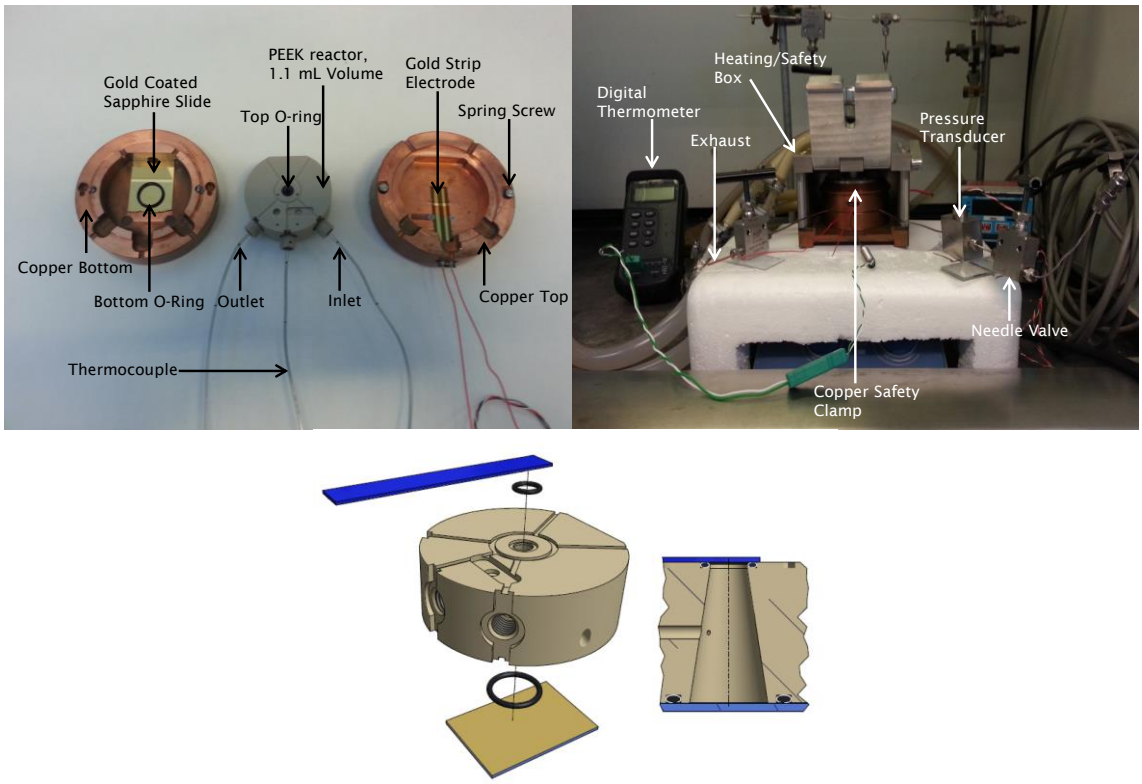

Figure 2.10. Picture of the disassembled cell (left), fully constructed (right) plastic reactor, picture depicting the O-ring seal to the PEEK body (bottom). The bottom image is courtesy of the Engineering Workshop of the Department of Physics, University of Southampton, UK. The reactor is approximately 3.8 cm high and 8 cm wide when fully assembled (outside of the safety mantle).

2.3.3 Steel and Plastic Reactor Preparation

2.3.3.1 Steel Cell

Electrolytes and metallocenes were introduced into the cell either as dry powders (R32) or solutions in acetonitrile ($scCO_2$/MeCN). This loading step was carried out in a dry, dinitrogen-purged glove box when air sensitive materials were employed. To introduce DMFc into the supercritical cell, small quantities of the solid were weighed out and then transferred to the N_2 purged glove box. Once in the N_2 purged glove box, the DMFc was dissolved in acetonitrile. The acetonitrile was weighed out in glove box to obtain the correct wt% or vol% (small errors can be introduced by this procedure as small changes in pressure in glove box can affect the weight reading). For higher concentrations of DMFc (where tens of milligrams are required), the solid DMFc was introduced into the cell directly. All other materials (e.g. decamethylcobaltocene, cobaltocenium etc.) were weighed out directly in glove box and placed in the supercritical cell.

2.3.3.2 Plastic Reactor

Stock solutions of DMFc (4.3 mM) and $[NBu_4^n][BF_4]$ (0.55 M) were dissolved in DCM and left in glove box. Materials were introduced by auto-pipette and the DCM left to evaporate, the resulting solid left behind will equal the mass required for the concentration desired in cell. The cell is then assembled.

2.3.3.3 Supercritical CO_2 – Acetonitrile Mixtures

The cell employed has been described in Section 2.3.2.1. A JASCO PU-1580-CO_2 pump (left under cylinder pressure, ~ 5 MPa) was used to introduce liquid CO_2 into the cell. The working pressure ranged from 17.2 to 17.9 MPa. The contents of the cell were stirred during pumping with a PTFE magnetic stirrer bar with an IKA® RCT basic heater/stirrer. The internal temperature of the cell was measured *in situ* using a thermocouple sealed in cell and connected to a standard portable thermometer (ST-9612 thermometer). The cell was heated using a home-made immersion water bath. Heated water is passed through a copper coil *via* a Grant TC-120 heater circulator. The electrochemical data was obtained using a PGSTAT101 with NOVA software. After each experiment, the contents of the cell were gradually depressurised through the use of a JASCO BP-1580-81 back pressure regulator. Figure 2.11 demonstrates the experimental setup used.

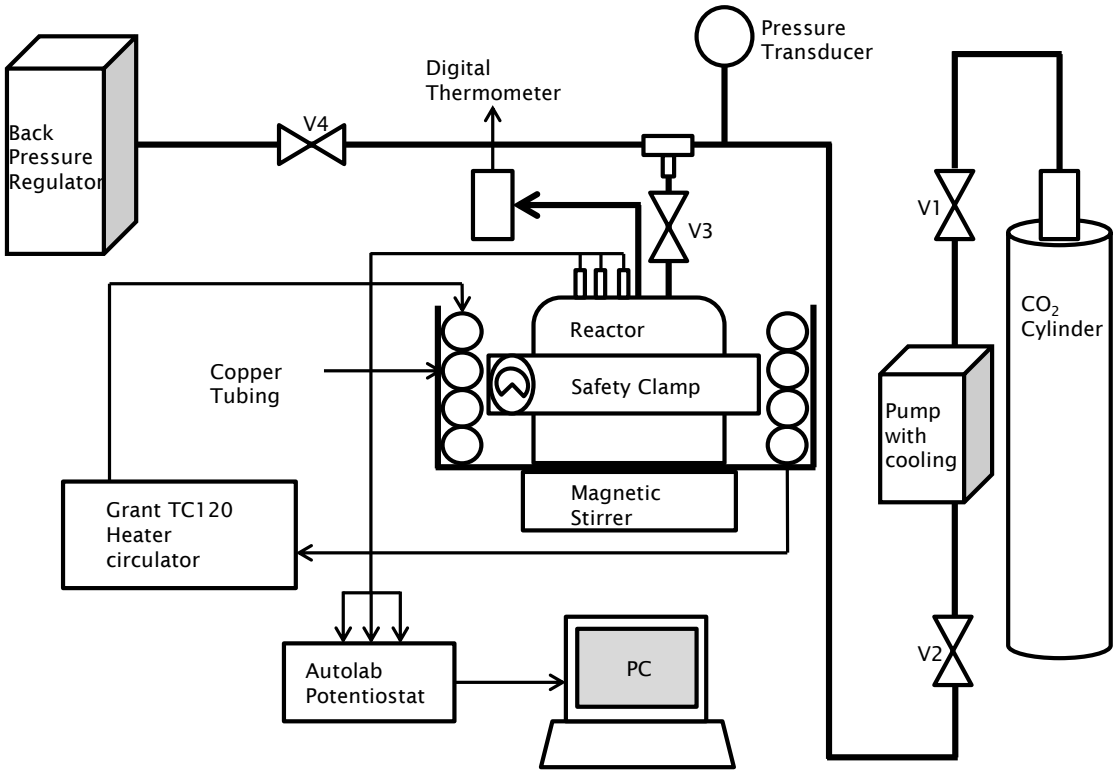

Fig 2.11. Schematic drawing of the experimental setup for scCO$_2$/MeCN.

Carbon dioxide was delivered through 1/16" high pressure tubing and an open HIP needle valve (Staffordshire Hydraulics Services Ltd.) to the JASCO pump, where it is cooled. The rate of pumping was set manually to 2 ml min^{-1}, as the rate of pressure is increased this was reduced to 1, 0.5, 0.2 and finally 0.1 ml min^{-1} until the desired pressure (max 20.7 MPa) was obtained. The time of each pumping rate was measured for calculating the volume of CO_2 introduced into the cell. The lowest pressure increase was observed between 6 to 8 MPa, which is the region of phase transition to the supercritical state. The pressure in the line was measured using a pressure transducer (model TJE, with E725 display, Honeywell).

2.3.3.4 Supercritical R32

The pump, working pressure and the stirring of the contents of the cell are all the same as those in Section 2.3.3.3. The cell was heated by an insulated band heater (Omega) and the temperature regulated by a bench-top controller (homemade controller provided by the Department of Physics at University of Southampton), which received feedback from a thermocouple mounted in a hole of an aluminium jacket at the bottom of the cell throughout the duration of the experiment. After each experiment the cell was gradually depressurised through exhaust tubing which lead to the fume cupboard exhaust. The experimental setup is shown in Figure 2.12. The delivery of R32, rate of pumping and the pressure was measured as outlined in Section 2.3.3.3.

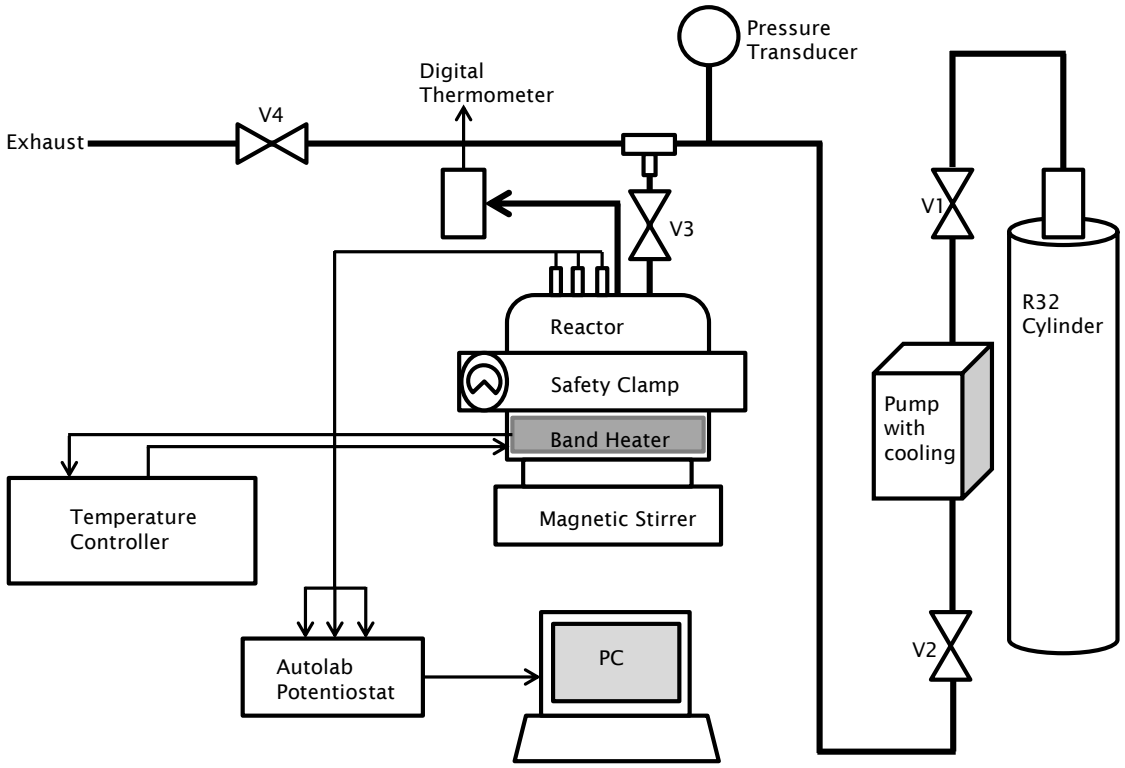

Figure 2.12. Schematic drawing of the experimental setup for scR32 in the steel cell.

2.3.3.5 Supercritical R32 (Plastic Reactor)

The cell employed has been detailed in Section 2.3.2.2. The pump, working pressure and the stirring of the contents have all been outlined in Section 2.3.3.3. The cell was heated by an ethylene glycol heater circulator (Lauda, ECO RE420). The tubing of the heater circulator is fed into a holding mantle for the cell which passes ethylene glycol uniformly across the bottom and top of the cell ensuring an even heating. After each experiment the cell was gradually depressurised through an exhaust system described in Section 2.3.3.4. The delivery of R32, rate of pumping and the pressure was measured as outlined in Section 2.3.3.4. For experimental setup see Figure 2.10 in Section 2.3.3.2. The electrodeposited film was analysed using a field emission gun scanning electron microscope equipped with EDX INCA software (Jeol JSM 6500F field emission gun scanning electron microscope (FEG-SEM) equipped with an Oxford Instruments EDX detector).

Chapter 3: Metallocenes in Non-Aqueous Solvents

In this work, four metallocenes, namely decamethylferrocene, decamethylcobaltocene, cobaltocenium hexafluorophosphate and decamethylcobaltocenium hexafluorophosphate and one non metallocene, namely sodium cobalticarborane were studied for their possible application as internal reference redox couples and as model redox species in both $scCO_2$/MeCN and scR32 systems. The complexes studied have a different charge associated with the redox couple, neutral, positive and negatively charged. This difference in charge would be important when studying diffusion into nanopores. All metallocenes are soluble in both supercritical systems and have been used in the literature as described in Chapter 1.3. Although decamethylcobaltocenium hexafluorophosphate is not described in the literature, it is an analogue of cobaltocenium hexafluorophosphate and thus should be soluble in a similar fashion.

In the non-steady state voltammetry experiments (i.e. macroelectrodes) the peak potentials and currents were used to characterise the redox system. The number of electrons transferred during a reversible oxidation or reduction at the electrode, *n*, can be determined from Equations 3.1 and 3.2, Equation 3.2 shows the processes for 298 K.

$$E_{pa} - E_{pc} = \frac{2.2RT}{nF} \tag{3.1}$$

$$E_{pa} - E_{pc} = \frac{0.0570}{n} \text{ at } 298 \text{ K} \tag{3.2}$$

The dependence of the peak current on scan rate for a reversible electrode process is described by the Randles-Sevčik (Equation 3.3), which for processes at 298 K is given by Equation 3.4. Irreversible electrode processes are described by Equations 3.5 and 3.6, where the latter is at 298 K[100-102].

$$i_p = \frac{0.446 n^{\frac{3}{2}} D^{\frac{1}{2}} A c \nu^{\frac{1}{2}} F^{\frac{3}{2}}}{(RT)^{\frac{1}{2}}} \tag{3.3}$$

$$i_p = 2.69\ x\ 10^5 n^{\frac{3}{2}} D^{\frac{1}{2}} A c \nu^{\frac{1}{2}} \tag{3.4}$$

$$i_p = \frac{0.496 n (\alpha n)^{\frac{1}{2}} D^{\frac{1}{2}} A c \nu^{\frac{1}{2}} F^{\frac{3}{2}}}{(RT)^{\frac{1}{2}}} \tag{3.5}$$

$$i_p = 2.99\ x\ 10^5\ n(\alpha n)^{\frac{1}{2}} D^{\frac{1}{2}} A c \nu^{\frac{1}{2}} \tag{3.6}$$

Where i_p is the peak current in units of Amps, *n* is the number of e^- transferred, *D* is the diffusion coefficient in units of $cm^2\ s^{-1}$, *A* is the area of the working electrode in units of cm^2,

c is the concentration in units of mol cm^{-3}, v is the scan rate in units of V s^{-1}, F is Faradays constant (96485.34 C mol^{-1}), R is the molar gas constant (8.314 J K^{-1} mol^{-1}), T is the temperature in units of Kelvin (K) and α is the transfer coefficient. These Equations were used to determine the diffusion coefficients of metallocenes for the non-steady experiments in all systems.

In the steady state experiments, in which microdisc electrodes of varying size were employed, the following expressions were used to analyse the voltammograms. The mass transport limited current used for estimating the diffusion coefficients of the various complexes is given by Equation 3.7.

$$i_L = 4nFDca \tag{3.7}$$

Where i_L is the mass transport limited current (also referred to as steady state current), a is the radius of the working electrode, all other terms are the same as those in Equations 3.3 - 3.6. The dependence of the limiting current on both concentration of species and the microdisc size were plotted to determine the diffusion coefficient, D.

The potential current correlation for the reversible steady state cyclic voltammetry at a microelectrode is given in Equation 3.8.

$$E = E_{1/2} + \frac{RT}{nF}\ln\left(\left(\frac{i_L}{i}\right) - 1\right) \tag{3.8}$$

Where $E_{1/2}$ is the half wave potential. The half wave potentials were found from the mass transport corrected Tafel analysis by plotting E *vs.* $\ln((i_L/i)-1)$ between $E_{1/4}$ and $E_{3/4}$. The $E_{1/2}$ values were determined from the intercept with the x-axis. The slope of the linear regression for a one e^- reversible transfer equals nF/RT[103].

Mirkin and Bard[104] provided a table for microdisc electrodes with values of transfer coefficients and rate constants for quasi-reversible and irreversible steady state voltammograms with known $E_{1/2}$, $E_{1/4}$ and $E_{3/4}$. The difference between the half wave potential and quartile potentials (Equations 3.9 and 3.10) which are higher than the 29 mV (at 298 K) estimated for a reversible process, can be compared to those listed by Mirkin and Bard[104] and the kinetic parameters listed.

$$\Delta E_{\frac{1}{4}} = E_{\frac{1}{2}} - E_{\frac{1}{4}} \tag{3.9}$$

$$\Delta E_{\frac{3}{4}} = E_{\frac{3}{4}} - E_{\frac{1}{2}} \tag{3.10}$$

Chronoamperometry can also be used to determine the diffusion coefficient and concentration of a given system. Denuault *et al*[105]. showed that the diffusion coefficient of an electroactive species can be determined without prior knowledge of the bulk concentration or the number of

electrons transferred. The direct determination of D at long times ($Dt/a^2 > 10^2$, for < 1% error) is given in Equation 3.11[105]

$$\frac{i}{i_L} = \frac{2a}{\pi^{\frac{3}{2}} D^{\frac{1}{2}}} \frac{1}{t^{\frac{1}{2}}} + 1 \qquad (3.11)$$

Where t is the time in units of seconds, all other terms have been described previously. From Equation 3.11, it is clear that a plot of i/i_L *vs.* $1/t^{1/2}$ will yield a straight line with a gradient proportional to the diffusion coefficient and intercept the *y*-axis at 1. This method was used when the concentration of the metallocene was not fully known, i.e. when performing experiments in a N_2-purged glove box as small changes in pressure can dramatically effect preparing solutions and change the mass readout. The mass readout can vary by 1 to 5 mg. This was also used when the metallocene complex had not fully dissolved.

3.1 Cyclic Voltammetry of Decamethylferrocene in Acetonitrile

Cyclic Voltammetry for a macroelectrode at various scan rates, and for microelectrodes of various sizes was carried out to examine the behaviour of the couple in MeCN with $[NBu_4^n][BF_4]$ as supporting electrolyte. The supporting electrolyte concentration used was comparable to the low concentration used in $scCO_2$/MeCN and scR32. The process studied is shown in Equation 3.13.

$$DmFc^0 \leftrightarrow DmFc^+ + e^- \qquad (3.13)$$

Cyclic voltammograms performed in a solution of acetonitrile containing 0.536 mM DMFc and 20 mM $[NBu_4^n][BF_4]$, for a 25 and 50 µm Ø Pt disc, at 298 K, are presented in Figure 3.1. The data obtained from the cyclic voltammograms are presented in Table 3.1. The limiting currents determined from Figure 3.1 for the 25 and 50 µm Ø Pt was 4.25 and 9.00 nA respectively. Using the limiting currents and Equation 3.7, the diffusion coefficient was calculated to be D = 1.64 x 10^{-5} cm^2 s^{-1} and D = 1.74 x 10^{-5} cm^2 s^{-1} for the 25 and 50 µm Ø Pt respectively. These values are slightly higher than those reported by Gennett *et al*[106]. and Matsumoto *et al*[107]. whom both report a value near to D = 1.30 x 10^{-5} cm^2 s^{-1} in acetonitrile at 298 K. The variation of D is most likely due to the difference in supporting electrolyte concentration, as both literature cases used an excess concentration of supporting electrolyte.

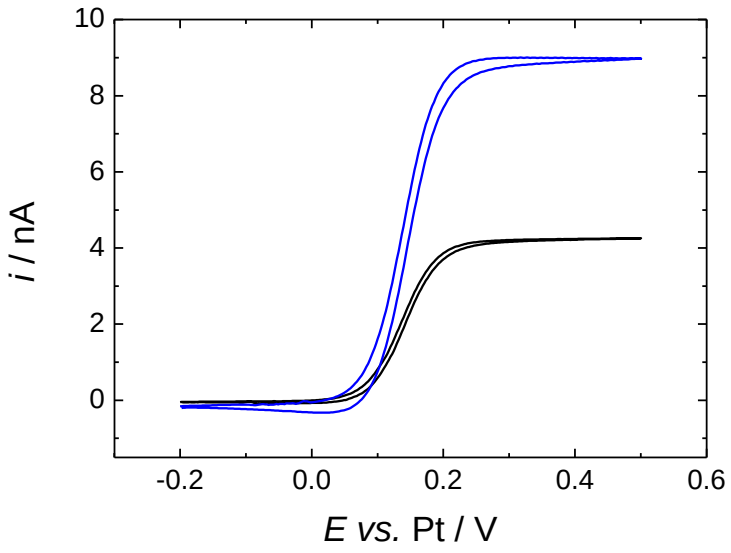

Figure 3.1. Cyclic voltammograms for a solution containing 0.536 mM DMFc and 20 mM [NBu_4^n][BF_4] in acetonitrile, v = 10 mV s^{-1} for both scans, T = 298 K. The working electrode was a Pt (25 µm Ø black line) disc and a Pt (50 µm Ø blue line) disc with a Pt gauze counter electrode and a Pt *Pseudo* (1 mm Ø disc) reference electrode. The experiment was performed in a nitrogen purged glove box.

Table 3.1. Cyclic voltammetry data obtained for experiments of 0.536 mM DMFc with 20 mM [NBu_4^n][BF_4] in MeCN at 298 K and 10 mV s^{-1} for varying sizes of microelectrode.

a / µm ± 0.5	i_L / nA ± 0.01	$\Delta E_{(1/4\text{-}3/4)}$ / mV ± 0.5	$E_{1/2}$ / V ± 0.001	$\Delta E_{1/4}$ / mV ± 0.5	$\Delta E_{3/4}$ / mV ± 0.5	$d\ln[(i_L/i)\text{-}1]/dE$ / V^{-1} ± 0.1	n ± 0.01
12.5	4.25	55.0	0.138	29.0	26.0	38.4	0.99
25.0	9.00	55.0	0.139	29.0	26.0	40.2	1.03

The half wave potentials and value of n for the steady-state voltammograms were determined from the mass transport corrected Tafel analysis, Equation 3.8, shown in Figure 3.2. The slope values for the 25 and 50 µm Ø Pt discs were 38.4 and 40.2 V^{-1}, respectively, which corresponds closely to the expected 39 V^{-1} at 298 K for a reversible one-electron process[103]. The difference between the half wave and quartile potentials are below 29 mV again suggesting a reversible process.

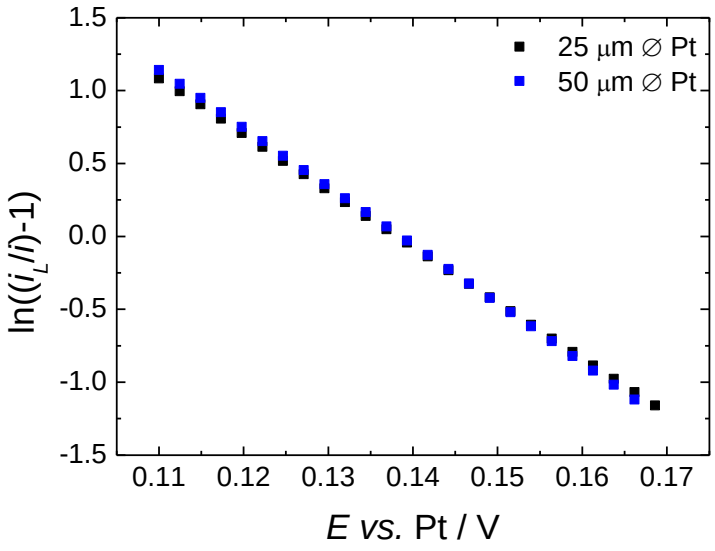

Figure 3.2. Mass transport corrected Tafel analysis for cyclic voltammetry of 0.536 mM DMFc and 20 mM [NBu_4^n][BF_4] in acetonitrile at 10 mV s^{-1}, at 298 K, for microelectrodes of 25 and 50 μm diameter.

Cyclic voltammetry recorded at various scan rates in a solution of 0.536 mM DMFc with 20 mM [NBu_4^n][BF_4] in MeCN, for 0.5 mm Ø Pt disc, at 298 K, are presented in Figure 3.3. The data obtained for the cyclic voltammograms is presented in Table 3.2. The peak potential difference was close to 77 mV for all scan rates. Noviandri *et al*[70]. reported a peak potential separation of 96 mV at scan rate of 0.1 V s^{-1} in MeCN with 0.1 M [NBu_4^n][BF_4], which increased further with scan rate. The larger than 59 mV separation was attributed to the uncompensated solution resistance[70]. The difference between the peak potential and the half wave potential was between 61 – 67 mV, which is close to the expected 59 mV potential separation. The ratio of the peak currents was unity.

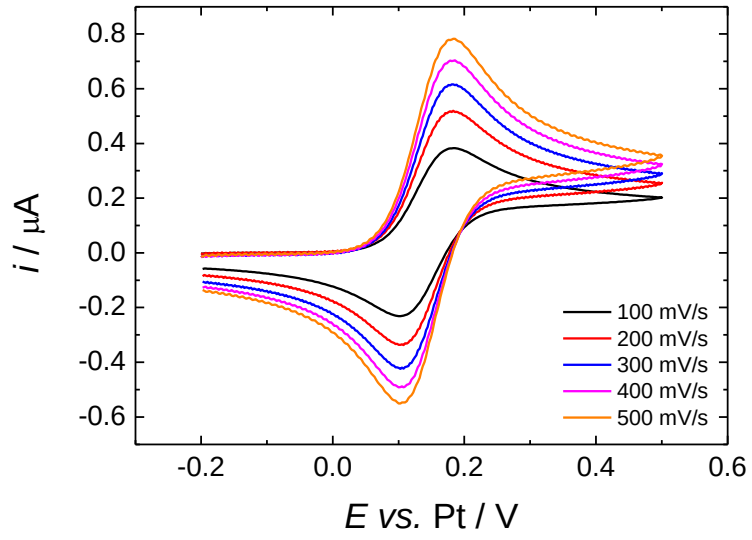

Figure 3.3. Cyclic voltammograms for a solution of 0.536 mM DMFc and 20 mM [NBu_4^n][BF_4] in MeCN at 298 K. The working electrode was a 0.5 mm Ø Pt disc with a Pt gauze counter electrode and a 1 mm Ø Pt disc reference electrode.

Table 3.2. Data obtained from cyclic voltammograms of 0.536 mM DMFc and 20 mM [NBu_4^n][BF_4] in MeCN at 298 K for various scan rates at a 0.5 mm Ø Pt disc.

v / V s^{-1}	E_{pa} / mV ± 1	E_{pc} / mV ± 1	ΔE_p / mV ± 1	$E_{pa/2}$ / mV ± 1	$E_{pc/2}$ / mV ± 1	$E_{pa} - E_{pa/2}$ / mV ± 1	$E_{pc} - E_{pc/2}$ / mV ± 1	i_{pa} / µA ± 0.001	i_{pc} / µA ± 0.001	i_{pa}/i_{pc} ± 0.01
0.1	181	104	77	120	167	61	63	0.381	0.376	1.01
0.2	183	104	79	119	168	64	64	0.517	0.508	1.02
0.3	181	104	77	120	171	61	67	0.616	0.616	1.00
0.4	181	104	77	118	167	63	63	0.702	0.697	1.01
0.5	181	104	77	119	169	62	65	0.779	0.768	1.01

The dependence of the peak current with scan rate at 298 K is described in Equation 3.4, from this Equation, the diffusion coefficient could be determined. A plot of the peak anodic and cathodic current against $v^{1/2}$ should yield a straight line plot which extrapolates to the origin, Figure 3.4. Although the linear fit for the peak anodic and cathodic current does not extrapolate to the origin in this case, the diffusion coefficient was still calculated. The linear fit not extending to the origin is most likely due to uncompensated solution resistance, although it should be noted that at zero current there will be zero *iR* drop. The low viscosity of MeCN (η = 0.341 mPa s at 298 K[107]) can lead to mixing of the solution which will give a small amount of convection, this is most likely the cause of the offset seen in the linear fit. The diffusion coefficient calculated from the peak anodic and peak cathodic plot was D = 1.17 x 10^{-5} cm^2 s^{-1} and 1.23 x 10^{-5} cm^2 s^{-1} respectively. These values are lower than those calculated for the microelectrode but are similar to those reported in literature[106,107]. DMFc has

been shown to be a reliable redox couple for future use in acetonitrile, and can be extended to $scCO_2$/MeCN mixtures.

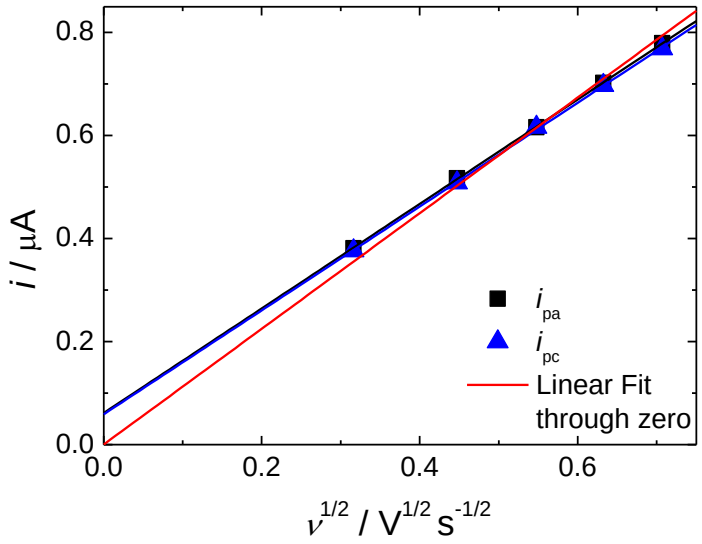

Figure 3.4. The dependence of peak currents on the scan rate for cyclic voltammetry of 0.536 mM DMFc and 20 mM [NBu_4^n][BF_4] in MeCN at 298 K, at 0.5 mm Ø Pt disc working electrode.

3.2 Cyclic Voltammetry of Decamethylcobaltocene in Acetonitrile

Cyclic Voltammetry for a macroelectrode at various scan rates, and voltammetry at a microelectrode was carried out to examine the behaviour of the couple in MeCN with [NBu_4^n][BF_4] as supporting electrolyte. The couple was studied before and after sublimation was performed for purification. The supporting electrolyte concentration used was comparable to the low concentration used in $scCO_2$/MeCN and scR32. The process studied is shown in Equation 3.14.

$$DmCo^0 \leftrightarrow DmCo^+ + e^- \qquad (3.14)$$

3.2.1 Before Sublimation

Cyclic voltammograms performed in a solution of acetonitrile containing 2 mM DmCo and 20 mM [NBu_4^n][BF_4], for a 10 µm Ø and 40 µm Ø Pt, at 298 K, are presented in Figure 3.5. The solution was made up in a nitrogen purged glove box and performed in the sc autoclave cell to reduce the dissolved oxygen content compared to a glass cell. Scans on both microelectrodes show an additional process occurring (at -0.15 V) and the current does not reach a steady state value. Additional peaks were also seen at a macro electrode, suggesting the compound was not

pure. Due to the unusual features seen in the voltammograms it was decided to sublime the compound to try and remove the impurity.

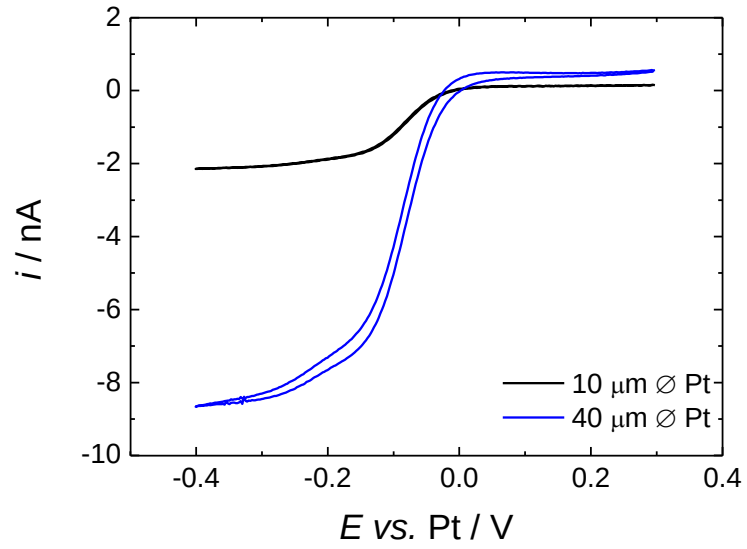

Figure 3.5. Cyclic voltammograms for a solution containing 2 mM DmCo and 20 mM [NBu_4^n][BF_4] in acetonitrile, v = 10 mV s^{-1} for both scans, T = 298 K. The working electrode was a Pt (10 µm Ø black line) disc and a Pt (40 µm Ø blue line) disc with a Pt wire counter electrode and a Pt *Pseudo* (0.5 mm Ø disc) reference electrode. The experiment was performed in a nitrogen purged glove box.

3.2.2 After Sublimation

Cyclic voltammetry performed in a solution of acetonitrile containing 0.433 mM DmCo and 20 mM [NBu_4^n][BF_4], for a 50 µm Ø Pt, at 298 K is displayed in Figure 3.6. The data obtained for the cyclic voltammetry is displayed in Table 3.3. The cyclic voltammetry shows a typical microelectrode process with no additional processes indicating the sublimation has removed an impurity. The limiting current obtained from the cyclic voltammetry was found to be -5.54 nA. Using Equation 3.7, the diffusion coefficient was calculated to be D = 1.33 x 10^{-5} cm^2 s^{-1}. The diffusion coefficient calculated was close to literature value (D = 1.30 x 10^{-5} cm^2 s^{-1})[106].

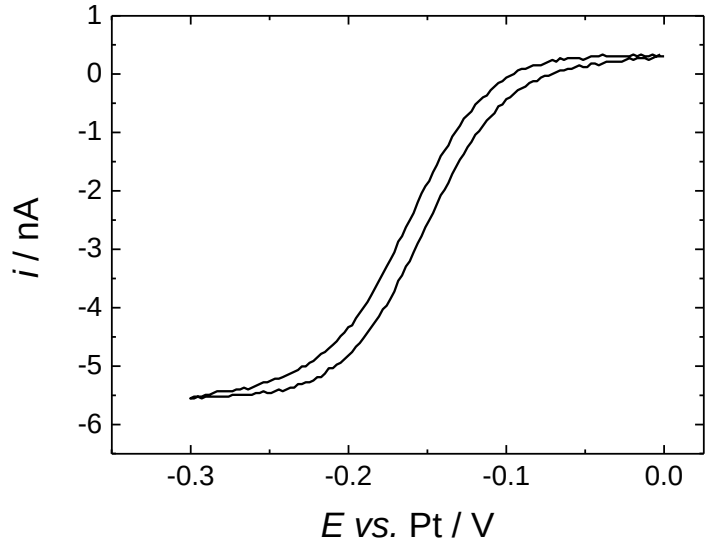

Figure 3.6. Cyclic voltammetry for a solution containing 0.433 mM DmCo and 20 mM [NBu_4^n][BF_4] in acetonitrile, v = 10 mV s^{-1}, T = 298 K. The working electrode was a Pt (50 µm Ø) disc a Pt wire counter electrode and a Pt wire reference electrode. The experiment was performed in a nitrogen purged glove box.

Table 3.3. Cyclic voltammetry data obtained for experiments of 0.433 mM DmCo with 20 mM [NBu_4^n][BF_4] in MeCN at 298 K and 10 mV s^{-1} for a 50 µm Ø Pt disc.

a / µm ± 0.5	i_L / nA ± 0.01	$\Delta E_{(1/4\text{-}3/4)}$ / mV ± 0.5	$E_{1/2}$ / V ± 0.001	$\Delta E_{1/4}$ / mV ± 0.5	$\Delta E_{3/4}$ / mV ± 0.5	$d\ln[(i_L/i)\text{-}1]/dE$ / V^{-1} ± 0.1	n ± 0.01
25.0	5.54	54.0	-0.154	27.3	27.0	41.2	1.06

The half wave potential and value for n for the steady-state voltammogram was determined from the mass transport corrected Tafel analysis from Equation 3.8, shown in Figure 3.7. The slope value was 41.2 V^{-1} which is close to the values determined for DMFc and close to the expected value of 39 V^{-1} at 298 K given in literature[103]. The difference between the quartile and half wave potentials are also below 29 mV again suggesting a reversible process.

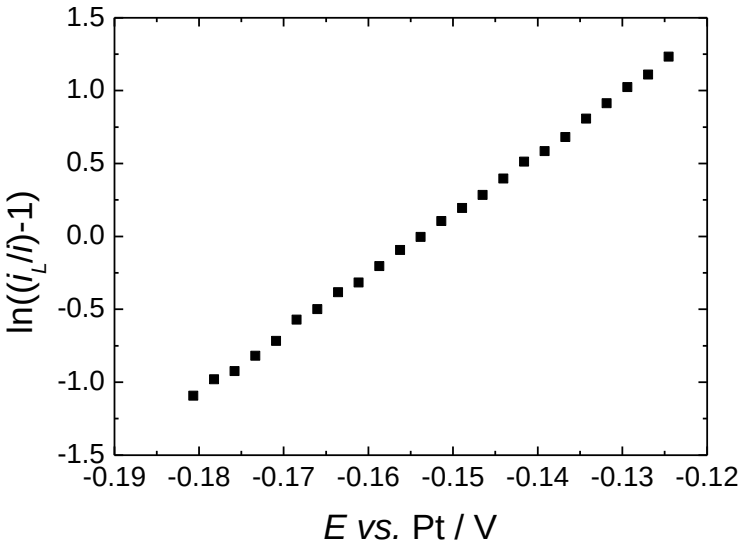

Figure 3.7. Mass transport corrected Tafel analysis for cyclic voltammetry of 0.433 mM DmCo and 20 mM [NBu_4^n][BF_4] in acetonitrile at 10 mV s^{-1}, at 298 K, for a microelectrode of 50 µm diameter.

Cyclic voltammetry recorded at various scan rates in a solution of acetonitrile containing 0.433 mM DmCo and 20 mM [NBu_4^n][BF_4] at 298 K, for a 0.5 mm Ø Pt disc, are presented in Figure 3.8. The data collected from the cyclic voltammograms is presented in Table 3.4. The peak potential separation was between 79.4 and 84.0 mV, these values are higher than those determined for DMFc. Again, like for DMFc, the larger than 59 mV peak potential separations was attributed to uncompensated solution resistance. The difference between the peak potential and the half wave potentials was between 59 and 66 mV, which are close to the expected 59 mV potential separation. The ratio of the peak currents was between 0.7 and 0.86, which suggests an irreversible system.

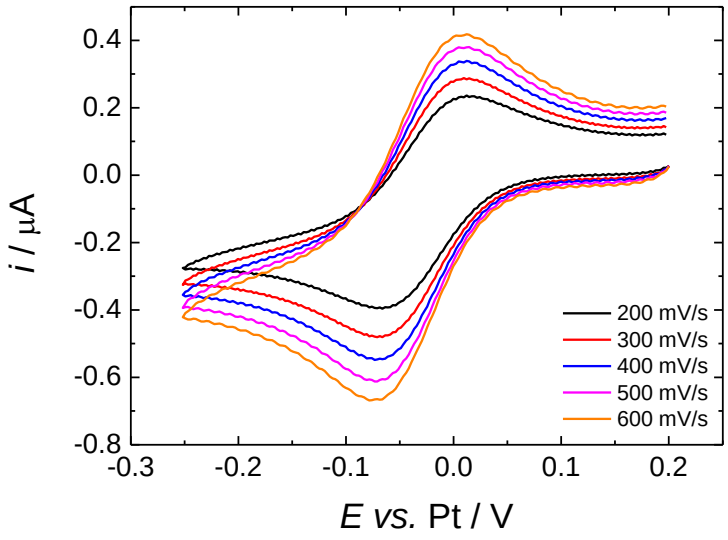

Figure 3.8. Cyclic voltammograms for a solution of 0.433 mM DmCo and 20 mM $[NBu_4^n][BF_4]$ in MeCN at 298 K. The working electrode was a 0.5 mm Ø Pt disc with a Pt wire counter electrode and a Pt wire reference electrode.

Table 3.4. Data obtained from cyclic voltammograms of 0.433 mM DmCo and 20 mM $[NBu_4^n][BF_4]$ in MeCN at 298 K for various scan rates at a 0.5 mm Ø Pt disc.

v / V s^{-1}	E_{pa} / mV ± 1	E_{pc} / mV ± 1	ΔE_p / mV ± 1	$E_{pa/2}$ / mV ± 1	$E_{pc/2}$ / mV ± 1	$E_{pa} - E_{pa/2}$ / mV ± 1	$E_{pc} - E_{pc/2}$ / mV ± 1	i_{pa} / μA ± 0.001	i_{pc} / μA ± 0.001	i_{pa}/i_{pc} ± 0.01
0.2	14	-68	82	-51	-6	65	-62	0.299	0.347	0.86
0.3	11	-69	80	-53	-10	64	-59	0.346	0.425	0.82
0.4	10	-69	79	-54	-9	64	-60	0.408	0.484	0.84
0.5	11	-70	81	-53	-10	64	-60	0.432	0.557	0.78
0.6	10	-74	84	-55	-9	65	-65	0.472	0.663	0.71

The dependence of the peak current with $v^{1/2}$ at 298 K at the 0.5 mm Ø Pt disc is presented in Figure 3.9. Like for DMFc, the linear fit for both the anodic and cathodic current does not extrapolate to the origin. Unlike for DMFc, the deviation from the origin is more apparent. For this case, it is clear that the Randles-Sevčik is not appropriate for calculating the diffusion coefficient of decamethylcobaltocene. Although DmCo does not exhibit ideal reversible electrochemistry at macroelectrodes, the voltammetry obtained and diffusion coefficient calculated for microelectrodes suggest it could be a useful redox probe in $scCO_2$/MeCN.

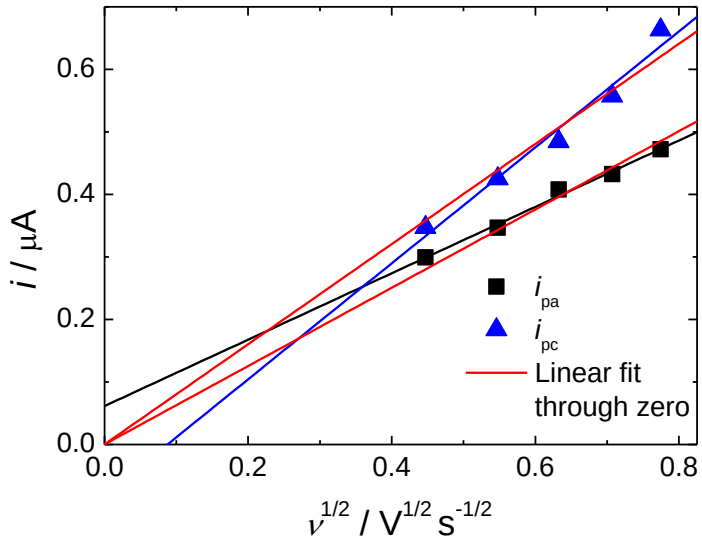

Figure 3.9. The dependence of peak currents on the scan rate for cyclic voltammetry of 0.433 mM DmCo and 20 mM [NBu_4^n][BF_4] in MeCN at 298 K, at 0.5 mm Ø Pt disc working electrode.

3.3 Cyclic Voltammetry of Cobaltocenium Hexafluorophosphate in Acetonitrile

Cyclic voltammetry for a macroelectrode at various scan rates, and voltammetry at a microelectrode was carried out to examine the behaviour of the couple in MeCN and [NBu_4^n][BF_4] as a supporting electrolyte. The supporting electrolyte concentration used was comparable to the low concentration used in $scCO_2$/MeCN and scR32. The process studied is shown in Equation 3.15.

$$CoCp_2^+ + e^- \leftrightarrow CoCp_2^0 \qquad (3.15)$$

Cyclic voltammetry for a solution of acetonitrile containing 0.524 mM [$CoCp_2$][PF_6] and 20 mM [NBu_4^n][BF_4] for a 25 µm Ø Pt, at 298 K, is displayed in Figure 3.10. The data obtained from the voltammetry is presented in Table 3.5. The limiting current determined from the voltammetry in Figure 3.10 was i_L = -6.27 nA. The diffusion coefficient was again calculated using the limiting current and was found to be D = 2.48 x 10^{-5} cm^2 s^{-1}. This value is higher than that quoted by Gennett *et al*. who reported a value of D = 1.80 x 10^{-5} cm^2 s^{-1} in acetonitrile at 298 K. Although the values of D may differ due to the low supporting electrolyte used in this system, it is most likely due to the concentration of the system. Weighing out metallocenes in a nitrogen purged glove box can be troublesome as small changes in pressure can drastically change the mass read out, especially when masses of < 10 mg are being used.

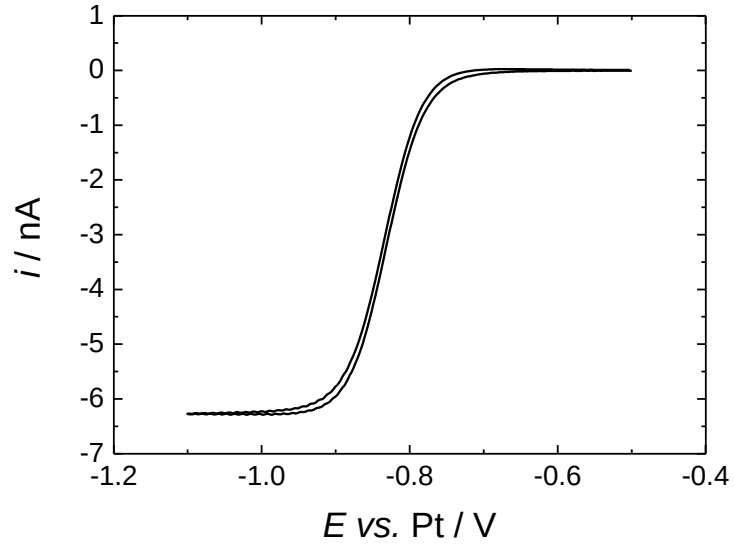

Figure 3.10. Cyclic voltammetry for a solution containing 0.524 mM $[CoCp_2][PF_6]$ and 20 mM $[NBu_4^n][BF_4]$ in acetonitrile, ν = 10 mV s^{-1}, T = 298 K. The working electrode was a Pt (25 µm Ø) disc a Pt gauze counter electrode and a Pt (1 mm Ø) disc reference electrode. The experiment was performed in a nitrogen purged glove box.

Table 3.5. Cyclic voltammetry data obtained for experiments of 0.524 mM $[CoCp_2][PF_6]$ with 20 mM $[NBu_4^n][BF_4]$ in MeCN at 298 K and 10 mV s^{-1} for a 25 µm Ø Pt disc.

a / µm ± 0.5	i_L / nA ± 0.01	$\Delta E_{(1/4\text{-}3/4)}$ / mV ± 0.5	$E_{1/2}$ / V ± 0.001	$\Delta E_{1/4}$ / mV ± 0.5	$\Delta E_{3/4}$ / mV ± 0.5	$d\ln[(i_L/i)\text{-}1]/dE$ / V^{-1} ± 0.1	n ± 0.01
12.5	6.27	59.0	-0.830	30.0	29.0	39.9	1.01

The half wave potential and n were once again determined from the mass transport corrected Tafel analysis, Figure 3.11. The slope was determined to be 39.9 V^{-1}, which is very close to the expected 39 V^{-1} and similar to that determined for DMFc. The difference between the quartile and the half wave potentials was close to the expected 29 mV for a reversible process at 298 K.

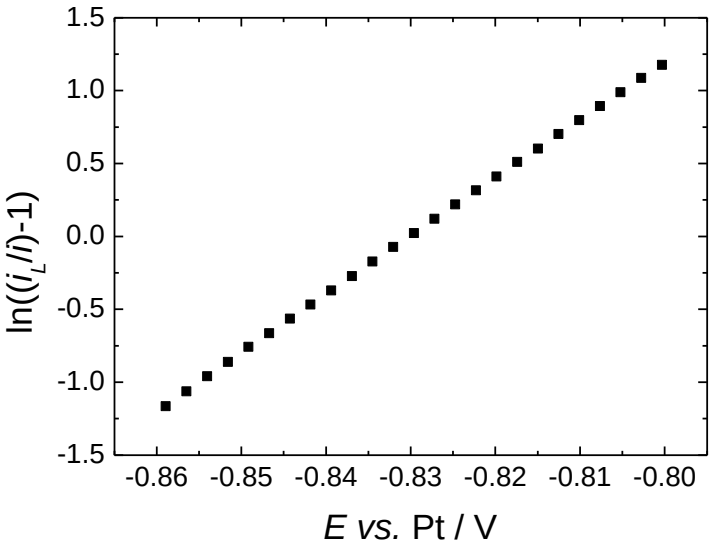

Figure 3.11. Mass transport corrected Tafel analysis for cyclic voltammetry of 0.524 mM $[CoCp_2][PF_6]$ and 20 mM $[NBu_4^n][BF_4]$ in acetonitrile at 10 mV s^{-1}, at 298 K, for a microelectrode of 25 µm diameter.

To more accurately obtain the diffusion coefficient and concentration of the system, chronoamperometry was performed at the microelectrode. A plot of i/i_L against $1/\sqrt{t}$ from Equation 3.11 is displayed in Figure 3.12. The noise seen in the plot is due to the lack of faraday cage in the nitrogen purged glove box. The plot intercepts at 0.93 on the y-axis and not the expected value of 1 from literature[105], this is most likely due to distortion experienced in the plot. Taking the value of the gradient leads to a diffusion coefficient value of D = 1.25 x 10^{-5} cm^2 s^{-1}, which is lower than the value of 1.80 x 10^{-5} cm^2 s^{-1} quoted in literature[106]. Using the value of the diffusion coefficient calculated from Figure 3.12 and Equation 3.7, the concentration of the system was calculated to be 1.04 mM. This is higher than the expected value from the mass placed into the system, affecting the diffusion coefficient calculated from the microdisc voltammetry. The concentration determined from the chronoamperometry was used in further analysis for the macro electrode.

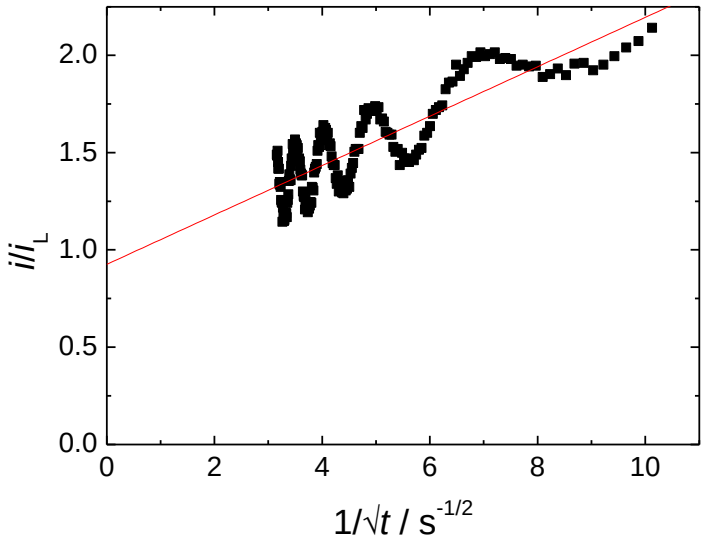

Figure 3.12. Plot of $i(t)/i_L$ against the inverse square root of time at a Pt (25 µm Ø) disc. The solution, counter, reference electrodes and conditions are described in Figure 3.10.

Cyclic voltammetry recorded at various scan rates in a solution of 1.04 mM $[CoCp_2][PF_6]$ and 20 mM $[NBu_4^n][BF_4]$ in MeCN, for a 0.5 mm Ø Pt disc, at 298 K, are presented in Figure 3.13. The data collected from the voltammetry is displayed in Table 3.6. The peak potential difference for $CoCp_2^+$ was measured between 77 and 80 mV, which is similar to that seen for DmCo in MeCN. The larger than expected 59 mV is the same as that seen for DMFc and DmCo. The difference between the half wave and peak potentials were between 60 and 63 mV which again is similar to those determined for DMFc and DmCo, and are close to the expected value of 59 mV. The ratio of the peak currents was found to be between 0.93 and 0.97. The values are higher than those determined for DmCo, but not unity like those determined for DMFc. This small variation from unity is most likely due to uncompensated solution resistance.

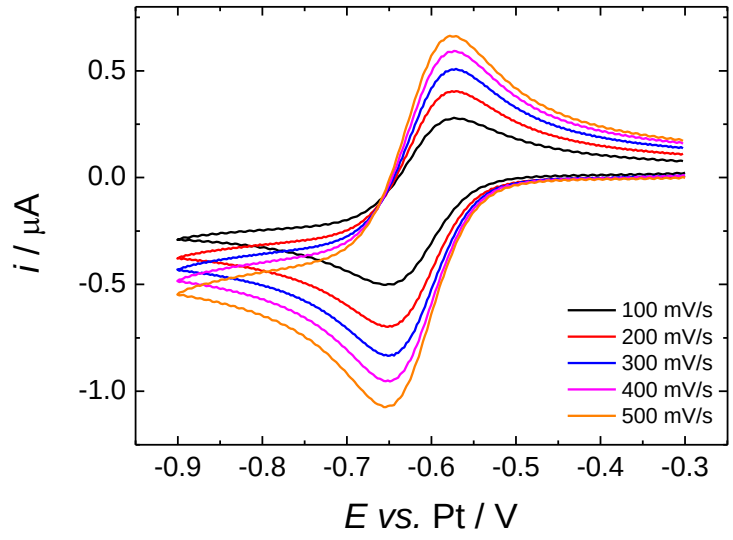

Figure 3.13. Cyclic voltammograms for a solution of 1.04 mM $[CoCp_2][PF_6]$ and 20 mM $[NBu_4^n][BF_4]$ in MeCN at 298 K. The working electrode was a 0.5 mm Ø Pt disc with a Pt gauze counter electrode and a 1 mm Ø Pt disc reference electrode.

Table 3.6. Data obtained from cyclic voltammograms of 1.04 mM $[CoCp_2][PF_6]$ and 20 mM $[NBu_4^n][BF_4]$ in MeCN at 298 K for various scan rates at a 0.5 mm Ø Pt disc.

v / V s^{-1}	E_{pa} / mV ± 1	E_{pc} / mV ± 1	ΔE_p / mV ± 1	$E_{pa/2}$ / mV ± 1	$E_{pc/2}$ / mV ± 1	$E_{pa} - E_{pa/2}$ / mV ± 1	$E_{pc} - E_{pc/2}$ / mV ± 1	i_{pa} / µA ± 0.001	i_{pc} / µA ± 0.001	i_{pa}/i_{pc} ± 0.01
0.1	-573	-653	80	-635	-592	62	-61	0.472	0.500	0.94
0.2	-573	-650	77	-635	-590	62	-60	0.643	0.695	0.93
0.3	-573	-650	77	-635	-590	62	-60	0.783	0.834	0.94
0.4	-573	-650	77	-635	-583	62	-67	0.885	0.954	0.93
0.5	-573	-654	79	-638	-592	63	-62	0.979	1.070	0.91

The dependence of the peak current with $v^{1/2}$ at 298 K for the 0.5 mm Ø Pt disc is presented in Figure 3.14. Although the linear fit does not extrapolate to the origin, the plot is close to that determined for DMFc, thus the diffusion coefficient was calculated. The diffusion coefficient calculated for the anodic and cathodic plot were D = 0.58 x 10^{-5} cm^2 s^{-1} and D = 0.65 x 10^{-5} cm^2 s^{-1} respectively. These values are lower than that determined at the microelectrode and lower than that reported in literature. Despite this variation in diffusion coefficient, $CoCp_2^+$ has been shown to be a reliable redox couple in acetonitrile and can be extended to the supercritical system.

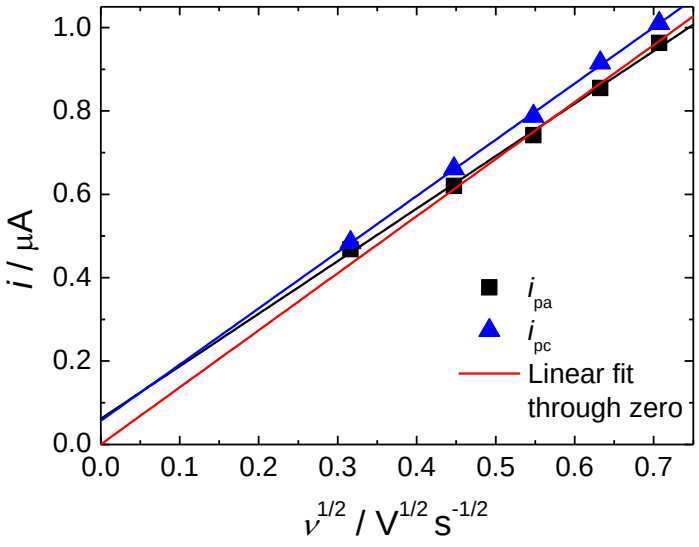

Figure 3.14. The dependence of peak currents on the scan rate for cyclic voltammetry of 1.04 mM $[CoCp_2][PF_6]$ and 20 mM $[NBu_4^n][BF_4]$ in MeCN at 298 K, at 0.5 mm Ø Pt disc working electrode for various scan rates.

3.4 Cyclic Voltammetry of Decamethylferrocene in Dichloromethane

Dichloromethane (DCM) was also used to test the redox properties of metallocenes. Dichloromethane was used as it is a liquid analogue to supercritical difluoromethane (scR32). Cyclic voltammetry for a macroelectrode at various scan rates, and for microelectrodes of various sizes was carried out to examine the behaviour of the couple in DCM with $[NBu_4^n][BF_4]$ as supporting electrolyte. The process studied is the same as described in Equation 3.13.

Cyclic voltammograms performed in a solution of DCM containing 0.479 mM DMFc and 20 mM $[NBu_4^n][BF_4]$, for a 25 and 50 µm Ø Pt, at 298 K, are presented in Figure 3.15. The data collected from the voltammetry is displayed in Table 3.7. The limiting currents determined from Figure 3.15 for the 25 and 50 µm Ø Pt were 3.36 and 6.85 nA respectively. Using Equation 3.7, the diffusion coefficients were calculated to be D = 1.45 x 10^{-5} cm^2 s^{-1} and 1.48 x 10^{-5} cm^2 s^{-1} for the 25 and 50 µm Ø respectively. These values are close to literature value presented by Gennett *et al*[106]. at 298 K in DCM of D = 1.30 x 10^{-5} cm^2 s^{-1}. Although these values are close to those presented by Gennett, Matsumoto *et al*[107]. determined a diffusion coefficient of 1.07 x 10^{-5} cm^2 s^{-1} for DMFc in DCM at 298 K. This could be caused by the difference in supporting electrolyte concentration; Matsumoto *et al*[107]. used an excess concentration of

supporting electrolyte ($[NBu_4^n][ClO_4]$ = 0.5 M) opposed to the low supporting electrolyte concentration used in this system ($[NBu_4^n][BF_4]$ = 20 mM).

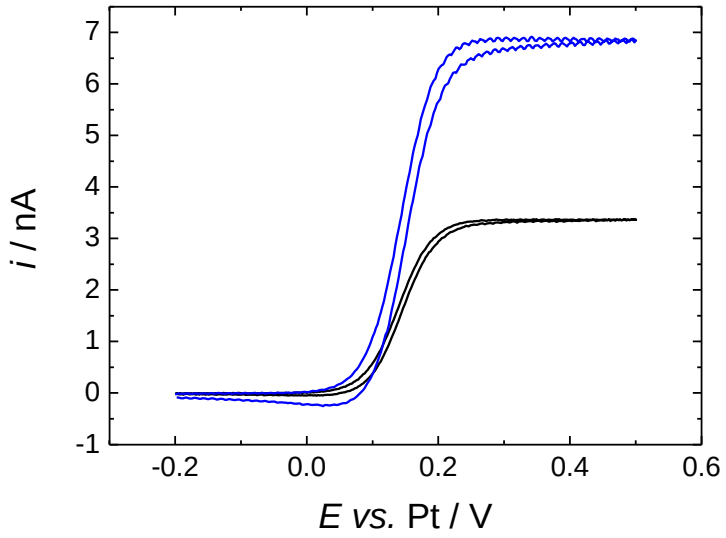

Figure 3.15. Cyclic voltammograms for a solution containing 0.479 mM DMFc and 20 mM $[NBu_4^n][BF_4]$ in dichloromethane, v = 10 mV s^{-1} for both scans, T = 298 K. The working electrode was a Pt (25 µm Ø black line) disc and a Pt (50 µm Ø blue line) disc with a Pt gauze counter electrode and a Pt *Pseudo* (1 mm Ø disc) reference electrode. The experiment was performed in a nitrogen purged glove box.

Table 3.7. Data obtained from cyclic voltammograms of 0.479 mM DMFc and 20 mM $[NBu_4^n][BF_4]$ in MeCN at 298 K and 10 mV s^{-1} at varying size of microelectrode

a / µm ± 0.5	i_L / nA ± 0.01	$\Delta E_{(1/4\text{-}3/4)}$ / mV ± 0.5	$E_{1/2}$ / V ± 0.001	$\Delta E_{1/4}$ / mV ± 0.5	$\Delta E_{3/4}$ / mV ± 0.5	$d\ln[(i_L/i)\text{-}1]/dE$ / V^{-1} ± 0.1	n ± 0.01
12.5	3.36	54.0	0.140	28	26.0	39.8	1.02
25.0	6.85	56.0	0.143	28	28.0	39.9	1.03

The half wave potentials and value of n for the steady-state voltammograms were determined from the mass transport corrected Tafel analysis, Equation 3.8, shown in Figure 3.16. The slope values for the 25 and 50 µm Ø Pt discs were 39.8 and 39.9 V^{-1}, respectively, which corresponds very closely to the expected 39 V^{-1} at 298 K for a reversible one-electron process[103]. The difference between the half wave and quartile potentials are below 29 mV again suggesting a reversible process. The results obtained in DCM correspond very closely to those obtained in MeCN, suggesting DMFc is good redox couple for both systems at microelectrodes. The shifting seen in Figure 3.16 is most likely caused by the Pt *pseudo* reference electrode.

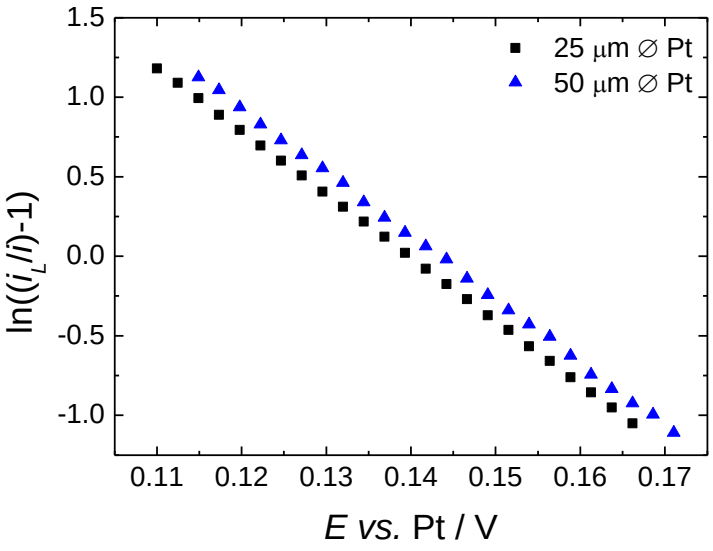

Figure 3.16. Mass transport corrected Tafel analysis for cyclic voltammetry of 0.479 mM DMFc and 20 mM [NBu_4^n][BF_4] in dichloromethane at 10 mV s^{-1}, at 298 K, for microelectrodes of 25 and 50 μm diameter.

Cyclic voltammetry recorded at various scan rates in a solution of DCM containing 0.479 mM DMFc and 20 mM [NBu_4^n][BF_4], for 0.5 mm Ø Pt, at 298 K, are presented in Figure 3.17. The data collected from the cyclic voltammograms is displayed in Table 3.8. The peak potential difference was determined to be between 79 and 91.4 mV, like for DMFc in MeCN the process can be considered quasi-reversible. The difference between the half wave and peak potentials was measured between 70 and 87 mV. The separation values are much larger than those recorded in MeCN for the other complexes. Noviandri *et al*[70]. reported a peak to peak separation of 60 mV at 22 ºC in DCM with an excess of supporting electrolyte. The strong deviation from the expected value of 59 mV in this system is most likely a cause of the uncompensated solution resistance. The ratio of the peak currents in this case are close to unity, which is comparable to DMFc in MeCN.

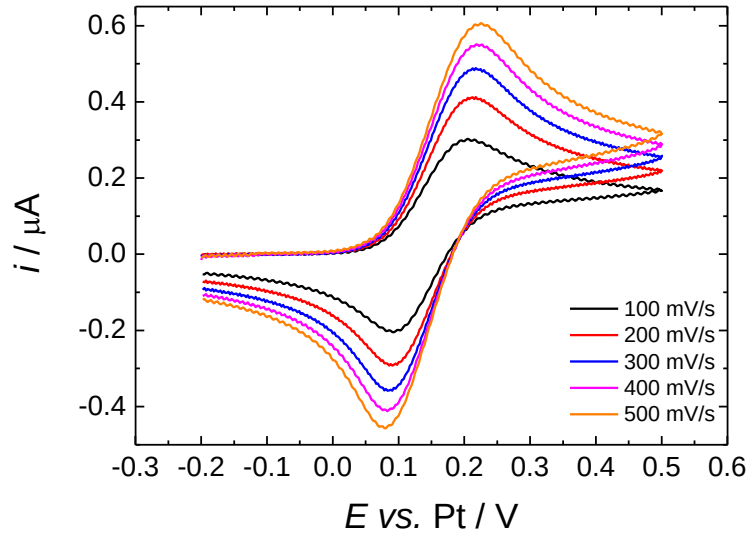

Figure 3.17. Cyclic voltammograms for a solution of 0.479 mM DMFc and 20 mM [NBu_4^n][BF_4] in DCM at 298 K. The working electrode was a 0.5 mm Ø Pt disc with a Pt gauze counter electrode and a 1 mm Ø Pt disc reference electrode.

Table 3.8. Data obtained from cyclic voltammograms of 0.479 mM DMFc and 20 mM [NBu_4^n][BF_4] in DCM at 298 K for various scan rates at a 0.5 mm Ø Pt disc.

v / V s^{-1}	E_{pa} / mV ± 1	E_{pc} / mV ± 1	ΔE_p / mV ± 1	$E_{pa/2}$ / mV ± 1	$E_{pc/2}$ / mV ± 1	$E_{pa} - E_{pa/2}$ / mV ± 1	$E_{pc} - E_{pc/2}$ / mV ± 1	i_{pa} / µA ± 0.001	i_{pc} / µA ± 0.001	i_{pa}/i_{pc} ± 0.01
0.1	205	91	114	130	162	75	71	0.300	0.307	0.98
0.2	213	90	123	132	163	81	73	0.403	0.412	0.98
0.3	218	86	132	134	162	84	76	0.485	0.495	0.98
0.4	220	83	137	135	159	85	76	0.548	0.556	0.99
0.5	225	79	146	138	158	87	79	0.603	0.609	0.99

The dependence of the peak current with $v^{1/2}$ at 298 K for the 0.5 mm Ø Pt disc is presented in Figure 3.18. As with DMFc in MeCN, the linear fits do not extrapolate to the origin. In order to compare the diffusion coefficient calculated at the microdisc and to compare the calculated diffusion coefficient for MeCN, the diffusion coefficient was calculated from Figure 3.18. The diffusion coefficient calculated from the peak anodic and peak cathodic current was D = 0.76 x 10^{-5} cm^2 s^{-1} and 0.83 x 10^{-5} cm^2 s^{-1} respectively. These values are lower than that calculated at the microdisc but are closer to the diffusion coefficient (D = 1.03 x 10^{-5} cm^2 s^{-1}) determined by Matsumoto *et al*[107]. These values for the diffusion coefficient for DMFc in DCM are also lower than those determined in MeCN, this is a reflection of the lower viscosity exhibited by MeCN. Matsumoto *et at*[107]. quotes the viscosity of MeCN at 298 K as η = 0.341 mPa s compared to DCM which has a viscosity of η = 0.411 mPa s at 298 K. Despite small variations in the calculated diffusion coefficient, DMFc has been shown to a well behaved

reliable redox couple in DCM and like for MeCN can be extended to its supercritical analogue of R32.

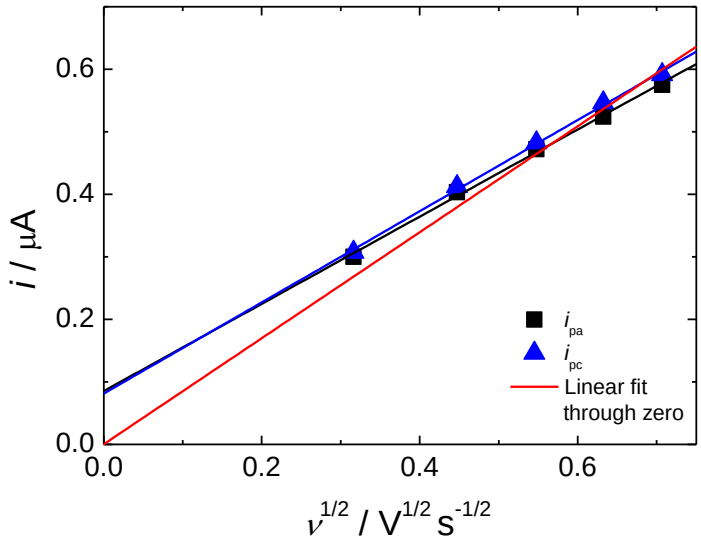

Figure 3.18. The dependence of peak currents on the scan rate for cyclic voltammetry of 0.479 mM DMFc and 20 mM [NBu_4^n][BF_4] in DCM at 298 K, at 0.5 mm Ø Pt disc working electrode for various scan rates.

3.5 Cyclic Voltammetry of Decamethylcobaltocenium hexafluorophosphate in Dichloromethane

Decamethylcobaltocenium hexafluorophosphate is similar in structure to decamethylcobaltocene, except with the addition of the hexafluorophosphate anion to stabilise the decamethylcobaltocenium cation. Cyclic voltammetry for a macroelectrode at various scan rates, and voltammetry at a microelectrode was carried out to examine the behaviour of the couple in DCM and [NBu_4^n][BF_4] as a supporting electrolyte. The process studied is the same as that shown in Equation 3.15.

Cyclic voltammetry for a solution of dichloromethane containing 0.466 mM [DmCo][PF_6] and 20 mM [NBu_4^n][BF_4] for a 25 µm Ø Pt, at 298 K, is displayed in Figure 3.19. The data obtained from the voltammetry is presented in Table 3.9. The limiting current determined from Figure 3.19 was found to be i_L = -2.94 nA. Again the diffusion coefficient was calculated using the limiting current in combination with Equation 3.7 and was found to be D = 1.31 x 10^{-5} cm^2 s^{-1}. The value obtained is in agreement with the diffusion coefficient calculated for DmCo in MeCN.

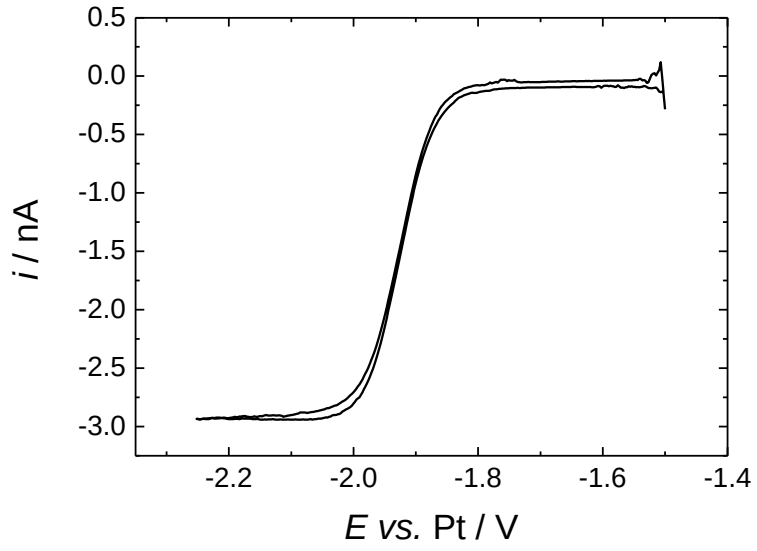

Figure 3.19. Cyclic voltammetry for a solution containing 0.466 mM [DmCo][PF_6] and 20 mM [NBu_4^n][BF_4] in DCM, v = 10 mV s^{-1}, T = 298 K. The working electrode was a Pt (25 µm Ø) disc a Pt gauze counter electrode and a Pt (0.5 mm Ø) disc reference electrode. The experiment was performed in a nitrogen purged glove box.

Table 3.9. Cyclic voltammetry data obtained for experiments of 0.466 mM [DmCo][PF_6] with 20 mM [NBu_4^n][BF_4] in DCM at 298 K and 10 mV s^{-1} for a 25 µm Ø Pt disc.

a / µm ± 0.5	i_L / nA ± 0.01	$\Delta E_{(1/4\text{-}3/4)}$ / mV ± 0.5	$E_{1/2}$ / V ± 0.001	$\Delta E_{1/4}$ / mV ± 0.5	$\Delta E_{3/4}$ / mV ± 0.5	$d\ln[(i_L/i)\text{-}1]/dE$ / V^{-1} ± 0.1	n ± 0.01
12.5	2.94	61.0	-1.920	31.0	30.0	35.4	0.91

The half wave potential and n were once again determined from the mass transport corrected Tafel analysis, Figure 3.20. The slope of the graph was found to be 35.4 V^{-1}; this is below the expected value of 39 V^{-1} and is much lower than the value obtained for DmCo in MeCN. The difference between the half wave and quartile potentials is also above 29 mV suggesting the kinetics and transfer coefficient (α) are not that of a reversible system. Using the table provided by Mirkin and Bard[104] was not possible as the values are low enough not to appear. Although this suggests that [DmCo][PF_6] may not be a suitable redox couple, analysis was also performed at a macro electrode.

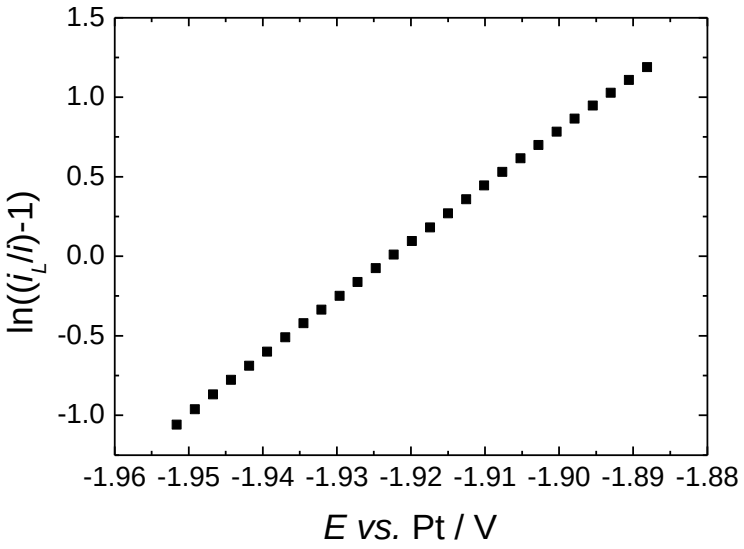

Figure 3.20. Mass transport corrected Tafel analysis for cyclic voltammetry of 0.466 mM [DmCo][PF_6] and 20 mM [NBu_4^n][BF_4] in DCM at 10 mV s^{-1}, at 298 K, for a microelectrode of 25 µm diameter.

Cyclic voltammetry recorded at various scan rates in a solution of DCM containing 0.466 mM [DmCo][PF_6] and 20 mM [NBu_4^n][BF_4], for 0.5 mm Ø Pt, at 298 K, are presented in Figure 3.17. The data collected from the cyclic voltammograms is displayed in Table 3.8. The peak potential measured for all scan rates was between 90 and 110 mV. The difference between the half wave and peak potentials was found to be between 60 and 80 mV. This variation in values is similar to that recorded for DMFc in DCM, but are much higher than those measured for DmCo in MeCN, suggesting the uncompensated solution resistance is not as pronounced in MeCN when compared to DCM. The ratio of the peak currents was also below the expected value of 1, and measured to be between 0.87 and 0.91.

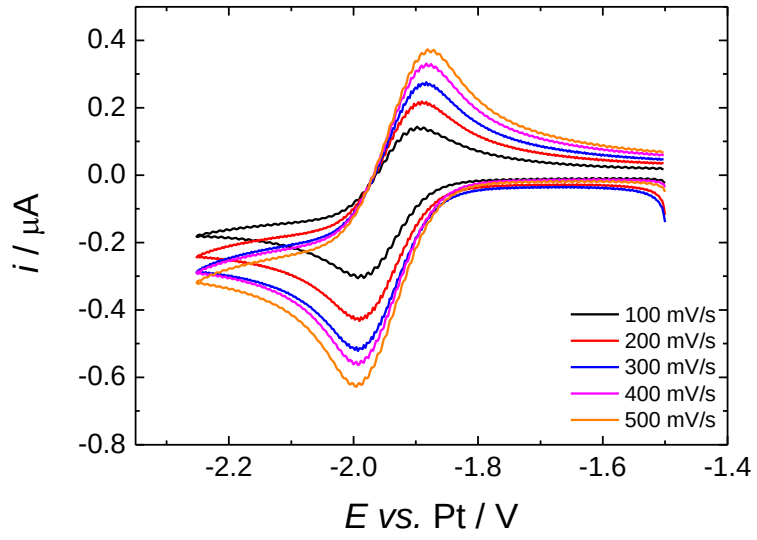

Figure 3.21. Cyclic voltammograms for a solution of 0.466 mM [DmCo][PF_6] and 20 mM [NBu_4^n][BF_4] in DCM at 298 K. The working electrode was a 0.5 mm Ø Pt disc with a Pt gauze counter electrode and a 0.5 mm Ø Pt disc reference electrode.

Table 3.10. Data obtained from cyclic voltammograms of 0.466 mM [DmCo][PF_6] and 20 mM [NBu_4^n][BF_4] in DCM at 298 K for various scan rates at a 0.5 mm Ø Pt disc.

v / V s^{-1}	E_{pa} / V ±0. 1	E_{pc} / V ± 0.1	ΔE_p / mV ± 1	$E_{pa/2}$ / V ± 0.01	$E_{pc/2}$ / V ± 0.01	$E_{pa} - E_{pa/2}$ / mV ± 1	$E_{pc} - E_{pc/2}$ / mV ± 1	i_{pa} / µA ± 0.001	i_{pc} / µA ± 0.001	i_{pa}/i_{pc} ± 0.01
0.1	-1.9	-2.0	100	-1.96	-1.92	60	70	0.246	0.272	0.90
0.2	-1.9	-2.0	100	-1.96	-1.91	70	80	0.343	0.378	0.91
0.3	-1.9	-2.0	100	-1.96	-1.91	80	80	0.410	0.454	0.90
0.4	-1.9	-2.0	100	-1.95	-1.92	70	70	0.458	0.524	0.87
0.5	-1.9	-2.0	100	-1.95	-1.92	70	70	0.524	0.575	0.91

The dependence of the peak currents with $v^{1/2}$, for the 0.5 mm Ø Pt disc, at 298 K, is presented in Figure 3.22. Like for all the compounds presented, the linear fit does not extrapolate to the origin in this case. The diffusion coefficient was calculated for both linear fits (to be able to compare to the microdisc case). The diffusion coefficient calculated for the anodic and cathodic peak current was determined to be D = 0.80 x 10^{-5} cm^2 s^{-1} and D = 1.00 x 10^{-5} cm^2 s^{-1} respectively. The values calculated from the Randles-Sevčik analysis are lower than that determined for the microdisc, and lower than the diffusion coefficient determined for DmCo in MeCN. Despite being a well behaved redox couple in DCM, the extreme cathodic reduction potential of $DmCo^+$ meant that it would not be suitable to study in scR32 with [NBu_4^n][BF_4] as a supporting electrolyte. The potential window of scR32 with [NBu_4^n][BF_4] as a supporting electrolyte *vs.* Pt reference electrode would cause an electrolyte breakdown before the redox couple could be seen. To study decamethylcobaltocenium hexafluorophosphate in scR32, a

different supporting electrolyte would need to be used. Chapter 4, Section 4.3.4 details the use of [Na][BARF] as a supporting electrolyte in scR32.

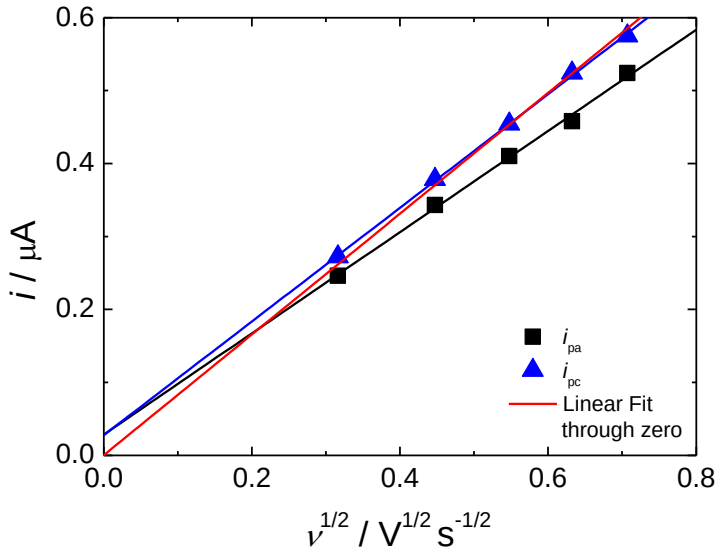

Figure 3.22. The dependence of peak currents on the scan rate for cyclic voltammetry of 0.466 mM [DmCo][PF_6] and 20 mM [NBu_4^n][BF_4] in DCM at 298 K, at 0.5 mm Ø Pt disc working electrode for various scan rates.

3.6 Cyclic Voltammetry of Sodium Cobalticarborane in Dichloromethane

Sodium cobalticarborane ($Na^+[CoC_4H_{22}B_{18}]^-$) was also selected to be tested as an internal reference redox couple for scR32. As dichloromethane is a liquid analogue of difluoromethane, it was important to study the redox behaviour of sodium cobalticarborane in DCM to see if it could be extended to supercritical fluids. When performing the experiment in DCM, the first thing that was noticed was that the complex is extremely insoluble in DCM. In this case, < 5 mg was weighed out to be placed into a 19 mL cell, which would yield a final concentration of 0.5 mM. Only small amounts of the solid went into solution, even when stirring and vigorous shaking were applied. It was assumed < 1 mg of product dissolved and the remaining mass was left at the bottom of cell, so the final concentration was unknown in this instance. Despite its insolubility, the results presented below give an indication as to whether this negatively charged species would be suitable an internal reference standard for scR32. The process studied is shown in Equation 3.16.

$$[CoC_4H_{22}B_{18}]^- \leftrightarrow [CoC_4H_{22}B_{18}] + e^- \qquad (3.16)$$

Cyclic voltammetry for a solution of dichloromethane containing an unknown concentration of $[Na][CoC_4H_{22}B_{18}]$ and 20 mM $[NBu_4^n][BF_4]$ for a 50 µm Ø Pt, at 298 K, is displayed in Figure 3.23. The voltammetry obtained is poor with no clearly defined limiting current and a large amount of hysteresis. It was also clear from the experiments that if the potential was swept beyond 1.3 V, electrolyte breakdown would occur. As the concentration of the system was unknown and no limiting current could be obtained, the diffusion coefficient of the species could not be calculated. Chronoamperometry performed contained a large amount of electrical interference, and a plot similar to that performed for $[CoCp_2][PF_6]$ intercepted the origin and not the expected value of 1. From these results it was clear the diffusion coefficient and concentration could not be calculated.

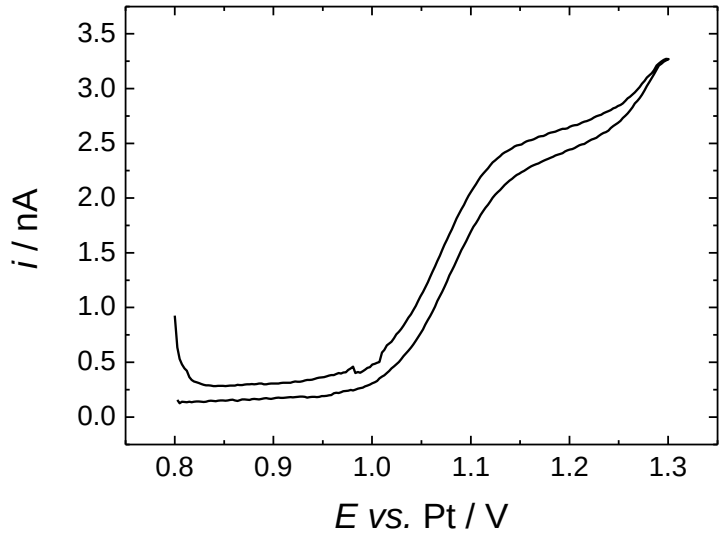

Figure 3.23. Cyclic voltammetry for a solution containing an unknown concentration of $[Na][CoC_4H_{22}B_{18}]$ and 20 mM $[NBu_4^n][BF_4]$ in DCM, v = 10 mV s^{-1}, T = 298 K. The working electrode was a Pt (50 µm Ø) disc a Pt wire counter electrode and a Pt wire reference electrode. The experiment was performed in a nitrogen purged glove box.

Cyclic voltammetry recorded at various scan rates in a solution of DCM containing an unknown concentration of $[Na][CoC_4H_{22}B_{18}]$ and 20 mM $[NBu_4^n][BF_4]$, for 0.5 mm Ø Pt, at 298 K, are presented in Figure 3.24. The voltammetry recorded at the macrodisc, as for the microdisc, is poor and the mass transport limited region is dominated by electrolyte breakdown. The electrolyte breakdown causes the true value of the cathodic peak current to be obscured. Although the concentration of the system is unknown and the cathodic peak current values could not be accurately obtained, a plot of the peak anodic current against $v^{1/2}$ should still yield a linear plot, Figure 3.25. The plot does yield a straight line and extrapolates close to the origin.

The Randles-Sevčik analysis for calculating the diffusion coefficient does apply in this case, but as the concentration is unknown, the diffusion coefficient cannot be calculated.

Although sodium cobalticarborane shows promise as a negative redox couple in DCM, the problems associated at microelectrodes and the lack of information that can be gained at macroelectrodes means it could not be extended to supercritical fluids. Also the insolubility of sodium cobalticarborane in DCM means it would most likely be insoluble in scR32. For these reasons, sodium cobalticarborane was not pursued further as an internal reference standard for supercritical fluids.

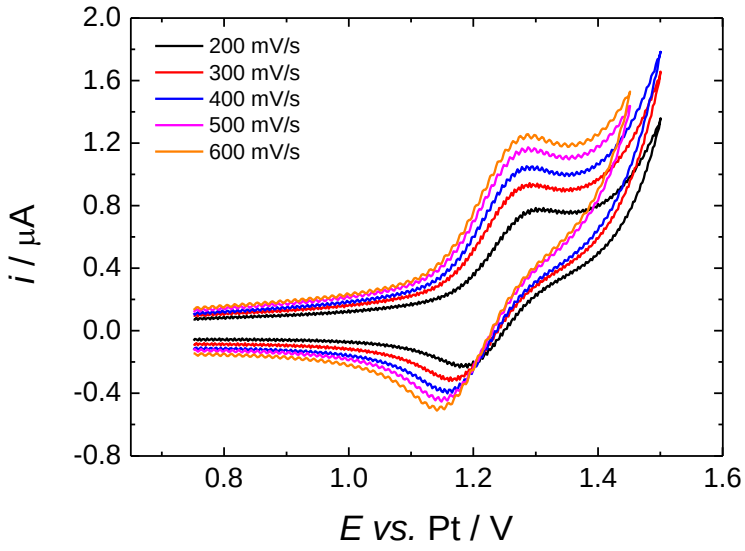

Figure 3.24. Cyclic voltammograms for a solution of [Na][$CoC_4H_{22}B_{18}$] and 20 mM [NBu_4^n][BF_4] in DCM at 298 K. The working electrode was a 1 mm Ø Pt disc with a Pt gauze counter electrode and a 0.5 mm Ø Pt disc reference electrode.

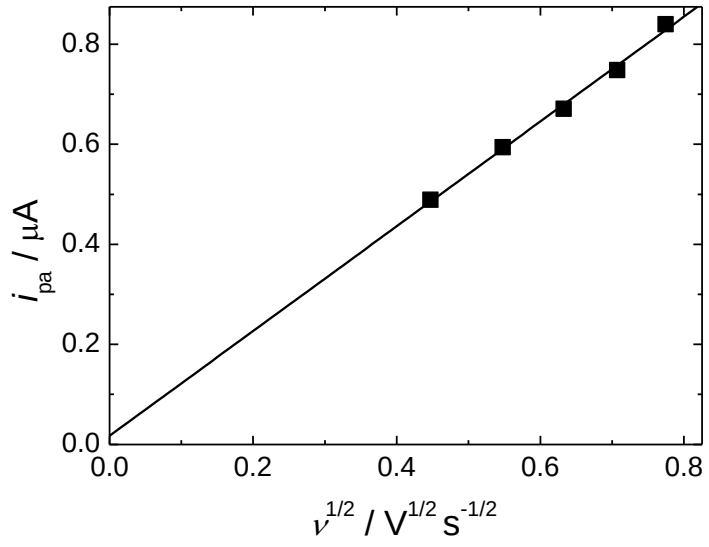

Figure 3.25. The dependence of the anodic peak current on the scan rate for cyclic voltammetry of [Na][$CoC_4H_{22}B_{18}$] and 20 mM [NBu_4^n][BF_4] in DCM at 298 K, at 1 mm Ø Pt disc working electrode for various scan rates.

3.7 Conclusions

This Chapter has demonstrated that various metallocenes are good internal reference complexes in both acetonitrile and dichloromethane that can be used further in both $scCO_2$/MeCN (15 wt%) and scR32. The metallocenes and complexes studied in acetonitrile were decamethylferrocene, decamethylcobaltocene and cobaltocenium hexafluorophosphate. The metallocenes and complex studied in dichloromethane were decamethylferrocene, decamethylcobaltocenium hexafluorophosphate and sodium cobalticarborane. Decamethylferrocene was shown to be a good internal reference standard in both MeCN and DCM at both micro and macro electrodes and could be extended to both supercritical systems. The diffusion coefficients were determined for both systems and the difference is a function of the lower viscosity of MeCN compared to DCM. Decamethylcobaltocene was shown to be a good internal reference standard in MeCN at both micro and macroelectrodes and could be extended to $scCO_2$/MeCN (15 wt%). Cobaltocenium hexafluorophosphate was also shown to be a good internal reference standard in both MeCN and DCM at both micro and macro electrodes and could also be extended to supercritical systems. Sodium cobalticarborane was tested in DCM as a negatively charged internal reference standard. Work performed at microelectrodes demonstrated that the complex is not suitable for further work in supercritical systems. This was also confirmed by the insolubility of the complex in DCM, as DCM is a liquid analogue of scR32 it can be assumed that the complex will also be insoluble in scR32.

Chapter 4: Metallocenes as Model Redox Systems in Supercritical Fluids

4.1 Cyclic Voltammetry of Decamethylferrocene in $scCO_2$/MeCN

It has been shown in Chapter 3 that decamethylferrocene is a good redox couple in acetonitrile at both micro and macro electrodes. This section details experiments performed with decamethylferrocene in $scCO_2$/MeCN mixtures at both micro and macro electrodes. The results obtained will be compared to those obtained in acetonitrile. The diffusion coefficients obtained in $scCO_2$/MeCN will be directly comparable to those obtained in acetonitrile.

4.1.1 Preconditioning Step at Platinum Microelectrodes

Cyclic voltammograms performed in a solution of $scCO_2$/MeCN (15 wt%) containing 0.43 mM DMFc and 20 mM $[NBu_4^n][BF_4]$, for a 20, 25 and 50 µm Ø Pt disc, at 309 K and ≈ 17.6 MPa. (17.58 MPa), are displayed in Figure 4.1. As can be seen from Figure 4.1, the current does not reach a steady state plateau as seen in liquid conditions. The voltammetry is suggestive of a semi-porous blocking film at the electrode surface. Upon cycling the electrode within the solvent potential window, (-0.2 V to 3 V then to -3 V, Figure 4.2), the voltammetry changes and the expected microelectrode redox wave is seen with a well-defined plateau. This was attributed to change of the formation of a film which is removed upon cycling over a wider potential range.

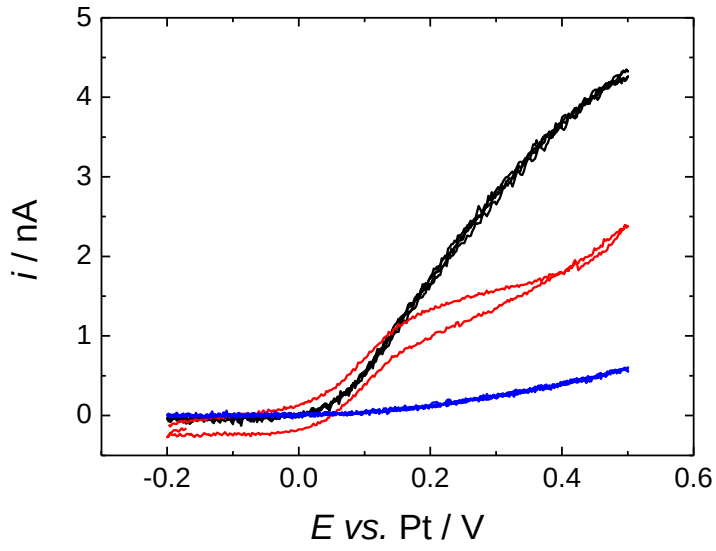

Figure 4.1. Cyclic voltammograms for a solution containing 0.43 mM DMFc and 20 mM $[NBu_4^n][BF_4]$ in $scCO_2$/MeCN (15 wt%), v = 10 mV s^{-1} for all scans, T = 309 K and $p \approx$ 17.6 MPa. The reference and counter electrodes were 0.5 mm Ø Pt wires. The working electrodes were 19 µm (black), 25.2 µm (red) and 49.4 µm (blue) Ø Pt discs.

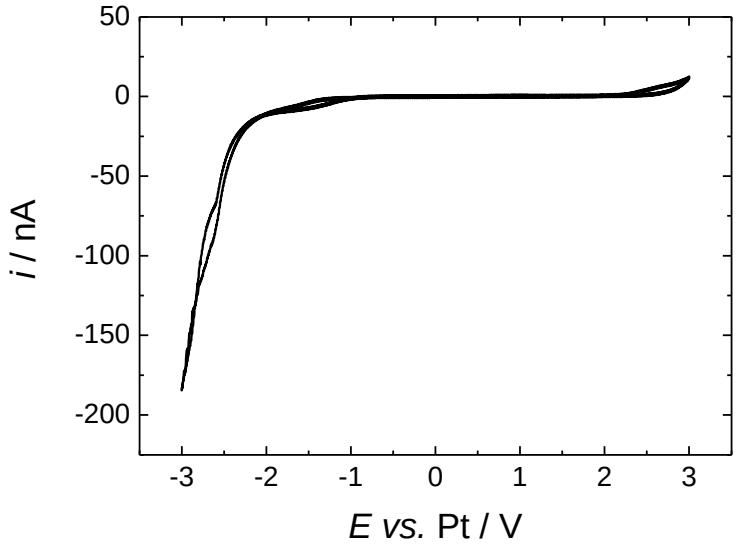

Figure 4.2. Cyclic voltammetry for a solution containing 0.43 mM DMFc and 20 mM $[NBu_4^n][BF_4]$ in $scCO_2$/MeCN (15 wt%), v = 10 mV s^{-1}, T = 309 K, p = 17.4 MPa. The working electrode was a 25.2 µm Ø Pt disc and the reference and counter electrodes were 0.5 mm Ø Pt wires.

To investigate the region over which the film was removed from the surface, the potential range of the conditioning cycle was altered. When the electrode was cycled from -0.2 V to 3 V, the film was not removed and the voltammetry was unchanged. However when the conditioning

cycle was set between –0.2 V to -3 V the film was removed and well behaved DMFc voltammetry was obtained as shown in Figure 4.3. It was therefore concluded that the blocking film at the electrode was removed by reduction. Once the preconditioning step is performed on an electrode, reproducible and stable voltammetry is seen and the preconditioning step does not need to be repeated during that experimental session. A similar problem was encountered by Crooks and Bard[22] when using ferrocene in supercritical acetonitrile. There they reported the presence of a passivating layer at the tungsten working electrode that could be removed by a short voltage pulse, but which did not affect subsequent electrochemical measurements. It is important to note that in these experiments it is not possible to polish the electrodes immediately before recording voltammetry and that it takes on the order of ½ day to assemble the high pressure cell, load it with electrolyte, reagent, acetonitrile and CO_2 and then bring it up to temperature and pressure.

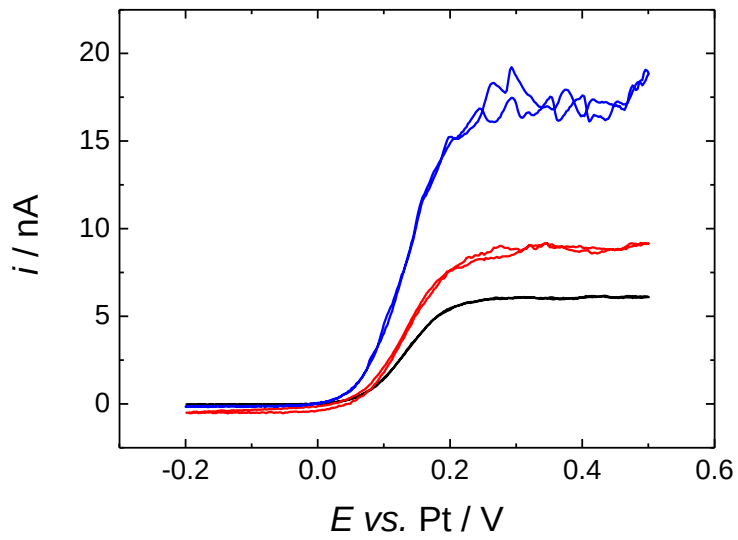

Figure 4.3. The solution, temperature, pressure, scan rate, reference and counter electrodes have all been described in Figure 4.1, recorded after performing the preconditioning step. The working electrodes were 19 µm (black), 25.2 µm (red) and 49.4 µm (blue) Ø Pt discs.

4.1.2 Electrochemistry of Decamethylferrocene in $scCO_2$/MeCN (15 wt%) at Microelectrodes

The preconditioning step has to be performed at all Pt microelectrodes before any reproducible voltammetry can be gained. The preconditioning step was performed at the start of each experiment, all voltammetry presented was performed after this step. The following section details experiments performed at microelectrodes over a range of concentrations and varying radii of microelectrodes. Varying the concentration of DMFc and radii of microelectrode would

allow a plot to be made against the steady state current as shown in Equation 3.7. As in Chapter 3, the half wave potentials have been determined by the mass transport corrected Tafel plots as described in Equation 3.8. The concentrations investigated ranged from 0.22 to 11 mM at a 20, 25 and 50 µm Ø Pt discs. The true radii of the microelectrodes were determined by acid voltammetry and by viewing in SEM as described in Chapter 2.

Cyclic voltammograms performed in a solution of $scCO_2$/MeCN (15 wt%) containing 0.43 mM DMFc and 20 mM $[NBu_4^n][BF_4]$, for a 20, 25 and 50 µm Ø Pt disc, at 309 K and ≈ 17.6 MPa are presented in Figure 4.4. Cyclic voltammograms performed in $scCO_2$/MeCN (15 wt%) containing 0.779 mM DMFc and 20 mM $[NBu_4^n][BF_4]$ at the same electrodes, temperature and pressure are presented in Figure 4.5. As it can be seen from both figures, the voltammetry recorded is similar to that recorded in liquid MeCN. The voltammetry is well behaved with a well-defined sigmoidal wave as expected for the steady state response at a microelectrode. The difference occurs on the limiting current of the sigmoidal wave. The limiting current recorded is not stable and fluctuates for all microelectrodes and never settles to a stable value. The magnitude of this noise is greater at the larger electrodes. The noise seen on the limiting current is attributed to natural convection of the supercritical fluid mixture, a process which has significant influence because of the low viscosity of the supercritical fluid and which is presumably driven by temperature gradients within the high pressure cell.

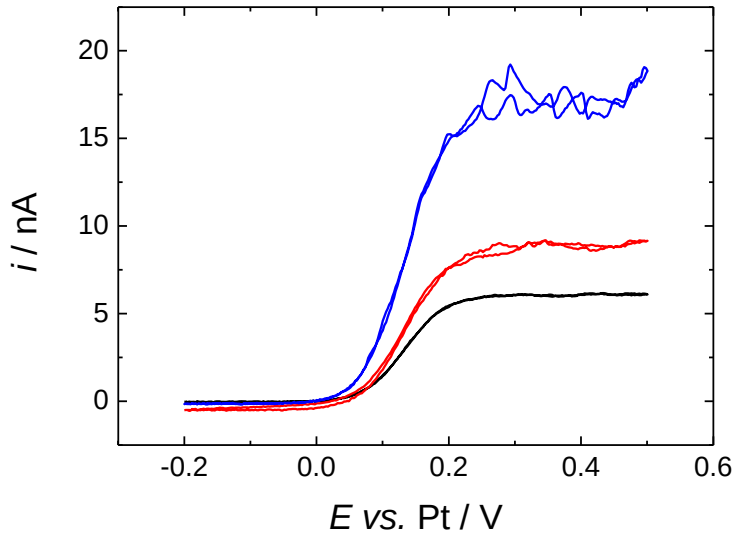

Figure 4.4. Cyclic voltammograms for a solution containing 0.43 mM DMFc and 20 mM $[NBu_4^n][BF_4]$ in $scCO_2$/MeCN (15 wt%), ν = 10 mV s^{-1} for all scans, T = 309 K and p ≈ 17.6 MPa. The reference and counter electrodes were 0.5 mm Ø Pt wires. The working electrodes were 19 µm (black), 25.2 µm (red) and 49.4 µm (blue) Ø Pt discs.

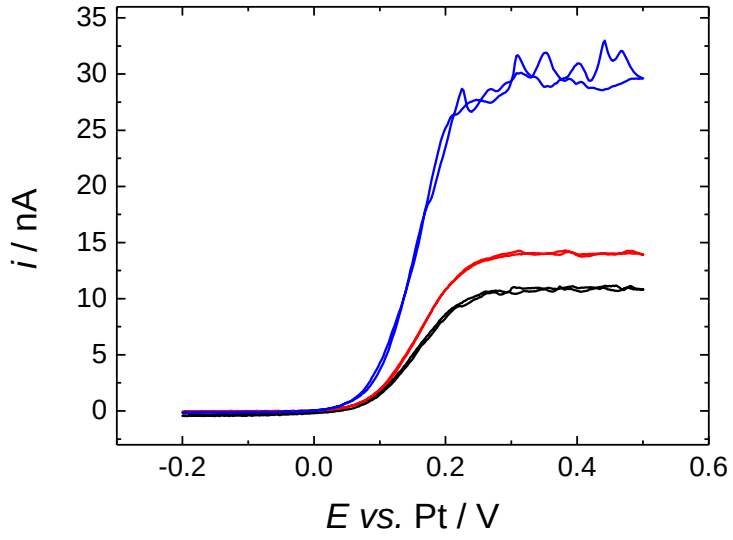

Figure 4.5. Cyclic voltammograms for a solution containing 0.779 mM DMFc and 20 mM [NBu_4^n][BF_4] in $scCO_2$/MeCN (15 wt%), ν = 10 mV s^{-1} for all scans, T = 309 K and $p \approx$ 17.6 MPa. The reference and counter electrodes were 0.5 mm Ø Pt wires. The working electrodes were 19 µm (black), 25.2 µm (red) and 49.4 µm (blue) Ø Pt discs.

To determine the limiting current at microelectrodes, repeated voltammetric scans are run to build up an averaged current response. Then to determine the diffusion limited current, it has to be recognised that the convection will cause an additional transport and flux of material to the microelectrode surface and therefore can only increase the current. Using this knowledge, the lower bounds of the current in the plateau region are used as the best estimate of the diffusion limited current at the microdisc. Figure 4.6 shows graphically how the limiting current is determined at a 50 µm Ø Pt disc. This method for determining the limiting current was used for all voltammetry and concentrations.

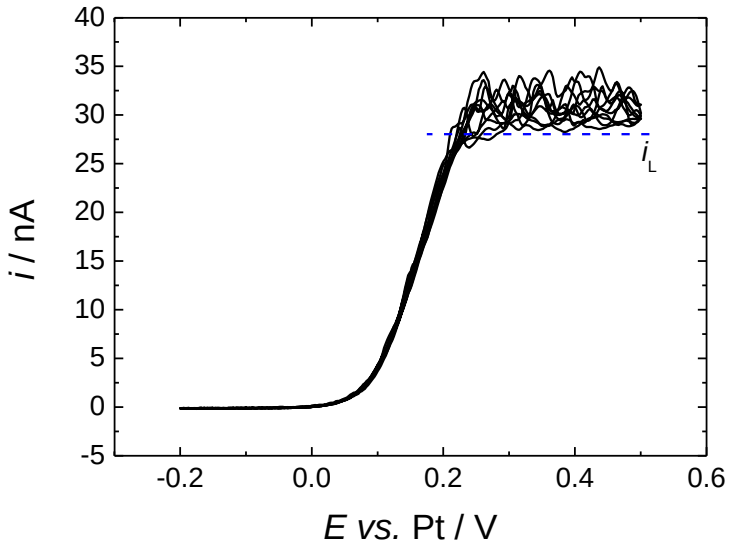

Figure 4.6. Cyclic voltammograms for a solution containing 0.779 mM DMFc and 20 mM [NBu_4^n][BF_4] in $scCO_2$/MeCN (15 wt%), ν = 10 mV s^{-1}, T = 309 K and $p \approx$ 17.6 MPa. The working electrode was a 49.4 µm Ø Pt disc, the reference and counter electrodes were 0.5 mm Ø Pt wires. The blue dashed line represents where the mass transport limited current was recorded.

Once the limiting current was determined from the voltammograms the data could be collected and these are presented in Table 4.1. Taking 0.43 mM DMFc as an example, the limiting current determined for the 19, 25.2 and 49.4 µm Ø Pt microelectrodes was 6.0, 8.23 and 16.05 nA respectively. Using Equation 3.7, the diffusion coefficients were calculated to be 3.81, 3.94 and 3.92 x 10^{-5} cm^2 s^{-1} respectively. These values are higher than those calculated in MeCN at 298 K, where the diffusion coefficient was calculated to be ≈ 1.70 x 10^{-5} cm^2 s^{-1}. It is considered that influences such as temperature will affect the mass transport and thus change the diffusion coefficient of a species. In the case of temperature the diffusion coefficient will increase 1-2% per degree Kelvin[100]. For example, if the diffusion coefficient was determined at 298 K and then the temperature was increased to 309 K, the diffusion coefficient would be higher. In this case, taking the diffusion coefficient determined at 25 ºC (1.70 x 10^{-5} cm^2 s^{-1}) and increasing it by 2% by every degree temperature rise then the diffusion coefficient at 309 K would be D = 2.11 x 10^{-5} cm^2 s^{-1}. As the diffusion coefficients calculated in $scCO_2$/MeCN are higher, it can be assumed temperature is not the only influence on the diffusion coefficient. As mentioned before the low viscosity of supercritical fluids means the mixture is closer to that of a dense gas allowing for material to diffuse at faster rates, this is reflected in the diffusion coefficient.

Table 4.1. Cyclic voltammetry data obtained for experiments with various concentrations of DMFc with 20 mM [NBu_4^n][BF_4] in $scCO_2$/MeCN (15 wt%) at 309 K, $p \approx 17.6$ MPa and $v = 10$ mV s^{-1} for varying sizes of microelectrode.

a / µm	c / mM ± 0.02	i_L / nA ± 0.1	$\Delta E_{(1/4\text{-}3/4)}$ / mV ± 1	$E_{1/2}$ / V ± 0.001	$\Delta E_{1/4}$ / mV ± 1	$\Delta E_{3/4}$ / mV ± 1	$d\ln[(i_L/i)\text{-}1]/dE$ / V^{-1} ± 0.1	n ± 0.01
9.5 ± 0.1	0.43	6.0	54	0.134	34	30	33.6	0.89
	0.78	10.6	73	0.154	38	35	30.0	0.80
	1.07	15.8	77	0.175	39	38	27.6	0.74
	5.20	70.4	117	0.254	61	56	18.5	0.49
	11.00	166.0	164	0.338	88	76	13.4	0.36
12.6 ± 0.2	0.22	4.1	60	0.119	31	29	37.5	1.00
	0.39	7.7	63	0.123	31	32	34.8	0.93
	0.43	8.2	67	0.131	33	34	33.8	0.90
	0.78	13.7	71	0.158	37	34	30.0	0.80
	1.07	21.9	79	0.178	40	39	27.8	0.74
	5.20	107.1	118	0.257	62	56	18.0	0.48
	11.00	217.0	165	0.338	88	77	13.3	0.35
24.7 ± 0.4	0.22	9.1	61	0.110	28	33	38.7	1.03
	0.39	15.0	62	0.122	35	27	33.8	0.90
	0.43	16.1	60	0.132	32	28	34.3	0.91
	0.78	28.4	63	0.154	36	27	33.9	0.90
	1.07	44.9	78	0.177	41	37	27.6	0.73
	5.20	221.3	131	0.280	71	60	16.6	0.44
	11.00	461.0	173	0.354	95	78	11.8	0.31

The half wave potentials and value for n for the steady state voltammograms were determined from the mass transport corrected Tafel analysis, Equation 3.8. As can be seen from Table 4.1, at low concentrations of DMFc (0.22 mM), the value of the slopes was close to the expected value of 37.56 V^{-1} for the 25 and 50 µm Ø Pt at 309 K, Figure 4.7. The value of n was also close to 1, which is expected for a reversible process and was seen in liquid MeCN. The difference between the half wave and quartile potentials were also close to the expected value of 29 mV at low concentration. Although as the concentration of analyte is increased across all electrodes, the value of slope, and thus the value of n deviates from ideality. This deviation from ideality is also reflected in the difference between the half wave and quartile potentials, the difference increases as the concentrations of DMFc are increased. This is most likely a function of uncompensated solution resistance becoming more apparent in the voltammetry. The concentration of the supporting electrolyte is kept constant at 20 mM while the concentration of the analyte is increased. For the lowest concentration of DMFc (0.22 mM) the supporting electrolyte concentration is 100x the concentration of DMFc, whereas at the highest concentration of DMFc (11.0 mM) the supporting electrolyte concentration is only double. This low ratio of analyte to supporting electrolyte concentration would cause a higher

uncompensated solution resistance to be more apparent even when microelectrodes are employed and thus the mass transport corrected Tafel analysis will deviate from ideality.

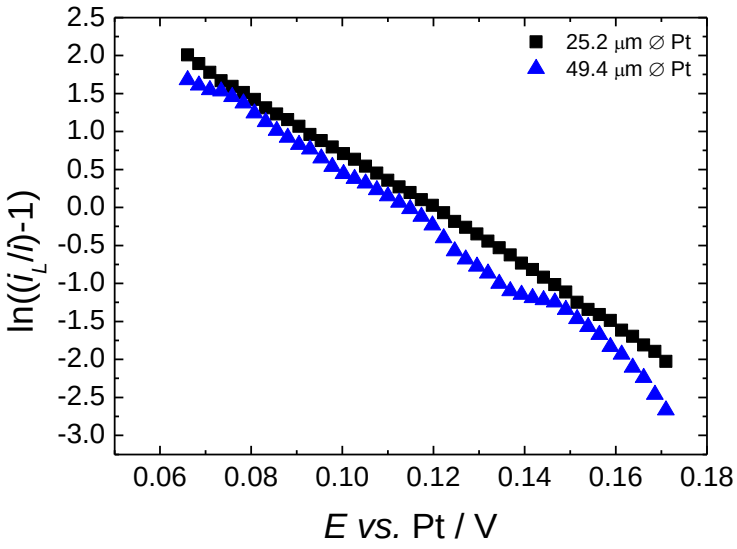

Figure 4.7. Mass transport corrected Tafel analysis for cyclic voltammetry of 0.22 mM DMFc and 20 mM $[NBu_4^n][BF_4]$ in $scCO_2$/MeCN (15 wt%) at 10 mV s^{-1}, at 309 K and $p \approx 17.6$ MPa, for Pt microelectrodes of 25.2 and 49.4 μm diameter.

4.1.3 Determination of the Diffusion Coefficient of DMFc in $scCO_2$/MeCN (15 wt%) at Microelectrodes

The diffusion controlled limiting current at a microdisc is given again in Equation 4.1,

$$i_L = 4nFDca \tag{4.1}$$

in order to confirm that the DMFc system obeys Equation 4.1, the limiting current was measured as a function of concentration, c, and microelectrode radius, a. The concentrations of DMFc studied were 0.22, 0.39, 0.43, 0.779, 1.07, 5.2 and 11 mM. The microelectrodes used in the study had radii of 9.5, 12.6 and 24.7 μm. This range of concentrations and radii will allow a graph of Equation 4.1 to be plotted which should extrapolate to the origin. This wide range of concentrations will also show if DMFc reaches its solubility limit in $scCO_2$/MeCN (15 wt%).

Figure 4.8 shows the plot obtained for the diffusion limited current against the concentration of DMFc over the range of concentrations stated for the three microdisc electrodes. As it can be seen from Figure 4.8, the limiting current increases linearly with concentration in all cases as anticipated from Equation 4.1. The plot also shows that the solubility limit of DMFc in $scCO_2$/MeCN (15 wt%) clearly exceeds 11 mM, no further concentrations of DMFc were

studied above 11 mM as this leads to heavily distorted voltammetry due to uncompensated solution resistance. Using the slopes of the plots determined in Figure 4.8 in combination with Equation 4.1 the value of the diffusion coefficient were calculated and are displayed in Table 4.2.

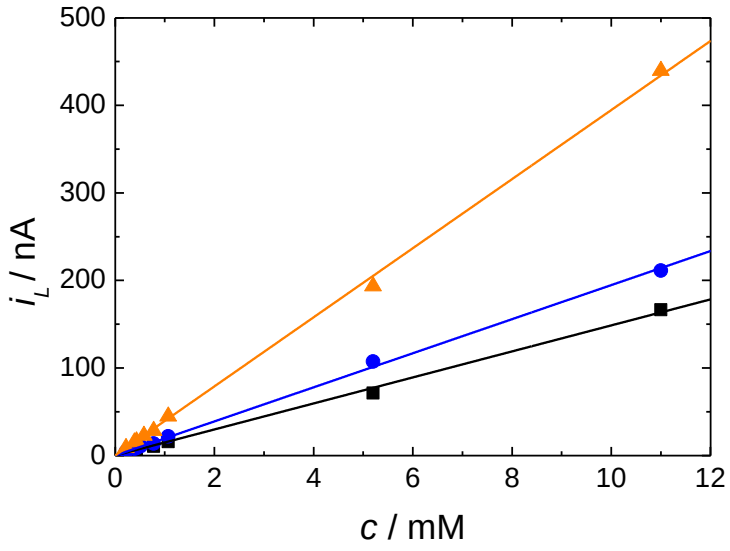

Figure 4.8. Plot of diffusion limited current *versus* the decamethylferrocene concentration for a series of cyclic voltammograms in supercritical CO_2 with 15 wt% MeCN and 20 mM $[NBu_4^n][BF_4]$ electrolyte. *T* = 309 K, *p* = 17.2 – 17.7 MPa. The working electrodes were a 19 (■), 25.2 (●) and 49.4 µm (▲) diameter platinum disc, the counter and reference electrode were 0.5 mm diameter wires.

Table 4.2. Variation of the diffusion coefficient with concentration of DMFc. The working electrodes were a 19, 25.2 and 49.4 µm diameter platinum disc, the counter and reference electrode were 0.5 mm diameter platinum wires. Solutions were $scCO_2$/MeCN (15 wt%), 20 mM $[NBu_4^n][BF_4]$. *T* = 309 K, *p* = 17.2 – 17.7 MPa.

***a* / µm**	***D* / cm^2 s^{-1}**
9.5 ± 0.1	4.05 x 10^{-5} ± 0.05 x 10^{-5}
12.6 ± 0.2	3.99 x 10^{-5} ± 0.06 x 10^{-5}
24.7 ± 0.4	4.14 x 10^{-5} ± 0.07 x 10^{-5}
Mean	**4.06 x 10^{-5} ± 0.06 x 10^{-5}**

From Table 4.2, it can be seen that the diffusion coefficient of DMFc in $scCO_2$/MeCN (15 wt%) at 309 K and ≈ 17.6 MPa is D = 4.06 ± 0.06 x 10^{-5} cm^2 s^{-1}. This is in agreement with the diffusion coefficients calculated from voltammetry and is higher than the diffusion coefficients calculated in liquid MeCN. In order to confirm the diffusion coefficient, the limiting current was also plotted as a function of microelectrode radius for a separate set of experiments using five

different DMFc concentrations, Figure 4.9. Again the results are fully consistent with Equation 4.1. The diffusion coefficients were again calculated from the slopes of the graphs from Equation 4.1 and are given in Table 4.3.

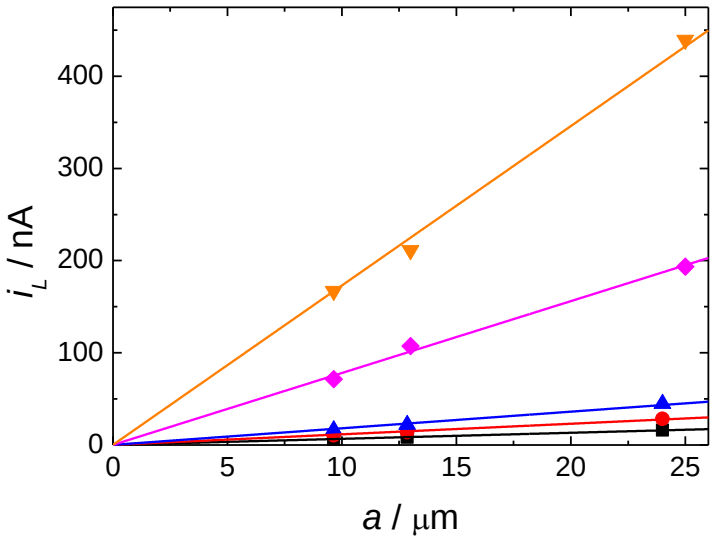

Figure 4.9. Plot of diffusion limited current *versus* the electrode radii for a series of cyclic voltammograms in supercritical CO_2 with 15 wt% MeCN and 20 mM $[NBu_4^n][BF_4]$ electrolyte. T = 309 K, p = 17.2 – 17.7 MPa. The concentrations were 0.43 (■), 0.78 (●), 1.07 (▲), 5.20 (♦), and 11.0 mM (▼). The counter and reference electrode were 0.5 mm diameter platinum wires.

Table 4.3. Variation of the diffusion coefficient with electrode radii. The working electrodes were a 19, 25.2 and 49.4 μm diameter platinum disc, the counter and reference electrode were 0.5 mm diameter platinum wires. Solutions were $scCO_2$/MeCN (15 wt%), 20 mM $[NBu_4^n][BF_4]$. T = 309 K, p = 17.2 – 17.7 MPa.

c / mM	D / cm^2 s^{-1}
0.43 ± 0.02	3.96 x 10^{-5} ± 0.16 x 10^{-5}
0.78 ± 0.02	3.81 x 10^{-5} ± 0.09 x 10^{-5}
1.07 ± 0.02	4.37 x 10^{-5} ± 0.08 x 10^{-5}
5.20 ± 0.02	3.89 x 10^{-5} ± 0.02 x 10^{-5}
11.00 ± 0.02	4.08 x 10^{-5} ± 0.01 x 10^{-5}
Mean	**4.02 x 10^{-5} ± 0.07 x 10^{-5}**

From Table 4.3, it can be seen that the diffusion coefficient calculated is in excellent agreement with the diffusion coefficient calculated in Table 4.2. From the two sets of experiments the diffusion coefficient of DMFc has been determined to be D = 4.05 x 10^{-5} cm^2 s^{-1} in $scCO_2$/MeCN (15 wt%) at 309 K and 17.6 MPa. This diffusion coefficient is comparable to diffusion coefficients previously reported by Cook *et al*[43]. in $scCO_2$/MeCN under similar conditions for $[Cu(MeCN)_4]^+$ of 2.30 x 10^{-5} cm^2 s^{-1} with $[NBu_4^n][BF_4]$ supporting electrolyte

and 3.30 x 10^{-5} cm^2 s^{-1} with $[NBu_4^n][B(3, 5\text{-}(CF_3)_2C_6H_3)]$ supporting electrolyte. This value for the diffusion coefficient is also higher than that recently reported by Toghill *et al*[44]. In their work they obtained a diffusion coefficient for DMFc of D = 1.86 x 10^{-5} cm^2 s^{-1} in $scCO_2$/MeCN (30 vol%) with an ionic liquid as supporting electrolyte in the form of $[N(C_{10}H_{11})_4][B(C_6F_5)_4]$. Their experiments were carried out at slightly higher temperature (313 K rather 309 K) but at a lower pressure (10 rather than 17 MPa). This lower diffusion coefficient is most likely a function of the higher mole fraction of acetonitrile. As the acetonitrile mole fraction is increased, the dielectric constant of the system increases. Thus it is crucial to add 10-18% (mole fraction) of acetonitrile into $scCO_2$ to achieve a dielectric constant of 7 to ensure sufficient dissociation of the electrolyte[64]. Adding much higher concentrations of acetonitrile (x_{CH3CN} > 0.5) will significantly reduce the electrostatic solvation energy, but will also make the solution more liquid-like and therefore slow down mass transport.

4.1.4 Electrochemistry of DMFc in $scCO_2$/MeCN (15 wt%) using a Microdisc Electrode with a Baffle

In order to clearly demonstrate that the instability in the limiting current seen at microdisc electrodes was due to natural convection, a baffled microdisc electrode was constructed, see Chapter 2 for construction details. The baffle electrode simply comprises of an extended piece of PEEK tubing which extends approximately 5 mm beyond the face of the electrode and surrounding insulation. The construction of the baffle was made to reduce the convective noise and see if the voltammetry recorded at the microelectrode would be altered. To demonstrate this, two 50 µm Ø Pt disc electrodes were constructed, one would have the extended baffle and one would be open to the solution as in the previous section. This would allow both the electrodes to be run in the same solution, in the same cell, during the same supercritical experiment. The use of a baffle electrode is novel and has not been reported in the literature. It is important to note that both the electrodes were subjected to the same preconditioning step (as detailed in Section 4.1.1) before recording any voltammograms.

Cyclic voltammograms recorded in a solution of $scCO_2$/MeCN (15 wt%) containing 1.42 mM DMFc and 20 mM $[NBu_4^n][BF_4]$ for a 25 (baffled), 50 (baffled) and 50 (non-baffled) µm Ø Pt disc, at 309 K and ≈ 17.6 MPa, are displayed in Figure 4.10. The data obtained from the cyclic voltammograms are presented in Table 4.4. As it can be seen from Figure 4.10 the baffled microelectrodes have significantly reduced noise on the limiting current when compared to the non-baffled microelectrode. The microdisc fitted with the baffle displays a stable steady state limiting current plateau which is analogous to liquid MeCN. The half wave potentials displayed in Table 4.4 also show an agreement across all three types of

microelectrode with a value of $E_{1/2}$ = 0.2 V. The values for n are also similar across all three types of microelectrode and are also in agreement with the values displayed in Table 4.1.

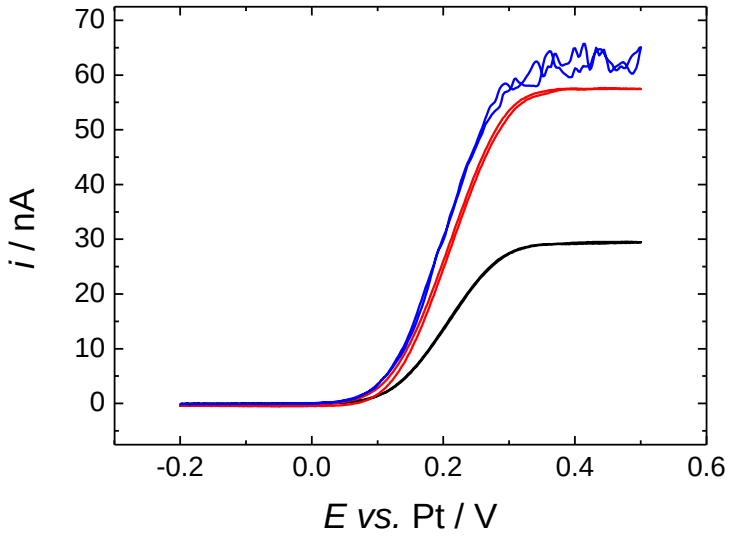

Figure 4.10. Cyclic voltammograms for a solution containing 1.42 mM DMFc and 20 mM [NBu_4^n][BF_4] in $scCO_2$/MeCN (15 wt%), v = 10 mV s^{-1} for all scans, T = 309 K and p ≈ 17.6 MPa. The reference and counter electrodes were 0.5 mm Ø Pt wires. The working electrodes were 25 µm (black, baffled), 50 µm (red, baffled) and 50 µm (blue, not baffled) Ø Pt discs.

Table 4.4. Cyclic voltammetry data obtained for experiments of 1.42 mM DMFc with 20 mM [NBu_4^n][BF_4] in $scCO_2$/MeCN (15 wt%) at 309 K, p ≈ 17.6 MPa and v = 10 mV s^{-1} for varying sizes of microelectrode. B = Baffled, NB = not baffled.

a / µm ± 0.5	i_L / nA ± 0.1	$\Delta E_{(1/4-3/4)}$ / mV ± 1	$E_{1/2}$ / V ± 0.001	$\Delta E_{1/4}$ / mV ± 1	$\Delta E_{3/4}$ / mV ± 1	$d\ln[(i_L/i)-1]/dE$ / V^{-1} ± 0.1	n ± 0.01
12.5 (B)	29.4	89	0.206	47	42	24.9	0.66
25.0 (B)	57.6	91	0.208	48	43	24.1	0.64
25.0 (NB)	58.8	81	0.197	43	38	25.0	0.67

It is also apparent from Figure 4.10, that the baffled microelectrode has a limiting current which is slightly below the minimum plateau current on the "bare" microdisc. This slight difference in limiting current at the two electrodes is due to difference in their radii. To confirm this difference in radii, the two electrodes were compared by performing voltammetry in an aqueous solution containing ruthenium(III) hexamine ($Ru(NH_3)_6Cl_3$) solution. Cyclic voltammetry recorded in an aqueous solution containing 2 mM $Ru(NH_3)_6Cl_3$ and 0.1 M KCl at the non-baffled 50 µm and baffled 50 µm Ø Pt electrodes is displayed in Figure 4.11. As it can be seen from Figure 4.11, the two electrodes give two different limiting current responses which

are analogous to that recorded in $scCO_2$/MeCN. Measuring the absolute difference in the limiting current for both $scCO_2$/MeCN and for the aqueous system should give a similar value. The absolute difference in the limiting current measured in $scCO_2$/MeCN was found to be i_L(NB, $scCO_2$/MeCN)/i_L (B, $scCO_2$/MeCN) = 1.02. The absolute difference in the aqueous system was measured to be i_L(NB, Ru)/i_L (B, Ru) = 1.07. These values are in good agreement with each other and confirm that the small difference in radii causes the limiting current of the baffled electrode to be slightly below the minimum plateau on the bare electrode.

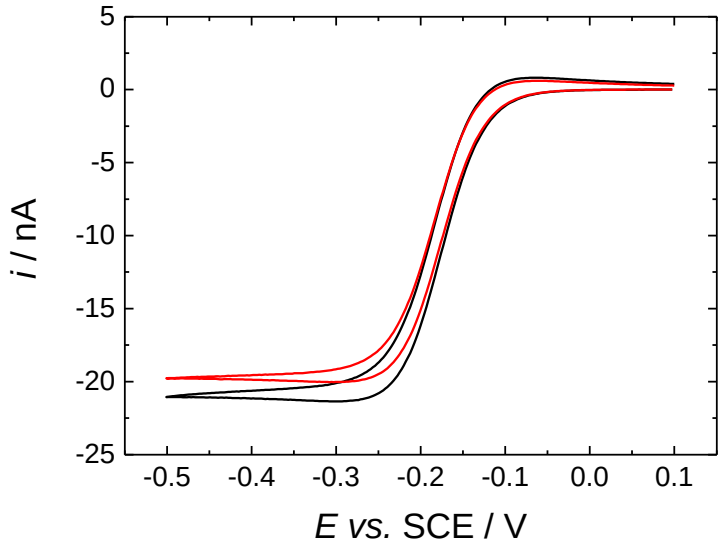

Figure 4.11. Cyclic voltammograms for an aqueous solution containing 2 mM $Ru(NH_3)_6Cl_3$ and 0.1 M KCl, v = 10 mV s^{-1} for both scans, T = 298 K. The reference electrode was a saturated calomel electrode (SCE) and the counter electrode was a Pt gauze. The black line represents the 50 µm Ø Pt disc which was not baffled in Figure 4.10, the red line represents the 50 µm Ø Pt disc which was baffled in Figure 4.10.

4.1.5 Electrochemistry of Decamethylferrocene in $scCO_2$/MeCN (15 wt%) at a Macroelectrode

Cyclic voltammetry for a macroelectrode at various scan rates was also carried out to examine the behaviour of the couple in $scCO_2$/MeCN (15 wt%) with [NBu_4^n][BF_4] as supporting electrolyte. The macrodisc used in this case was a 0.5 mm Ø Au disc. It is interesting to note that the polymeric acetonitrile layer that forms on Pt microdiscs does not occur at Au macrodiscs and thus it was not necessary to cycle the electrode to cathodic potentials to clean the surface.

Cyclic voltammetry recorded at various scan rates in a solution of $scCO_2$/MeCN (15 wt%) containing 0.638 mM DMFc with 20 mM [NBu_4^n][BF_4] for 0.5 mm Ø Au disc, at 309 K and

≈ 17.6 MPa are displayed in Figure 4.12. The data collected from the voltammograms is presented in Table 4.5. As can be seen from Figure 4.12, the voltammograms are not significantly distorted by the convection within the cell but the effects of *iR* drop are significant. The peak to peak potential separation increases from 221 to 353 mV between scan rates of 100 to 500 mV/s. This is a huge increase from the same system in liquid MeCN where the peak to peak separation was about 77 mV for all scan rates. The dashed lines in Figure 4.12 connect the peak currents at the different scan rates and provide a simple way to correct for the effects of *iR* drop since for the reversible case the peak potentials should be independent of scan rate. The slopes of the dashed lines give an estimate of the uncompensated resistance of 0.14 MΩ which is reasonable given the known conductivity of this electrolyte[46]. The separation between the two lines was found to be 83 mV, which is close to the expected value of 61.2 mV for a reversible 1 e^- process at 309 K and is close to the peak to peak potential separation found in liquid MeCN. From the cyclic voltammetry and using Equation 3.3 in Chapter 3, the diffusion coefficient was estimated to be $D = 5.05 \pm 0.28 \times 10^{-5}$ cm^2 s^{-1} which compares well with the results presented for the microelectrodes. The peak current was plotted against $v^{1/2}$ (Figure 4.13), although yielding a straight line for both anodic and cathodic peak currents; the straight line does not extrapolate to the origin. This is comparable to plots performed with DMFc in MeCN (Section 3.1), where the small amount of convection seen at 298 K caused deviation from the origin. As $scCO_2$/MeCN (15 wt%) is at 309 K and naturally more convective (due to the properties of supercritical fluids) the deviation from the origin is more apparent. The intercepts of the graphs indicate Randles-Sevčik analysis cannot be applied in this case to calculate the diffusion coefficient.

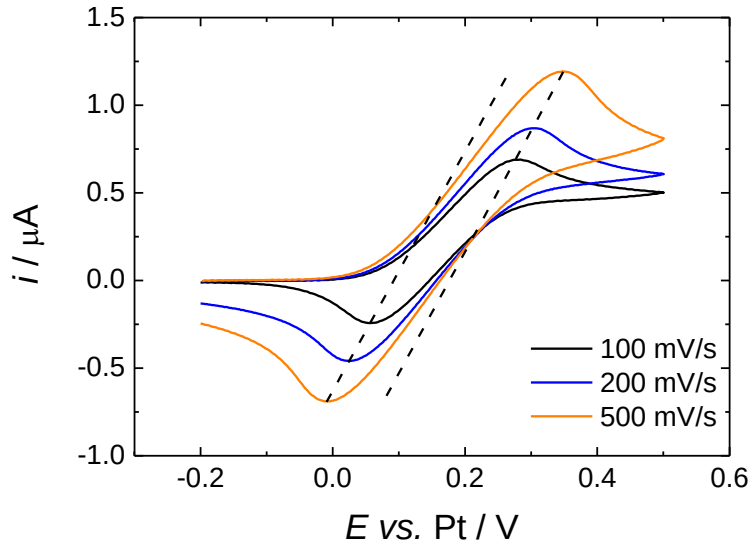

Figure 4.12. Cyclic voltammograms for a solution of 0.638 mM DMFc and 20 mM $[NBu_4^n][BF_4]$ in $scCO_2$/MeCN (15 wt%) at 309 K, $p \approx 17.6$ MPa. The working electrode was a 0.5 mm Ø Au disc, the reference and counter electrode were 0.5 mm Ø Pt wires.

Table 4.5. Data obtained from cyclic voltammograms of 0.638 mM DMFc and 20 mM $[NBu_4^n][BF_4]$ in $scCO_2$/MeCN (15 wt%) at 309 K and $p \approx 17.6$ MPa for various scan rates at a 0.5 mm Ø Au disc.

v / V s^{-1}	E_{pa} / mV ± 1	E_{pc} / mV ± 1	ΔE_p / mV ± 1	$E_{pa/2}$ / mV ± 1	$E_{pc/2}$ / mV ± 1	$E_{pa} - E_{pa/2}$ / mV ± 1	$E_{pc} - E_{pc/2}$ / mV ± 1	i_{pa} / µA ± 0.001	i_{pc} / µA ± 0.001	i_{pa}/i_{pc} ± 0.01
0.1	279	58	221	162	172	117	114	0.685	0.649	1.06
0.2	304	25	279	172	165	132	140	0.834	0.861	0.97
0.5	349	-4	353	193	161	156	165	1.126	1.102	1.02

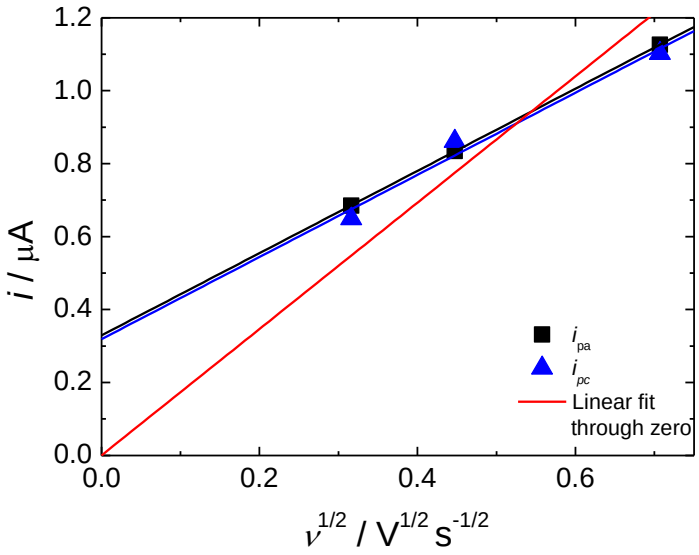

Figure 4.13. The dependence of peak currents on the scan rate for cyclic voltammetry of 0.638 mM DMFc and 20 mM [NBu_4^n][BF_4] in $scCO_2$/MeCN (15 wt%) at 309 K and $p \approx 17.6$ MPa at a 0.5 mm Ø Au disc working electrode.

Taking the values for the calculated solution resistance and diffusion coefficient, simulations were performed on Digielch software to compare the voltammetry. Simulations were run for scan rates of 100, 200 and 500 mV/s using an internal solution resistance value of 0.14 MΩ, c = 0.638 mM and D = 5.05 x 10^{-5} cm^2 s^{-1}. To simulate the effect of convection, a finite 1D simulation was run with a thickness layer of 0.0156 cm, Figure 4.14. As can be seen from Figure 4.14, the simulated data correlates well with the experimental voltammetry. The peak currents correlate well for both the anodic and cathodic current suggesting the convection has an influence on the magnitude of the current recorded. This will be discussed further in Section 4.2.4 where a baffled macro electrode can be used to dampen the effects of intrinsic convection.

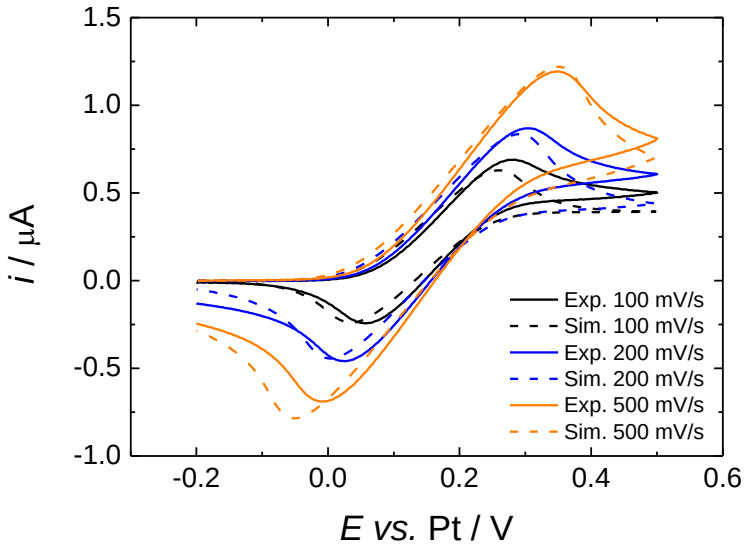

Figure 4.14. Comparison of experimental data (Figure 4.12, solid line) with simulated data (dashed line). Conditions used in the simulation were c = 0.638 mM, A = 0.00196 cm^2, R = 0.14 MΩ, D = 5.05 x 10^{-5} cm^2 s^{-1}, T = 309 K and a convection thickness layer of 0.0156 cm.

At lower scan rates the voltammetry at the gold macrodisc is significantly distorted, as expected, by convection within the cell. Figure 4.15 displays the voltammetry recorded at a gold macrodisc, in the same solution as described above, at 10 mV/s. As it can be seen from Figure 4.15 the voltammetry displays an expected sigmoidal shape (similar to microelectrodes) for hydrodynamic voltammetry and shows significant noise at anodic potentials where the current becomes mass transport limited. This type of behaviour shows that the polymeric layer seen at Pt microelectrodes is unique to the Pt metal itself. If a polymeric layer, or film, were present at the electrode surface, no convective noise would be seen in the voltammetry. A baffled macroelectrode was considered for use in scCO_2/MeCN, but was never fully tested in the system. The concept of a baffled macroelectrode was extended to scR32; the results for this can be seen in Chapter 4.2.4.2.

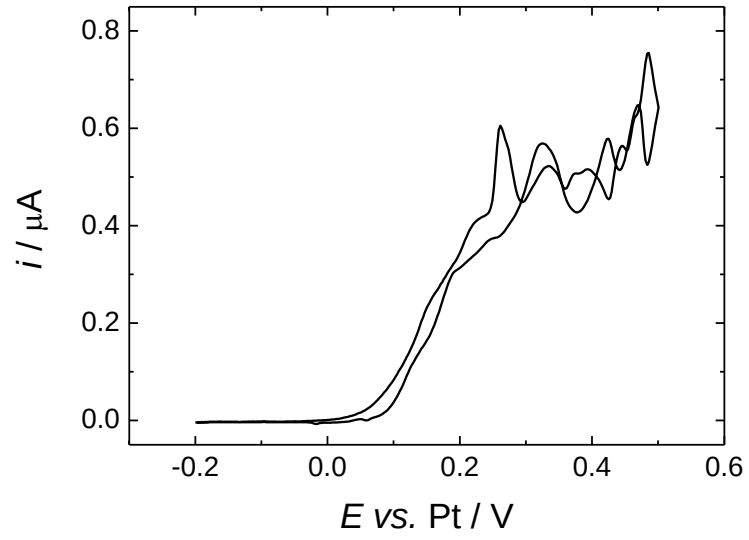

Figure 4.15. Cyclic voltammetry for a solution of 0.638 mM DMFc and 20 mM $[NBu_4^n][BF_4]$ in $scCO_2$/MeCN (15 wt%) at 309 K, $p \approx 17.6$ MPa, $\nu = 10$ mV s^{-1}. The working electrode was a 0.5 mm Ø Au disc, the reference and counter electrode were 0.5 mm Ø Pt wires.

4.2 Cyclic Voltammetry of Decamethylferrocene in scR32

It has been shown in Chapter 3 that decamethylferrocene is a good redox couple in dichloromethane which is a liquid analogue of supercritical difluoromethane (scR32). This section details experiments performed with DMFc in scR32 at both micro and macro electrodes. It has been shown in the previous section that a baffle electrode can be used to dampen the intrinsic natural convection seen in cyclic voltammetry. As the temperature is increased from 309 to 360 °C, which is required for scR32, the natural convection in the cell will be amplified. The baffle electrode is demonstrated again at microelectrodes but can also be extended to macro electrodes. It was also shown in the previous sections that a preconditioning step was required to gain stable reproducible voltammetry in $scCO_2$/MeCN. As scR32 has no acetonitrile co-solvent for the dissolution of analyte, a preconditioning step is no longer required to gain stable reproducible voltammetry. This further confirms that the blocking layer seen in $scCO_2$/MeCN is due to a polymeric acetonitrile layer as seen by Crooks and Bard[22].

4.2.1 Electrochemistry of Decamethylferrocene in scR32 at Microelectrodes

In order to directly compare the scR32 system to the $scCO_2$/MeCN system, a range of concentrations of DMFc that parallel the $scCO_2$/MeCN system and electrodes of similar radii were studied. As scR32 requires higher temperatures to gain a single phase mixture, it was found the electrodes made for $scCO_2$/MeCN would fail easily in the new system. The reason for

this, the Ag epoxy used to contact the microwire sealed in glass to the stainless steel contact softens at the higher temperatures and effectively break the connection. To alleviate this problem, new microelectrodes were constructed. The new contact consisted of a mechanical contact between a NiCr wire and the Pt microwire. The contact between the two metals is then sealed in glass in a similar fashion, thus the connection cannot be affected by temperature or pressure, see Chapter 2.2.2, Figure 2.4 for construction details.

Cyclic voltammograms performed in a solution of scR32 containing 0.53 mM DMFc and 20 mM $[NBu_4^n][BF_4]$ for a 19.89, 26 and 49.3 µm Ø Pt disc at 360 K and ≈ 17.6 MPa are presented in Figure 4.16. Cyclic voltammograms performed in a solution of scR32 containing 1.06 mM DMFc and 20 mM $[NBu_4^n][BF_4]$ for the same microelectrodes, temperature and pressure are presented in Figure 4.17. The voltammetry recorded is comparable to that recorded in liquid DCM. The limiting current on the sigmoidal wave also shows signs of natural convection which is similar to that recorded in $scCO_2$/MeCN (15 wt%). As it can be seen from Figure 4.16 and 4.17; the magnitude of the natural convection is bigger in scR32. This increase in the natural convection is due to the increase in temperature required to gain a single phase mixture in scR32 (T = 360 K) compared to $scCO_2$/MeCN (T = 309 K). Figure 4.18 compares the voltammetry obtained for similar concentrations of DMFc in $scCO_2$/MeCN and scR32 at two nominally 50 µm Ø Pt disc electrodes.

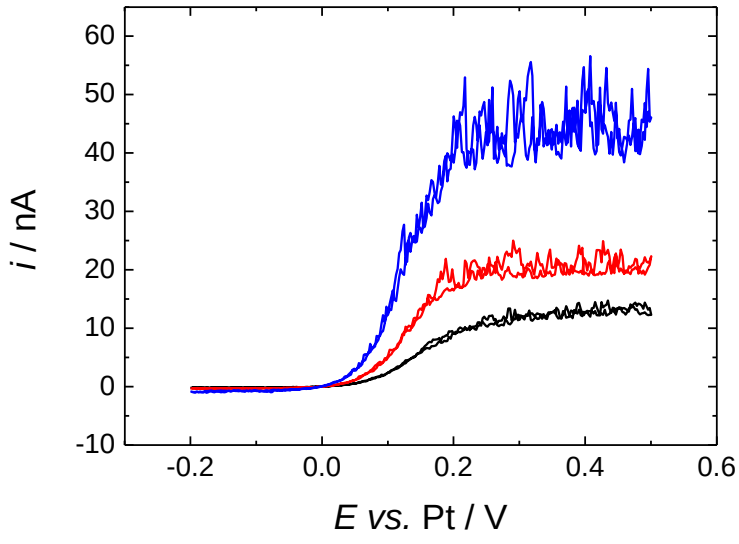

Figure 4.16. Cyclic voltammograms for a solution containing 0.53 mM DMFc and 20 mM $[NBu_4^n][BF_4]$ in scR32, v = 10 mV s^{-1} for all scans, T = 360 K and p ≈ 17.6 MPa. The reference and counter electrodes were 0.5 mm Ø Pt wires. The working electrodes were 19.89 µm (black), 26 µm (red) and 49.3 µm (blue) Ø Pt discs.

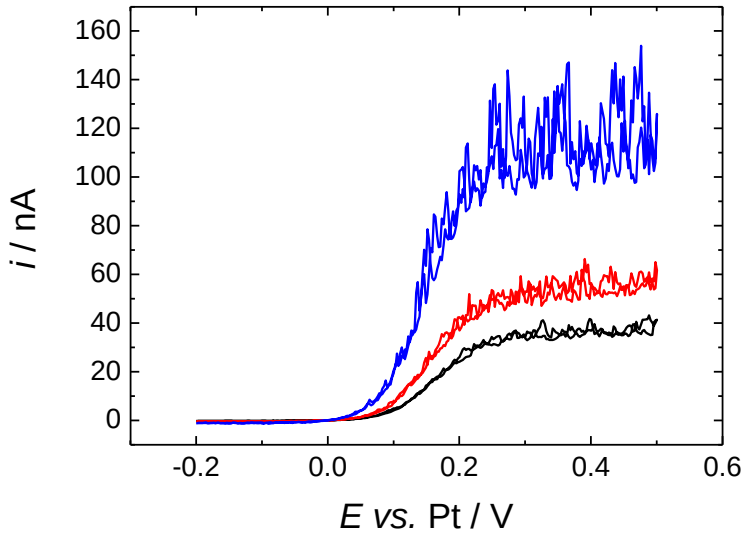

Figure 4.17. Cyclic voltammograms for a solution containing 1.06 mM DMFc and 20 mM [NBu_4^n][BF_4] in scR32, v = 10 mV s^{-1} for all scans, T = 360 K and p ≈ 17.6 MPa. The reference and counter electrodes were 0.5 mm Ø Pt wires. The working electrodes were 19.89 µm (black), 26 µm (red) and 49.3 µm (blue) Ø Pt discs.

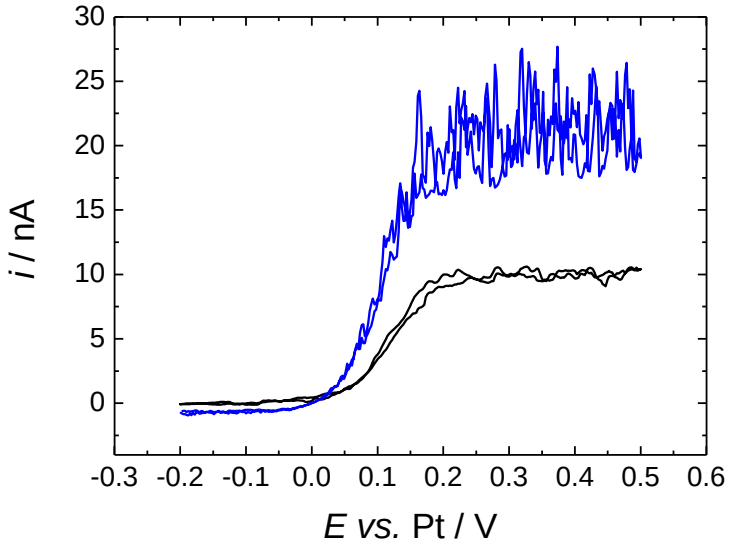

Figure 4.18. Black line: Cyclic voltammetry for a solution containing 0.22 mM DMFc and 20 mM [NBu_4^n][BF_4] in $scCO_2$/MeCN (15 wt%), T = 309 K and p ≈ 17.6 MPa. The working electrode was a 49.4 µm Ø Pt disc. Blue line: Cyclic voltammetry for a solution containing 0.2 mM DMFc and 20 mM [NBu_4^n][BF_4] in scR32, T = 360 K and p ≈ 17.6 MPa. The working electrode was a 49.3 µm Ø Pt disc. The scan rate was 10 mV s^{-1} for both scans. The reference and counter electrodes were 0.5 mm Ø Pt wires for both systems.

As it can be seen from Figure 4.18, the voltammetry obtained in scR32 is similar to that obtained in $scCO_2$/MeCN (15 wt%). It can also be seen that the limiting current obtained in scR32 is higher than that observed in $scCO_2$/MeCN. There are two possible reasons that the limiting current could be increased, one, the temperature increase from 309 to 360 K, or two, the diffusion coefficient is increased between the two systems.

The limiting current obtained from the voltammograms was taken from the lowest point of convection as described in Chapter 4.1.2. Again, once the limiting current was determined the data from the voltammograms could be collected and are presented in Table 4.6. Using Equation 3.7, the diffusion coefficient was again estimated from the voltammetry obtained for 1.06 mM DMFc at the 19.89, 26 and 49.3 µm Ø Pt disc and found to be 8.24×10^{-5}, 9.04×10^{-5} and 9.41×10^{-5} $cm^2 s^{-1}$ respectively. This is much higher than the diffusion coefficient calculated in liquid DCM where $D = 1.46 \times 10^{-5}$ cm^2 s^{-1}. As with $scCO_2$/MeCN, the diffusion coefficient from DCM is used and assumed that D increases by 2% per temperature unit, in this case $D_{87°C} = 4.98 \times 10^{-5}$ cm^2 s^{-1}. This value is much lower than that calculated from voltammetry, so it can be assumed that again temperature is not the only factor increasing the diffusion coefficient. Performing the same calculation using the diffusion coefficient calculated in $scCO_2$/MeCN ($D = 4.03 \times 10^{-5}$ cm^2 s^{-1}) and taking the temperature from 309 to 360 K and assuming a 2% increase per degree K leads to a value of $D = 1.09 \times 10^{-4}$ cm^2 s^{-1}. This value is close to the value determined by voltammetry. To gain a more accurate value of the diffusion coefficient, a concentration plot was performed along with varying sizes of microelectrode similar to that performed in Chapter 4.1.3.

Table 4.6. Cyclic voltammetry data obtained for experiments with various concentrations of DMFc with 20 mM [NBu_4^n][BF_4] in scR32 at 360 K, $p \approx 17.6$ MPa and $v = 10$ mV s^{-1} for varying sizes of microelectrode.

a / µm	c / mM ± 0.02	i_L / nA ± 0.1	$\Delta E_{(1/4\text{-}3/4)}$ / mV ± 1	$E_{1/2}$ / V ± 0.001	$\Delta E_{1/4}$ / mV ± 1	$\Delta E_{3/4}$ / mV ± 1	$d\ln[(i_L/i)\text{-}1]/dE$ / V^{-1} ± 0.1	n ± 0.01
9.95	0.20	6.0	66	0.119	34	32	29.6	0.92
± 0.1	0.53	12.2	80	0.153	41	39	22.4	0.69
	1.06	33.5	70	0.164	42	28	28.1	0.87
	2.13	64.9	57	0.187	38	29	31.9	0.99
13.0	0.20	8.3	60	0.108	33	27	40.9	1.27
± 0.2	0.53	18.1	60	0.126	32	27	33.2	1.03
	1.06	48.1	73	0.154	40	33	26.9	0.83
	2.13	79.4	73	0.190	38	35	26.8	0.83
	5.14	208.9	70	0.201	37	33	32.7	1.01
	11.20	450.4	73	0.227	38	35	29.5	0.91
24.7	0.20	17.1	54	0.102	33	21	31.5	0.98
± 0.4	0.53	38.2	64	0.120	31	33	34.8	1.08
	1.06	94.9	59	0.136	30	29	37.6	1.17
	2.13	178.6	60	0.169	31	29	38.0	1.18
	5.14	408.4	70	0.192	38	32	31.6	0.98
	11.20	943.1	73	0.220	40	33	29.7	0.92

The half wave potentials and value for n were again calculated from the mass transport correct Tafel analysis. Although in this case as the temperature is raised to 360 K the slope of the graph should equal 32.24 V^{-1} for a 1 e^- reversible process. The values for n for each electrode radii, at nearly all concentrations are close to the expected value of 1. This is in contrast to those determined in $scCO_2$/MeCN (15 wt%) where the value of n increased as the concentration of DMFc was increased. The increase of n was attributed to the increase in uncompensated solution resistance in $scCO_2$/MeCN as the analyte concentration was increased. The above results suggests that voltammetry at microelectrodes in scR32 is not as effected by iR drop. The difference between the half-wave and quartile potentials is between 21 and 42 mV, although in most cases they are close to the expected 29 mV for all concentrations. This is again in contrast to $scCO_2$/MeCN where the difference between the half-wave and quartile potentials were nearly 29 mV at low concentrations and increased as the DMFc concentration is increased. This is again suggestive that the uncompensated solution resistance in scR32 is not as pronounced at microelectrodes as it is in $scCO_2$/MeCN. The half-wave potential does shift as the concentration of DMFc is increased suggesting that uncompensated solution is still having a small effect on the voltammetry but not to the same extent as $scCO_2$/MeCN. This shift in half-wave potential could also be caused by the pseudo reference electrode. The variations in the slope of the mass transport corrected Tafel analysis plots, Figure 4.19, show distinctive signs of being affected by

convection. The natural convection could be affecting the slope of the plots and bringing the values away from ideality.

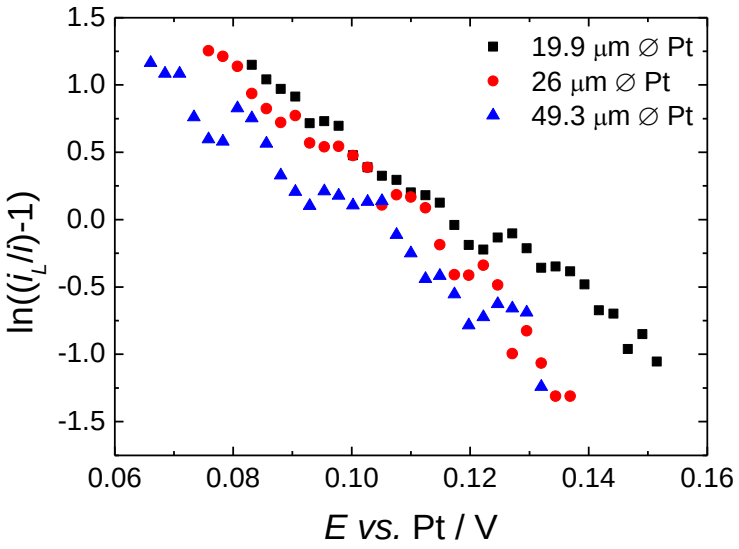

Figure 4.19. Mass transport corrected Tafel analysis for cyclic voltammetry of 0.2 mM DMFc and 20 mM [NBu_4^n][BF_4] in scR32 at 10 mV s^{-1}, at 360 K and $p \approx 17.6$ MPa, for Pt microelectrodes of 19.9, 26 and 49.3 μm diameter.

4.2.2 Determination of the Diffusion Coefficient of Decamethylferrocene at Microelectrodes in scR32

As demonstrated in Chapter 4.1.3, a range of concentrations of DMFc at varying radii of microelectrode can be used to determine the diffusion coefficient of DMFc in scR32. The concentrations of DMFc used in this case were 0.2, 0.53, 1.06, 2.13, 5.14 and 11.2 mM. The radii of microelectrode used were 9.945, 13 and 24.65 μm Ø Pt discs. Although in this case, only four concentrations were probed with the 9.945 μm Pt disc. This was not due to a failure under temperature and pressure, as has been explained in Chapter 4.2.1, but rather when the electrode was polished the NiCr wire contact was exposed rendering the electrode unusable. The 13 and 24.65 μm Pt discs were used for all experiments and concentrations.

Figure 4.20 shows the plot obtained for the diffusion limited current against the concentration of DMFc over the range of concentrations stated for the three microdisc electrodes. As it can be seen from Figure 4.20, the limiting current increases linearly with concentration in all cases as anticipated from Equation 4.1. The plot also shows that the solubility limit of DMFc in scR32 clearly exceeds 11 mM, like in the case of $scCO_2$/MeCN (15 wt%), see Figure 4.8. Using the

slopes of the plots determined in Figure 4.20 in combination with Equation 4.1 the value of the diffusion coefficient were calculated and are displayed in Table 4.7.

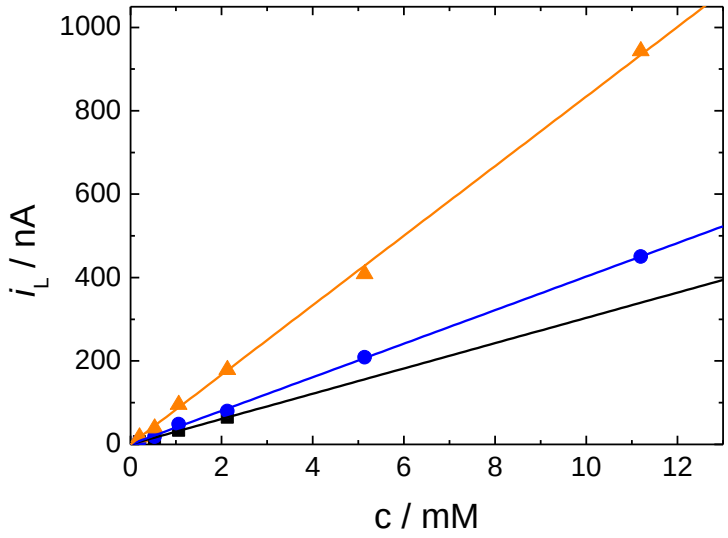

Figure 4.20. Plot of diffusion limited current *versus* the decamethylferrocene concentration for a series of cyclic voltammograms in supercritical R32 and 20 mM [NBu_4^n][BF_4] electrolyte. T = 360 K, p = 17.2 – 17.7 MPa. The working electrodes were a 19.9 (■), 26 (●) and 49.3 µm (▲) diameter platinum disc, the counter and reference electrode were 0.5 mm diameter wires.

Table 4.7. Variation of the diffusion coefficient with concentration of DMFc. The working electrodes were a 19.9, 26 and 49.3 µm diameter platinum disc, the counter and reference electrode were 0.5 mm diameter platinum wires. Solutions were scR32, 20 mM [NBu_4^n][BF_4]. T = 360 K, p = 17.2 – 17.7 MPa.

a **/ µm**	***D*** **/ cm^2 s^{-1}**
10.0 ± 0.1	7.9 x 10^{-5} ± 0.05 x 10^{-5}
13.0 ± 0.2	8.02 x 10^{-5} ± 0.06 x 10^{-5}
24.7 ± 0.4	8.77 x 10^{-5} ± 0.07 x 10^{-5}
Mean	**8.23 x 10^{-5} ± 0.06 x 10^{-5}**

From Table 4.7, it can be seen that the diffusion coefficient of DMFc in scR32 at 360 K and ≈ 17.6 MPa is D = 8.23 ± 0.06 x 10^{-5} cm^2 s^{-1}. This is in agreement with the diffusion coefficients calculated from voltammetry and is higher than the diffusion coefficients calculated in liquid DCM and in $scCO_2$/MeCN (15 wt%). In order to confirm the diffusion coefficient, the limiting current was also plotted as a function of microelectrode radius for a separate set of experiments using five different DMFc concentrations, Figure 4.21. Again the results are fully consistent with Equation 4.1. The diffusion coefficients were again calculated from the slopes of the graphs from Equation 4.1 and are given in Table 4.8.

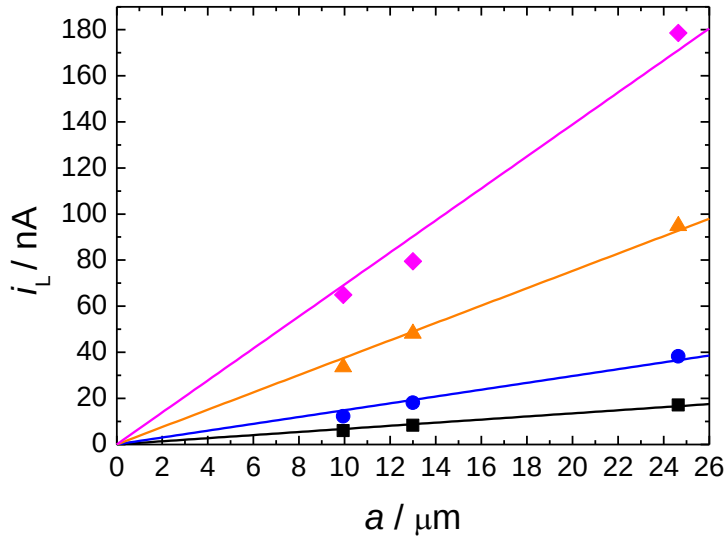

Figure 4.21. Plot of diffusion limited current *versus* the electrode radii for a series of cyclic voltammograms in supercritical R32 and 20 mM $[NBu_4^n][BF_4]$ electrolyte. T = 360 K, p = 17.2 – 17.7 MPa. The concentrations were 0.2 (■), 0.53 (●), 1.06 (▲) and 2.12 mM (♦). The counter and reference electrode were 0.5 mm diameter platinum wires.

Table 4.8. Variation of the diffusion coefficient with electrode radii. The working electrodes were a 19.9, 26 and 49.3 μm diameter platinum disc, the counter and reference electrode were 0.5 mm diameter platinum wires. Solutions were R32, 20 mM $[NBu_4^n][BF_4]$. T = 360 K, p = 17.2 – 17.7 MPa

***c* / mM**	***D* / cm^2 s^{-1}**
0.20 ± 0.02	8.72 x 10^{-5} ± 0.79 x 10^{-5}
0.53 ± 0.02	7.24 x 10^{-5} ± 0.25 x 10^{-5}
1.06 ± 0.02	9.22 x 10^{-5} ± 0.16 x 10^{-5}
2.12 ± 0.02	8.48 x 10^{-5} ± 0.07 x 10^{-5}
Mean	**8.42 x 10^{-5} ± 0.32 x 10^{-5}**

The diffusion coefficient calculated for DMFc in scR32 at 360 K, and ≈ 17.6 MPa in Table 4.8 is in excellent agreement with the diffusion coefficient calculated in Table 4.7. From the two sets of experiments the diffusion coefficient for DMFc has been calculated to be 8.33 x 10^{-5} cm^2 s^{-1} in scR32 at 360 K and ≈ 17.6 MPa. The diffusion coefficient calculated here is lower than that calculated by Olsen and Tallman[84] who studied the voltammetry of ferrocene in sub and supercritical chlorodifluoromethane (CDFM). Olsen and Tallman[84] determined the diffusion coefficient of ferrocene in scCDFM to be D = 1.30 x 10^{-4} cm^2 s^{-1} at 388 K and 9 MPa. Although using a different temperature and pressure, which can change the density and viscosity of a supercritical media, the values are comparable.

4.2.3 Electrochemistry of Decamethylferrocene in scR32 using a Microdisc Electrode with a Baffle

As was demonstrated in Chapter 4.1.4, the use of a baffle at the end of a microelectrode can significantly reduce the natural convection seen on the mass transport limited current. It has also been shown previously (Chapter 4.2.1) that natural convection is much more prominent in scR32 due to the increased temperatures required. Using a baffle electrode in scR32 should sufficiently dampen the natural convection as was seen in $scCO_2$/MeCN.

Cyclic voltammograms recorded in a solution of scR32 containing 0.567 mM DMFc and 20 mM $[NBu_4^n][BF_4]$ for a 25 (baffled) and 25 (non-baffled) µm Ø Pt disc, at 360 K and ≈ 17.6 MPa, are displayed in Figure 4.22. The data obtained from the voltammograms is also displayed in Table 4.9. As it can be seen from Figure 4.22, the natural convection seen on the limiting current is significantly reduced at the baffled electrode, as was seen in $scCO_2$/MeCN. The baffle electrode again displays a steady state limiting current plateau, similar to that seen in liquid DCM and at the baffle electrode in $scCO_2$/MeCN. The values of the half-wave potential are in agreement between the two electrodes, $E_{1/2}$ = 0.138. It can also be seen in Table 4.9 that the different between the three quarter ($E_{3/4}$) and half-wave potential are close to the expected 29 mV expected for a reversible process and are in agreement with the data presented in Table 4.6. The slopes of the mass transport corrected Tafel analysis (Figure 4.23) are close to the expected value of 32.24 V^{-1} at 360 K, leading to the values of *n* being close to 1 in the system. It can also be seen in Figure 4.23 that the plot for the baffle electrode is more linear compared to the non-baffled electrode, this is also due to dampening natural convection. The diffusion coefficient calculated at the baffle electrode was D = 7.23 x 10^{-5} cm^2 s^{-1}, which is in agreement with diffusion coefficient calculated from the plots in Figures 4.19 and 4.20.

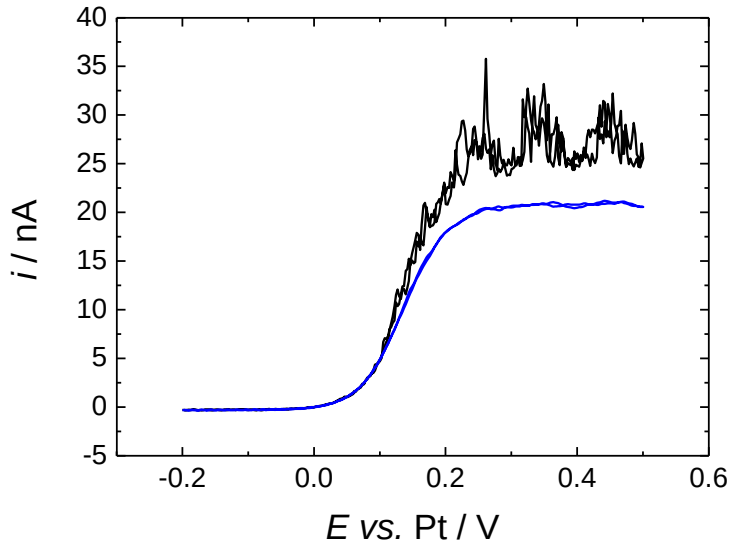

Figure 4.22. Cyclic voltammograms for a solution containing 0.567 mM DMFc and 20 mM [NBu_4^n][BF_4] in scR32, v = 10 mV s^{-1} for all scans, T = 360 K and p ≈ 17.6 MPa. The reference and counter electrodes were 0.5 mm Ø Pt wires. The working electrodes were 28.4 µm (black, not baffled) and 25.9 µm (blue, baffled) Ø Pt discs.

Table 4.9. Cyclic voltammetry data obtained for experiments of 0.567 mM DMFc with 20 mM [NBu_4^n][BF_4] in scR32 at 360 K, p ≈ 17.6 MPa and v = 10 mV s^{-1} for varying sizes of microelectrode. B = Baffled, NB = not baffled.

a / µm ± 0.5	i_L / nA ± 0.01	$\Delta E_{(1/4\text{-}3/4)}$ / mV ± 1	$E_{1/2}$ / V ± 0.001	$\Delta E_{1/4}$ / mV ± 1	$\Delta E_{3/4}$ / mV ± 1	$d\ln[(i_L/i)\text{-}1]/dE$ / V^{-1} ± 0.1	n ± 0.01
14.2 (NB)	24.03	58	0.138	35	23	36.5	1.13
12.9 (B)	20.46	70	0.137	38	32	30.7	0.95

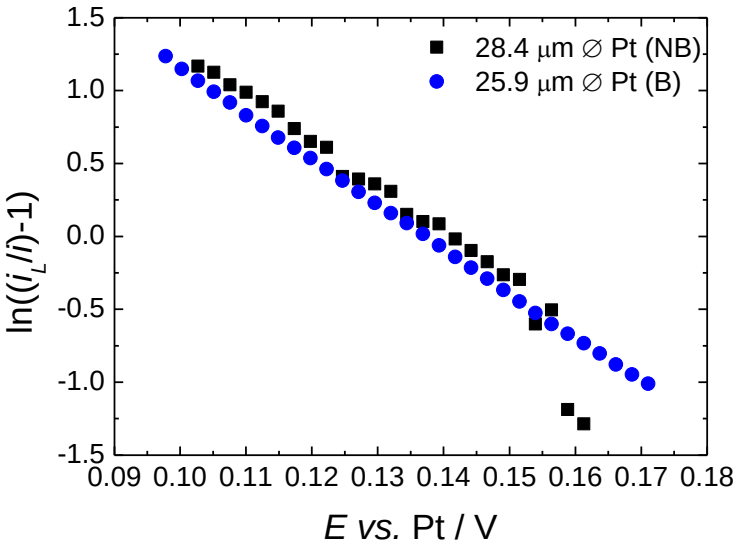

Figure 4.23. Mass transport corrected Tafel analysis for cyclic voltammetry of 0.567 mM DMFc and 20 mM [NBu_4^n][BF_4] in scR32 at 10 mV s^{-1}, at 360 K and $p \approx 17.6$ MPa, for microelectrodes of 28.4 and 25.9 μm diameter. NB = not baffled and B = baffled.

As was the case in $scCO_2$/MeCN, the limiting current of the baffled electrode in Figure 4.22 does not lie on the minimum plateau of the limiting current for the "bare" electrode. Like for $scCO_2$/MeCN it was assumed the two nominally sized microelectrodes had different radii. To determine if the two electrodes did indeed have differently sized radii, SEM imaging was performed, the pictures taken along with measurements of the electrodes are shown in Figure 4.24. As it can be seen in Figure 4.24 the non-baffled electrode clearly has a larger radius in certain areas when compared to the baffled electrode. Previously we have considered the electrode as a circular disk with an average radius; we will now consider the electrode as an elliptical disk to account for the electrode having a larger radius in one axis. Bruckenstein and Janiszewska[108] discussed diffusion currents to (ultra)microelectrodes of various geometries including ellipsoids, spheroids and elliptical disks. The semi-infinite limiting diffusion current for species A at an elliptical disk, $I_{ell,lim}$, is given in Equation 4.2

$$I_{ell,lim} = \frac{2\pi nFD_A C_A^b a}{K\left([1-b^2a^{-2}]^{\frac{1}{2}}\right)}, a \geq b \tag{4.2}$$

where a and b are the major and minor semiaxes of the ellipse and $K(m)$ is the complete integral of the first kind[108]. Defining $m = [1 - b^2a^{-2}]^{1/2}$, gives Equation 4.3

$$I_{ell,lim} = \frac{2\pi nFD_A C_A^b a}{K(m)} = \frac{4nFD_A C_A^b a}{G(m)} \tag{4.3}$$

where $G(m) = 2K(m)/\pi$ and the function $K(m)$ has values in the range $\pi/2 \leq K(m) \leq \infty$ for $0 \leq m \leq 1$ and $G(m)$ has values in the range $1 \leq G(m) \leq \infty$ for $0 \leq m \leq 1$ [108]. Bruckenstein and Janiszewska[108] provided absolute values of elliptical disk electrodes limiting current in a Table in terms of b/a and $G(m)$. In this case, b = 13.15 µm (26.3 µm Ø) and a = 16.35 µm (32.7 µm Ø) taken from Figure 4.24 which leads to b/a = 0.804, this correlates to a $G(m)$ value of 0.8303 [108]. When comparing to a circular disk, this means the elliptical disk current should be considered as 83.03% of the total current recorded[108]. This correlates well with the experimental data, taking the values for the steady state current at both disks (Table 4.9) the difference found is 85.1%. Rearrangement of Equation 4.3 leads to Equation 4.4, where it can be seen that when the limiting current of the elliptical disk is multiplied by the $G(m)$ value will give the steady state equation for a spherical disk (Equation 4.1).

$$I_{ell,lim}\, x\, G(m) = 4nFD_A C_A^b a \tag{4.4}$$

Taking Equation 4.4, the two voltammograms can be compared and this is presented in Figure 4.25. As can be seen from Figure 4.25, the limiting current recorded at the spherical disk (baffled) lies at the minimum plateau of the "elliptical bare" electrode. This helps to confirm, along with the data obtained with in aqueous conditions with ruthenium in Chapter 4.1.4, that the limiting current of microelectrodes in supercritical fluids should be taken from the lowest point of the natural convection.

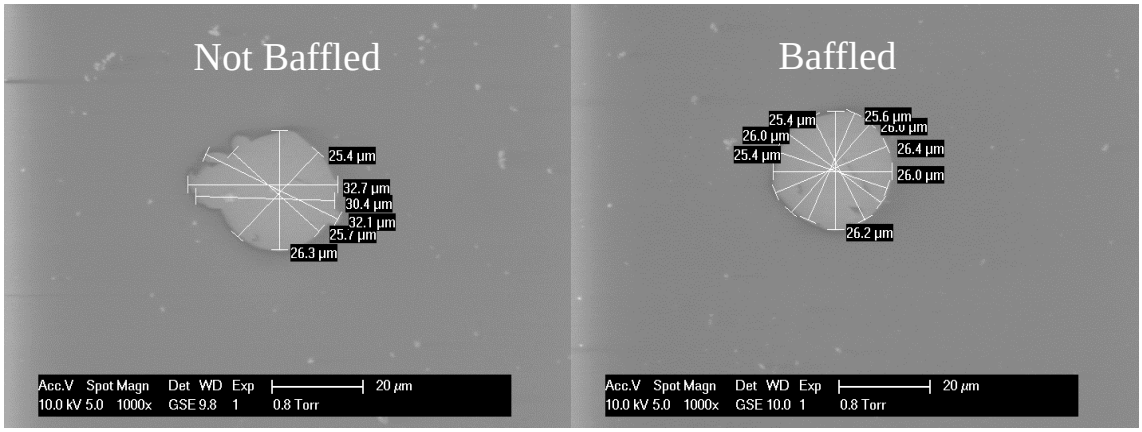

Figure 4.24. SEM image of the baffled and unbaffled microelectrodes described in Figure 4.22.

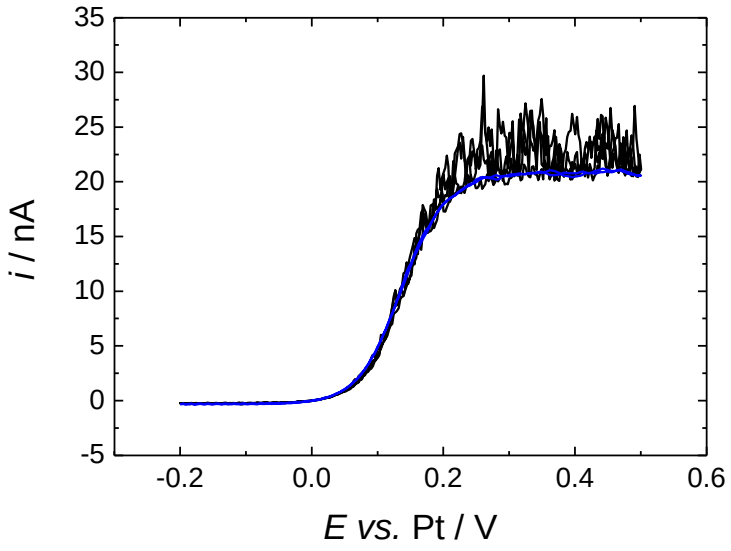

Figure 4.25. The solution, scan rate, temperature, pressure, reference and counter electrodes have been described in Figure 4.22. The black line represents the "bare" electrode (where the current has been corrected by Equation 4.4) and the blue line represents the baffled electrode.

4.2.4 Electrochemistry of Decamethylferrocene in scR32 at a Macroelectrode with and without a Baffle

Cyclic voltammetry for a macroelectrode at various scan rates was also carried out to examine the behaviour of the couple in scR32 with $[NBu_4^n][BF_4]$ as supporting electrolyte. The macrodisc used in this case was a 1.0 mm Ø Au disc. The following sections outline why the use of a bare macroelectrode does not lead to well-defined voltammetry in scR32. This section also demonstrates why the use of a baffle electrode is essential for well-defined voltammetry at macro electrodes in scR32.

4.2.4.1 Electrochemistry of Decamethylferrocene in scR32 at a Macroelectrode without a Baffle

Cyclic voltammograms performed in a solution of scR32 containing 0.39 mM DMFc and 20 mM $[NBu_4^n][BF_4]$ for a 1 mm Ø Au disc at 360 K and ≈ 17.6 MPa, are displayed in Figure 4.26. In this case the voltammograms are significantly distorted by the natural convection within the cell, but are not affected by *iR* drop. This is the reverse of what was seen in $scCO_2$/MeCN where the voltammograms were more affected by *iR* than convection. At a scan rate of 1000 mV/s, the voltammetry begins to look more like that expected of a macroelectrode. As the voltammograms are severely affected by natural convection, no usable information can be gained. As Section 4.2.3 has shown, a baffle electrode can significantly

dampen the effects of natural convection. To test if this could be extended to macroelectrodes, a macroelectrode with a baffle was constructed. This would hopefully alleviate the natural convection seen in the scans and give well-defined voltammetry as seen in liquid conditions and like that seen in $scCO_2$/MeCN.

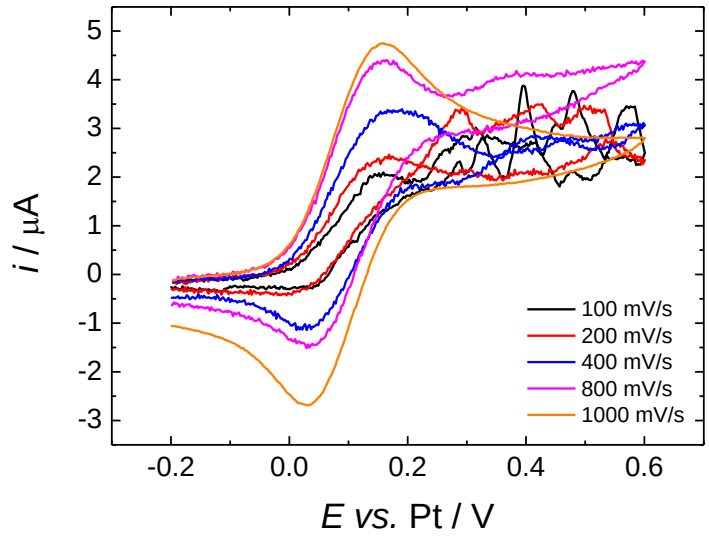

Figure 4.26. Cyclic voltammograms for a solution of 0.39 mM DMFc and 20 mM [NBu_4^n][BF_4] in scR32 at 360 K, $p \approx 17.6$ MPa. The working electrode was a 1 mm Ø Au disc, the reference and counter electrode were 0.5 mm Ø Pt wires.

4.2.4.2 Electrochemistry of Decamethylferrocene in scR32 at a Macroelectrode with a Baffle

Cyclic voltammograms performed in a solution of scR32 containing 0.39 mM DMFc and 20 mM [NBu_4^n][BF_4] for a baffled 1 mm Ø Au disc at 360 K and ≈ 17.6 MPa, are displayed in Figure 4.27. The data obtained from the voltammetry is displayed in Table 4.10. As can be seen from Figure 4.27, the voltammetry obtained at the baffled macro electrode shows well defined voltammetry with little to no natural convective influence. The uncompensated solution resistance becomes more apparent at higher scan rates at the baffled macro electrode as indicated by the increase in peak potentials from 154 to 208 mV. The voltammetry is similar to that recorded in $scCO_2$/MeCN, but is not as heavily distorted by *iR* drop as $scCO_2$/MeCN. Similar peak to peak potential separation values were seen in liquid DCM and increased as the scan rate was increased. The difference between the half wave and peak potentials was measured between 92 to 119 mV. The large difference seen is most likely due to the uncompensated solution resistance; the same increase was seen in liquid DCM. The ratio of the peak currents was unity for all scan rates. The same ratio of peak currents was measured in

liquid DCM and in $scCO_2$/MeCN. Performing a similar analysis as seen in Figure 4.12 for $scCO_2$/MeCN, the uncompensated solution resistance was estimated to be 13.1 kΩ, and the separation of the two lines through the peak currents was estimated to be 95.8 mV. This is close to the expected value of 71.3 mV for a reversible 1 e^- process at 360 K. The resistance of the system is again reasonable given the known conductivity of the system[63].

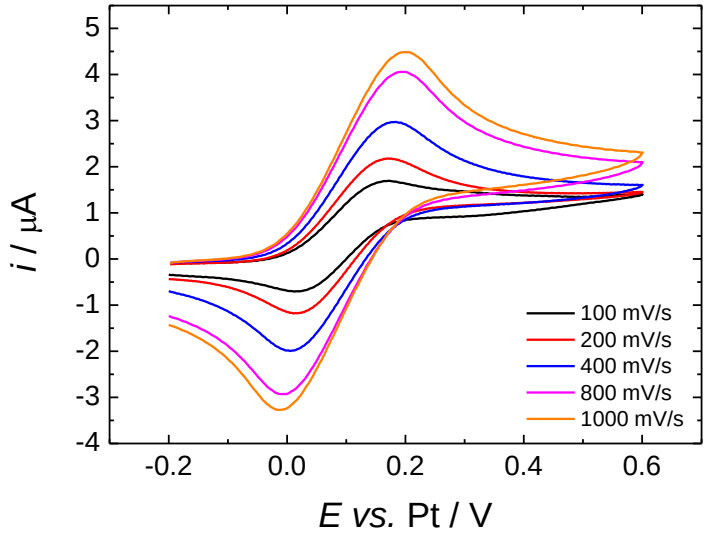

Figure 4.27. Cyclic voltammograms for a solution of 0.39 mM DMFc and 20 mM [NBu_4^n][BF_4] in scR32 at 360 K, $p \approx 17.6$ MPa. The working electrode was a baffled 1 mm Ø Au disc, the reference and counter electrode were 0.5 mm Ø Pt wires.

Table 4.10. Data obtained from cyclic voltammograms in 0.39 mM DMFc and 20 mM [NBu_4^n][BF_4] in scR32 at 360 K and $p \approx 17.6$ MPa for various scan rates at a baffled 1 mm Ø Au disc.

v / V s^{-1}	E_{pa} / mV ± 1	E_{pc} / mV ± 1	ΔE_p / mV ± 1	$E_{pa/2}$ / mV ± 1	$E_{pc/2}$ / mV ± 1	$E_{pa} - E_{pa/2}$ / mV ± 1	$E_{pc} - E_{pc/2}$ / mV ± 1	i_{pa} / µA ± 0.01	i_{pc} / µA ± 0.001	i_{pa}/i_{pc} ± 0.01
0.1	170	16	154	70	108	100	92	1.67	1.47	1.14
0.2	170	16	154	70	114	100	98	2.17	2.17	1.00
0.3	178	12	166	73	112	105	100	2.61	2.55	1.02
0.4	182	7	175	75	110	107	103	2.97	2.90	1.02
0.5	184	4	180	74	110	110	106	3.28	3.20	1.03
0.6	186	1	185	78	107	108	107	3.56	3.50	1.02
0.7	194	-3	197	78	106	116	109	3.81	3.62	1.05
0.8	194	-8	202	79	107	115	115	4.07	3.92	1.04
0.9	195	-7	202	79	105	116	112	4.27	4.14	1.03
1.0	199	-9	208	80	105	119	114	4.48	4.28	1.04

As the peak currents could be determined over a range of scan rates, Randles-Sevčik analysis was used to determine the diffusion coefficient at the macro electrode in scR32. The dependence of the peak current with $v^{1/2}$ at 360 K for the 1.0 mm Ø Au is presented in Figure 4.28. As with DMFc in liquid DCM, the linear fits do not extrapolate to the origin. The

intercept of the graph is similar to that seen in liquid DCM and is close to the origin, so the diffusion coefficient could be calculated from Figure 4.28. The diffusion coefficient calculated from the peak anodic and peak cathodic current was D = 2.78 ± 0.26 x 10^{-5} cm^2 s^{-1} and 2.46 ± 0.23 x 10^{-5} cm^2 s^{-1} respectively. These values for the diffusion coefficient are much lower than those calculated at the microdisc for this system; they are also lower than the diffusion coefficient determined in $scCO_2$/MeCN. Although the experiments were repeated on many different occasions, the diffusion coefficient calculated was always of a similar value, irrespective of the concentration of DMFc. The electrode area was also confirmed by SEM, suggesting it has no effect on the calculation. It has also been shown in Section 4.2.3 that the diffusion coefficient calculated at the baffled microdisc electrode was in good agreement with the previous data. This suggests that the baffle is having no hindering factors on the diffusion of materials. It is still unclear why the calculated diffusion coefficient for DMFc in scR32 at 360 K and ≈ 17.6 MPa is so low for a baffled macro disc electrode.

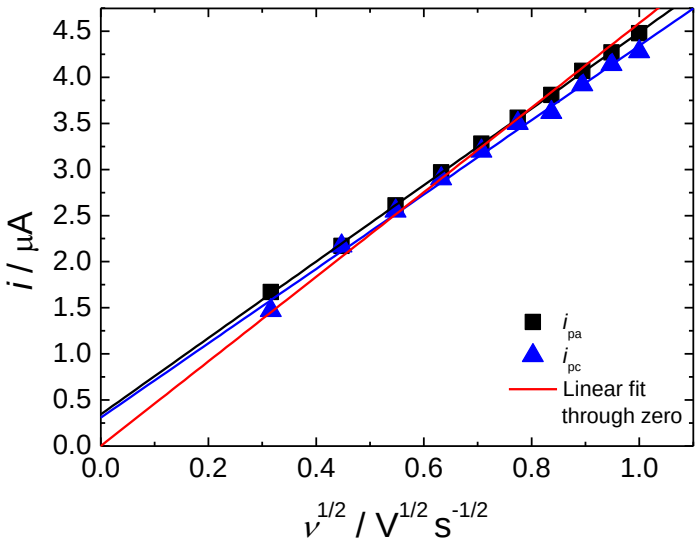

Figure 4.28. The dependence of peak currents on the scan rate for cyclic voltammetry of 0.39 mM DMFc and 20 mM [NBu_4^n][BF_4] in scR32 at 360 K and ≈ 17.6 MPa, at a baffled 1 mm Ø Pt disc working electrode.

As the baffled and non-baffled macro electrodes were in the same solution, a comparison between the two electrodes at 400 mV/s is displayed in Figure 4.29. As it can be seen from Figure 4.29, at 400 mV/s for an unbaffled macro electrode the voltammetry seen is not well defined and the diffusion limited region is affected by natural convection. In contrast, at the baffled macro electrode at 400 mV/s, well defined voltammetry is seen and no influence of the natural convection is seen. Although not showing major influences of natural convection at 400 mV/s at the baffled macro electrode, below this scan rate (< 400 mV/s), small amounts of

natural convection can sometimes be experienced. Thus it can be seen that the minimum scan rate required to remove natural convection at a baffled macro electrode is 400 mV/s. If one scan is from -0.2 V to 0.6 V (which is a total of 0.8 V) at 400 mV/s, then the time taken to reach 0.6 V is 2 s. Thus it can be deduced that the natural convection within the cell is influential at times > 2 s for a macro electrode in scR32 at 360 K.

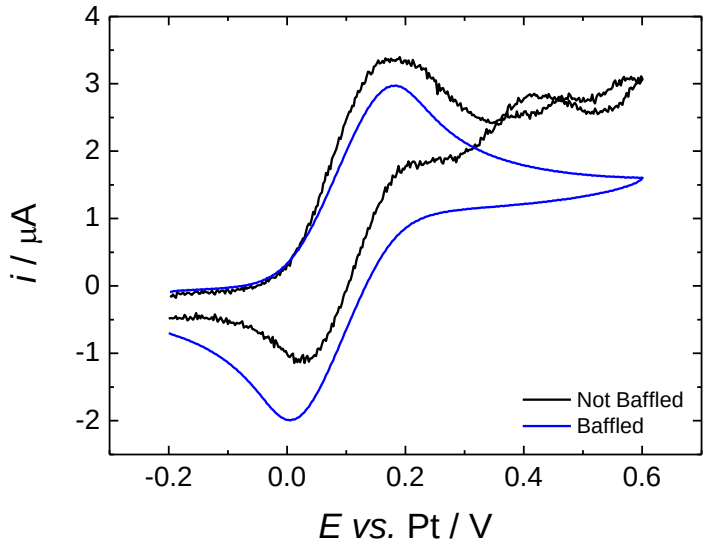

Figure 4.29. Cyclic voltammograms for a solution of 0.39 mM DMFc and 20 mM [NBu_4^n][BF_4] in scR32 at 360 K, $p \approx 17.6$ MPa, $v = 400$ mV s^{-1}. The reference and counter electrode were 0.5 mm Ø Pt wires. Black line: The working electrode was an unbaffled 1 mm Ø Au disc. Blue line: The working electrode was a baffled 1 mm Ø Au disc.

4.3 Cyclic Voltammetry of Cobaltocenes in Supercritical Fluids

It has been shown in Chapter 3 that both decamethylcobaltocene and cobaltocenium hexafluorophosphate were good redox couples in acetonitrile at both micro and macro electrodes. It has also been shown that decamethylcobaltocenium hexafluorophosphate was a good redox couple at both micro and macro electrodes in dichloromethane. This section details experiments performed with the various cobaltocene complexes in both $scCO_2$/MeCN (15 wt%) and in scR32. In both solvents, the cobaltocene complexes never give good well defined, reproducible voltammetry at either macro or micro electrodes. This is in contrast to DMFc which gives well defined, reproducible voltammetry in both supercritical solvents.

4.3.1 Cyclic Voltammetry of Cobaltocenium Hexafluorophosphate in $scCO_2$/MeCN (15 wt%)

Cyclic voltammograms for a solution of $scCO_2$/MeCN (15 wt%) containing 1.04 mM $[CoCp_2][PF_6]$ and 20 mM $[NBu_4^n][BF_4]$, for a 50 µm Ø Pt, at 309 K and ≈ 17.2 MPa are displayed in Figure 4.30. A second repeat at the same microelectrode, in the same solution, after a short period of time is also presented in Figure 4.31. As it can be seen from Figures 4.30 and 4.31, the voltammetry at a microelectrode does not show the expected sigmoidal wave seen with DMFc in $scCO_2$/MeCN. The scans show a response which is more conventional of a macro electrode only without an anodic current peak. It is also interesting to note that the current recorded diminishes between scans in Figure 4.30. At the end of the scan, ~ -1.75 V, the current starts to increase, this is most likely due to breakdown of the supporting electrolyte. A similar trend is seen in Figure 4.31, but the current recorded in each scan is not reproducible. Although the reduction of $CoCp_2^+$ starts at the same potential on each scan, the peak potential decreases after three scans. The reduction of $CoCp_2^+$ does appear at the same potential as that recorded in MeCN, suggesting the reduction is that of $CoCp_2^+$. This trend was seen for all experiments performed with $CoCp_2^+$ in $scCO_2$/MeCN, so it was decided to not to pursue the metallocene as a redox probe in the system. Further work would need to be performed to confirm the cause of the voltammetry seen in Figures 4.30 and 4.31.

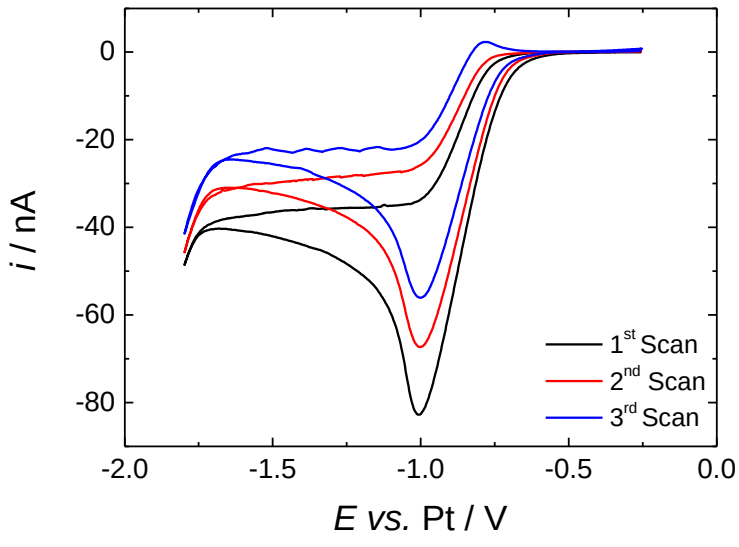

Figure 4.30. Cyclic voltammograms for a solution of 1.04 mM $[CoCp_2][PF_6]$ and 20 mM $[NBu_4^n][BF_4]$ in $scCO_2$/MeCN (15 wt%) at 309 K, p ≈ 17.2 MPa, v = 20 mV s^{-1}. The working electrode was a 50 µm Ø Pt disc, the reference and counter electrode were 0.5 mm Ø Pt wires.

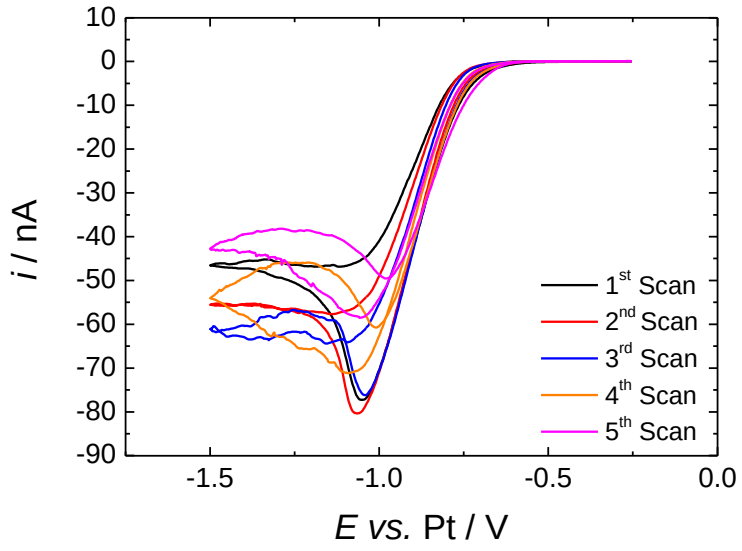

Figure 4.31. Repeat at the same micro electrode described in Figure 4.30 after an extended period of time. The solution, electrodes, scan rate, temperature and pressure have been described in Figure 4.30.

4.3.2 Cyclic Voltammetry of Decamethylcobaltocene in $scCO_2$/MeCN (15 wt%)

Cyclic voltammograms for a solution of $scCO_2$/MeCN (15 wt%) containing ≈ 1 mM DmCo and 20 mM $[NBu_4^n][BF_4]$, at a 10 and 40 µm Ø Pt disc, at 309 K and ≈ 17.2 MPa, are displayed in Figures 4.32 and 4.33 respectively. As can be seen from Figures 4.32 and 4.33, the voltammetry obtained at the microdiscs, again, does not show a well-defined sigmoidal wave voltammetry as expected. In Figure 4.32, the first scan shows a higher current and then on subsequent scans the current decreases and is of the same value in the third scan. The reduction potential in Figure 4.32 also shifts between scans; this is most likely due to the Pt pseudo reference electrode. The voltammetry in Figure 4.33 is more affected by the potential shifting. The reduction potentials seen in $scCO_2$/MeCN are more cathodic than those seen in liquid MeCN. The half wave potential recorded for DmCo in MeCN was $E_{1/2}$ = - 0.154 V. In $scCO_2$/MeCN the half wave potential has shifted 600 mV. The voltammetry in Figure 4.33 also stabilises at the same value for scans two and three as was seen in Figure 4.32. When the experiment was repeated, the results obtained were not reproducible, and did not give any redox process. As DmCo is a similar redox couple to DMFc, it was decided that DMFc was the superior couple for studying neutral to positive species. It was also decided to not pursue decamethylcobaltocene in scR32 as demonstrated in Section 4.2; DMFc is a superior redox couple with better reproducible and well defined voltammetry.

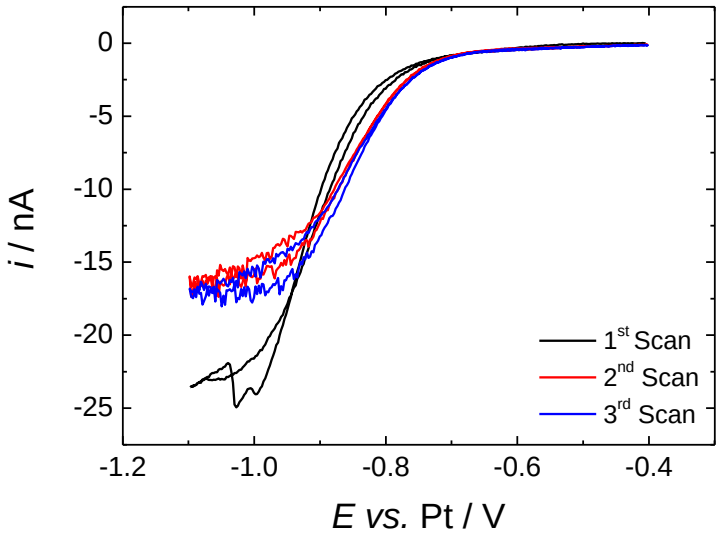

Figure 4.32. Cyclic voltammograms for a solution of 1.04 mM DmCo and 20 mM $[NBu_4^n][BF_4]$ in $scCO_2$/MeCN (15 wt%) at 309 K, $p \approx 17.2$ MPa, $v = 20$ mV s^{-1}. The working electrode was a 10 µm Ø Pt disc, the reference and counter electrode were 0.5 mm Ø Pt wires.

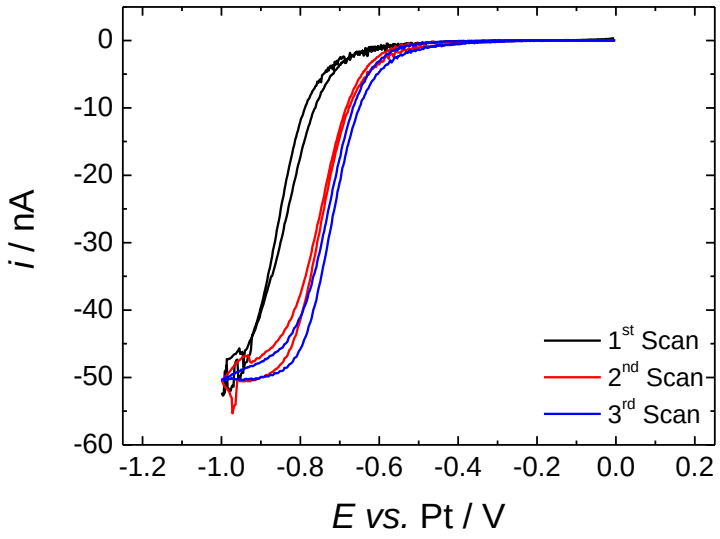

Figure 4.33. The working electrode was a 40 µm Ø Pt disc. The solution, temperature, pressure, scan rate, reference and counter electrode have been described in Figure 4.32.

4.3.3 Cyclic Voltammetry of Cobaltocenium Hexafluorophosphate in scR32

Cyclic voltammetry for a solution of scR32 containing 0.38 mM $[CoCp_2][PF_6]$ and 20 mM $[NBu_4^n][BF_4]$ for 50 µm Ø Pt disc, at 360 K and ≈ 17.9 MPa is displayed in Figure 4.34. As can be seen from Figure 4.34, the voltammetry has a sigmoidal wave shape with a mass

transport limited current, but with more hysteresis than was seen for DMFc. From the voltammetry the limiting current was determined to be -37.1 nA. Using Equation 4.1, the diffusion coefficient was determined to be D = 1.01 x 10^{-4} cm^2 s^{-1}, which is close to the diffusion coefficient determined by Olsen and Tallman in supercritical chlorodifluoromethane[59]. Although giving well defined voltammetry for one scan, subsequent scanning leads to highly resistive voltammetry. After the resistive scans begin, no more voltammetry could be obtained. To determine if a film had formed on the surface of the electrode, the voltammetry was run between 3 and -3 V, the same as was used for the preconditioning step in $scCO_2$/MeCN. This cycling has no effect on the voltammetry and subsequently no more voltammetry was obtained for the system. Repeating the experiments with a concentration of 0.45 mM $[CoCp_2][PF_6]$ at a similar pressure and a 25 µm Ø Pt disc did not yield the same results seen in Figure 4.34. Results at a baffled macrodisc were obtained and will be discussed later. Instead the voltammetry would show the start of a redox process, but then return to a zero current response in the same scan, Figure 4.35. As the reduction potential in Figure 4.35 is the same as that seen in Figure 4.34, it can be assumed it is the $CoCp_2^+$ species. It is not clear why the results from Figure 4.34 could not be repeated at microdiscs.

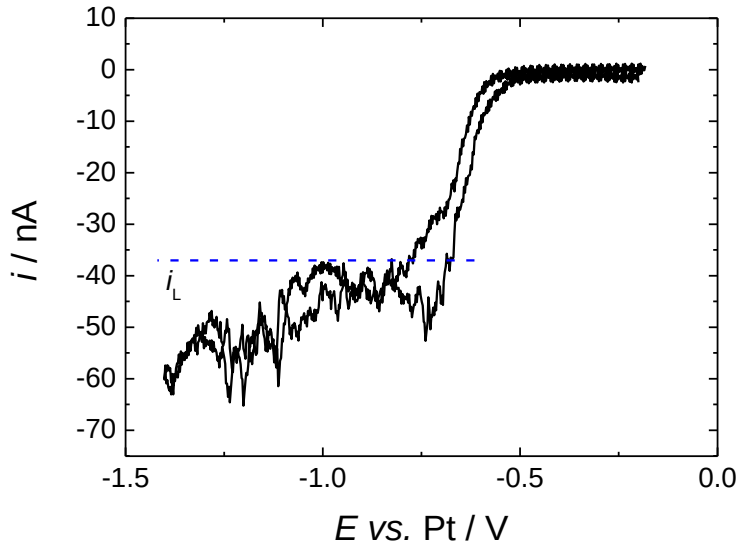

Figure 4.34. Cyclic voltammetry for a solution of 0.38 mM $[CoCp_2][PF_6]$ with 20 mM $[NBu_4^n][BF_4]$ in scR32 at 360 K, $p \approx 17.9$ MPa, $\nu = 50$ mV s^{-1}. The working electrode was a 50 µm Ø Pt disc. The reference and counter electrode were 0.5 mm Ø Pt wires. The blue dashed line represents where the mass transport limited current was recorded.

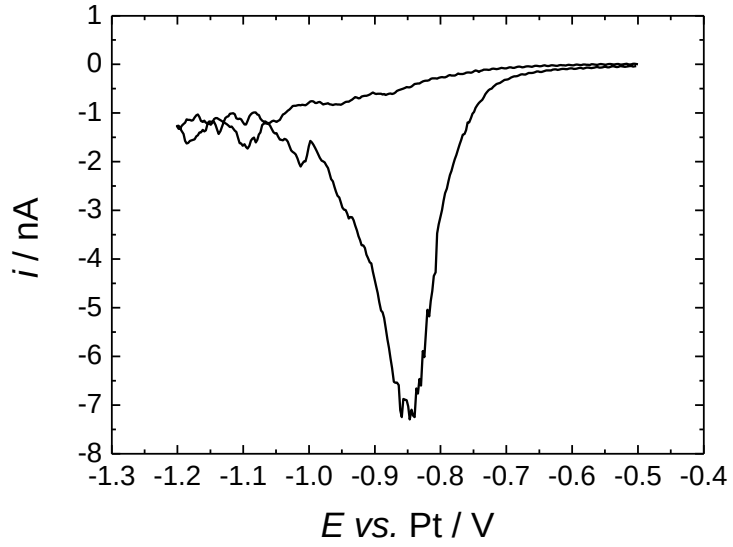

Figure 4.35. Cyclic voltammetry for a solution of 0.45 mM [$CoCp_2$][PF_6] with 20 mM [NBu_4^n][BF_4] in scR32 at 358 K, $p \approx 14.5$ MPa, $\nu = 10$ mV s^{-1}. The working electrode was a 25 µm Ø Pt disc. The reference and counter electrode were 0.5 mm Ø Pt wires.

Cyclic voltammograms for a solution of scR32 containing 0.45 mM [$CoCp_2$][PF_6] and 20 mM [NBu_4^n][BF_4] for a baffled 1 mm Ø Au disc, at 358 K and ≈ 14.5 MPa are displayed in Figure 4.36. As can be seen from Figure 4.36, the voltammetry obtained at the baffled macrodisc shows a redox process occurring but does not show well defined peak anodic and peak cathodic currents as seen with DMFc. The most noticeable feature is the absence of a peak cathodic current, a peak anodic current is present but it does not scale with $\nu^{1/2}$ as with Randles-Sevčik analysis. The results from the micro and macro electrode suggest that cobaltocenium hexafluorophosphate is not a good internal reference standard for scR32. Further work would need to be performed to determine the cause of the problems seen in the voltammetry. One reason may be the reaction of the species with oxygen. As of yet, the oxygen content of the cell cannot be determined in supercritical fluids. There are cases in literature of the reaction between cobaltocene species and oxygen, the oxygen forms a bridge between the two cobalt centres[109-111]. This phenomenon may be the cause of the voltammetry seen. Cooper and Bond[112] also studied evidence for the adsorption of the cobaltocenium cation and precipitation of uncharged cobaltocene at platinum microelectrodes in the absence of supporting electrolyte. The results seen in Figure 4.35 are similar to those seen by Copper and Bond in acetonitrile and dichloromethane with no supporting electrolyte. They theorised that the rise in current at rather negative potentials was due to the reduction of the surface Co^0 precipitate[112]. This precipitation of the neutral species could also be the cause of the voltammetry seen; further studies would need to be performed to confirm this process.

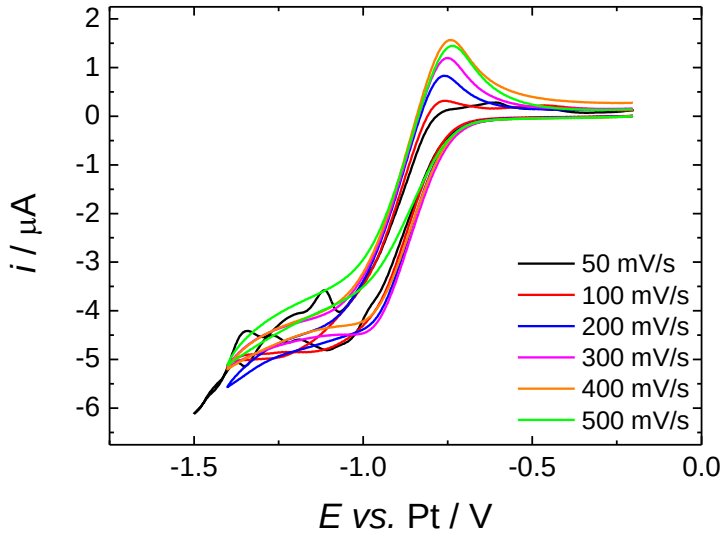

Figure 4.36. Cyclic voltammograms for a solution of 0.45 mM $[CoCp_2][PF_6]$ and 20 mM $[NBu_4^n][BF_4]$ in scR32 at 358 K, $p \approx 14.5$ MPa for various scan rates. The working electrode was a baffled 1 mm Ø Au disc, the reference and counter electrode were 0.5 mm Ø Pt wires.

4.3.4 Cyclic Voltammetry of Decamethylcobaltocenium Hexafluorophosphate in scR32 using [Na][BARF] as Supporting Electrolyte

It has been shown in Chapter 3.5 that $DmCo^+$ is a good redox couple in liquid DCM. It was also shown that the reduction of $DmCo^+$ starts at reasonably negative potentials, -1.8 V. This highly negative potential means that electrochemistry performed using $[NBu_4^n][BF_4]$ as supporting electrolyte would not be possible as breakdown of the electrolyte in supercritical conditions would occur before the reduction of the analyte. Changing the electrolyte can extend the potential window; by changing the $[NBu_4^n]$ cation for a [Na] cation will extend the cathodic potential window.

Cyclic voltammetry for a solution of scR32 containing 1.02 mM $[DmCo][PF_6]$ and 20 mM [Na][BARF] for a 50 µm Ø Pt disc at 360 K and ≈ 17.9 MPa is displayed in Figure 4.37. As can be seen from Figure 4.37, no redox process is seen for $DmCo^+$. The process that occurs at ~ -1.6 V shows characteristics of an electrodeposition, this is also evident from the broad stripping peak seen on the reverse scan. This process is most likely the deposition of Na from the supporting electrolyte. Although extending the potential window of the electrolyte, the deposition of the metal means no redox electrochemistry was seen. This suggests that the supporting electrolyte is not suitable for the system and that the $DmCo^+$ may still be a good redox couple in scR32. Further studies with different supporting electrolytes would need to be

performed in order to confirm if $DmCo^+$ could be used as an internal reference standard in scR32.

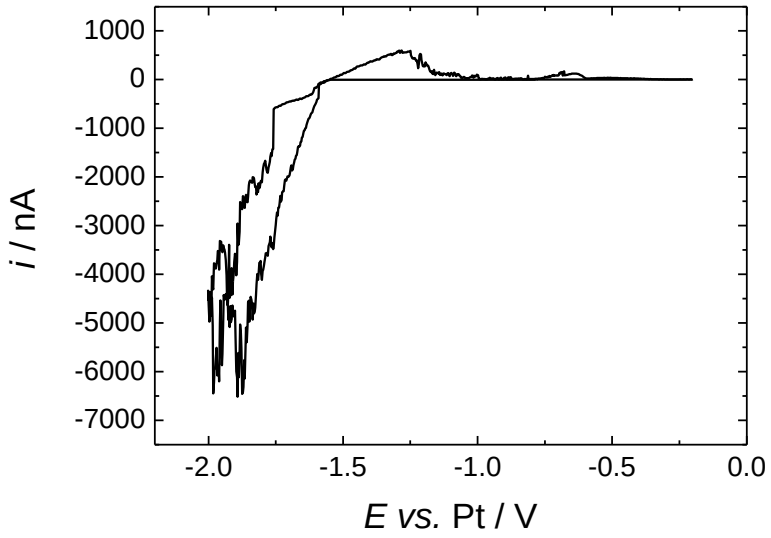

Figure 4.37. Cyclic voltammetry for a solution of 1.02 mM [DmCo][PF_6] with 20 mM [Na][BARF] in scR32 at 360 K, $p \approx 17.9$ MPa, $v = 10$ mV s^{-1}. The working electrode was a 50 µm Ø Pt disc. The reference and counter electrode were 0.5 mm Ø Pt wires.

4.4 Conclusions

This Chapter has demonstrated that decamethylferrocene can be used as good internal reference standards in both $scCO_2$/MeCN (15 wt%) and in scR32. A pre-conditioning step is required to gain reproducible voltammetry in $scCO_2$/MeCN (15 wt%). This film is attributed to the formation of a polyacetonitrile layer on the surface of the Pt electrode which is removed by cycling cathodically (-3 V). As scR32 does not require acetonitrile as a co-solvent to dissolve materials, the pre-conditioning step is not required to gain reproducible voltammetry in scR32. Results at microelectrodes, in both supercritical fluids, follow the limiting current equation against both concentration of decamethylferrocene and radii of microelectrode. Results at microelectrodes also show that decamethylferrocene exhibits a reversible 1 e^- transfer process as demonstrated by mass transport corrected Tafel plots. The diffusion coefficient measured at microelectrodes approximately doubles when going from $scCO_2$/MeCN (15 wt%, $D = 4.05 \times 10^{-5}$ cm^2 s^{-1}) to scR32 ($D = 8.33 \times 10^{-5}$ cm^2 s^{-1}).

This Chapter also demonstrated the use of baffle electrodes to dampen the intrinsic convection of supercritical fluids. Natural convection causes instability of the limiting current at microelectrodes and distorts the voltammetry obtained at macro electrodes. The limiting current

obtained at microelectrodes is analogous to that recorded in liquid conditions when a baffle is used. Results obtained in scR32 showed that the limiting current at a baffled microelectrode lies on the minimum plateau of the bare electrode, confirming this is where the limiting current should be measured at bare electrodes. When a baffle is used at a macro electrode in scR32, reproducible voltammetry is obtained with no signs of convection at scan rates of $\geq$ 400 mV/s.

This Chapter provided preliminary experiments performed with various cobaltocene complexes in supercritical fluids. Although voltammetry was obtained for all complexes tested, none of the complexes showed reproducible voltammetry. Experiments performed with cobaltocenium hexafluorophosphate in $scCO_2$/MeCN (15 wt%) showed a process occurring at microelectrodes, but the process recorded on each scan was not reproducible. Cobaltocenium hexafluorophosphate was also tested in scR32, although showing a reproducible process at macroelectrodes the peak current does not scale with scan rate as expected from theory. This could be due to oxygen bridging between the cobaltocene centres or due to an absorption of the cation ($CoCp_2^+$) and precipitation of the neutral complex ($CoCp_2$) on the electrode surface. Decamethylcobaltocenium hexafluorophosphate was tested with [Na][BARF] as supporting electrolyte, this showed that electrodeposition of Na occurs before any reduction potential of the cobaltocene was seen. Further work needs to be performed with cobaltocene complexes in supercritical fluids to determine if they could be used as internal reference standards.

Chapter 5: Studying Diffusion of Decamethylferrocene in Nanoporous Templated Electrodes

It has been shown in Chapters 3 and 4 that decamethylferrocene is a good internal reference standard in acetonitrile, $scCO_2$/MeCN (15 wt%) and scR32. As electrodeposition of metals in high aspect ratio nanopores (< 3 nm Ø, 50 µm length) is an important part of the SCFED project, it is important to understand the fundamental diffusion into these nanopores. It has been shown in the literature that it is possible to electrodeposit metals into these nanoporous templated electrodes[14,64], but there have been no studies of diffusion into nanopores under supercritical conditions. This Chapter details experiments performed using decamethylferrocene as a redox probe into anodic alumina oxide (AAO) templates. Two sizes of nanopores were studied, 13 nm Ø pores in MeCN and $scCO_2$/MeCN (15 wt%), 13 nm Ø and 55 nm Ø were studied in scR32. Construction of the electrodes has been outlined in Section 2.2.3. The two sizes of nanopores could help to further understanding of size restriction and pore wall effects. The results obtained can be compared between the supercritical systems and the diffusion coefficient obtained in each fluid could be directly compared.

5.1 Cyclic Voltammetry of Decamethylferrocene in Nanoporous Templated Electrodes in MeCN

Cyclic voltammograms recorded at various scan rates in a solution of MeCN containing 0.58 mM DMFc and 20 mM $[NBu_4^n][BF_4]$ for a 13 nm Ø AAO electrode at 294 K are displayed in Figure 5.1. The data collected from the voltammograms is presented in Table 5.1. As can be seen from Figure 5.1, cyclic voltammetry performed on the nanoporous electrode showed the presence of DMFc in solution through a reproducible redox process. This suggests that some proportion (possibly all) of the pores were open to solution. The ratio of the peak currents is close to unity for all scan rates, which is comparable to that determined at a Pt macro disc in MeCN which was unity for the same range of scan rates (Section 3.1). The peak potential difference was measured between 72 to 86 mV. This is larger than the expected value of 59 mV for a reversible 1 e^- process but it is again comparable to the peak potential separation measured at a Pt macro disc in MeCN (77 to 79 mV). The difference between the peak potential and the half wave potential was measured between 60 to 72 mV. This is close to the expected 59 mV potential separation and is again comparable to the values obtained at a Pt macro disc in MeCN. The half-wave potential was measured using Equation 5.4

$$E_{mid} = \frac{1}{2}(E_{\mathrm{pa}} + E_{pc}) \quad (5.4)$$

where E_{pa} and E_{pc} are the peak anodic and peak cathodic potentials respectively. The half-wave potential was measured to be E_{mid} = 0.14 V *vs.* Pt for a scan rate of 500 mV/s. This is in agreement with the half wave potential measured at Pt macro electrode in MeCN at 500 mV/s (E_{mid} = 0.15 V *vs.* Pt).

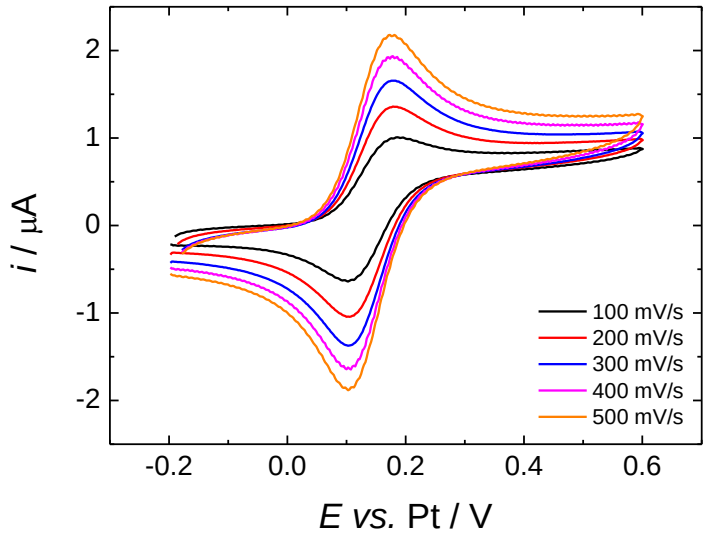

Figure 5.1. Cyclic voltammograms for a solution of 0.58 mM DMFc and 20 mM [NBu_4^n][BF_4] in MeCN at 294 K. The working electrode was a 13 nm Ø AAO electrode, the reference electrode was a 0.5 mm Ø Pt disc, the counter electrode was Pt gauze.

Table 5.1. Data obtained from cyclic voltammograms of 0.58 mM DMFc and 20 mM [NBu_4^n][BF_4] in MeCN at 294 K for various scan rates at a 13 nm Ø AAO electrode.

v / V s^{-1}	E_{pa} / mV ± 1	E_{pc} / mV ± 1	ΔE_{p} / mV ± 1	$E_{\mathrm{pa/2}}$ / mV ± 1	$E_{\mathrm{pc/2}}$ / mV ± 1	$E_{\mathrm{pa}} - E_{\mathrm{pa/2}}$ / mV ± 1	$E_{\mathrm{pc}} - E_{\mathrm{pc/2}}$ / mV ± 1	i_{pa} / µA ± 0.01	i_{pc} / µA ± 0.01	$i_{\mathrm{pa}}/i_{\mathrm{pc}}$ ± 0.01
0.1	188	102	86	116	166	72	64	1.00	1.07	0.93
0.2	180	104	76	115	168	65	64	1.35	1.46	0.92
0.3	176	104	72	114	165	62	61	1.66	1.77	0.94
0.4	176	104	72	113	164	63	60	1.92	2.02	0.95
0.5	174	102	72	110	165	64	63	2.18	2.24	0.97

Using Equation 3.3, the diffusion coefficient for DMFc into the nanopores could be calculated. To calculate the diffusion coefficient the electroactive area of gold was calculated. Equations 5.1 to 5.3 demonstrate how the area was calculated

$$A = \rho_{\mathrm{pore}} \times A_{\mathrm{pore}} \times A_{\mathrm{membrane}} \quad (5.1)$$

$$A = 1\,x\,10^{11}\ \text{pore cm}^{-2}\ \text{x}\ (1.33\ \text{x}\ 10^{-12}\ \pm 0.41\ \text{x}\ 10^{-12}\ \text{cm}^2\ \text{pore}^{-1})\ \text{x}\ 0.07\ \text{cm}^2 \quad (5.2)$$

$$A = 0.009\ \pm 0.003\ \text{cm}^2 \quad (5.3)$$

where ρ_{pore} represents the pore density, A_{pore} is the area of the pore (area of a circle) and the radius was quoted by the supplier (r = 6.5 x 10^{-7} ± 1 x 10^{-7} cm), $A_{membrane}$ is the area of gold on which the template is mounted e.g. the area of a square. The diffusion coefficient was calculated from the peak anodic and peak cathodic current at 500 mV/s and was calculated to be D = 0.5 x 10^{-5} ± 0.4 x 10^{-5} cm^2 s^{-1} and D = 0.5 x 10^{-5} ± 0.4 x 10^{-5} cm^2 s^{-1} respectively. The large error associated with the diffusion coefficient comes from the large error associated with the electroactive area. The error in the area comes from the error associated with the pore diameter. The error associated with the area is unlikely to be this high, because if the pore diameter is changed this will affect the porosity (pore cm^{-2}), thus if the diameter of the pore is larger or smaller it will mean the porosity value will be lower or higher depending. Multiple repeats on separate electrodes (from independent experiments) give similar values for the diffusion coefficient, indicating that the electroactive area is not changing dramatically between membranes. These values of the diffusion coefficient are lower than those observed for DMFc in liquid MeCN at Pt macro electrodes (D = 1.20 x 10^{-5} cm^2 s^1). To confirm that the concentration of the system was as intended (0.58 mM), cyclic voltammetry was performed at a microdisc and the diffusion coefficient was calculated. The diffusion coefficient determined at the 25 µm Ø Pt disc was calculated to be D = 1.80 x 10^{-5} cm^2 s^{-1}, this is in complete agreement with the diffusion coefficient calculated at the same size electrode in liquid MeCN in Section 3.1. This suggests that the concentration of the system was 0.58 mM as intended. To confirm the diffusion coefficient, Randles-Sevčik analysis was performed. The dependence of the peak current with respect to $v^{1/2}$ for the 13 nm Ø AAO electrode is presented in Figure 5.2.

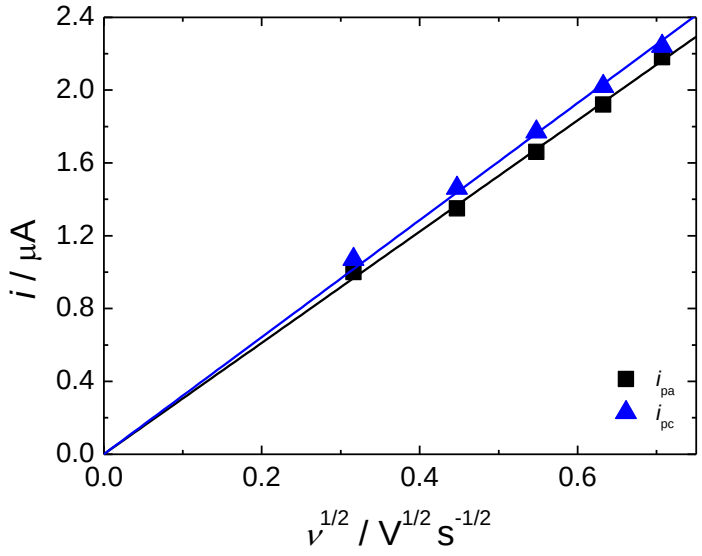

Figure 5.2. The dependence of the peak currents on the scan rate for cyclic voltammetry of 0.5 mM DMFc and 20 mM [NBu_4^n][BF_4] in MeCN at 294 K at a 13 nm Ø AAO electrode.

As can be seen from Figure 5.2, the linear fits extrapolate to the origin for both the peak anodic and peak cathodic currents. The diffusion coefficients calculated from the peak anodic and peak cathodic current was D = 0.5 x 10^{-5} ± 0.4 x 10^{-5} cm^2 s^{-1} and D = 0.5 x 10^{-5} ± 0.4 x 10^{-5} cm^2 s^{-1} respectively. These values are in complete agreement with the diffusion coefficients calculated from voltammetry. It has been shown that DMFc is a good internal reference standard for nanoporous templated electrode in MeCN and is suitable for use in supercritical systems.

5.2 Cyclic Voltammetry of Decamethylferrocene in Nanoporous Templated Electrodes in $scCO_2$/MeCN

Cyclic voltammograms performed in a solution of $scCO_2$/MeCN (15 wt%) containing 0.638 mM DMFc and 20 mM [NBu_4^n][BF_4] for a 13 nm Ø AAO electrode (A = 0.016 ± 0.005 cm^2, $A_{membrane}$ = 0.12 cm^2) at 309 K and ≈ 17.2 MPa, are displayed in Figure 5.3. The data obtained from the voltammetry for scan rates of 100, 200 and 500 mV/s are displayed in Table 5.2. As can be seen from Figure 5.3, the voltammetry obtained at the AAO electrode under supercritical conditions is vastly different to that obtained in MeCN (Figure 5.1). At slower scan rates, e.g. ≤ 50 mV/s, there is a sigmoidal wave response, similar to that seen at microelectrodes which gives a diffusion limited current on the anodic scan. At faster scan rates, e.g. ≥ 100 mV/s, there is a peak current response on the anodic scan. However, for the cathodic scan a peak current response is seen for all scan rates. This suggests that the

diffusion into nanopores under supercritical conditions is different to that observed in acetonitrile. The reason for the response seen at high and slow scan rate will be discussed later. It can also be seen in Figure 5.3 that the effects of *iR* drop are significant. The peak to peak potential separation increases from 283 to 351 mV between scan rates of 100 to 500 mV/s. These values are closely comparable to the peak to peak potential separation measured at a gold disc in $scCO_2$/MeCN (15 wt%) for a similar concentration of DMFc. The difference between the half-wave and peak potentials was measured between 137 and 167 mV. These values are comparable to those obtained at a macroelectrode in $scCO_2$/MeCN (15 wt%). The half-wave potential was measured using Equation 5.4 using a scan rate of 500 mV/s for the 13 nm Ø AAO electrode and was found to be E_{mid} = 0.082 V *vs.* Pt. This is in comparison to E_{mid} = 0.17 V *vs.* Pt measured at the macro electrode in $scCO_2$/MeCN (15 wt%) and E_{mid} = 0.14 V *vs.* Pt measured at the 13 nm Ø AAO in MeCN, this shift is most likely due to a shift in the Pt quasi electrode. The composition of the fluid in the nanopores under supercritical conditions is unknown at this time. The composition in the pores could be $MeCN_{(l)}$, $CO_{2(l)}$, $scCO_2$ or $scCO_2$/MeCN (15 wt%). The voltammetry obtained in Figure 5.3 compared to Figure 5.1 suggests that the composition in the pores is not $MeCN_{(l)}$. It is also reasonable to assume that the composition is not $CO_{2(l)}$ or $scCO_2$ as the materials would be insoluble and no electrochemistry would be observed. As the peak to peak potential separation and difference between the half wave and peak potentials are comparable to that seen at a bare gold disc, it is reasonable to assume that the fluid in the pores is $scCO_2$/MeCN (15 wt%).

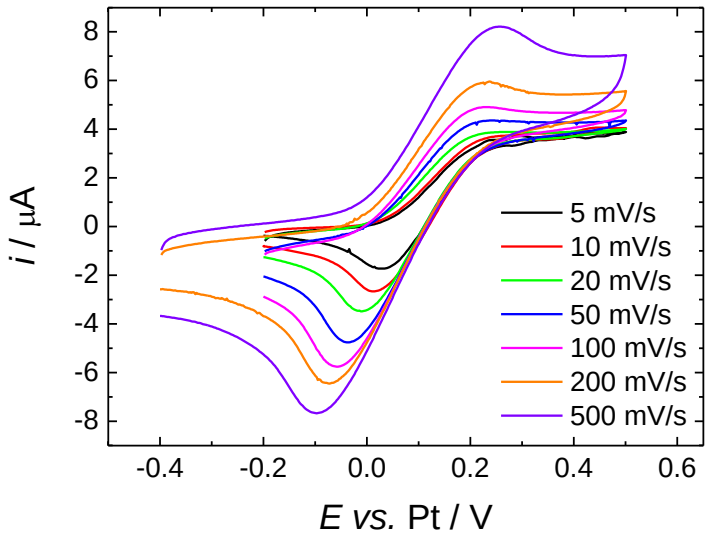

Figure 5.3. Cyclic voltammograms for a solution of 0.638 mM DMFc and 20 mM $[NBu_4^n][BF_4]$ in $scCO_2$/MeCN (15 wt%) at 309 K, $p \approx 17.2$ MPa. The working electrode was a 13 nm Ø AAO electrode (A = 0.016 cm^2), the reference and counter electrode were 0.5 mm Ø Pt wires.

Table 5.2. Data obtained from cyclic voltammograms of 0.638 mM DMFc and 20 mM $[NBu_4^n][BF_4]$ in $scCO_2$/MeCN (15 wt%) at 309 K and $p \approx 17.2$ MPa for various scan rates at a 13 nm Ø AAO electrode ($A = 0.016$ cm^2).

v / V s^{-1}	E_{pa} / mV ± 1	E_{pc} / mV ± 1	ΔE_p / mV ± 1	$E_{pa/2}$ / mV ± 1	$E_{pc/2}$ / mV ± 1	$E_{pa} - E_{pa/2}$ / mV ± 1	$E_{pc} - E_{pc/2}$ / mV ± 1	i_{pa} / µA ± 0.01	i_{pc} / µA ± 0.01	i_{pa}/i_{pc} ± 0.01
0.1	225	-58	283	88	86	137	144	5.45	8.25	0.66
0.2	229	-71	300	91	81	138	152	6.05	9.04	0.67
0.5	257	-94	351	92	73	165	167	8.22	9.78	0.84

From the cyclic voltammetry and using Equation 3.3 in Chapter 3, the diffusion coefficient for the anodic and cathodic peak current at 500 mV/s for an electroactive area of 0.016 ± 0.005 cm^2 was determined to be $D = 1.9 \times 10^{-5} \pm 1.4 \times 10^{-5}$ cm^2 s^{-1} and $D = 2.6 \times 10^{-5} \pm 1.7 \times 10^{-5}$ cm^2 s^{-1} respectively. These values of the diffusion coefficient are comparable with those recorded in liquid MeCN at the same sized AAO electrode. The diffusion coefficients are also lower than those recorded in $scCO_2$/MeCN (15 wt%) at microelectrodes in Section 4.2.2. To determine the diffusion coefficient at scan rates of ≤ 50 mV/s, the system must be modelled by steady state 1D diffusion down the pore with a well-mixed solution outside the template, as the plateau suggests that the concentration drops uniformly across the length of the pore. Equation 5.4 shows how the current response relates to the diffusion coefficient with steady state 1D diffusion down the pore with a well-mixed bulk outside the pore

$$i = \frac{nFADc_{\text{bulk}}}{l} \tag{5.4}$$

where l is the length of the pore (e.g. 50 µm), all other terms have been described in Chapter 3. Using 10 mV/s as an example, the limiting current was determined to be 3.84 µA. From this value the diffusion coefficient was determined to be $D = 2.0 \times 10^{-5} \pm 2.2 \times 10^{-5}$ cm^2 s^{-1}, this is in good agreement with the diffusion coefficient calculated at 500 mV/s.

The peak anodic current response at high scan rates is due to the size of diffusion layer probed. At slow scan rates, the diffusion layer probed into solution is much larger than at high scan rates where a small diffusion layer is established. Equations 5.5 to 5.6 describe how the diffusion layer thickness can be determined[113]

$$\delta \approx \sqrt{Dt} \tag{5.5}$$

$$\delta \approx \sqrt{D\ x\ \frac{RT}{Fv}} \tag{5.6}$$

where δ is the diffusion layer thickness in units of cm, all other terms have already been described in Chapter 3. As can be seen from Equations 5.5 and 5.6 the diffusion layer thickness

can be estimated from the diffusion coefficient and the constants associated. For example, using Equation 5.6, taking the scan rate at 10 mV/s (Figure 5.4) and a diffusion coefficient of 1.95 x 10^{-5} cm^2 s^{-1}, the diffusion layer thickness is estimated to be δ = 72 x 10^{-4} cm, which is 72 µm. Using the same Equation and taking a scan rate of 500 mV/s (Figure 5.5) with a diffusion coefficient of 1.86 x 10^{-5} cm^2 s^{-1}, the diffusion layer thickness is estimated to be δ = 10 x 10^{-4} cm, which is 10 µm. As stated previously, the length of the AAO pores is 50 µm. From these two values it can be seen that for low scan rates such as 10 mV/s, the diffusion layer extends the length of the pore and into the bulk. Whereas at higher scan rates such as 500 mV/s, the diffusion layer is much shorter and only extends 1/5th of the pore length, thus the diffusion profile only takes place within the pore. As the diffusion layer extends further into solution at long times, the response seen is a sigmoidal wave giving a limiting current response with a small amount of convection seen. As the distance between the pores is sufficiently small, a peak current response should be seen for all scan rates in a stationary solution due to overlapping diffusion profiles at the opening of the pore[90,94,95]. Due to the convective nature of supercritical fluids, the opening of the pores experience a well-mixed bulk solution, thus overlapping diffusion layers cannot occur. This causes each nanopore to act as an individual nanoelectrode at long time scales leading to sigmoidal response. This is in contrast to short times where the diffusion layer is much shorter and gives a peak current response for the anodic scan. The peak shape seen is due to the linear diffusion within the nanopore and has also been observed in the literature[95].

As mentioned previously and can be seen from Figure 5.3, a cathodic peak current can be seen for all scan rates. This could be due to a number of reasons. The first reason could be due to a partitioning of material into the pores. This again is unlikely as taking the number of pores (1.2 x 10^{10}), their combined volume (7.96 x 10^{-5} cm^3) and the concentration of the bulk (0.638 x 10^{-6} mol cm^{-3}), leads to a charge that is 1/5th of the charge determined from the CV, the charge from the CV is too large to just be $DMFc^+$ in the pore at bulk concentration. The second reason, a triple ion could be forming between the $DMFc^+$ and the BF_4^- anion. This again is unlikely as the size of the triple ion would be considerably smaller than the overall size of the pore, the triple ion formation would not hinder its diffusion out of the pore. The third reason, the $DMFc^+$ could be precipitating at the bottom of the pore leading to the peak current seen. This is again unlikely as the CVs are very reproducible, more than 10 scans can be performed without a change in the limiting current. If a precipitate were forming at the bottom of the pore it would lead to a passivation of the electrode surface, which would in turn, lead to a lower limiting current on subsequent scans. The fourth reason could be $DMFc^+$ interacting with the pore wall leading to adsorption as build-up of material. Calculating the amount of material from the charge for the cathodic peak (2.75 x 10^{-10} mol) suggests it is possible for a monolayer to form.

To calculate the number of moles that would cover the walls of the cylindrical pores, the surface area of the combined pores (245 cm^2) was calculated. The hydrodynamic radii of ferrocene in acetonitrile is quoted by Olsen and Tallman[59] as 0.28 nm. Taking this value and assuming the ferrocene is spherical, the area for one molecule was calculated (2.46 x 10^{-15} cm^2), this leads to an estimate of the total number of ferrocene molecules needed to cover the pore walls (9.96 x 10^{16}). This can then be converted to a value of 1.65 x 10^{-7} mol through Avogadro's number. This value is 600x the total amount calculated from the CV; this suggests that an adsorbed layer could be a possible cause of the peak. This means that the $DMFc^+$ will be adsorbed along a length of the pore wall; in this case the length will be around 31 nm. As this effect is not seen at a 55 nm Ø AAO electrode (see Section 5.3), it suggests that the constriction and smaller size of the pore play a role in the effect. As the DMFc is oxidised to $DMFc^+$, the small size of the pore could restrict its diffusion from the electrode surface due to the charged pore wall, which causes $DMFc^+$ to adsorb. This adsorbed $DMFc^+$ could be the cause of the additional current and peak seen in the voltammetry. These calculations do not prove that an absorbed layer is formed but it is clearly a possibility.

The last explanation could be due to a drastic change in diffusion coefficient between the oxidised and reduced species. Large changes in the diffusion coefficient (1 – 2 orders of magnitude difference) have been reported in the literature leading to similar shaped voltammetry[114-116]. Buzzeo *et al*[116]. reported on the voltammetry of oxygen in room temperature ionic liquids showing steady state and transient behaviour in the same cyclic voltammogram which was the result of widely different diffusion coefficients of oxygen and superoxide. The paper describes the higher viscosity of a particular ionic liquid which gives a two order of magnitude difference in the diffusion coefficients of oxygen and superoxide (D_{O2} = 1.48 x 10^{-10} m^2 s^{-1}, $D_{O2^{\bullet-}}$ = 4.66 x 10^{-12} m^2 s^{-1})[116]. The voltammetry recorded showed a steady state transient on the forward scan and a peak current on the reverse scan, the peak current was due to the lower diffusion coefficient of the superoxide species[116]. The difference in diffusion coefficient could be an explanation for the voltammetry seen in this system as similar voltammetry is seen. The same effect is not seen in the 55 nm Ø AAO in scR32, this will be further discussed in Section 5.3. If the wall of the AAO has a partial charge associated with it, the pore could have its own double layer. This build-up of the double layer could be responsible for trapping the $DMFc^+$ leading to it diffusing more slowly out of the pore and giving it a drastically different diffusion coefficient compared to the DMFc species. Assuming the dielectric constant of $scCO_2$/MeCN (15 wt%) is ε = 8 and T = 309 K we can estimate the Debye length that will be associated with the charged pore wall for varying concentrations of supporting electrolyte. Varying the concentration of the supporting electrolyte will change the extent of ion pairing that can occur[60]. It has also been shown that there is ion pairing in the

electrolyte from conductivity studies performed with $[NBu_4^n][BF_4]$ in $scCO_2$/MeCN[46], so it is likely that the concentration of free ions is less than 20 mM. Taking a concentration of 20 mM the Debye length is estimated to be 0.7 nm, for 5 mM the Debye length is estimated to be 1.4 nm and for 1 mM the Debye length is estimated to be 3.12 nm. If we assume that the Debye length will be 3.12 nm, this means that this length is experienced around the entire pore. This will reduce the pore diameter from 13 nm to 7 nm. If the double layer also has an interaction with the $DMFc^+$, this could lead to a restriction in its diffusion out of the pore leading to a drastic change in diffusion coefficient. This will be discussed further in Section 5.3 where a comparison of pore diameters will be discussed.

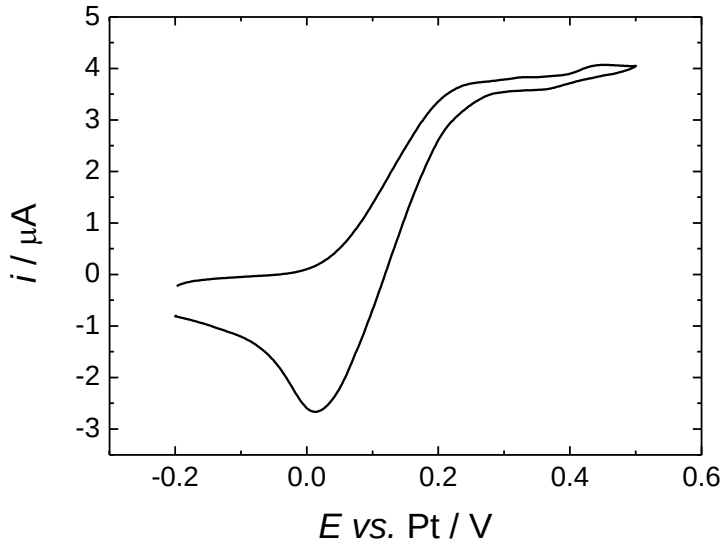

Figure 5.4. Cyclic voltammetry for a solution of 0.638 mM and 20 mM $[NBu_4^n][BF_4]$ in $scCO_2$/MeCN (15 wt%) at 309 K, $p \approx 17.2$ MPa, $v = 10$ mV s^{-1}. The working electrode was a 13 nm Ø AAO electrode ($A = 0.016$ cm^2), the reference and counter electrode were 0.5 mm Ø Pt wires.

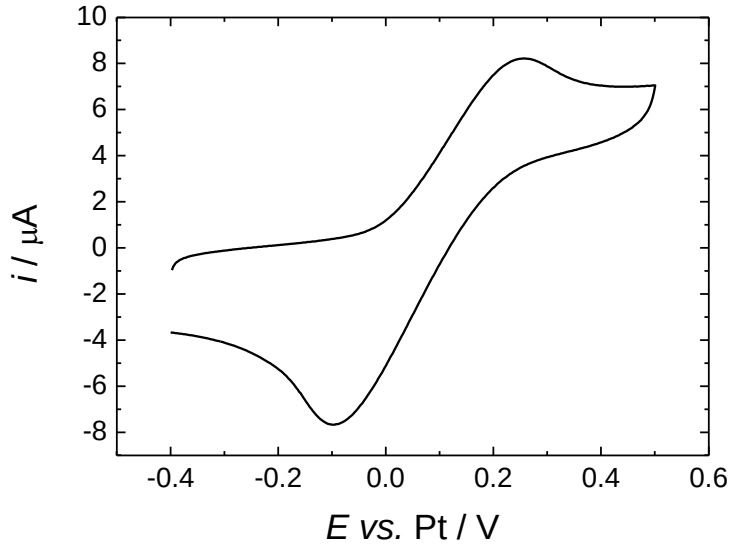

Figure 5.5. The solution, temperature, operating pressure and electrodes are described in Figure 5.4, v = 500 mV s^{-1}.

From cyclic voltammetry it is possible to estimate the area of an electrode from the double layer charging current. Using the double layer charging current, in this case the current recorded at the end of the anodic scan and the start of the cathodic scan (e.g. 0.45 V for Figures 5.4 and 5.5 respectively), the capacitance of an electrode can be determined. The end of the cathodic scan cannot be taken due to the additional effect of the $DmFc^+$ peak seen in the voltammetry. Taking an electrode with a known area and determining the capacitance associated with it, one can determine the area of an unknown electrode. Equations 5.5 to 5.7 demonstrate how the unknown area can be determined

$$C = \frac{i_{\mathrm{dl}}}{v} \tag{5.5}$$

$$C_{\mathrm{A}} = \frac{C}{A} \tag{5.6}$$

$$\text{Unknown Area} = \frac{C_{\mathrm{U}}}{C_{\mathrm{A}}} \tag{5.7}$$

where C is the capacitance in units of Farad, i_{dl} is the double layer charging current in units of Amp, v is the scan rate in units of V s^{-1}, A is the area of the working electrode, C_{A} is the capacitance at the electrode of known area in units of F cm^{-2} and C_{U} is the capacitance at the electrode of unknown area (the 13 nm Ø AAO electrode in this case). The electrode area estimated for the 13 nm Ø AAO electrode for 200 and 500 mV/s (using the 0.5 mm Ø Au used in $scCO_2$/MeCN (15 wt%) as standard, Section 4.1.5), are displayed in Table 5.3.

Table 5.3. Estimation of the active working area of a 13 nm Ø AAO (A = 0.016 cm^2) electrode using the capacitance values determined by cyclic voltammetry (0.45 V) at varying scan rates. The solution was 0.638 mM DMFc and 20 mM [NBu_4^n][BF_4] in scCO_2/MeCN (15 wt%) at 309 K and $p \approx$ 17.2 MPa. The reference and counter electrodes were 0.5 mm Ø mm Pt discs.

v / V s^{-1}	i / µA	C_U / µF	C_A / µF	A / cm^2 (standard)	C_A / mF cm^{-2}	A / cm^2 (AAO electrode)
0.2	1.19	5.95	0.67	0.00196	0.34	0.017
0.5	2.26	4.52	0.50	0.00196	0.26	0.018
Mean						**0.0175**

As can be seen from Table 5.3 the average area for the 13 nm Ø AAO estimated from the capacitance is A = 0.0175 cm^2. This is very close to the area calculated from Equations 5.1 to 5.3. This value of the area is reasonable given the experimental conditions and is in reasonable agreement with the area calculated from Equations 5.1 to 5.3.

To test if the anodic and cathodic peak currents followed Randles-Sevčik analysis, the peak current was plotted against $v^{1/2}$ and is displayed in Figure 5.6. As can be seen from Figure 5.6 although fitting linearly neither the anodic or cathodic peak currents tend toward the origin. This suggests that Randles-Sevčik analysis is not applicable to the templated electrodes. Although not applicable in this case, the diffusion coefficients were estimated for the anodic and cathodic peak current from the Randles-Sevčik plot. The diffusion coefficient for the anodic and cathodic peak currents were estimated to be D = 7.3 x 10^{-6} cm^2 s^{-1} and D = 1.9 x 10^{-6} cm^2 s^{-1} respectively. These values are lower than those determined by voltammetry. It is interesting to note that the diffusion coefficient for the cathodic peak current is much lower than that determined for the anodic peak current. As DMFc has been shown to be a good redox couple for investigating the diffusion into nanopores, similar experiments were performed in scR32 for comparison.

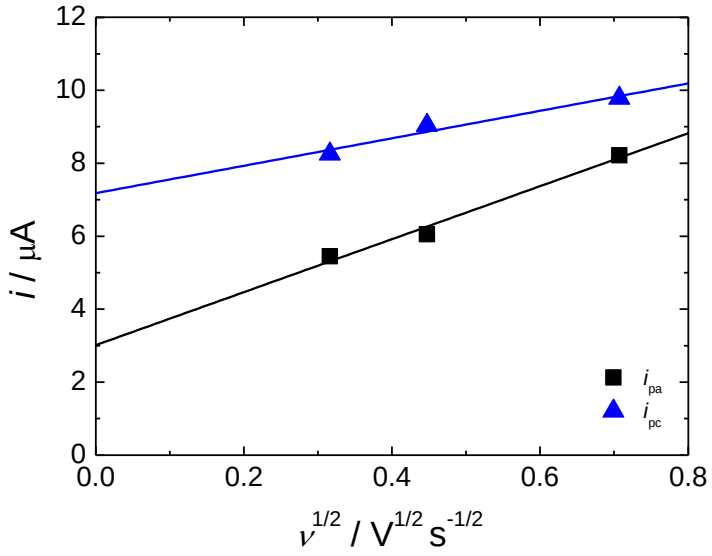

Figure 5.6. The dependence of the peak currents on the scan rate for cyclic voltammetry of 0.638 mM DMFc and 20 mM [NBu_4^n][BF_4] in $scCO_2$/MeCN (15 wt%) at 309 K and $p \approx 17.2$ MPa at a 13 nm Ø AAO electrode.

5.3 Cyclic Voltammetry of Decamethylferrocene in Nanoporous Templated Electrodes in scR32

Cyclic voltammograms recorded at various scan rates in a solution of scR32 containing 0.992 mM DMFc and 20 mM [NBu_4^n][BF_4] for a 13 nm (A = 0.0293 ± 0.009 cm^2, $A_{membrane}$ = 0.22 cm^2) and 55 nm Ø (A = 0.020 ± 0.004 cm^2, $A_{membrane}$ = 0.14 cm^2) AAO electrode at 360 K and ≈ 17.8 MPa are displayed in Figures 5.7 and 5.8 respectively. The data obtained from the voltammograms for the 13 nm and 55 nm Ø AAO are presented in Tables 5.4 and 5.5 respectively. As can be seen from Figure 5.7, the voltammetry obtained in scR32 is comparable to that obtained in $scCO_2$/MeCN (15 wt%). At low scan rates, e.g. ≤ 100 mV/s, a similar sigmoidal wave response is seen with a limiting current observed. At higher scan rates, e.g. ≥ 200 mV/s, a peak current is observed on the anodic sweep. A peak cathodic current is seen for all scan rates at the 13 nm Ø AAO electrode, which is analogous to $scCO_2$/MeCN (15 wt%). A similar response is seen in Figure 5.8 at the 55 nm Ø AAO electrode for the anodic scans. At low scan rates, a sigmoidal wave response is seen which becomes a peak anodic current at scan rates of 200 mV/s. However, a peak cathodic current is not observed until a scan rate of 200 mV/s is used. There are two reasons why this effect could be seen. The first reason is that the larger diameter and area of the pore means that the $DMFc^+$ does not adsorb close to the bottom of the pore wall, but diffuses away from the electrode surface and adsorbs further up. This means a peak current would not be seen on the cathodic scan. The

second reason could be that the diameter of the pores is sufficiently big that the Debye length of 3.12 nm surrounding the pore does not hinder the diffusion of $DMFc^+$ to the same extent as the smaller pore. Further experiments would need to be performed to test this theory, the first would be to perform experiments with pore diameters that are between 13 and 55 nm Ø. This would require that these size nanopores can be purchased from the same company that supplied the original AAO electrodes. The second, would be to change the concentration of supporting electrolyte to see what effect this has on the voltammetry in 13 nm Ø AAO pores. This change in supporting electrolyte should change any double layer length giving a different response if the theory is correct. The third, modification of the pore wall could remove the partial charge associated with the pore wall, which would in turn remove the double layer or adsorption effect. Although, this could add further complications, there could be an interaction or reaction between the DMFc and the modified wall. The last would be to use a positively charged redox probe to see if it experiences the same behaviour seen for $DMFc^+$, as both explanations assume that the pore wall is carrying a negative charge. Although, all efforts to use a positively charged redox probe (cobaltocenium) have thus far, proved unsuccessful (see Chapter 4).

As can also be seen from Figures 5.7 and 5.8, the *iR* drop is significantly lower in scR32 when compared to $scCO_2$/MeCN (15 wt%). This is also reflected in the peak to peak potential separation which was measured to be between 156 to 181 mV and 123 to 148 mV for the 13 nm and 55 nm Ø AAO electrodes respectively. This is in comparison to 283 to 351 mV for the 13 nm Ø AAO electrode in $scCO_2$/MeCN (15 wt%). The difference between the half wave and peak potentials was measured between 95 to 115 mV and 87 to 105 mV for the 13 nm and 55 nm Ø AAO electrodes respectively. The values obtained at the 13 nm Ø AAO electrode are much lower than those obtained in $scCO_2$/MeCN (15 wt%). The values are however comparable to the values obtained at a baffled macro electrode in scR32, they are also lower than the values obtained at a macro electrode in $scCO_2$/MeCN (15 wt%). This again suggests that the uncompensated solution resistance is lower in scR32 when compared to $scCO_2$/MeCN (15 wt%). The half-wave potentials were again measured for the 13 and 55 nm Ø AAO electrodes at 500 mV/s and calculated to be E_{mid} = 0.09 V *vs.* Pt and E_{mid} = 0.15 V *vs.* Pt respectively. The half-wave potential measured at the baffled 1 mm Ø Au electrode in the same solution was found to be E_{mid} = 0.16 V *vs.* Pt. The half-wave values measured are in agreement with that measured at the baffled electrode and the minimal shifting seen at the 13 nm Ø AAO electrode is most likely due to a shift in the reference electrode. The ratio of the peak currents at the 13 nm Ø AAO electrode was measured between 0.52 to 0.81, the same ratio was measured at the 13 nm Ø AAO in $scCO_2$/MeCN (15 wt%). However, the

ratio of the peak currents at the 55 nm Ø AAO was measured as unity across all scan rates; this is again comparable to the ratio of peak current measured at a baffled macro electrode in scR32.

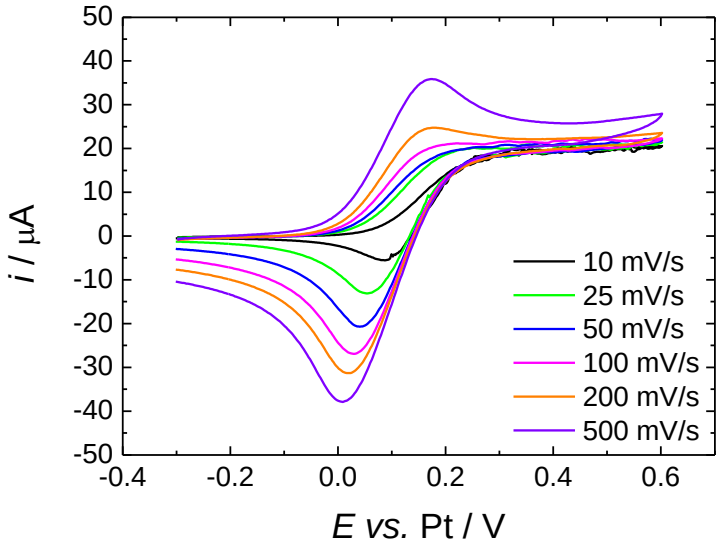

Figure 5.7. Cyclic voltammograms for a solution of 0.992 mM DMFc and 20 mM [NBu_4^n][BF_4] in scR32 at 360 K, $p \approx 17.8$ MPa. The working electrode was a 13 nm Ø AAO electrode, the reference and counter electrode were 0.5 mm Ø Pt wires.

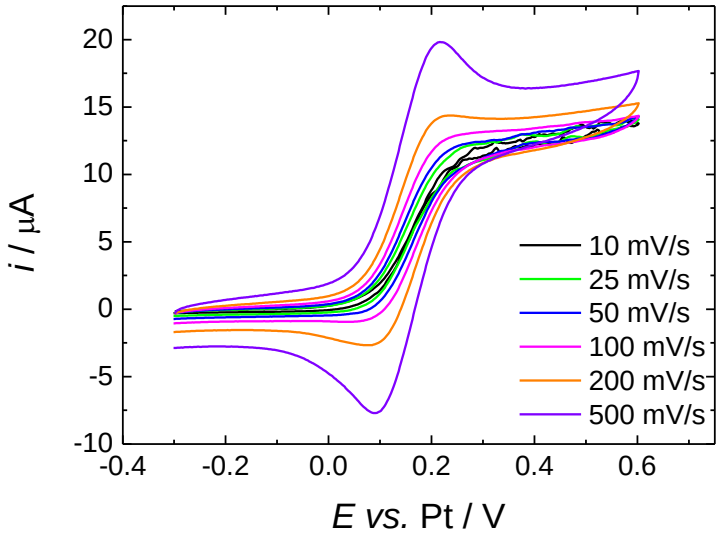

Figure 5.8. The solution, temperature, operating pressure, reference and counter electrode have been described in Figure 5.7. The working electrode was a 55 nm Ø AAO electrode.

Table 5.4. Data obtained from cyclic voltammograms of 0.992 mM DMFc and 20 mM $[NBu_4^n][BF_4]$ in scR32 at 360 K and $p \approx 17.8$ MPa for various scan rates at a 13 nm Ø AAO electrode.

v / V s^{-1}	E_{pa} / mV ± 1	E_{pc} / mV ± 1	ΔE_p / mV ± 1	$E_{pa/2}$ / mV ± 1	$E_{pc/2}$ / mV ± 1	$E_{pa} - E_{pa/2}$ / mV ± 1	$E_{pc} - E_{pc/2}$ / mV ± 1	i_{pa} / µA ± 0.1	i_{pc} / µA ± 0.1	i_{pa}/i_{pc} ± 0.01
0.2	174	18	156	74	123	100	105	24.8	47.9	0.52
0.3	173	16	157	74	118	99	102	28.9	48.8	0.59
0.4	169	10	159	74	117	95	107	32.2	51.1	0.63
0.5	173	8	165	73	120	100	112	35.8	55.2	0.65
0.6	175	5	170	72	114	103	109	39.3	56.5	0.70
0.7	174	6	168	74	116	100	110	42.3	58.8	0.72
0.8	180	1	179	72	115	108	114	44.9	59.1	0.76
0.9	177	1	176	75	116	102	115	47.1	60.5	0.78
1.0	184	3	181	76	114	108	111	50.0	62.1	0.81

Table 5.5. The solution, temperature and operating pressure are described in Table 5.3. The working electrode was a 55 nm Ø AAO electrode.

v / V s^{-1}	E_{pa} / mV ± 1	E_{pc} / mV ± 1	ΔE_p / mV ± 1	$E_{pa/2}$ / mV ± 1	$E_{pc/2}$ / mV ± 1	$E_{pa} - E_{pa/2}$ / mV ± 1	$E_{pc} - E_{pc/2}$ / mV ± 1	i_{pa} / µA ± 0.1	i_{pc} / µA ± 0.1	i_{pa}/i_{pc} ± 0.01
0.2	229	81	148	124	182	105	101	13.6	12.8	1.06
0.3	220	91	129	120	181	100	90	15.0	13.9	1.08
0.4	214	91	123	118	178	96	87	16.6	15.0	1.11
0.5	214	89	125	117	178	97	89	18.1	16.7	1.08
0.6	218	87	131	116	180	102	93	19.6	18.2	1.08
0.7	220	87	133	116	180	104	93	21.2	19.5	1.09
0.8	220	86	134	118	178	102	92	21.9	20.4	1.07
0.9	222	85	137	117	176	105	91	23.4	21.8	1.07
1.0	222	83	139	117	176	105	93	24.6	22.6	1.09

Taking the cyclic voltammetry and using Equation 3.3 in Chapter 3, the diffusion coefficient for the 13 nm Ø AAO electrode from the anodic and cathodic peak current at 500 mV/s for an electroactive area of 0.0293 cm^2 was determined to be $D = 5.1 \times 10^{-5} \pm 3.8 \times 10^{-5}$ cm^2 s^{-1} and $D = 1.2 \times 10^{-4} \pm 0.9 \times 10^{-4}$ cm^2 s^{-1} respectively. The large diffusion coefficient calculated for the cathodic peak current is most likely due to the added complication of the $DMFc^+$ species. The same calculation for the diffusion coefficients was performed for the 55 nm Ø AAO electrode from the anodic and cathodic peak current at 500 mV/s for an electroactive area of 0.020 cm^2, $D = 2.8 \times 10^{-5} \pm 1.2 \times 10^{-5}$ cm^2 s^{-1} and $D = 2.4 \times 10^{-5} \pm 1.0 \times 10^{-5}$ cm^2 s^{-1} respectively. The diffusion coefficients measured at the 13 nm Ø AAO electrode are much larger (nearly an order of magnitude larger for the cathodic peak) than those measured in $scCO_2$/MeCN (15 wt%), but are comparable to those measured at microdiscs in scR32. This is similar to the diffusion coefficients measured at microelectrodes in different supercritical fluids which nearly doubles when changing from $scCO_2$/MeCN (15 wt%) to scR32. However, the diffusion coefficients measured at the 55 nm Ø AAO electrode are comparable to those measured in $scCO_2$/MeCN (15 wt%) at the 13 nm Ø AAO electrode and smaller than those measured at the

same size nanopores in scR32. Using Equation 5.4, the diffusion coefficient was again calculated at 10 mV/s for the 13 nm and 55 nm Ø AAO electrodes, the length of the pore is the same as stated in Section 5.2. The diffusion coefficient for the 13 nm and 55 nm Ø AAO was determined to be D = 3.6 x 10^{-5} ± 1.2 x 10^{-5} cm^2 s^{-1} and D = 3.6 x 10^{-5} ± 0.8 x 10^{-5} cm^2 s^{-1} respectively. The diffusion coefficients are the same for both sizes of nanopores with different electroactive areas. This suggests that the diffusion from the bulk over the length of the pore is the same at slow scan rates. This also suggests that the added complication of the cathodic peak in 13 nm Ø AAO means the diffusion coefficient cannot be calculated using this method for the cathodic scan. Figures 5.9 and 5.10 compare the current density recorded at the 13 nm and 55 nm Ø AAO electrodes at 10 mV/s and 500 mV/s respectively.

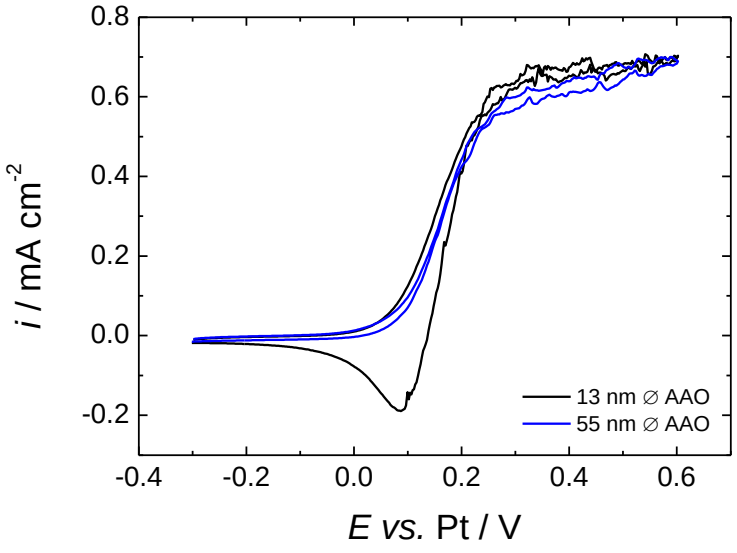

Figure 5.9. Comparison of the current density recorded at a 13 nm Ø (Black line) and 55 nm Ø (Blue line) AAO electrode at scan rate of 10 mV s^{-1}. The solution was 0.992 mM DMFc and 20 mM [NBu_4^n][BF_4] in scR32 at 360 K and p ≈ 17.8 MPa. The reference and counter electrode were 0.5 mm Ø Pt wires.

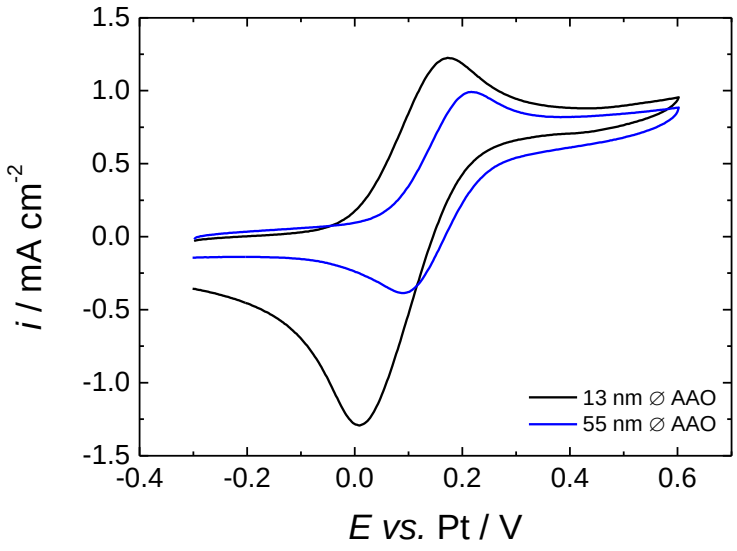

Figure 5.10. Comparison of the current density recorded at a 13 nm Ø (Black line) and 55 nm Ø (Blue line) AAO electrode at scan rate of 500 mV s^{-1}. The solution, temperature, operating pressure, reference and counter electrode have been described in Figure 5.9.

It was shown in Section 5.2 that the electroactive area of the AAO electrodes can be estimated from the capacitance measured by the double layer charging current (again taken at 0.45 V in the voltammetry in this case) at the templated electrode and from a known standard electrode. The known standard used in this case was a baffled 1 mm Ø Au electrode which was used in the same solution as the templated electrodes. The area of the templated electrodes was calculated using Equations 5.4 to 5.6. The values determined for the 13 nm and 55 nm Ø AAO electrodes at scan rates of 500, 700 and 1000 mV/s are displayed in Tables 5.6 and 5.7 respectively.

Table 5.6. Estimation of the active working area of a 13 nm Ø AAO electrode using the capacitance values determined by cyclic voltammetry (0.45 V) at varying scan rates. The solution was 0.992 mM DMFc and 20 mM [NBu_4^n][BF_4] in scR32 at 360 K and $p \approx 17.8$ MPa. The reference and counter electrodes were 0.5 mm Ø mm Pt discs.

v / V s^{-1}	i / µA	C_U / µF	C_A / µF	A / cm^2 (standard)	C_A / mF cm^{-2}	A / cm^2 (AAO electrode)
0.5	4.74	9.48	0.73	0.00785	0.09	0.10
0.7	6.58	9.40	0.97	0.00785	0.12	0.08
1.0	7.58	7.58	1.60	0.00785	0.20	0.04
Mean						**0.07**

Table 5.7. Estimation of the active working area of a 55 nm Ø AAO electrode using the capacitance values determined by cyclic voltammetry (0.45 V) at varying scan rates. The solution was 0.992 mM DMFc and 20 mM [NBu_4^n][BF_4] in scR32 at 360 K and $p \approx 17.8$ MPa. The reference and counter electrodes were 0.5 mm Ø mm Pt discs.

v / V s^{-1}	i / µA	C_U / µF	C_A / µF	A / cm^2 (standard)	C_A / mF cm^{-2}	A / cm^2 (AAO electrode)
0.5	3.83	7.66	0.73	0.00785	0.09	0.08
0.7	4.70	6.71	0.97	0.00785	0.12	0.05
1.0	6.28	6.28	1.60	0.00785	0.20	0.03
Mean						**0.05**

As can be seen from Table 5.6 the mean area calculated for the 13 nm Ø AAO electrode from the capacitance is 0.07 ± 0.03 cm^2; within experimental error this is somewhat higher than the calculated area (0.029 ± 0.009 cm^2). This is comparable to the area calculated for the 55 nm Ø AAO electrode which was found to be 0.05 ± 0.02 cm^2; again this is double the calculated area (0.02 ± 0.004 cm^2). This is different to the values obtained in $scCO_2$/MeCN (15 wt%). This suggests that the templated electrode is rougher than expected. If the templated electrode exhibited a roughness factor of 2 compared to the standard electrode, the area of the templated electrode would be half the calculated value. This would give an area of the templated electrode close to the theoretical values. To get a more accurate value for the electroactive area of the electrode, impedance should be performed, but these values are reasonable given the experimental conditions and are in reasonable agreement with the area calculated from Equations 5.1 to 5.3.

It was shown in Chapter 5.2 that Randles-Sevčik analysis was not viable for calculating the diffusion coefficient at the 13 nm Ø AAO electrode in $scCO_2$/MeCN (15 wt%). As can be seen from Figure 5.10, the voltammetry obtained at the 55 nm Ø AAO electrode closely resembles that seen at the baffled macro electrode in scR32. The dependence of the peak current with $v^{1/2}$ (for scan rates ≥ 500 mV/s) at 360 K for the 55 nm Ø AAO electrode is presented in Figure 5.11. As can be seen from Figure 5.11, the linear fits extrapolate to the origin in both cases. The intercept of the graph suggests that Randles-Sevčik analysis is viable in this case, and the diffusion coefficient can be calculated from Figure 5.11. The diffusion coefficient calculated from the peak anodic and peak cathodic current was D = 2.6 x 10^{-5} ± 1.1 x 10^{-5} cm^2 s^{-1} and D = 2.2 x 10^{-5} ± 1.0 x 10^{-5} cm^2 s^{-1} respectively. These values of the diffusion coefficient are comparable to those calculated from voltammetry and the diffusion coefficients determined at the baffled macroelectrode in scR32. This value of the diffusion coefficient is still lower than that recorded at microelectrodes in scR32, and is lower than that recorded at 10 mV/s. As shown previously, the difference in scan rate changes the length of the diffusion layer. The higher diffusion coefficient recorded at 10 mV/s could be due to a combination of diffusion within the

pore and contribution from the bulk diffusion. At 500 mV/s, the diffusion layer is within the pore and thus gains no additional contribution from the bulk diffusion.

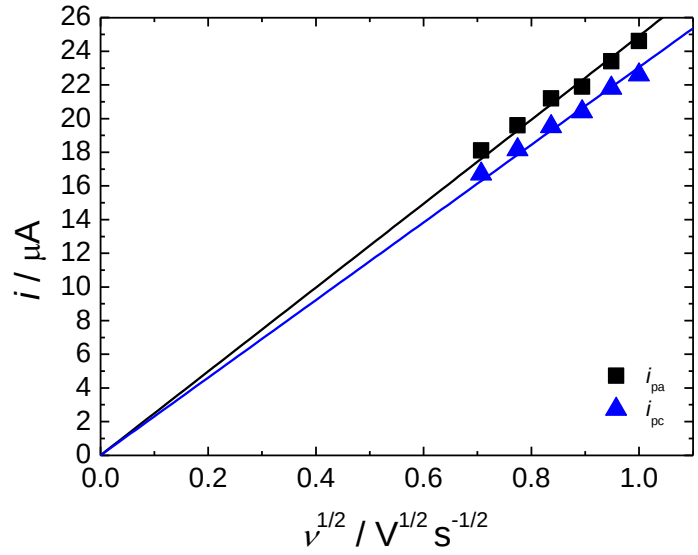

Figure 5.11. The dependence of the peak currents on the scan rate for cyclic voltammetry of 0.992 mM DMFc and 20 mM [NBu_4^n][BF_4] in scR32 at 360 K and $p \approx 17.8$ MPa at a 55 nm Ø AAO electrode.

Using Equation 5.4, it can be seen that varying the concentration of DMFc will yield a plot that will allow the diffusion coefficient to be calculated at slow scan rates more accurately. Figures 5.12 and 5.13 compare the current density obtained at varying concentrations of DMFc at the 13 nm and 55 nm Ø AAO electrode respectively. Although the two different sizes of AAO electrode were used in the same solution for each experiment, the voltammetry recorded at lower concentrations of DMFc at the 55 nm Ø AAO showed signs that the non-conductive epoxy resin had perished revealing additional active areas of Au. As can be seen from Figures 5.12 and 5.13 the limiting current scales in a similar fashion to that seen at microelectrodes in scR32 for both the 13 nm and 55 nm Ø AAO electrodes. The small amount of convection seen on the limiting current is similar to that seen at the baffled microelectrode in scR32. This suggests that the minimal convection seen on the limiting current is due to the diffusion layer probing out into the bulk solution. It can also be seen in Figure 5.12 that increasing the concentration of DMFc also increases the peak cathodic current, this cathodic peak is not seen at the 55 nm Ø AAO for any concentration of DMFc studied. This again suggests that this phenomenon is unique to the 13 nm Ø AAO electrode. Plots of the limiting current density against concentration of DMFc for the 13 nm Ø and 55 nm Ø AAO electrodes are shown in Figures 5.14 and 5.15 respectively.

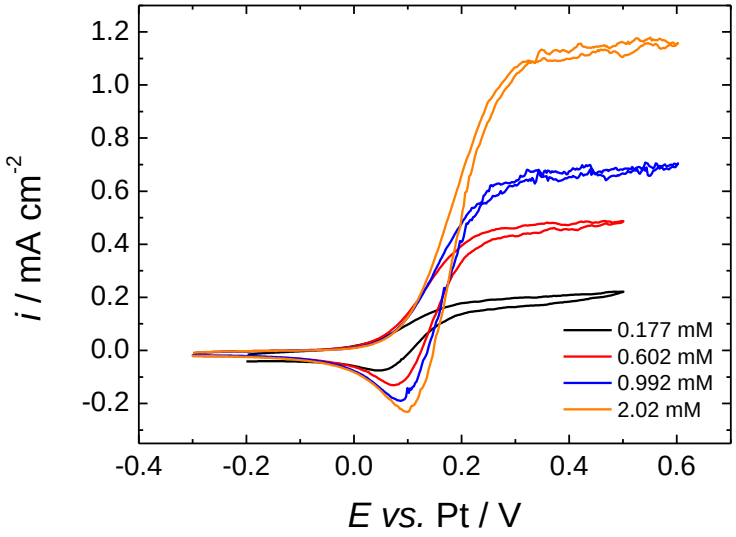

Figure 5.12. Comparison of the current density recorded at a 13 nm Ø AAO electrode at scan rates of 10 mV s^{-1}. The solution contained varying concentrations of DMFc and 20 mM $[NBu_4^n][BF_4]$ in scR32 at 360 K and $p \approx 17.8$ MPa. The reference and counter electrode were 0.5 mm Ø Pt wires.

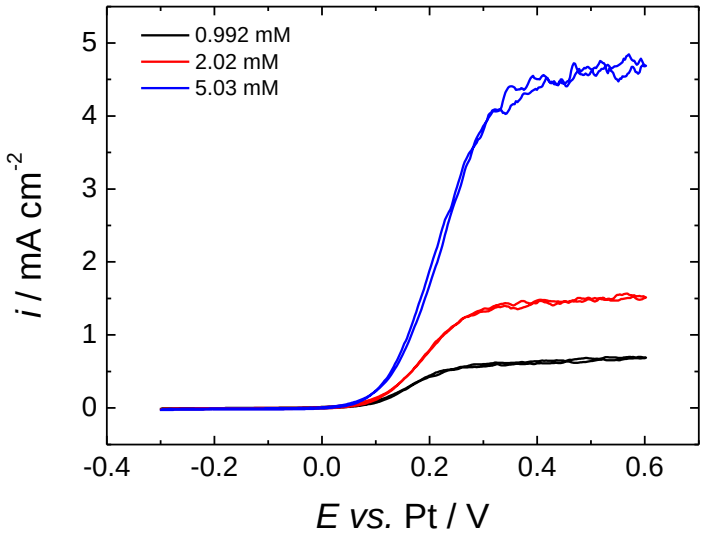

Figure 5.13. Comparison of the current density recorded at a 55 nm Ø AAO electrode at scan rates of 10 mV s^{-1}. The solution, temperature, operating pressure, reference and counter electrode have been described in Figure 5.12.

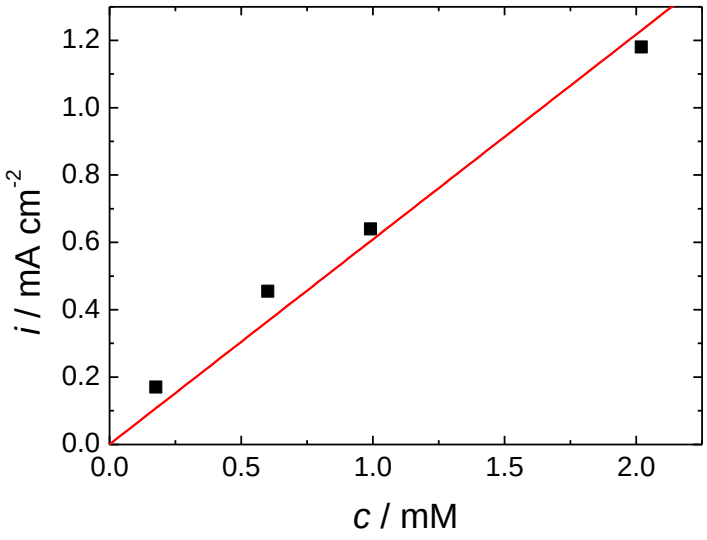

Figure 5.14. Plot of the current density *versus* the decamethylferrocene concentration for a series of cyclic voltammograms in scR32 with 20 mM [NBu_4^n][BF_4], T = 360 K, $p \approx$ 17.8 MPa. The working electrode was a 13 nm Ø AAO electrode, the reference and counter electrode were 0.5 mm Ø Pt wires.

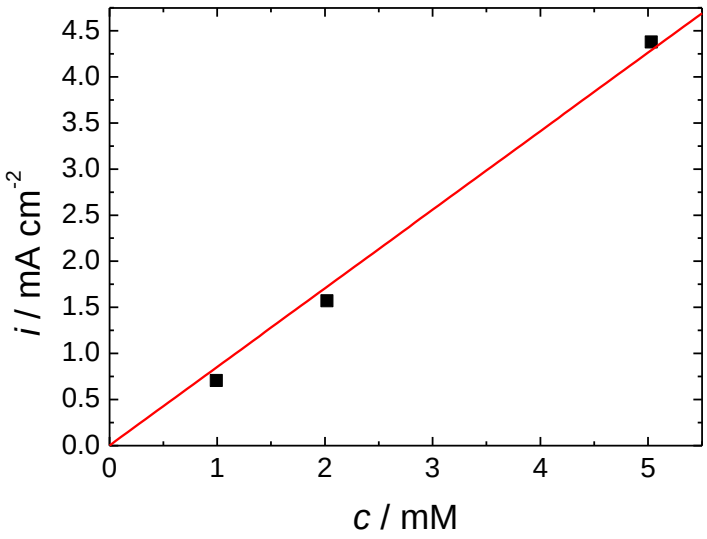

Figure 5.15. Plot of the current density *versus* the decamethylferrocene concentration for a series of cyclic voltammograms in scR32 with 20 mM [NBu_4^n][BF_4], T = 360 K, $p \approx$ 17.8 MPa. The working electrode was a 55 nm Ø AAO electrode, the reference and counter electrode were 0.5 mm Ø Pt wires.

As can be seen from Figures 5.14 and 5.15, both linear fits extrapolate to the origin. The diffusion coefficients for the 13 nm and 55 nm Ø AAO electrodes were determined to be D = 3.2 x 10^{-5} cm^2 s^{-1} and D = 4.4 x 10^{-5} cm^2 s^{-1} respectively. These values are closely

comparable to those calculated from the voltammetry. From the sets of experiments performed the diffusion coefficient for DMFc at the 13 nm Ø AAO at 10 mV/s and 500 mV/s has been calculated to be D = 3.6 x 10^{-5} ± 1.2 x 10^{-5} cm^2 s^{-1} and D = 8.5 x 10^{-5} ± 6.4 x 10^{-5} cm^2 s^{-1} respectively at 360 K and ≈ 17.8 MPa. The diffusion coefficient has also been determined for DMFc at the 55 nm Ø AAO electrode at 10 mV/s and 500 mV/s and was calculated to be D = 3.6 x 10^{-5} ± 0.8 x 10^{-5} cm^2 s^{-1} and D = 2.6 x 10^{-5} ± 1.1 x 10^{-5} cm^2 s^{-1} respectively at 360 K and ≈ 17.8 MPa. The diffusion coefficients are comparable at 10 mV/s; at 500 mV/s the diffusion coefficient is much higher at the 13 nm Ø AAO electrode compared to the 55 nm Ø AAO. This could be due to a concentration build-up in the constricted pores which leads to a higher current response.

5.4 Conclusions

This Chapter has demonstrated that it is possible to study the diffusion of decamethylferrocene into nanoporous templated electrodes in MeCN, $scCO_2$/MeCN (15 wt%) and scR32. Studies of the peak to peak potential separation in MeCN gave values comparable to those recorded at a macro disc for the same solution. The diffusion coefficient calculated in MeCN at the 13 nm Ø AAO electrode were lower than those determined at micro and macro electrodes in MeCN. Randles-Sevčik analysis performed at the 13 nm Ø AAO electrode showed a linear trend which extrapolated to the origin.

Studies performed at a 13 nm Ø AAO electrode in $scCO_2$/MeCN (15 wt%) showed that diffusion into nanopores changes under supercritical conditions. At slow scan rates, ≤ 50 mV/s, a sigmoidal wave response is observed on the anodic scan which is analogous to microelectrodes. At faster scan rates, ≥ 100 mV/s, a peak current response is recorded on the anodic scan. This is due to the difference in diffusion length probed at different scan rates. At slow scan rates the diffusion length extends the length of the pore and into the bulk solution, but does not form an overlapping diffusion profile as predicted by theory[90,94,95] due to convection. However at fast scan rates the diffusion length is confined within the pores giving a peak current response. The diffusion coefficient was calculated for $scCO_2$/MeCN (15 wt%) and these were higher than those determined for MeCN. Randles-Sevčik analysis was performed again which gave a linear trend which did not extrapolate to the origin.

Studies of diffusion were performed at two different sized nanoporous (13 nm Ø and 55 nm Ø) electrodes in scR32. Studies performed at the 13 nm Ø AAO electrode showed voltammetry that was comparable to those recorded in $scCO_2$/MeCN (15 wt%). A cathodic peak was seen at all scan rates at the 13 nm Ø AAO electrode in both supercritical systems. This is either due to an adsorption of $DMFc^+$ to the pore wall or the charged and neutral DMFc species have vastly

different diffusion coefficient due to the presence of a double layer from the charged pore wall. Studies performed at the 55 nm Ø AAO electrode showed a sigmoidal response at slow scan rates and peak current at faster scan rates. A cathodic peak was not seen at slow scan rates at the 55 nm Ø AAO electrode; this is most likely due to its larger diameter and area. The diffusion coefficients were determined at the 13 nm Ø and 55 nm Ø AAO electrodes in scR32 and were higher than those recorded in scCO_2/MeCN (15 wt%). Randles-Sevčik analysis was viable at the 55 nm Ø AAO; the analysis was not viable at the 13 nm Ø AAO electrode.

To confirm the presence of the negatively charged pore wall, metallocenes and complexes with varying charges could be studied. Chapters 3 and 4 demonstrated tests of negatively and positively charged complexes for use in supercritical systems. Sodium cobalticarborane was tested as a negatively charged internal reference complex in DCM but its insolubility meant further experiments could not be performed in supercritical conditions. Positively charged metallocenes were also tested in the form of cobaltocenium complexes. Although proving successful in liquid analogues, tests in supercritical conditions showed inconsistent voltammetry with no reproducible results. Further work to find suitable negatively and positively charged redox couples would lead to further information of the diffusion in AAO templated electrodes.

Chapter 6: Electrochemistry in a Newly Designed High Pressure Reactor

The results presented in Chapters 3, 4 and 5 describe experiments performed in a steel cell. There are drawbacks when using a steel cell for electrochemical measurements. The time taken to set up the experiments is the biggest drawback. To prepare the electrodes, prepare the cell, heat the cell and finally pressurise takes on the order of a ½ day. This process means the electrodes cannot be polished immediately before taking electrochemical measurements; it also means if anything should go wrong at any stage a lot of time is wasted. To overcome these drawbacks, a new design of reactor was developed.

The new reactor (hereby referred to as the plastic reactor) was developed to be a faster and more convenient solution to the steel cell. The bulk of the reactor is made from polyether ether ketone (PEEK), the same material that houses the electrodes in the steel cell. The reactor was made from PEEK to reduce impurities and also allow for the study of materials that would be corrosive to stainless steel. The plastic reactor was also specially designed to house commercially available electrodes and those that could be easily made by lithography. This would save time from making, preparing and polishing electrodes along with one time use. The plastic reactor would also allow for uniform heating in a heating mantle, this heating mantle also serves as a safety mantle. Once placed in the heating mantle a safety brace is tightened to seal the O-rings and allow for safe unexpected depressurisations. The cell is then heated through a heater circulator which heats both the top and bottom of the cell uniformly. The heating of the cell is very quick and the cell can be at operating temperature within 20 minutes, compared to 60 minutes in the steel cell which relies on band heaters with non-uniform heating. The small volume of the reactor (1.1 mL compared to 8.65 mL in the steel cell) allows for very small chemical waste in an experiment and compounds that take a long time to synthesise can be used sparingly. The new design allows experiments to be performed daily or even twice daily depending on the experiment being performed.

The experiments described within this Chapter show that the plastic reactor can be used to study the electrochemistry of decamethylferrocene and the electrodeposition of metals. In order for electrochemical measurements to be performed, many O-rings were tested for sealing the electrodes. The O-rings tested were mostly unsuitable due to a shorting of the electrodes. This was determined by measuring the resistance between the two gold strips on the electrode. The resistance measured between the two electrodes was $\geq$ 20 MΩ before being placed in the cell. When at operating temperature and pressure, this resistance would drop to kΩ. This was due to the O-rings becoming conductive at the operating temperature. The O-rings are loaded with

carbon black for mechanical support and it is thought this was the cause of the conductivity. The O-rings used in these experiments were Kalrez O-rings (custom O-ring compound 4079, 5 mm ID x 1 mm, Kalrez); at operating temperature and pressure the resistance measured between the electrodes was ≥ 15 MΩ. This is a sufficient resistance to stop the shorting of the electrodes and allow electrochemical measurements to be made.

6.1 Electrochemistry Performed in the "Plastic Reactor" using Kalrez O-rings

6.1.1 Electrochemistry of the Background Electrolyte in the Plastic Reactor

In order to determine if the plastic reactor was free of electrochemical impurities, background scans in scR32 were performed at single strip Au electrodes. The background scans consisted of performing cyclic voltammetry in a solution of 20 mM $[NBu_4^n][BF_4]$ in scR32, at 360 K and ≈ 18 MPa, shown in Figure 6.1, these conditions replicate those used in the steel cell. As can be seen from Figure 6.1, the background scan shows no signs of contamination, the high currents recorded are due to the large area of the electrode. The features seen at 1.5 V and – 2.1 V are those caused by electrolyte breakdown. The feature seen at - 1 V appears after the electrode has been cycled to 1.5 V where electrolyte breakdown has occurred. This feature could be associated to a product formed in this breakdown. As the background showed no signs of contamination or additional features, the reactor was assumed to be suitable for electrochemical measurements. Additional testing of the reactor was performed in the form of studying DMFc in scR32 and the electrodeposition of bismuth.

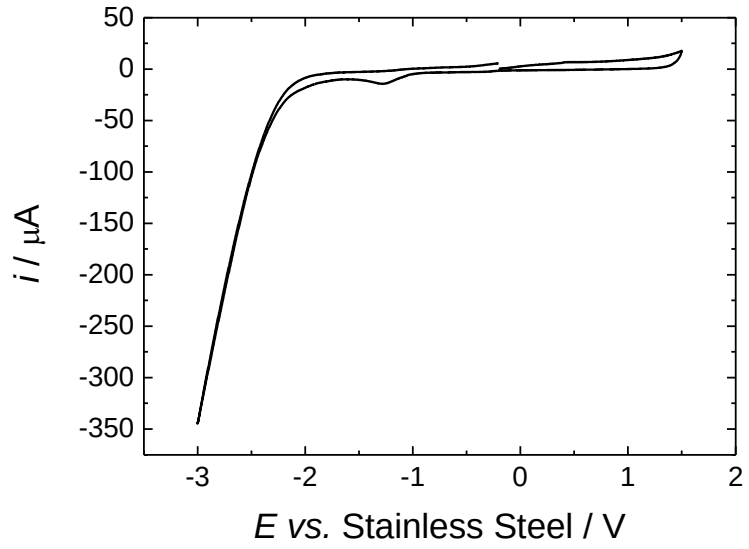

Figure 6.1. Cyclic voltammetry for a solution containing 20 mM [NBu_4^n][BF_4] in scR32, ν = 100 mV s^{-1}, T = 360 K and $p \approx$ 18 MPa. The working electrode was an evaporated gold strip (A = 0.12 cm^2), the reference electrode was a stainless steel coated thermocouple and the counter electrode was an evaporated gold sapphire slide.

6.1.2 Electrochemistry of Decamethylferrocene in scR32 in the Plastic Reactor

Initial experiments involved using a TiN wafer with two evaporated gold strips to provide a reference and working electrode in the system. The electrodes could be used as a reference and working electrode when Kalrez O-rings were employed due to the high resistivity provided in supercritical conditions. The only drawback is that when the system is under supercritical conditions, the O-ring will swell. This swelling of the O-ring meant that the electroactive area of the electrode could not be fully realised. To rectify this situation, only one strip was evaporated onto to the TiN wafer. The width of this electrode was designed to sit in the middle of the O-ring which would not be covered even if the O-ring swelled. As only one strip was used on the TiN wafer, the thermocouples stainless steel exterior was used as the reference electrode. Multiple scans showed that the drift of the reference was minimal and could be used for further testing with decamethylferrocene. The following section details experiments with single strip Au electrodes with the stainless steel casing of the thermocouple used as a reference electrode.

Cyclic voltammograms performed in a solution of scR32 containing 0.4 mM DMFc and 20 mM [NBu_4^n][BF_4] for a single strip Au electrode at 359.5 K and ≈ 18.6 MPa, are displayed in Figure 6.2. The data obtained from the voltammetry is displayed in Table 6.1. As can be seen from Figure 6.2 the voltammetry obtained in the plastic reactor shows well defined voltammetry with little to no intrinsic convection, even at scan rates of ≤ 100 mV/s. This is in contrast to the

voltammetry obtained at the baffled macro electrode in the steel cell which shows convective noise at scan rates ≤ 400 mV/s. The plastic reactor design even allows scans to be performed at scan rates as low as 10 mV/s, Figure 6.3; this is not possible in the steel reactor at the same conditions even with a baffle electrode. The potential peak separation increases from 186 to 368 mV, this is higher, but comparable to, the peak potential separation recorded in the steel cell. The difference between the half wave and peak potentials was measured between 104 and 168 mV, again this is comparable to that recorded in the steel cell and suggests the *iR* drop for both systems is comparable. Connecting the peak currents at different scan rates provides a simple way to correct for the effects of *iR* drop and is the same analysis performed in Chapter 4. The separation of the two lines through the peak currents was estimated to be 82 mV. This is comparable to the value obtained in the steel cell (95.8 mV) and is also close to the expected value of 71.3 mV for a reversible 1 e^- process at 360 K. The uncompensated solution resistance was also estimated from a slope of the lines and was found to be 1.88 kΩ. This is comparable to that estimated for the steel cell (13.1 kΩ). The ratio of the peak currents was close to unity for all scan rates.

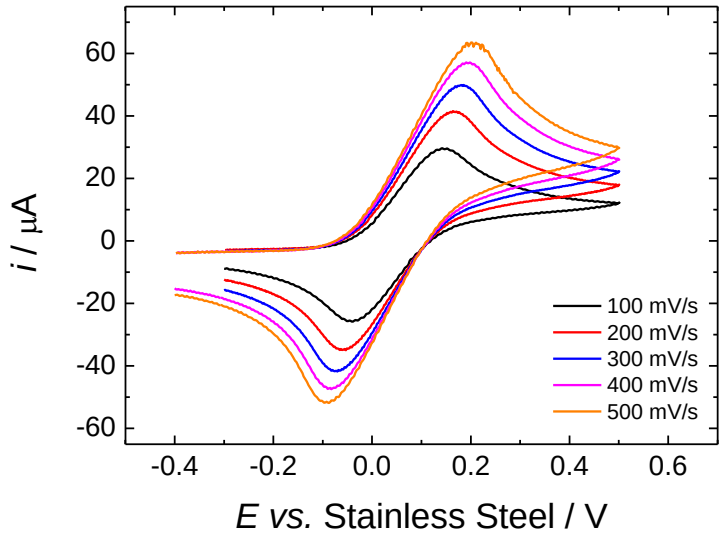

Figure 6.2. Cyclic voltammograms for a solution of 0.4 mM DMFc and 20 mM [NBu_4^n][BF_4] in scR32 at 359.5 K, p ≈ 18.6 MPa. The working electrode was an evaporated gold strip (A = 0.12 cm^2), the reference electrode was the stainless steel coating of the thermocouple and the counter electrode was an evaporated gold sapphire slide.

Table 6.1. Data obtained from cyclic voltammograms of 0.4 mM DMFc and 20 mM [NBu_4^n][BF_4] in scR32 at 359.5 K and $p \approx 18.6$ MPa for various scan rates at an evaporated gold strip electrode ($A = 0.12$ cm^2), the reference electrode was the stainless steel coating of the thermocouple.

v / V s^{-1}	E_{pa} / mV ± 1	E_{pc} / mV ± 1	ΔE_p / mV ± 1	$E_{pa/2}$ / mV ± 1	$E_{pc/2}$ / mV ± 1	$E_{pa} - E_{pa/2}$ / mV ± 1	$E_{pc} - E_{pc/2}$ / mV ± 1	i_{pa} / µA ± 0.1	i_{pc} / µA ± 0.1	i_{pa}/i_{pc} ± 0.01
0.1	145	-41	186	41	64	104	105	32.2	30.2	1.07
0.2	165	-59	224	50	59	115	117	43.7	40.0	1.09
0.3	181	-72	253	55	60	126	132	52.4	47.5	1.10
0.4	193	-84	277	62	55	131	139	59.5	53.7	1.11
0.5	204	-92	296	67	53	137	145	65.4	57.7	1.13
0.6	216	-101	317	72	53	144	154	71.5	63.6	1.12
0.7	223	-104	327	77	50	146	154	76.6	67.0	1.14
0.8	231	-109	340	79	45	152	154	80.6	71.1	1.13
0.9	238	-116	354	83	48	155	164	84.8	73.7	1.15
1.0	246	-122	368	86	46	160	168	87.9	75.8	1.16

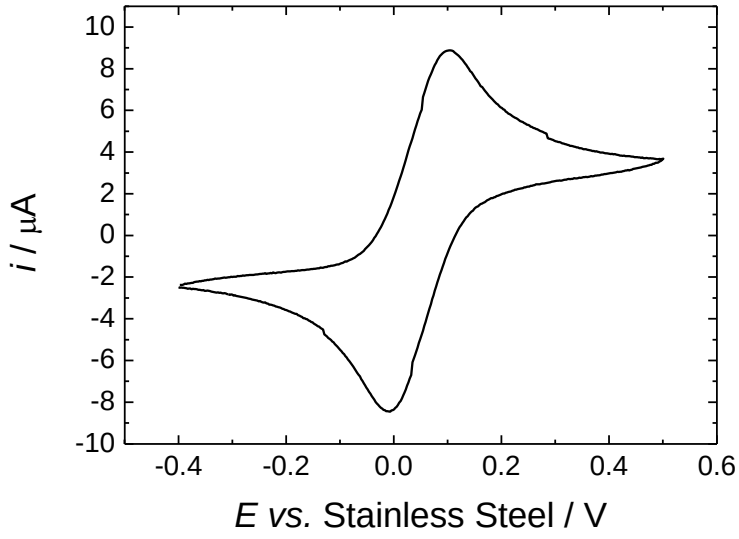

Figure 6.3. Cyclic voltammetry for a solution of 0.4 mM DMFc and 20 mM [NBu_4^n][BF_4] in scR32 at 359.5 K and $p \approx 18.6$ MPa, $v = 10$ mV s^{-1}. The working electrode was an evaporated gold strip ($A = 0.12$ cm^2), the reference electrode was the stainless steel coating of the thermocouple and the counter electrode was an evaporated gold sapphire slide.

Randles-Sevčik analysis was used to determine the diffusion coefficient at the Au strip electrode in scR32. The dependence of the peak current with $v^{1/2}$ at 360 K for the 0.12 cm^2 Au electrode is presented in Figure 6.4. As with the baffle electrode in the steel cell, the linear fits do not extrapolate to the origin. To compare to the baffle electrode in the steel cell, the diffusion coefficient was still estimated from Figure 6.4. The diffusion coefficient calculated from the peak anodic and peak cathodic current was $D = 4.89 \times 10^{-5}$ cm^2 s^{-1} and $D = 3.31 \times 10^{-5}$ cm^2 s^{-1} respectively. These values are lower than those determined at microdiscs in the steel cell but are in agreement with diffusion coefficients calculated at the baffled macro electrode in scR32. The diffusion coefficient was also estimated from the peak anodic current determined at 500 mV/s.

In this case the diffusion coefficient was calculated to be D = 6.19 x 10^{-5} cm^2 s^{-1}. This value is higher than that calculated by Randles-Sevčik analysis and is in agreement with the diffusion coefficient calculated at microelectrodes in the steel cell in scR32. It was noticed that when the electrode was removed from the plastic reactor the Au working area was darker. As this electrode was used for testing the background electrolyte it was subjected to high potential ranging (3 to -3 V). This may have caused the Au to alloy with the Cr adhesion layer beneath. To see if the results were repeatable, another experiment was performed with DMFc in scR32 at a new Au strip electrode.

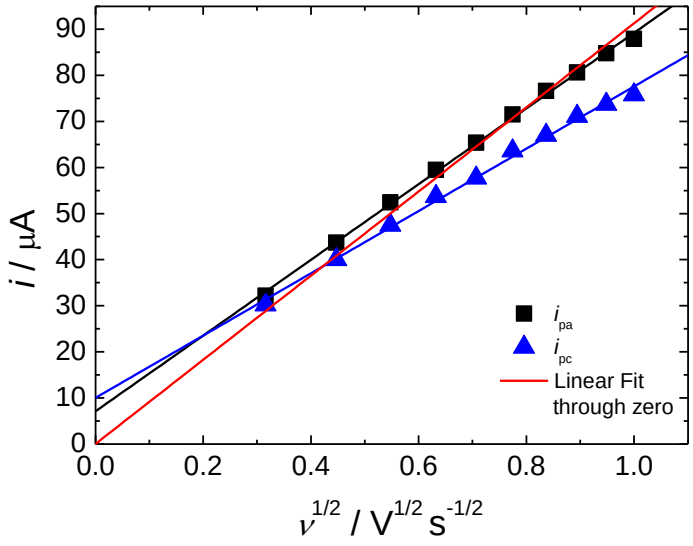

Figure 6.4. The dependence of the peak currents on the scan rate for cyclic voltammetry of 0.4 mM DMFc and 20 mM [NBu_4^n][BF_4] in scR32 at 359.5 K and p ≈ 18.6 MPa at an evaporated gold strip electrode (A = 0.12 cm^2).

6.1.3 Electrochemistry of Decamethylferrocene in scR32 in the Plastic Reactor at a new Gold Strip Electrode

Cyclic voltammograms performed in a solution of scR32 containing 0.8 mM DMFc and 20 mM [NBu_4^n][BF_4] for a single strip Au electrode at 359.6 K and ≈ 18.8 MPa are displayed in Figure 6.5. The data obtained from the voltammetry is displayed in Table 6.2. As can be seen from Figure 6.5, the voltammetry obtained again shows well defined voltammetry with little to no intrinsic convection even at slow scan rates (< 100 mV/s). The voltammetry obtained is in complete agreement with those obtained in Section 6.1.2, and scans could again be obtained at 10 mV/s with no convective influence. The potential peak separation increases from 358 to 744 mV, this is higher than that measured in the steel cell and is also higher than those measured in the plastic reactor at half the concentration. The difference between the half wave

and peak potentials was measured between 157 to 288 mV. This is higher than those measured in the plastic reactor at 0.4 mM, suggesting that as the concentration of DMFc is increased, the *iR* drop increases. The peak currents were connected to correct for the *iR* drop as performed in Section 6.1.2, the separation between the points was found to be 147 mV. This is higher than that estimated at the lower concentration in the plastic reactor (82 mV) and also in the steel cell. The uncompensated solution resistance was also estimated from the slope of the line and was estimated to be 2.05 kΩ. This is comparable to the measurement made at the lower concentration of DMFc in the plastic reactor. This suggests that the additional resistance is due to the orientation of the reference electrode to the working electrode. This can be rectified by replacing the thermocouple (as the temperature of the system stays constant at 360 K) with a platinum wire which is angled towards the working electrode in a similar vein to a luggin capillary. This should reduce the *iR* drop by reducing the distance between the reference and the working electrode. Another way of reducing the *iR* drop would be to increase the supporting electrolyte concentration which can be up to 50 mM without affecting the phase behaviour of the supercritical fluid.

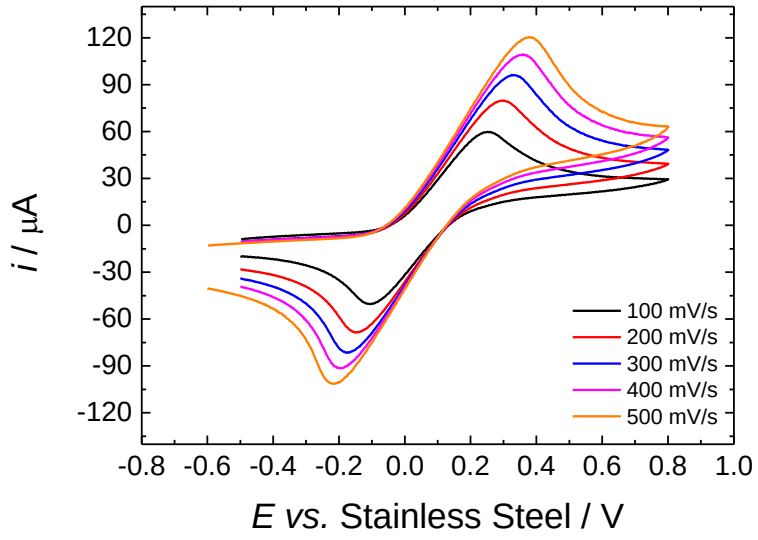

Figure 6.5. Cyclic voltammograms for a solution of 0.8 mM DMFc and 20 mM [NBu_4^n][BF_4] in scR32 at 359.6 K, $p \approx 18.8$ MPa. The working electrode was an evaporated gold strip ($A = 0.135$ cm^2), the reference electrode was the stainless steel coating of the thermocouple and the counter electrode was an evaporated gold sapphire slide.

Table 6.2. Data obtained from cyclic voltammograms of 0.8 mM DMFc and 20 mM $[NBu_4^n][BF_4]$ in scR32 at 359.6 K and $p \approx 18.8$ MPa for various scan rates at an evaporated gold strip electrode ($A = 0.135$ cm^2) the reference electrode was the stainless steel coating of the thermocouple.

v / V s^{-1}	E_{pa} / mV ± 1	E_{pc} / mV ± 1	ΔE_p / mV ± 1	$E_{pa/2}$ / mV ± 1	$E_{pc/2}$ / mV ± 1	$E_{pa} - E_{pa/2}$ / mV ± 1	$E_{pc} - E_{pc/2}$ / mV ± 1	i_{pa} / µA ± 1.0	i_{pc} / µA ± 1.0	i_{pa}/i_{pc} ± 0.01
0.1	252	-106	358	95	56	157	162	60	58	1.03
0.2	298	-146	444	113	40	185	186	81	80	1.02
0.3	328	-173	501	129	33	199	206	98	97	1.01
0.4	354	-197	551	140	32	214	229	109	108	1.01
0.5	379	-217	596	142	22	237	239	122	116	1.05
0.6	400	-228	628	160	21	240	249	130	125	1.04
0.7	418	-245	663	168	25	250	270	139	135	1.03
0.8	434	-260	694	177	9	257	269	146	144	1.01
0.9	449	-276	725	181	2	268	278	156	149	1.05
1.0	461	-283	744	190	5	271	288	161	155	1.04

Randles-Sevčik analysis was again performed to determine the diffusion coefficient at the Au strip electrode in scR32. The dependence of the peak current with $v^{1/2}$ at 360 K for the 0.135 cm^2 Au electrode is presented in Figure 6.6. As with the steel cell and the previous experiments performed in the plastic reactor, the linear fits do not extrapolate to the origin. In order to compare to the value obtained for the previous experiment, the diffusion coefficients were determined from the plot. The diffusion coefficient calculated from the peak anodic and peak cathodic current was $D = 3.09 \times 10^{-5}$ cm^2 s^{-1} and $D = 2.80 \times 10^{-5}$ cm^2 s^{-1} respectively. These values are close to those determined previously in the plastic reactor and also in agreement with the value determined at the baffled macro electrode in the steel cell. To compare to the previous experiment, the diffusion coefficient was estimated from the cyclic voltammetry at 500 mV/s, this was calculated to be $D = 4.26 \times 10^{-5}$ cm^2 s^{-1}. This is lower than the diffusion coefficient determined in Section 6.1.2, but is in agreement with the diffusion coefficient calculated from Randles-Sevčik analysis for $c = 0.4$ mM. When the electrode was removed from the system, there was no darkened gold in the working electrode area; this is in contrast to the electrode removed in Section 6.1.2. This suggests that the previous electrode had alloyed with the Cr adhesion layer when it was cycled to very cathodic and anodic potentials. It has been shown that cyclic voltammetry can be performed in the plastic reactor; the next step was to perform an electrodeposition. This would confirm that the working electrode area is confined by the O-ring and demonstrate that it is possible to electrodeposit materials in the plastic reactor.

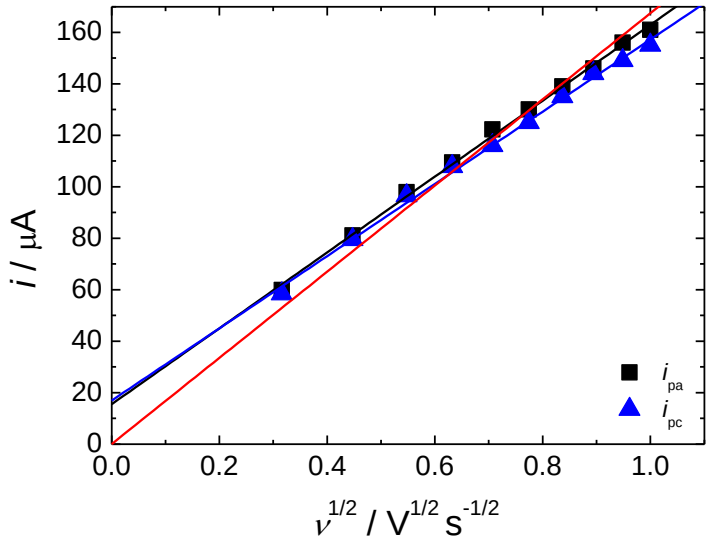

Figure 6.6. The dependence of the peak currents on the scan rate for cyclic voltammetry of 0.8 mM DMFc and 20 mM [NBu_4^n][BF_4] in scR32 at 359.6 K and $p \approx 18.8$ MPa at an evaporated gold strip electrode ($A = 0.135$ cm^2).

6.2 Electrodeposition of Bismuth from scR32 in the Plastic Reactor

It has been shown in the previous section that it is possible to reproducibly study decamethylferrocene in the plastic reactor. An important aspect of the reactor is the electrodeposition of metals and semi-conductor from supercritical fluids at a quicker rate than is possible with the steel cell. This is accomplished with the single use electrodes and quicker heating/cooling cycles. The amount of metal complex used in each experiment is also greatly reduced as the volume of the plastic reactor cell is 1.1 mL compared to the steel cell volume which is 8.65 mL, making the electrodeposition process much more efficient. As the body of the reactor is comprised of PEEK, this means corrosive materials that would not be suitable in the steel cell can now be used in the plastic reactor. This section details the electrodeposition of bismuth from scR32 at a single gold strip electrode.

6.2.1 Cyclic voltammetry of [NBu_4^n][$BiCl_4$] from scR32 in the Plastic Reactor

Cyclic voltammograms performed in a solution of scR32 containing 1 mM [NBu_4^n][$BiCl_4$] and 50 mM [NBu_4^n][Cl] for a single strip Au electrode at a scan rate of 50 mV/s, at 359.7 K and 19.3 MPa are displayed in Figure 6.7. The cyclic voltammetry performed for the first scan under the same conditions is presented in Figure 6.8. As can be seen from Figures 6.7 and 6.8, there are characteristic deposition and stripping peaks, along with a nucleation loop seen only on the

first scan. The process in which bismuth deposits onto the electrode surface is shown in Equation 6.1.

$$Bi^{3+} + 3e^{-} \rightarrow Bi^{0} \quad (6.1)$$

It can also been seen in Figure 6.7 that the onset of deposition starts at - 0.35 V and shifts to -0.28 V after three scans, this is due bismuth not being 100% stripped from the electrode surface which causes a shift in the deposition potential as bismuth deposits onto residual bismuth. Taking the first scan (Figure 6.8), the total bismuth stripping charge to plating charge can be calculated. The total plating charge was calculated to be 2.05 mC, whereas the total stripping charge was calculated to be 0.83 mC, this leads to the total stripping being 40.5% of the total plating charge. This value is lower than that reported in literature where studying the same bismuth complex in DCM the total stripping charge was found to be 91.1 % of the total plating charge[117]. Although the deposition of bismuth was studied at glassy carbon electrodes[117] and not evaporated gold used here. The low stripping charge could also be due to a low dissolution of bismuth back into solution.

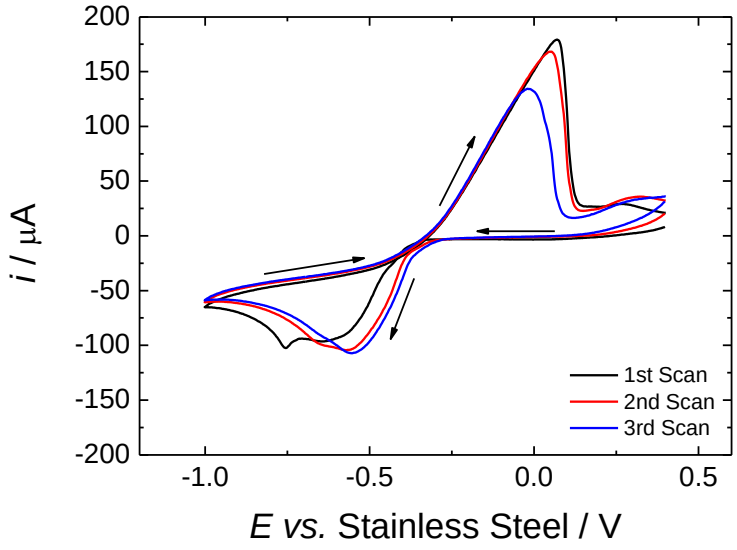

Figure 6.7. Cyclic voltammograms for a solution of 1 mM [NBu_4^n][$BiCl_4$] and 50 mM [NBu_4^n][Cl] in scR32, v = 50 mV s^{-1} for all scans, T = 359.7 K and $p \approx$ 19.3 MPa. The working electrode was an evaporated gold strip (A = 0.135 cm^2), the reference electrode was the stainless steel coating of the thermocouple and the counter electrode was an evaporated gold sapphire slide.

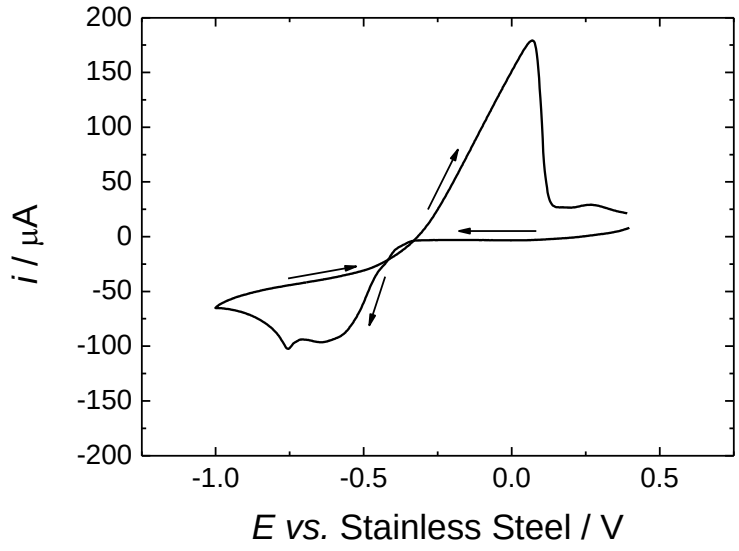

Figure 6.8. All parameters have been described in Figure 6.7; the 1st cyclic voltammetry performed is displayed.

Using Randles-Sevčik analysis (Equation 3.7), the diffusion coefficient could be estimated from the peak deposition current. The peak deposition current was determined to be 96.20 μA, the area of the electrode was found to be 0.135 cm^2, thus the diffusion coefficient was determined to be D = 1.69 x 10^{-4} cm^2 s^{-1}. This is higher than the diffusion coefficient determined for DMFc (D = 4.89 x 10^{-5} cm^2 s^{-1}) in the plastic reactor (Section 6.1.2) at a similar temperature and pressure. This value for the diffusion coefficient is also higher than that determined for DMFc (D = 8.33 x 10^{-5} cm^2 s^{-1}) at microelectrodes in scR32 in the steel reactor at similar temperatures and pressures (Section 4.2.2).

6.2.2 Electrodeposition of Bismuth from scR32 in the Plastic Reactor

6.2.2.1 Performing Electrodeposition of Bismuth

The electrodeposition of bismuth was performed in the same solution as was outlined in Section 6.2.1. The deposition potential was determined from the peak deposition current on the third scan displayed in Figure 6.7, and was chosen to be -0.6 V. In order to analyse the electrodeposit by SEM and EDX, the electrodeposited film needs to be of sufficient thickness. It was decided that a 1 μm thick deposited film would be sufficient for analysis. Equations 6.2 to 6.5 demonstrate how the calculated charge relates to the thickness of the electrodeposited film

$$V = dA \tag{6.2}$$

$$mass = V\rho \tag{6.3}$$

$$m = \frac{mass}{MM} \tag{6.4}$$

$$Q = nmF \tag{6.5}$$

where V is the volume the deposit occupies in units of cm^{-3}, d is the thickness of the deposited film in units of µm, A is the working area of the electrode (A = 0.135 cm^2), ρ is the density of the bismuth (ρ_{Bi} = 9.78 g cm^{-3}), m is mol, MM is atomic mass (MM_{Bi} = 208.98), n is the number of electrons transferred (n = 3), F is Faraday's constant (96485.34 C mol^{-1}) and Q is the charge passed in units of C. The charge required to electrodeposit a 1 µm thick deposit was calculated to be 183 mC. The deposition was held at constant potential of -0.6 V for 8475 s. The total charge passed for this electrodeposition was 64 mC, which yields a deposit thickness of d = 0.35 µm. The chronoamperogram for the experiment is displayed in Figure 6.9, it should be noted that the electrodeposition time was extended *in situ* which caused the first 1100 s of the current trace to be erased. A picture of the electrode upon disassembly of the cell is displayed in Figure 6.10.

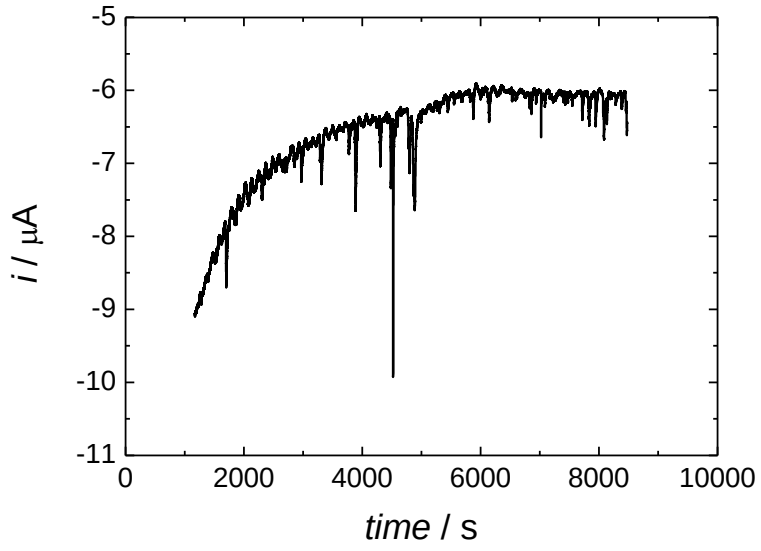

Figure 6.9. Current-time response recorded at an evaporated gold slide (A = 0.135 cm^2), the potential was held at -0.6 V for 8475 s. The solution, temperature, pressure, reference and counter electrode have all been described in Figure 6.7.

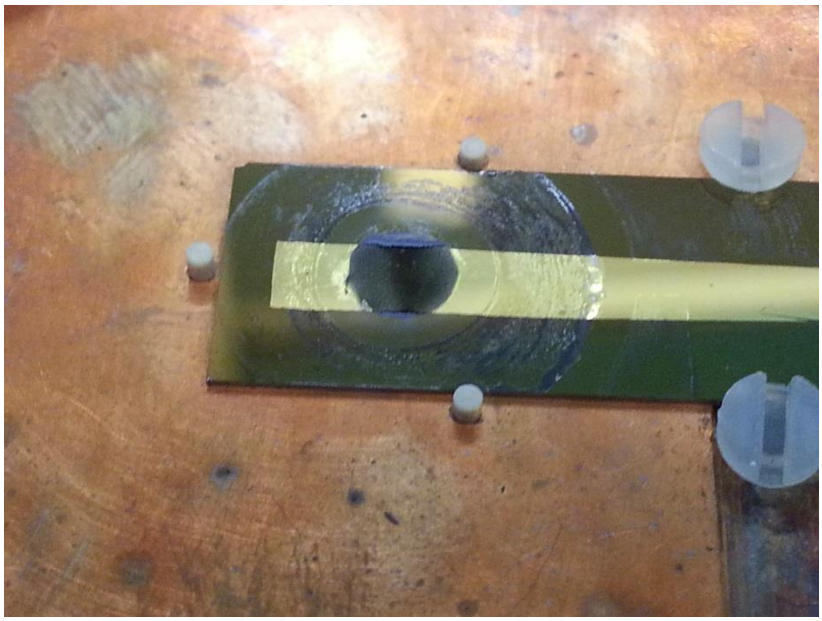

Figure 6.10. A picture of the working electrode upon disassembly of the plastic reactor.

As can be seen from Figure 6.10, the deposit is confined by the O-ring; this confirms that the O-ring forms a good seal with the electrode. It can also be seen that the deposit is uniform across the electrode surface with thicker deposits being more apparent at the edges of the metal strip. This is because diffusion can occur perpendicularly and at 90° to the electrode surface, but the rate of mass transport to the edge is always higher when compared to that of the centre[100]. The bismuth film was washed in acetone and IPA prior to analysis and the film was adherent to the electrode surface. The electrode was then cleaved and analysed by SEM and EDX.

6.2.2.2 SEM and EDX Analysis of Bismuth Deposit

To analyse the morphology and composition of the bismuth deposit, SEM and EDX were performed. SEM was performed on a field emission gun scanning electron microscope (FEGSEM) with the aid of Dr. Pete Richardson; the corresponding EDX was performed using INCA software. Figure 6.11 shows a SEM image taken of the electrode working area; the labels demonstrate the areas of focus for additional imaging and the Figure they correspond to.

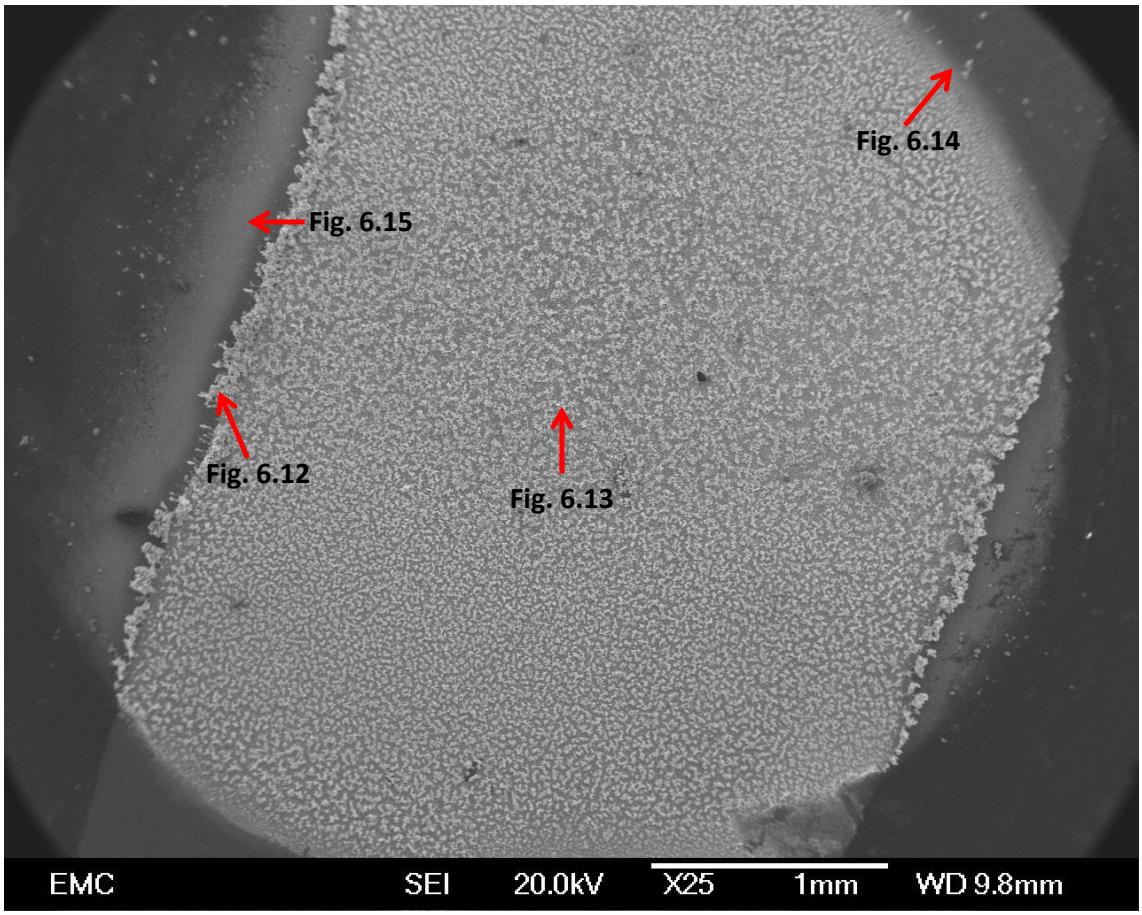

Figure 6.11. SEM image of the working electrode area with reference labels for areas of focus for additional imaging.

As can be seen from Figure 6.11, there is predominant growth on the gold working area which is confined by the O-ring placement. There are small areas of deposit outside of the gold working area; this could be due to an incomplete TiO_2 insulating layer which protects the electroactive TiN substrate from solution. The edge deposition was analysed first as it showed the thickest deposition of Bi, Figure 6.12 shows the image along with the corresponding EDX spectrum and Table 6.3 shows the data acquired from the EDX spectrum.

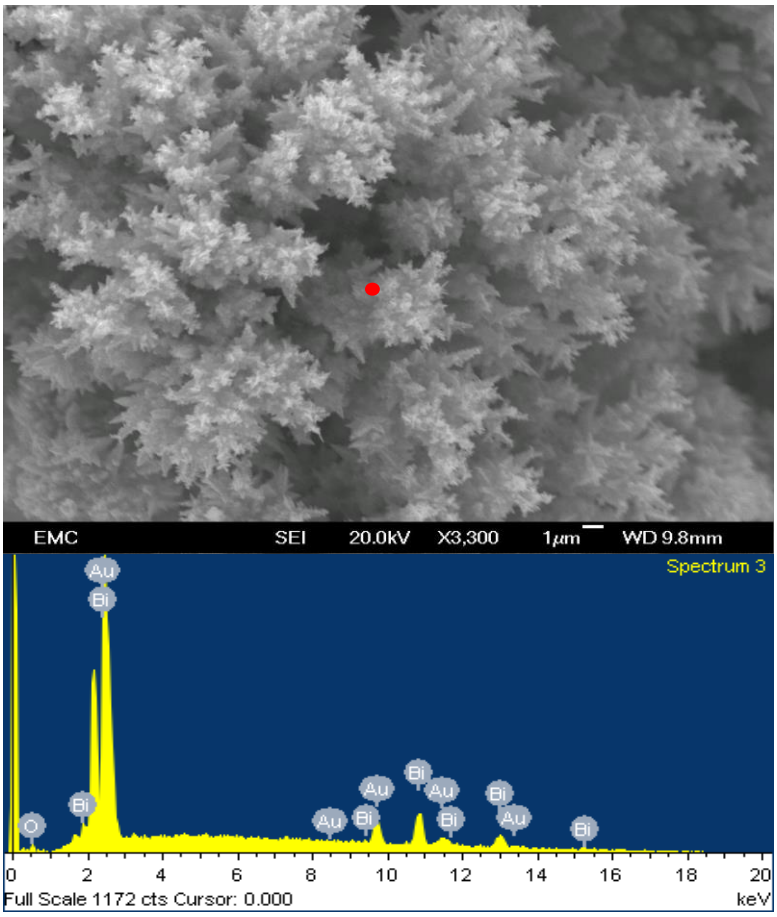

Figure 6.12. SEM image of the thickest edge of electrodeposition, the red spot represents where the EDX spectrum was obtained.

Table 6.3. Data obtained from EDX analysis from Figure 6.12.

Element	Weight%	Atomic%
O K	3.50	31.67
Au M	35.46	26.06
Bi M	61.04	42.27
Totals	100.00	

As can be seen from Figure 6.12, the bismuth deposit is thick and the EDX spectrum shows a strong bismuth signal with a high atomic% and no signs of contaminants. There is also a strong gold signal in the EDX; this is most likely from the evaporated gold substrate that the bismuth is deposited on. It can also be seen in Figure 6.12 and in Table 6.3 that there is an oxygen peak identified in the EDX. The oxygen is most likely from where the sample was handled in air after disassembly and then placing the sample in the FEGSEM. This could also be from the electrode which has a TiO_2 layer to insulate the TiN electroactive surface. The morphology of the deposit looks crystalline and the ends of the crystals have an almost "christmas tree" or "aloe vera leaf" like appearance. The main bulk of the deposit is flower like in growth; this morphology can be seen in more detail in Figure 6.13.

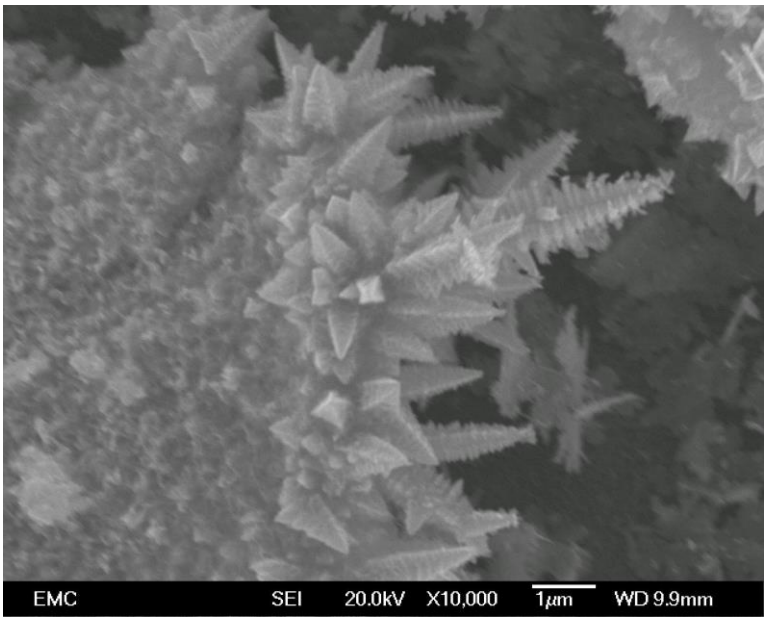

Figure 6.13. SEM image of Figure 6.12 at higher magnification.

The next area imaged was taken from the centre of the working electrode, the SEM image and associated EDX can be seen in Figure 6.14. The results of the EDX can be seen in Tables 6.4a, 6.4b and 6.4c corresponding to spectrums 1 (red dot), 2 (blue dot) and 3 (green dot) respectively.

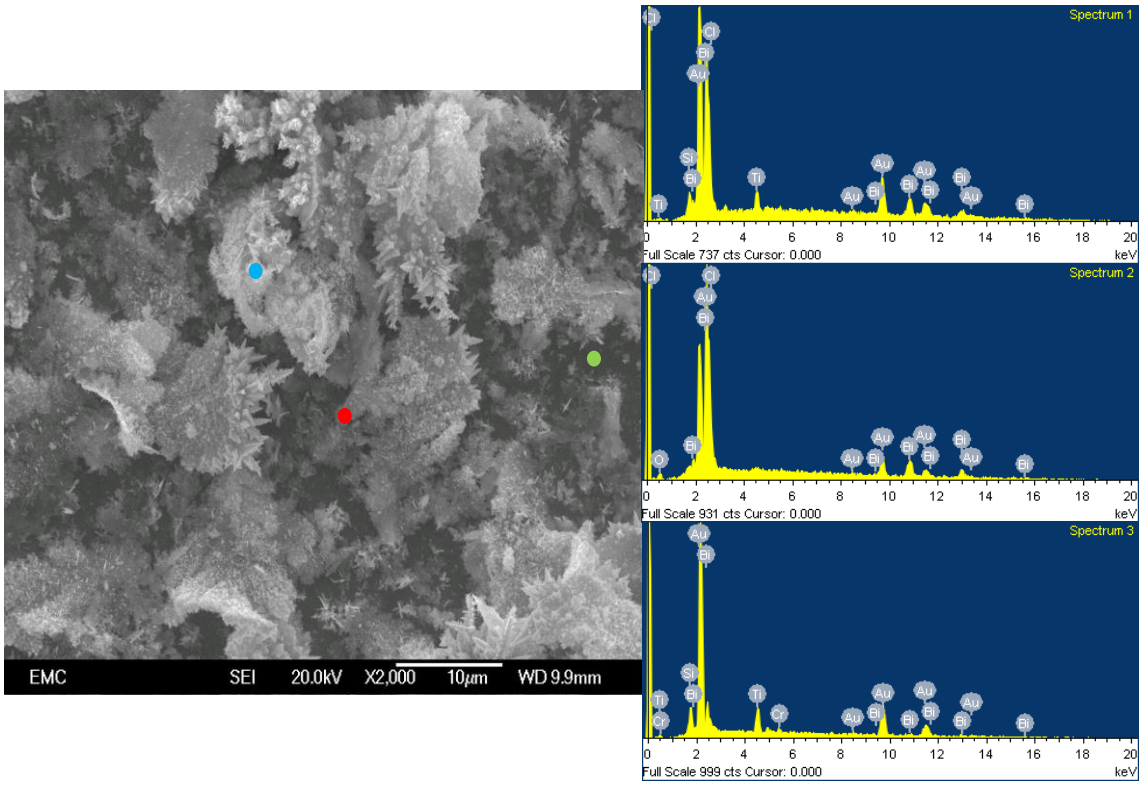

Figure 6.14. SEM image of the centre of the working electrode area, the red spot correlates to EDX spectrum 1, the blue spot correlates to EDX spectrum 2, and the green spot correlates to EDX spectrum 3.

Table 6.4. Data obtained from EDX analysis, Table 6.4a corresponds to spectrum 1, Table 6.4b corresponds to spectrum 2, and Table 6.4c corresponds to spectrum 3.

Table 6.4a

Element	Weight%	Atomic%
Si K	1.21	6.98
Cl K	1.50	6.86
Ti K	3.22	10.93
Au M	44.35	36.58
Bi M	49.72	38.65
Totals	100.00	

Table 6.4b

Element	Weight%	Atomic%
O K	2.85	24.35
Cl K	3.43	13.21
Au M	30.37	63.35
Bi M	63.35	41.39
Totals	100.00	

Table 6.4c

Element	Weight%	Atomic%
Si K	2.67	13.33
Ti K	6.59	19.32
Cr K	1.57	4.25
Au M	77.31	55.13
Bi M	11.87	7.97
Totals	100.00	

As can be seen from Figure 6.14, the morphology of the deposit is very similar to that displayed in Figure 6.13. Three areas were chosen for analysis, a thin area of deposit (red dot, spectrum 1), a thick area of deposit (blue dot, spectrum 2) and an area where it appeared no deposit had occurred (green dot, spectrum 3). As can be seen from Table 6.4a, the thinner area of deposit also shows a strong bismuth signal suggesting that the deposit is mostly bismuth. There is also silicon, titanium and gold, this is most likely from the electrode as it is a silicon wafer with TiN and gold layers. It can also be seen that there is a small amount of chlorine; this could be from the supporting electrolyte or from the bismuth complex which was not removed in the washing step. This feature in the EDX maybe misidentified as chlorine, bismuth and chlorine have

similar energies and the overlap of the signals can be hard to distinguish, further analysis using WDX would clarify the presence of chlorine but was not performed in this work. The thicker area of deposit, Table 6.4b, there is oxygen again which is most likely for reasons discussed earlier. The thicker area of deposit again shows a strong bismuth signal from the deposit. The area where it appeared that no deposit had occurred shows signs of bismuth but it is a lot weaker when compared to thicker areas. The EDX also shows signs of chromium; this is again from the electrode which uses a chromium adhesion layer for the evaporated gold.

The next area sampled was taken at the top of the electrode where the O-ring is placed under pressure (see Figure 6.12 for reference); this is shown in Figure 6.15 along with the associated EDX spectrum. The results of the EDX can be seen in Tables 6.5a, 6.5b and 6.5c corresponding to spectrum's 1 (red dot), 2 (blue dot) and 3 (green dot) respectively.

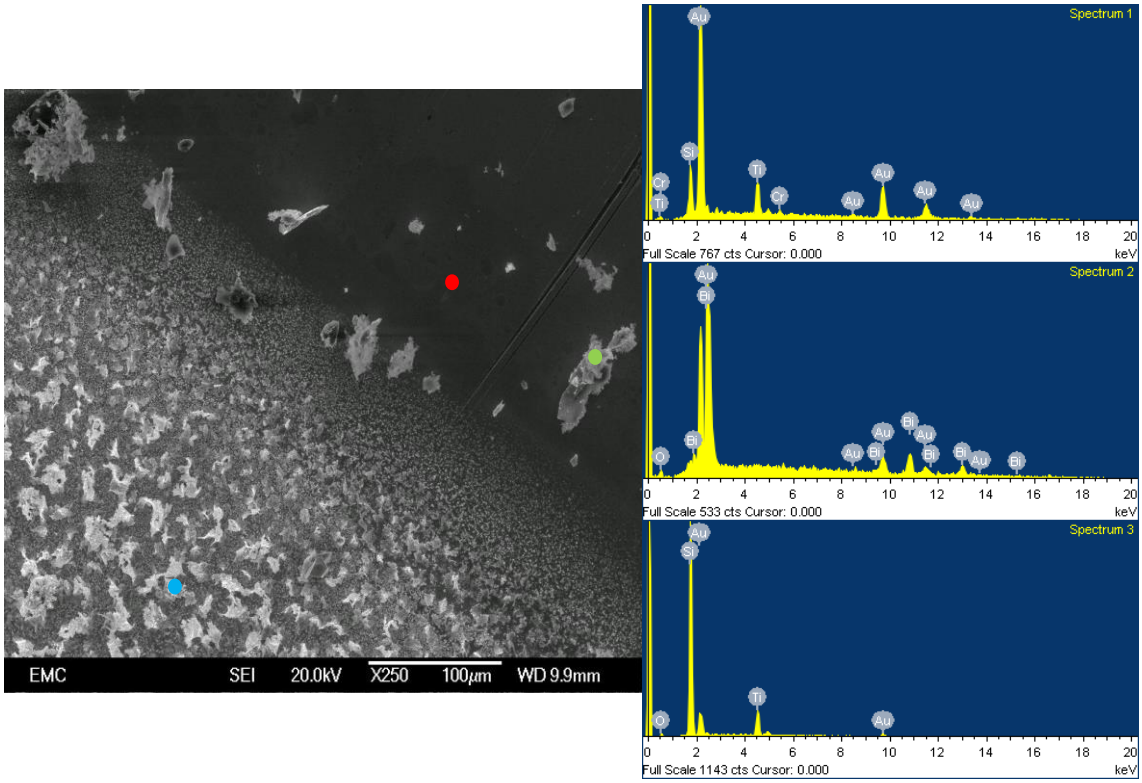

Figure 6.15. SEM image of the top edge of the working electrode area, the red spot correlates to EDX spectrum 1, the blue spot correlates to EDX spectrum 2, and the green spot correlates to EDX spectrum 3.

Table 6.5. Data obtained from EDX analysis, Table 6.5a corresponds to spectrum 1, Table 6.5b corresponds to spectrum 2, and Table 6.5c corresponds to spectrum 3.

Table 6.5a		
Element	**Weight%**	**Atomic%**
Si K	4.64	20.44
Ti K	9.14	23.59
Cr K	1.06	2.52
Au M	85.16	53.45
Totals	100.00	

Table 6.5b		
Element	**Weight%**	**Atomic%**
O K	3.11	29.08
Au M	34.62	26.31
Bi M	62.27	44.60
Totals	100.00	

Table 6.5c		
Element	**Weight%**	**Atomic%**
O K	7.05	16.70
Si K	48.26	65.14
Ti K	15.96	12.63
Au M	28.73	5.53
Totals	100.00	

The areas chosen for analysis were an area of no deposit (e.g. bare electrode, red dot, spectrum 1), the working electrode area with deposit (blue dot, spectrum 2), and an area which appeared to have a feature outside the confines of the working electrode area (green dot, spectrum 3). As can be seen from Table 6.5a, the area of no deposit shows no sign of bismuth and only shows elements that make up the substrate. Table 6.5b shows a strong bismuth signal with a small amount of oxygen which again is most likely from atmosphere and no signs of contaminants. The third area analysed shows oxygen, silicon, titanium and gold in the EDX spectrum (Table 6.5c). This suggests that this feature is not a deposited product as no bismuth is recorded in the spectrum. This could be an additional product which has been picked up during the washing of the electrode. It could also be a fragment of the substrate which could have been picked up after cleaving the electrode.

The last area investigated was outside the edge of the gold working area, this was to investigate if the deposit has grown on a supposedly insulating area, (see Figure 6.12 for reference). The SEM image and associated EDX can be seen in Figure 6.16 and the results of the EDX can be seen in Table 6.6.

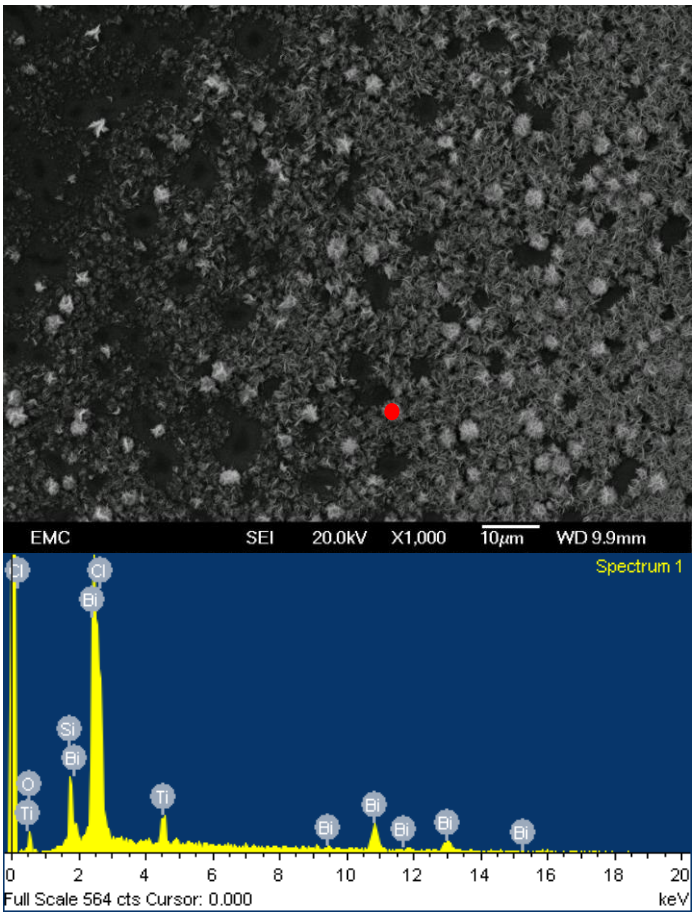

Figure 6.16. SEM image of the furthest left edge of the working electrode area, the red spot represents where the EDX spectrum was obtained.

Table 6.6. Data obtained from EDX analysis for Figure 6.16.

Element	Weight%	Atomic%
O K	8.58	36.52
Si K	4.24	10.28
Cl K	12.17	23.39
Ti K	4.89	6.96
Bi M	70.11	22.85
Totals	100.00	

As can be seen from Figure 6.16, it appears that there are areas of deposited material on the insulating TiO_2 area, along with holes where no deposited material is present. This could be due to an incomplete insulating area, as supercritical fluids have a lack of surface tension they can penetrate very small diameter nanopores. If the insulating layer has pin holes or the insulating layer has been mechanical scratched during handling, the conducting TiN layer could be exposed to the supercritical fluid leading to a deposition of material. It can also be seen from Table 6.6 that the EDX shows strong signs of bismuth suggesting the deposited material is bismuth. The EDX also shows titanium, silicon, oxygen and chlorine, this is mostly the make-

up of the substrate. The chlorine could have come from undeposited complex or supporting electrolyte and was not removed during washing. When the cell is depressurised, unreacted materials can be left on the surface of the electrode, this area could also easily be unreacted complex which has not been removed. In conclusion, the bismuth deposited films show good adherence to the gold substrate and the thickest areas of deposit show no impurities.

6.3 Conclusions

This Chapter has demonstrated that the newly designed high pressure reactor is suitable for electrochemical experiments; this has been demonstrated by performing cyclic voltammetry of decamethylferrocene and the electrodeposition of bismuth. The speed of experiments has been increased with more efficient heating and cooling, lithographically produced electrodes and the efficiency of materials has been increased by exploiting a smaller cell volume. Cyclic voltammetry of the background electrolyte showed no signs of contamination and the features seen were that of electrolyte breakdown at high potential. Results obtained using decamethylferrocene as redox couple showed well behaved voltammetry with little to no signs of natural convection, which has been reduced due to uniform heating of the cell. This was demonstrated by performing cyclic voltammetry at low scan rates (< 100 mV/s) which was not possible in the steel cell. The cyclic voltammetry also showed signs of *iR* drop but analysis demonstrated that this value of resistance is comparable to the steel cell suggesting the electrode orientation is the cause of additional resistive features. The cyclic voltammetry and electrodeposition of bismuth was also discussed in this Chapter. Cyclic voltammetry of bismuth showed typical plating and stripping features with a diffusion coefficient that was higher than any recorded for decamethylferrocene in the same system. The electrodeposition of bismuth produced a film that was adherent to the electrode surface which was black/blue in colour. SEM performed showed that the deposit is confined to the working area of the electrode and is constrained by the O-ring under pressure. EDX of the thickest areas of the deposit showed a strong bismuth signal with only minor contaminants, some oxygen was detected but this was most likely due to the sample being exposed to air after disassembly. Further modifications to the plastic reactor will be to remove the thermocouple (as the temperature does not fluctuate) and replacing it with a platinum wire, this wire can then be angled towards the working electrode in a similar vein to a luggin capillary. The reactor can now be used throughout the project and further tests will include the electrodeposition of metals into high aspect ratio nanopores.

Chapter 7: Conclusions and Further Work

7.1 Conclusions

The aim of thesis has been to investigate a range of metallocenes as internal reference standards in supercritical fluids, which could then be extended to the development of a new high pressure reactor. A range of metallocenes were investigated in liquid analogues of the supercritical fluids (acetonitrile and dichloromethane) to determine their suitability for use in supercritical fluids. Once the suitability of these metallocenes had been determined, they were extended to the supercritical systems (supercritical carbon dioxide with acetonitrile ($scCO_2$/MeCN (15 wt%)) and supercritical difluoromethane (scR32). The diffusion coefficients were determined at both micro and macro electrodes in supercritical fluids. Baffle electrodes were used to show that the intrinsic convection experienced in supercritical fluids can be dampened. The diffusion of metallocenes in nanoporous templated substrates of anodic aluminium oxide (13 and 55 nm diameter cylindrical pores) was also successfully investigated. The development of a new high pressure reactor has led to the first successful electrodeposition of bismuth in the reactor.

Chapter 1 gave an overview of supercritical fluid development from the discovery of a new fluid to its use in electrochemical measurements. Chapter 2 gave an overview of the experimental set-up and methods used throughout the thesis.

Chapter 3 showed the study of a variety of metallocenes in acetonitrile (MeCN) and dichloromethane (DCM). The metallocenes studied were decamethylferrocene (neutral to cation), decamethylcobaltocene (neutral to cation), cobaltocenium hexafluorophosphate (cation to neutral), decamethylcobaltocenium hexafluorophosphate (cation to neutral); one non-metallocene was also studied in dichloromethane in the form of sodium cobalticarborane (anion to neutral). Each compound was studied at micro and macro electrodes to determine their suitability for use in supercritical fluids, it was also important that the compounds be soluble in the liquid analogues of the supercritical fluids. Cyclic voltammetry was performed at micro and macro electrodes to determine the diffusion coefficient and reversibility of the redox couples. Analysis performed at micro electrodes through mass transport corrected Tafel analysis showed that all metallocenes exhibited 1 e^- process; the only metallocene that did not follow this trend was decamethylcobaltocenium hexafluorophosphate. Analysis performed at macro electrodes included Randles-Sevčik analysis and determination of the peak to peak potential separations. Randles-Sevčik analysis performed showed a linear plot that did not extrapolate to the origin in most cases, this was attributed to the lower viscosity of MeCN and DCM compared to aqueous systems leading to a mixing of the solution which contributes a small amount of convection.

Sodium Cobalticarborane was shown to not be suitable for further study in supercritical fluids due to its insolubility in DCM. Decamethylcobaltocenium hexafluorophosphate was also not studied further due to its extreme cathodic reduction potential. The diffusion coefficient for the compounds that were used in supercritical fluids were also determined at both micro and macro electrodes; a breakdown of these values can be seen in Table 7.1.

Table 7.1. Comparison of the diffusion coefficients determined from various solvents at different types of electrode, T = 298 K.

	MeCN / Micro-electrode	**DCM / Micro-electrode**	**MeCN / Macro-electrode**	**DCM / Macro-electrode**
DmFc	1.69×10^{-5} cm^2 s^{-1}	1.47×10^{-5} cm^2 s^{-1}	1.20×10^{-5} cm^2 s^{-1}	0.80×10^{-5} cm^2 s^{-1}
DmCo	1.33×10^{-5} cm^2 s^{-1}	N/A	N/A	N/A
$CoCp_2^+$ PF_6^-	1.90×10^{-5} cm^2 s^{-1}	N/A	1.31×10^{-5} cm^2 s^{-1}	N/A
$DmCo^+$ PF_6^-	N/A	1.31×10^{-5} cm^2 s^{-1}	N/A	0.90×10^{-5} cm^2 s^{-1}
Sodium cobalticarborane	N/A	N/A	N/A	N/A

Chapter 4 showed the study of the suitable metallocenes in the supercritical fluid equivalent of the liquid systems, supercritical carbon dioxide with acetonitrile co-solvent ($scCO_2$/MeCN (15 wt%) and supercritical difluoromethane (scR32). Decamethylferrocene was first studied in $scCO_2$/MeCN (15 wt%) at both micro and macro electrodes. Initial results performed at microelectrodes showed the presence of a film at the surface of the electrode. This film was removed using a preconditioning step; this preconditioning step involves cycling the electrode from -0.2 V to -3 V. Once this step has been performed, it does not need to be repeated during that experimental session. Voltammetry performed at micro electrodes showed a fluctuating steady state current which is caused by the intrinsic convection experienced when using supercritical fluids. Analysis performed at micro electrode through mass transport corrected Tafel analysis exhibited 1 e^- process for low concentrations but deviates from ideality as the concentration of DMFc was increased. This was attributed to higher uncompensated solution resistance from the low ratio of analyte to supporting electrolyte. The diffusion coefficient was determined at micro electrodes by plotting the diffusion limiting current against either the concentration of DMFc or the radii of the electrode. A baffle electrode was used to demonstrate that the natural convection of the supercritical fluid can be dampened. The voltammetry acquired at baffled microelectrodes showed results that are analogous to microelectrodes in liquid conditions. Results obtained at a macroelectrode showed that the uncompensated solution resistance of $scCO_2$/MeCN was 0.14 MΩ and the ratio of the peak currents were close to 1 for all scan rates. Comparison with simulated data showed good correlation when a convection layer of 0.016 cm was taken into consideration. A

preconditioning step did not need to be performed at the gold macro electrode suggesting the polymeric layer seen at micro electrodes is unique to the Pt metal itself.

Decamethylferrocene was also studied in scR32 at micro and macro electrodes. A preconditioning step is not required in scR32 suggesting the polymeric layer is due to the acetonitrile co solvent. The magnitude of natural convection seen on the diffusion limiting current at microelectrodes in scR32 is much larger compared to that in $scCO_2$/MeCN (15 wt%). This is due to the increase of temperature required to gain a single phase in scR32 (T = 360 K) compared to $scCO_2$/MeCN (T = 309 K). The diffusion coefficient determined at microelectrodes in scR32 is also higher than that determined for $scCO_2$/MeCN, Table 7.2. Analysis performed at microelectrodes through mass transport corrected Tafel analysis showed DMFc exhibited a 1 e^- process for all concentrations and did not deviate from ideality. The use of a baffle electrode demonstrated that the diffusion limited current should be taken from the minimum plateau of the "bare" electrode. Experiments performed at a macroelectrode showed that no well-defined voltammetry could be obtained until scan rates of 1 V/s, unless a baffled macroelectrode was used. Analysis at a baffled macro electrode showed the ratio of the peak currents was close to 1 for all scan rates. The diffusion coefficient determined at baffled macroelectrodes was much lower than those determined through microelectrodes, although it is unclear why this is the case.

Table 7.2. Comparison of the diffusion coefficients determined in different supercritical fluids, $scCO_2$/MeCN (15 wt%) (T = 309 K, p = 17.2 – 17.7 MPa) and scR32 (T = 360 K, p = 17.2 – 17.7 MPa)

DMFc	$scCO_2$/MeCN (15 wt%)	scR32
Microelectrode	$4.05 \pm 0.07 \times 10^{-5}$ cm^2 s^{-1}	$8.33 \pm 0.19 \times 10^{-5}$ cm^2 s^{-1}
Macroelectrode	$5.05 \pm 0.28 \times 10^{-5}$ cm^2 s^{-1}	$2.62 \pm 0.25 \times 10^{-5}$ cm^2 s^{-1}

Chapter 4 also provided the initial experiments of using cobaltocene complexes in supercritical fluids. Voltammetry was obtained for all complexes, but none showed any reproducible electrochemistry. Experiments performed with cobaltocenium hexafluorophosphate in $scCO_2$/MeCN (15 wt%) showed a process occurring at microelectrodes, but the process recorded on each scan was not reproducible. Cobaltocenium hexafluorophosphate was also tested in scR32, although not showing a reproducible process at macroelectrodes, the peak current does not scale with scan rate as expected from theory. This was attributed to oxygen bridging between the cobaltocene centres but could also be due to absorption of the cation ($CoCp_2^+$) and precipitation of the neutral complex ($CoCp_2$) on the electrode surface. Decamethylcobaltocenium hexafluorophosphate was tested with [Na][BARF] as supporting electrolyte, this showed that electrodeposition of Na occurs before any reduction potential of the cobaltocene was seen.

Chapter 5 demonstrated that decamethylferrocene can be used to study diffusion in templated nanoporous electrodes (anodic aluminium oxide, AAO) in supercritical fluids. Two sizes of nanopore were studied, 13 nm Ø AAO were studied in MeCN and $scCO_2$/MeCN (15 wt%), 13 and 55 nm Ø AAO were studied in scR32. Studies of decamethylferrocene in 13 nm Ø AAO in MeCN showed a redox process occurring and the ratio of the peak currents was close to one for all scan rates. Randles-Sevčik analysis was performed and the linear fit extrapolated to the origin, the diffusion coefficient was determined to be $D = 0.50 \times 10^{-5}$ cm^2 s^{-1} from the plot. Experiments performed in $scCO_2$/MeCN, using 13 nm Ø AAO electrodes, showed vastly different voltammetry to that obtained in MeCN. The electrochemical process (DMFc to $DMFc^+$) seen is the same but the diffusion and template effects are different in supercritical fluids. At slower scan rates, e.g. $\leq$ 50 mV/s, a sigmoidal wave response is seen on the anodic scan with a peak current response seen on the cathodic scan. At faster scan rates, e.g. $\geq$ 100 mV/s, a peak current response is seen on the anodic and cathodic scan. The sigmoidal response seen is due to the diffusion layer thickness, which at slow scan rates, extends the length of the pore and into the bulk. At faster scan rates the diffusion profile (e.g. the diffusion layer) only takes place within the pore. The cathodic peak seen on the reverse scan at slow scan rates could be due to either the adsorption of the $DMFc^+$ on the pore wall due to its small size, which is due to a negative charge associated with the pore wall. Another reason could be the build-up of a double layer (from the negative charge associated with the pore wall) which is responsible for trapping the $DMFc^+$ leading to it diffusing more slowly out of the pore and giving it a drastically different diffusion coefficient compared to the DMFc species. The diffusion coefficient calculated at 10 and 500 mV/s for the anodic scan was determined to be $D = 2.0 \times 10^{-5} \pm 2.2 \times 10^{-5}$ cm^2 s^{-1} and $D = 1.9 \times 10^{-5} \pm 1.4 \times 10^{-5}$ cm^2 s^{-1} respectively at $T = 309$ K and $\approx$ 17.2 MPa.

Decamethylferrocene was also studied in two sizes of nanopore (13 nm and 55 nm Ø AAO) in scR32. The voltammetry of DMFc recorded in 13 nm Ø AAO was analogous to that recorded in $scCO_2$/MeCN (15 wt%). Voltammetry of DMFc in 55 nm Ø AAO electrode showed a sigmoidal wave response for lower scan rates and did not show the cathodic peak recorded in 13 nm Ø AAO. The cathodic peak not being seen in the 55 nm Ø AAO is most likely due to its bigger diameter and area compared to the 13 nm Ø AAO. This means either the double layer does not hinder the diffusion $DMFc^+$ to the same extent, or the $DMFc^+$ adsorbs to the pore wall further away from the electrode surface. The ratio of the peak current was measured between 0.52 and 0.81 for the 13 nm Ø AAO electrode but was close to 1 for all scan rates in the 55 nm Ø AAO. The diffusion coefficient determined for the 13 nm Ø and 55 nm Ø AAO electrode at 10 mV/s was the same for both types and was determined to be $D = 3.6 \times 10^{-5}$ cm^2 s^{-1}. The diffusion coefficient at 500 mV/s for the 13 nm Ø and 55 nm Ø was

calculated to be $D = 8.5 \times 10^{-5} \pm 6.4 \times 10^{-5}$ cm^2 s^{-1} and $D = 2.6 \times 10^{-5} \pm 1.1 \times 10^{-5}$ respectively at $T = 360$ K and ≈ 17.8 MPa. The higher diffusion coefficient seen in the 13 nm Ø AAO electrode is most likely due to the higher current recorded because of the added complications of $DMFc^+$. Randles-Sevčik analysis was viable for the 55 nm Ø AAO electrode but not for the 13 nm Ø AAO electrode, this is most likely due to the complications of the cathodic peak seen in the 13 nm Ø AAO electrode.

Chapter 6 demonstrated that a newly designed high pressure reactor is suitable for electrochemical experiments through the study of decamethylferrocene and the electrodeposition of bismuth. Voltammetry performed in the plastic reactor showed that well-defined voltammetry (with little to no intrinsic convection) could be obtained at scan rates as low as 10 mV/s. The voltammetry obtained in the plastic reactor was comparable to that obtained in the steel cell. The uncompensated solution resistance estimated from the voltammetry in the plastic reactor was also comparable to that obtained in the steel cell. The ratio of the peak currents was close to 1 for all scan rates and was comparable to that obtained in the steel cell at macro electrodes. The diffusion coefficient was calculated to be $D = 6.19 \times 10^{-5}$ cm^2 s^{-1} (at 500 mV/s, $c = 0.4$ mM), which is again comparable to the diffusion coefficient determine at microelectrodes in the scR32. The first successful electrodeposition of bismuth was also performed in the newly developed reactor. Voltammetry of $[NBu_4^n][BiCl_4]$ showed characteristics deposition and stripping peaks along with a nucleation loop on the first scan. The diffusion coefficient of the $[NBu_4^n][BiCl_4]$ complex was determined to be $D = 1.69 \times 10^{-4}$ cm^2 s^{-1} which was higher than that recorded for DMFc at the same electrode and higher than that recorded at microelectrodes for DMFc in scR32. The morphology of the deposited product looked crystalline and had a “christmas tree” or “aloe vera leaf” like appearance. The thickest areas of deposit showed a strong bismuth signal with no impurities. Oxygen was observed in some EDX spectrum, but this was attributed to the samples being handled in air before being placed into the SEM for analysis. The bismuth films also showed good adherence to the gold substrate upon which it was deposited.

7.1 Further Work

As mentioned in the conclusions, the cobaltocene complexes failed to produce any reproducible electrochemistry in the supercritical fluids. Further investigations are required to gain reproducible voltammetry of the cobaltocene complexes in scR32. The use of charged cobaltocene complexes (e.g. $[CoCp_2]^+[PF_6]^-$) will allow a second redox couple to be studied as an internal reference standard in scR32. These could also be used in conjunction with DMFc to study the half wave potential separation in different supercritical solvents.

Decamethylcobaltocenium hexafluorophosphate shows the most promise for use as a charged cobaltocene complex in scR32. Further investigations would need to be performed to find a suitable supporting electrolyte that would allow the reduction of decamethylcobaltocenium hexafluorophosphate to be studied. These charged cobaltocene complexes would also be important to understanding the diffusion in nanoporous templated electrodes. The use of a positively charged cobaltocene complexes would help to confirm the presence of a negative charged associated with the AAO pore wall. A negatively charged redox couple would also be useful in this instance. Further investigations would be required to find a suitable negatively charged redox couple for use in supercritical fluids.

Further investigations will need to be performed to confirm the presence of the negative charge associated with the AAO pore wall under supercritical conditions. As mentioned, a positively or negatively charged redox species could be used to study their diffusion in nanopores under supercritical conditions. Further experiments would involve varying the concentration of supporting electrolyte when studying the diffusion of DMFc in nanopores under supercritical conditions. The change in concentration of supporting electrolyte should change any double layer length, giving a different electrochemical response if the theory is correct. Modification of the pore wall could also be made to negate the negative charge associated with the pore wall.

This thesis also presented the first experiments performed in the newly designed high pressure reactor. The plastic reactor could be modified to have a Pt wire replace the thermocouple, once this has been performed, further experiments with DMFc could be performed to see if the *iR* drop seen in the voltammetry is reduced. Further experiments in the plastic reactor would involve the use of complexes and reagents that are corrosive to stainless steel. If successful electrochemistry can be performed with these complexes, then the plastic reactor will have met another of its goal and could be used as an alternative to the steel reactor. Further investigations in the plastic reactor would also involve the use of a new template (Matefi-Tempfli, AAO nanopores, with shorter length pores (500 to 1500 nm length) which can be made on any substrate (Au, Pt, TiN etc.)) which can be used to electrodeposit the first nanowires from the new reactor

References

1. Cagniard de la Tour, C. *Ann. Chim. Phys.* **1822**, *21*, 127.
2. Cagniard de la Tour, C. *Ann. Chim. Phys.* **1823**, *22*, 410.
3. Berche, B.; Henkel, M.; Kenna, R. *J. Phys. Stud.* **2009**, *31*, 2602.1.
4. Faraday, M. *Philosophical Transactions* **1845**, *135*, 155.
5. Mendeleev, D. *Annalen der Chemie und Pharmazie* **1861**, *119*, 1.
6. Andrews, T. *Phil. Trans. Roy. Soc. Lond.* **1869**, *159*, 575.
7. Romang, A. H.; Watkins, J. J. *Chem. Rev.* **2009**, *110*, 459.
8. Abbott, A. P.; Harper, J. C. *Phys. Chem. Chem. Phys.* **1999**, *1*, 839.
9. Abbott, A. P.; Eardley, C. A. *J. Phys. Chem. B* **1999**, *103*, 2504.
10. Barrett, C. A.; Gunning, R. D.; Hantschel, T.; Arstila, K.; O'Sullivan, C.; Geaney, H.; Ryan, K. M. *J. Mater. Chem.* **2010**, *20*, 135.
11. Cabanas, A.; Long, D. P.; Watkins, J. J. *Chem. Mater.* **2004**, *16*, 2028.
12. Chung, S. T.; Tsai, W. T. *Thin Solid Films* **2010**, *518*, 7236.
13. Karanikas, C. F.; Watkins, J. J. *Microelectron. Eng.* **2009**, *87*, 566.
14. Ke, J.; Su, W. T.; Howdle, S. M.; George, M. W.; Cook, D.; Perdjon-Abel, M.; Bartlett, P. N.; Zhang, W. J.; Cheng, F.; Levason, W.; Reid, G.; Hyde, J.; Wilson, J.; Smith, D. C.; Mallik, K.; Sazio, P. *Proc. Natl. Acad. Sci. U. S. A.* **2009**, *106*, 14768.
15. Cabrera, C. R.; Bard, A. J. *J. Electroanal. Chem.* **1989**, *273*, 147.
16. Goldfarb, D. L.; Corti, H. R. *J. Phys. Chem. B* **2004**, *108*, 3358.
17. Abbott, A. P.; Corr, S.; Durling, N. E.; Hope, E. G. *J. Phys. Chem. B* **2003**, *107*, 10628.
18. Abbott, A. P.; Eltringham, W.; Hope, E. G.; Nicola, M. *Green Chemistry* **2005**, *7*, 721.
19. Silvestri, G.; Gambino, S.; Filardo, G.; Cuccia, C.; Guarino, E. *Angewandte Chemie-International Edition in English* **1981**, *20*, 101.
20. Savage, P. E.; Gopalan, S.; Mizan, T. I.; Martino, C. J.; Brock, E. E. *AlChE J.* **1995**, *41*, 1723.
21. Cabrera, C. R.; Garcia, E.; Bard, A. J. *J. Electroanal. Chem.* **1989**, *260*, 457.
22. Crooks, R. M.; Bard, A. J. *J. Electroanal. Chem.* **1988**, *243*, 117.
23. Crooks, R. M.; Bard, A. J. *J. Electroanal. Chem.* **1988**, *240*, 253.
24. Crooks, R. M.; Bard, A. J. *J. Phys. Chem.* **1987**, *91*, 1274.
25. McDonald, A. C.; Fan, F. R. F.; Bard, A. J. *J. Phys. Chem.* **1986**, *90*, 196.
26. Flarsheim, W. M.; Tsou, Y. M.; Trachtenberg, I.; Johnston, K. P.; Bard, A. J. *J. Phys. Chem.* **1986**, *90*, 3857.
27. Crooks, R. M.; Fan, F. R. F.; Bard, A. J. *J. Am. Chem. Soc.* **1984**, *106*, 6851.
28. Bard, A. J.; Flarsheim, W. M.; Johnston, K. P. *J. Electrochem. Soc.* **1988**, *135*, 1939.
29. Michael, A. C.; Wightman, R. M. *Anal. Chem.* **1989**, *61*, 2193.
30. Abbott, A. P.; Harper, J. C. *J. Chem. Soc.-Faraday Trans.* **1996**, *92*, 3895.
31. Goldfarb, D. L.; Fernandez, D. P.; Corti, H. R. *Fluid Phase Equilib.* **1999**, *158*, 1011.
32. Abbott, A. P.; Eardley, C. A. *J. Phys. Chem. B* **2000**, *104*, 775.
33. Blackburn, J. M.; Long, D. P.; Cabanas, A.; Watkins, J. J. *Science* **2001**, *294*, 141.
34. Yoshida, H.; Sone, M.; Mizushima, A.; Abe, K.; Tao, X. T.; Ichihara, S.; Miyata, S. *Chem. Lett.* **2002**, 1086.
35. Badlani, R. N.; Mayer, J. L.; Anderson, P. E.; Mabrouk, P. A. *Abstracts of Papers American Chemical Society* **2002**, *224*, 587.
36. Anderson, P. E.; Badlani, R. N.; Mayer, J.; Mabrouk, P. A. *J. Am. Chem. Soc.* **2002**, *124*, 10284.
37. Hunde, E. T.; Watkins, J. J. *Chem. Mater.* **2004**, *16*, 498.
38. Yoshida, H.; Sone, M.; Wakabayashi, H.; Yan, H.; Abe, K.; Tao, X. T.; Mizushima, A.; Ichihara, S.; Miyata, S. *Thin Solid Films* **2004**, *446*, 194.
39. Kim, M. S.; Kim, J. Y.; Kim, C. K.; Kim, N. K. *Chemosphere* **2005**, *58*, 459.
40. Yan, H.; Sato, T.; Komago, D.; Yamaguchi, A.; Oyaizu, K.; Yuasa, M.; Otake, K. *Langmuir* **2005**, *21*, 12303.
41. O'Neil, A.; Watkins, J. J. *Chem. Mater.* **2007**, *19*, 5460.

42. Kong, C. Y.; Nakamura, M.; Sone, K.; Funazukuri, T.; Kagei, S. *J. Chem. Eng. Data* **2010**, *55*, 3095.
43. Cook, D.; Bartlett, P. N.; Zhang, W. J.; Levason, W.; Reid, G.; Ke, J.; Su, W. T.; George, M. W.; Wilson, J.; Smith, D.; Mallik, K.; Barrett, E.; Sazio, P. *Phys. Chem. Chem. Phys.* **2010**, *12*, 11744.
44. Toghill, K. E.; Voyame, P.; Momotenko, D.; Olaya, A. J.; Girault, H. H. *Phys. Chem. Chem. Phys.* **2013**, *15*, 972.
45. Bartlett, P. N.; Perdjon-Abel, M.; Cook, D.; Reid, G.; Levason, W.; Cheng, F.; Zhang, W.; George, M. W.; Ke, J.; Beanland, R.; Sloan, J. *ChemElectroChem* **2014**, *1*, 187.
46. Bartlett, P. N.; Cook, D. C.; George, M. W.; Ke, J.; Levason, W.; Reid, G.; Su, W. T.; Zhang, W. J. *Phys. Chem. Chem. Phys.* **2009**, *12*, 492.
47. Yoshida, H.; Sone, M.; Mizushima, A.; Yan, H.; Wakabayashi, H.; Abe, K.; Tao, X. T.; Ichihara, S.; Miyata, S. *Surface & Coatings Technology* **2003**, *173*, 285.
48. Ohde, H.; Hunt, F.; Kihara, S.; Wai, C. M. *Anal. Chem.* **2000**, *72*, 4738.
49. Cabanas, A.; Blackburn, J. M.; Watkins, J. J. *Microelectron. Eng.* **2002**, *64*, 53.
50. Byun, H. S.; Hasch, B. M.; McHugh, M. A. *Fluid Phase Equilib.* **1996**, *115*, 179.
51. Licence, P.; Dellar, M. P.; Wilson, R. G. M.; Fields, P. A.; Litchfield, D.; Woods, H. M.; Poliakoff, M.; Howdle, S. M. *Rev. Sci. Instrum.* **2004**, *75*, 3233.
52. Wakayama, H.; Fukushima, Y. *Ind. Eng. Chem. Res* **2006**, *45*, 3328.
53. Niehaus, D.; Philips, M.; Michael, A.; Wightman, R. M. *J. Phys. Chem.* **1989**, *93*, 6232.
54. Kazemi, S.; Belandria, V.; Janssen, N.; Richon, D.; Peters, C. J.; Kroon, M. C. *J. Supercrit. Fluids* **2012**, *72*, 320.
55. Yan, H.; Sone, M.; Sato, N.; Ichihara, S.; Miyata, S. *Surface & Coatings Technology* **2004**, *182*, 329.
56. Chanfreau, S.; Cognet, P.; Camy, S.; Condoret, J. S. *J. Electroanal. Chem.* **2007**, *604*, 33.
57. Abbott, A. P.; Eardley, C. A.; Harper, J. C.; Hope, E. G. *J. Electroanal. Chem.* **1998**, *457*, 1.
58. Abbott, A. P.; Eardley, C. A. *J. Phys. Chem. B* **2000**, *104*, 9351.
59. Olsen, S. A.; Tallman, D. E. *Anal. Chem.* **1996**, *68*, 2054.
60. Abbott, A. P.; Eardley, C. A. *J. Phys. Chem. B* **1999**, *103*, 6157.
61. Abbott, A. P.; Corr, S.; Durling, N. E.; Hope, E. G. *J. Chem. Eng. Data* **2002**, *47*, 900.
62. Abbott, A. P.; Hope, E. G.; Palmer, D. J. *Anal. Chem.* **2005**, *77*, 6702.
63. Bartlett, P. N.; Cook, D. C.; George, M. W.; Ke, J.; Levason, W.; Reid, G.; Su, W.; Zhang, W. *Phys. Chem. Chem. Phys.* **2011**, *13*, 190.
64. Bartlett, P. N.; Cook, D. A.; George, M. W.; Hector, A. L.; Ke, J.; Levason, W.; Reid, G.; Smith, D. C.; Zhang, W. *Phys. Chem. Chem. Phys.* **2014**, *16*, 9202.
65. Williams, R. A.; Naidith, S. *Phys. Chem. Liq.* **1970**, *2*, 67.
66. Atobe, M.; Ohsuka, H.; Fuchigami, T. *Chem. Lett.* **2004**, *33*, 618.
67. Cabanas, A.; Shan, X. Y.; Watkins, J. J. *Chem. Mater.* **2003**, *15*, 2910.
68. Ke, J.; Bartlett, P. N.; Cook, D.; Easun, T. L.; George, M. W.; Levason, W.; Reid, G.; Smith, D.; Su, W. T.; Zhang, W. J. *Phys. Chem. Chem. Phys.* **2012**, *14*, 1517.
69. Dayeh, S. A.; Picraux, S. T. *Nano Lett.* **2010**, *10*, 4032.
70. Noviandri, I.; Brown, K. N.; Fleming, D. S.; Gulyas, P. T.; Lay, P. A.; Masters, A. F.; Phillips, L. *J. Phys. Chem. B* **1999**, *103*, 6713.
71. Gritzner, G.; Kuta, J. *Pure Appl. Chem.* **1984**, *56*, 461.
72. Rogers, E. I.; Silvester, D. S.; Poole, D. L.; Aldous, L.; Hardacre, C.; Compton, R. G. *Journal of Physical Chemistry C* **2008**, *112*, 2729.
73. Bashkin, J. K.; Kinlen, P. J. *Inorg. Chem.* **1990**, *29*, 4507.
74. Gennett, T.; Milner, D. F.; Weaver, M. J. *The Journal of Physical Chemistry* **1985**, *89*, 2787.
75. Koelle, U.; Khouzami, F. *Angewandte Chemie International Edition in English* **1980**, *19*, 640.
76. Robbins, J. L.; Edelstein, N.; Spencer, B.; Smart, J. C. *J. Am. Chem. Soc.* **1982**, *104*, 1882.

77. Ching, S.; McDevitt, J. T.; Peck, S. R.; Murray, R. W. *J. Electrochem. Soc.* **1991**, *138*, 2308.
78. Richardson, J. N.; Harvey, J.; Murray, R. W. *The Journal of Physical Chemistry* **1994**, *98*, 13396.
79. Stojanovic, R. S.; Bond, A. M. *Anal. Chem.* **1993**, *65*, 56.
80. Aranzaes, J. R.; Daniel, M. C.; Astruc, D. *Canadian Journal of Chemistry-Revue Canadienne De Chimie* **2006**, *84*, 288.
81. Barrosse-Antle, L. E.; Bond, A. M.; Compton, R. G.; O'Mahony, A. M.; Rogers, E. I.; Silvester, D. S. *Chemistry-an Asian Journal* **2010**, *5*, 202.
82. Lewandowski, A.; Waligora, L.; Galinski, M. *Electroanalysis* **2009**, *21*, 2221.
83. Torriero, A. A. J.; Sunarso, J.; Forsyth, M.; Pozo-Gonzalo, C. *Phys. Chem. Chem. Phys.* **2013**, *15*, 2547.
84. Olsen, S. A.; Tallman, D. E. *Anal. Chem.* **1994**, *66*, 503.
85. Goldfarb, D. L.; Corti, H. R. *Electrochem. Commun.* **2000**, *2*, 663.
86. Goldfarb, D. L.; Corti, H. R. *J. Phys. Chem. B* **2004**, *108*, 3368.
87. Toghill, K. E.; Méndez, M. A.; Voyame, P. *Electrochem. Commun.* **2014**, *44*, 27.
88. Wu, X.-J.; Zhu, F.; Mu, C.; Liang, Y.; Xu, L.; Chen, Q.; Chen, R.; Xu, D. *Coord. Chem. Rev.* **2010**, *254*, 1135.
89. Md Jani, A. M.; Losic, D.; Voelcker, N. H. *Prog. Mater Sci.* **2013**, *58*, 636.
90. Davies, T. J.; Compton, R. G. *J. Electroanal. Chem.* **2005**, *585*, 63.
91. Bartlett, P. N.; Taylor, S. L. *J. Electroanal. Chem.* **1998**, *453*, 49.
92. Amatore, C.; Oleinick, A. I.; Svir, I. *Anal. Chem.* **2009**, *81*, 4397.
93. Guo, J.; Lindner, E. *J. Electroanal. Chem.* **2009**, *629*, 180.
94. Arrigan, D. W. M. *Analyst* **2004**, *129*, 1157.
95. Perera, D. M. N. T.; Ito, T. *Analyst* **2010**, *135*, 172.
96. Trasatti, S.; Petrii, O. A. *Pure Appl. Chem.* **1991**, *63*, 711.
97. Elliott, J. M.; Birkin, P. R.; Bartlett, P. N.; Attard, G. S. *Langmuir* **1999**, *15*, 7411.
98. Jerkiewicz, G.; Vatankhah, G.; Lessard, J.; Soriaga, M. P.; Park, Y. S. *Electrochim. Acta* **2004**, *49*, 1451.
99. Giovanelli, D.; Lawrence, N. S.; Compton, R. G. *Electroanalysis* **2004**, *16*, 789.
100. Pletcher, D. *A First Course in Electrode Processes*; 2nd ed.; RSC Publishing: Cambridge, 2009.
101. Sevcik, A. *Collect. Czech. Chem. Commun.* **1948**, *13*, 349.
102. Randles, J. E. B. *Trans. Farad. Soc* **1948**, *44*, 322.
103. Klymenko, O. V.; Compton, R. G. *J. Electroanal. Chem.* **2004**, *571*, 207.
104. Mirkin, M. V.; Bard, A. J. *Anal. Chem.* **1992**, *64*, 2293.
105. Denuault, G.; Mirkin, M. V.; Bard, A. J. *J. Electroanal. Chem.* **1991**, *308*, 27.
106. Gennett, T.; Milner, D. F.; Weaver, M. J. *J. Phys. Chem.* **1985**, *89*, 2787.
107. Matsumoto, M.; Swaddle, T. W. *Inorg. Chem.* **2004**, *43*, 2724.
108. Bruckenstein, S.; Janiszewska, J. *J. Electroanal. Chem.* **2002**, *538–539*, 3.
109. Kojima, H.; Takahash.S; Yamazaki, H.; Hagihara, N. *Bull. Chem. Soc. Jpn.* **1970**, *43*, 2272.
110. Kojima, H.; Takahash.S; Hagihara, N. *Journal of the Chemical Society-Chemical Communications* **1973**, 230.
111. Kojima, H.; Takahash.S; Hagihara, N. *Tetrahedron Lett.* **1973**, 1991.
112. Cooper, J. B.; Bond, A. M. *Anal. Chem.* **1993**, *65*, 2724.
113. Bard, A. J.; Faulkner, L. R. *Electrochemical Methods: Fundamentals and Applications*; 2nd ed.; John Wiley & Sons, 2001; Vol. 2nd Ed.
114. Lodge, A. W.; Lacey, M. J.; Fitt, M.; Garcia-Araez, N.; Owen, J. R. *Electrochim. Acta* **2014**, *140*, 168.
115. Barnes, A. S.; Rogers, E. I.; Streeter, I.; Aldous, L.; Hardacre, C.; Wildgoose, G. G.; Compton, R. G. *Journal of Physical Chemistry C* **2008**, *112*, 13709.
116. Buzzeo, M. C.; Klymenko, O. V.; Wadhawan, J. D.; Hardacre, C.; Seddon, K. R.; Compton, R. G. *J. Phys. Chem. A* **2003**, *107*, 8872.

117. Bartlett, P. N.; Cook, D.; de Groot, C. H.; Hector, A. L.; Huang, R.; Jolleys, A.; Kissling, G. P.; Levason, W.; Pearce, S. J.; Reid, G. *Rsc Advances* **2013**, *3*, 15645.